MONTE CARLO SIMULATIONS OF MARTENSITIC STRAIN-PSEUDOSPIN MODELS

A thesis submitted in partial fulfillment for the award of the Degree of

DOCTOR OF PHILOSOPHY

in

PHYSICS

by

NADDI SHANKARAIAH

SCHOOL OF PHYSICS
UNIVERSITY OF HYDERABAD
HYDERABAD 500 046, INDIA
June 2012

DECLARATION

I here by declare that the work reported in this thesis entitled **"Monte Carlo simulations of Martensitic strain-pseudospin models"** has been carried out by me independently in the School of Physics, University of Hyderabad, under the supervision of Prof. K.P.N. Murthy. I also declare that this is my own work and effort, and it has not been submitted at any other University or Institution for any degree.

Date: (N. Shankaraiah)

Place:

CERTIFICATE

This is to certify that the work contained in this thesis entitled **"Monte Carlo simulations of Martensitic strain-pseudospin models"** has been carried out by Mr. **NADDI SHANKARAIAH** (Reg. No. 06PHPH09), under my direct supervision and the same has not been submitted for the award of research degree of any University.

Date:
Place:

Prof. K.P.N. Murthy
Thesis Supervisor

The Dean
School of Physics
University of Hyderabad

To

My Parents & Teachers

ACKNOWLEDGEMENTS

It is my pleasure to thank Prof. K.P.N. Murthy for his wonderful, friendly guidance and for teaching me Monte Carlo techniques.
I would like to express my deepest gratitude to Prof. Subodh R. Shenoy for his guidance, patience, motivation, encouragement, and support in many ways from the beginning to submission of this thesis. I would not have completed this work without him. Thank you Sir for being with me in all times during the evolution of my scientific knowledge over these years.
My sincere thanks to Prof. Turab Lookman for his help, encouragement and active collaboration throughout this work.
I thank Prof. V.S.S. Sastry for being my doctoral committee member and teaching me Quantum Mechanics, and for thought provoking ideas.
I would like to thank Dean School of Physcis, Prof. C. Bansal for allowing me to use the facilities in the School.
I am greatful to thank Dr. Venkatesh Shenoi (CDAC-PUNE), for his friendship and help and also Dr. Rajeev Kapri (IISER-Mohali) for his help.
I also would like to thank Dr. V. Ashoka, for his valuable suggestions and help regarding submission of programs on APPLE cluster in WAX-Lab, where I carried out most of the Monte Carlo simulations related to this thesis.
I thank all my PhD course work teachers: Prof. Subodh.R. Shenoy, Prof. A.K. Kapoor, Prof. V.S.S. Sastry, Prof. K.P.N. Murthy. I would like to thank Prof. Bindu A. Bambah for giving me an oppurtunity as a tutor to learn group theory and complex numbers.
It is my pleasure to thank my PhD-2006 batchmates (Yugandhar, Arun, Ali, Vasu, Bheemalingam, Anil, Venkaiah, Vijayan, Rambabu, Sita, Balaji, Parthasarathy, Sendil, Deepak, Rangababu), and PhD juniors and seniors for their friendship and help in good and bad times. I would like to thank to

M.Tech (CT) batch (2006-2008) for their friendship and help. I also would to thank WAX-lab members Sudha and Anil for their help and patience for tolerating me all these years.

I would definitely thank my sweet juniors M. Suman Kalyan and S. Siva Nasarayya Chari for their help and friendship in all these years. I also would like to thank Boltzmann group members for sharing their ideas.

Abraham, Pentaiah, and Chandrapal are acknowledged for their help.

Financial support in the form of PhD Fellowship from University (BBL), UGC-CAS, and BSR is greatly acknowledged. PURSE-Grant for financial support to attend ICMAT-2011, at Singapore is appreciated. I thank CMSD for computational support, ICTP for (partial) financial support for a short visit, and IISER-TVM for supporting my stay during my visit.

My lovely parents, supported and encouraged me to complete this work on every tick of the clock. Without their LOVE, I would not have completed any of this work. I also would like to thank Anji and my other family members for their support.

Finally, to the beautiful University of Hyderabad for creating a wonderful work environment with its beauty inspite of all complications around.

N. Shankaraiah

ABSTRACT

We apply martensitic strain-pseudospin models to understand delay time issues in martensitic materials and general re-equilibration issues in nonequilibrium aging systems. Systematic Monte Carlo temperature quench simulations on pseudospin models shows that the athermal/isothermal martensites classification is a matter of material parameters. In the athermal regime, there are fast conversions below a spinodal temperature and delay tails above it as in experiment. We find the conversion delays have Vogel-Fulcher divergences at a temperature, that is well below the Landau transition temperature, and Log-normal distributions from rare conversion channels and insensitivity to Hamiltonian energy scales, as a signature of entropy barrier dominance. In the re-equilibration process after a temperature quench, we find that the system behaves as 'temporarily microcanonical' or it is partially equilibriated on a constant energy surface at a time-dependent effective temperature. The effective temperature reaches the bath-temperature in the equilibrium. The concepts of golf holes and funnels from protein folding models; and partial equilibration, effective temperatures, and entropy barriers from models for glasses are used to understand the re-equilibration processes in martensites.

Contents

1

Introduction

In this thesis, we apply discrete-strain pseudospin clock-zero models using Monte Carlo simulations to study two problematic themes: (i) a materials science theme, of the onset of ordering in structural transitions; and (ii) a nonequilibrium statistical mechanics theme, of re-equilibration of aging systems after deep temperature quenches. In this introductory Chapter, we outline how these two problems are clarified by models of martensitic transformations, that occur in functional materials such as steels and shape memory alloys. We briefly discuss the Metropolis algorithm that we use to carry out systematic temperature quench Monte Carlo simulations on pseudospin models derived from suitably scaled strain free energies. Finally, we present a brief summary of the Chapters that treat the above two themes.

1.1 Martensitic transformations

In phase transitions, an *order parameter* (OP) is an important physical quantity, that is zero in the (single) disordered phase and nonzero in ordered phase, with the different non-zero values characterising the ordered phases. For example, magnetization is the OP for the paramagnetic to ferromagnetic phase transition, with different possible directions. In classic work, Ginzburg and Landau introduced a phenomenological approach for first and second order phase transitions, in terms of symmetry-allowed polynomials in the characteristic OP.

By the text book definition (Kittel), a unit cell is a building block of a crystal that is a regular periodic array of atoms, identical in arrangement, composition and orientation. For crystalline materials that can undergo structural phase transformations on cooling below the transition temperature, the shape of the unit cell can spontaneously change, with its distortion relative to the high-temperature unit cell described by a *strain tensor*. A subset of strain components form the OP, in terms of which there is *spontaneous strain* on ordering. In martensitic materials, the (single) high-temperature unit cell or parent phase is called '*austenite*' and low-temperature unit cell or product phase is '*martensite*' after the discoverers Austen and Martens, respectively. The several degenerate unit cells in martensite are called *'variants'*. Steels, shape memory alloys, high-T_c superconductors, ferroelastics, and ferroelectrics are examples of materials that can have structural transformations on cooling, or under an external stress. A better understanding of their transformation dynamics could help to improve material functionalities.

Martensitic transformations are characterised as diffusionless, and lattice-distortive transitions with no compositional change, whose kinetics and morphology are dominated by strain energy [1–3]. On quenching below the transition temperature, instead of a uniform, single-variant state, martensites

can show mesoscale *twinned* states or a spatial coexistence of N_V different variants, separated by domain walls, that are oriented in preferred crystallographic directions [1, 4, 5]. A nanoscale 'tweed' texture, or cross-hatched pattern of variants can appear near transition as a twin precursor [5]. The orientations of the elastic domain walls can be understood from the presence of power-law anisotropic potentials $1/R^d$ (where d is the dimension) were first found by Kartha et al [6], and are related to the elastic potential of twins found by Barsch et al [6]. These potentials between OP strains are induced from the no-defect *St.Venant compatibility constraint*, that says no dislocations are generated during the spontaneous distortion of the unit cells as in Chandrasekharaiah and Debnath; and Baus and Lovett [6].

In ferroelastic martensites, the symmetry of the low-temperature unit cell can be subgroup of the high-temperature unit cell symmetry. This is shown in Figure 1.1 for a square-rectangle transition in 2-dimensions (2D) and a cubic-tetragonal transition in 3-dimensions (3D).

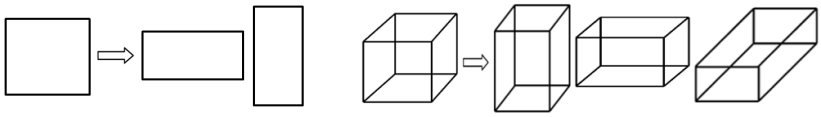

Figure 1.1: *Ferroelastic structural transitions:* (a). A square-rectangle transition has a single high temperature parent phase 'austenite' (square) and two low temperature product phases or 'martensite' variants (rectangles). Note the symmetry group of rectangle is a subgroup of the symmetry group of square. (b). Similarly, a cubic-tetragonal transition has a single cubic 'austenite' phase and three tetragonal 'martensite' variants.

Martensitic transformations are typically first-order phase transitions, with consequent hysteresis. On temperature cycling through the transition, martensitic materials can show acoustic emissions and latent heat releases and other memory effects [7].

On cooling below transition, martensites are classified as *athermal*, with *fast* conversions in milli-seconds below a martensite start temperature M_s; and *isothermal*, with *slow* conversions in minutes or hours [2, 17]. In a Temperature -Time -Transformation (TTT) diagram, that is familiar in steels [2, 8], the classical isothermal conversion curve is 'C'-shaped in temperature (y-axis) versus time (x-axis) plots; whereas the classical athermal curve was believed to be flat at 'zero' conversion time, right up to a vertical boundary at M_s. See Figure 1.2. The 'C'-shaped isothermal curve is understood as the activation delay over *energy* barriers, involving a competition on cooling, between a decrease in free energy, and a rise in activated costs $\sim e^{\frac{1}{T}}$. By contrast, athermal martensites were believed to have no such activation barriers, and so converted explosively, immediately below M_s, and not at all, above it.

1.2 Motivation

We now discuss the specific questions in martensitic materials and general issues in nonequilibrium systems, that we attempt to understand in this thesis. We use simple statistical mechanics models to make contact with some of the literature [1–52].

1.2.1 Conversion-delay issues in athermal martensites

As mentioned, athermal martensites were believed to have fast austenite-martensite conversions on cooling below M_s and no conversions above it [2, 17]. Experiments on an athermal martensitic alloy Fe-Ni and shape memory alloy Cu-Al-Ni by Kakeshita et al [9] indeed found fast conversions below M_s as expected. However, on holding at temperatures $\sim 4\%$ *above* M_s, there were unexpected *delayed conversions* taking thousands of seconds, in a class

of materials that supposedly had no energy barriers; and in a temperature region where only austenite should exist. This result called into question the whole traditional classification of martensites. Klemradt et al [10] confirmed such conversion-delay tails in another athermal martensitic alloy, Ni-Al. A statistical model for nucleated clusters or droplets, with inverse conversion times as probabilities [11], found times to rise exponentially in $T - M_s$ as in data. Planes et al [12, 13] considered metastable austenite in a triple-well Landau free energy. The stochastic first-passage-times for austenite converting to martensite became detectably small only around a temperature $M_s \gtrsim$ just above the austenite spinodal T_c; and very large much above M_s [13]. Both models [11, 13] imply that for *any* temperature in between, $T_0 > T > M_s$, there should be a conversion, if one waits long enough. Here, T_0 is the thermodynamic transition temperature, where the austenite and martensite minima are degenerate. On the other hand, in Ti-Ni athermal martensitic alloy, Otuska et al [14] found *no* delayed conversions on holding at temperatures $\sim 2\%$ above M_s, even after annealing for 21 days (!). In an interesting review by Müller et al [15], it is suggested that these three results need to be reconciled, to clarify the distinction between athermal/isothermal martensites. These three scenarios are shown schematically in Figure 1.2, where we plot time (y-axis) versus temperature (x-axis), so the isothermal 'C'-curve becomes a 'U'-curve.

The above conversion issue is a puzzling delay tail appearing in an athermal material. However there are older conversion issues, including a given material showing both athermal and isothermal curves, depending on *initial conditions*. In early work, Pati and Cohen [16] have measured and modeled the conversion times in Ni-Mn alloys and found that the isothermal slow conversions can change to athermal fast conversions, for fixed martensite fraction, but with *larger* (and hence fewer) initial martensite seeds. Under magnetic field and hydrostatic pressure, Kakeshita et al [16] found that the

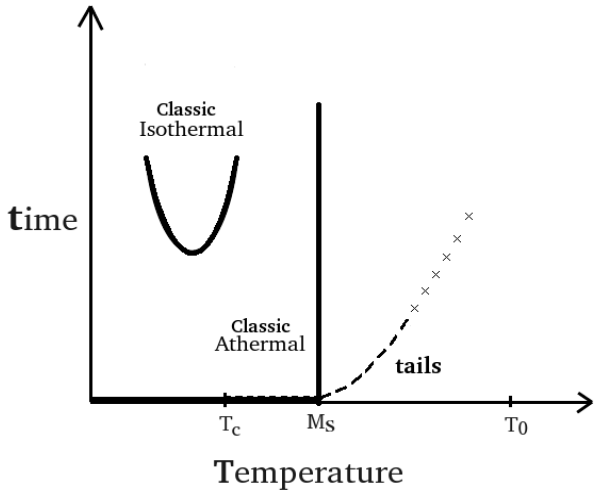

Figure 1.2: *Schematic of athermal/ isothermal TTT curves:* Heavy lines: classic isothermal and athermal boundaries, with athermal 'martensite-start' temperature M_s marked. Temperatures T_0, T_c are the Landau transition and (uniform) austenite spinodal [12] respectively. Dash-line: conversion-delays as found [9, 10]. Cross-line: conversion not found [14].

athermal conversions can change to isothermal or vice versa, in iron-based alloys. The slow conversions at high temperatures above M_s have already been mentioned. So, it is not that one class of materials is intrinsically 'fast' (athermal) and the other is intrinsically 'slow' (isothermal). The same material can be fast or slow, depending on conditions. Furthermore, the phenomenon of *incubation* or seemingly flat values of a measured parameter for very long times, and then sudden changes, is a long-standing puzzle [17].

Broadly, the issues in martensitic evolution that need to be understood are:

- What is the physical basis for the athermal/isothermal classification ?
- Why are conversion-delay tails or incubations seen in athermal marten-

sites, that are supposedly have no energy barriers, and so no activated costs; and what is the nature of the delay-causing barriers ?

- How can evolution kinetics be so qualitatively different, for different initial seeds ?

1.2.2 Nonequilibrium issues in aging systems

Physical systems that also show long time-delays as in athermal martensites, are glass-forming supercooled liquids [18], that take long (indeed, divergent) times to freeze to a crystal; and proteins, that can have both surprisingly fast folding dynamics (Levinthal paradox), and slow unfolding dynamics [19–22]. Above glassy freezing, a singularly divergent time $t \sim e^{\frac{1}{|T-T_K|}}$ was found in the 1920's by Vogel and Fulcher, where T_K is the Kauzmann temperature [18]. Interestingly, Vogel-Fulcher delays are also seen in protein unfolding [21]. Powerlaw, or infinite-range interactions considered by Ruffo et al [46] are known to produce quasi-stationary states or slow relaxation.

A central idea in this thesis is that barriers can be of *two* types, as times depend on free energy barriers ΔF as $\{t \sim e^{\frac{\Delta F}{T}}\}$ and $\Delta F = \Delta U - T\Delta S$. Hence, there can be both energy barriers ($\Delta U > 0$) and *entropy barriers* ($|\Delta S| = -\Delta S > 0$) with times in general depending on both as $\{t \sim e^{\frac{\Delta U}{T}} e^{+|\Delta S|}\}$. One can have regimes in which dominant delays are activated over energy barriers $\{t \sim e^{\frac{\Delta U}{T}}\}$; and regimes where no energy barriers are crossed $\Delta U = 0$, but the non-activated dominant delays caused by entropy barriers $\{t \sim e^{|\Delta S|}\}$.

Ritort proposed a non-interacting particle model *without* energy barriers [23], and found slow aging dynamics from entropy barriers only. Bicout and Szabo considered toy models for protein folding, involving Brownian particles randomly moving into *golf holes* containing *funnels* [20], with entropy barriers to finding the energy-lowering pathways. Non-interacting oscillator

models, with energies relaxing as $E(t) \sim 1/log(t)$ under analytic Monte Carlo dynamics, show an *effective temperature*, that evolves to bath temperature for long holding times [24]. An effective temperature is also defined from the conformations of the proteins undergoing folding [22], and is measured in an aging polymer glass [25]. Martensites can show aging behaviour as in Deng et al [24].

One sees that the general idea common to all these very different systems, is that a slowly evolving aging system is *partially equilibrated* at some effective temperature. It then faces high entropy barriers, during inefficient searches for rare energy reducing pathways, with a low success rate (or low Monte Carlo acceptance). Clearly, the materials science issues in martensitic evolution could benefit from borrowing these concepts of nonequilibrium statistical mechanics and protein folding. Conversly, the pseudospin models could make explicit and clarify, the nonequilibrium issues.

Broadly, the questions in nonequilibrium aging systems that need to be understood are:

- How does the system re-equlibrate after a deep temperature quench ?
- What are the paths taken and barriers faced, in going from initial to final equilibrium states in configuration space; and is the golf hole idea from protein folding, conceptually useful ?
- How do the nonequilibrium distributions reach their respective final forms, and is there any effective temperature or internally developed energy scale, that eventually evolves to the bath temperature ?

We next discuss the discrete-strain pseudospin models that are applied to study both the sets of questions mentioned, using Monte Carlo simulations under systematic temperature quenches, followed by long holding times at fixed temperatures.

1.3 Discrete-strain models and Monte Carlo simulations

On cooling, martensites can show a variety of microstructures [1–5]. Under an electron microscope, for example there are twins and tweed in $NiAl$; star-like textures in Pb_3VO_4; and crossed twins in $NiMnGa$ alloys. To understand these complex microstructures, nonlinear free energy functionals have been explored: through relaxational simulations in terms of phase fields describing different variants [26]; through Monte Carlo simulations with displacement as the working variable [27]; through numerical solutions of dynamics with strain tensors as displacement-gradients [28]; through molecular dynamics for a system of particles with two-body potentials and displacement as the working variable [8]; and through relaxational and underdamped dynamics in OP strains as the working variable, (following the 1D dynamics of Bales and Gooding [29]) including power-law anisotropic long range interactions [29], with extension to plasticity behaviour [30]. These continuous variable models are successful in reproducing the microstructures as seen in experiments [1–5], but can be time-consuming. A reduced model would be useful.

Discrete-spin variable (S) models are well-known in statistical physics to model phase transitions. The most familiar are the Ising model with 2-states ($S = \pm 1$) for ferromagnetism; the Spin-1 Blume-Capel model with 3-states ($S = 0, \pm 1$) for He^3/He^4 mixtures; and q-state potts models or *clock* models $\mathbb{Z}_q$, for systems with many degrees of freedom [31, 45]. In a similar spirit, spin models have been used to model microstructures in ferroelastic martensites [32–34].

1.3.1 Strain-pseudospin or clock-zero models

Recently, continuous-strain free energies for different ferroelastic transitions in 2D and 3D, with characteristic OP components $N_{OP} = 1, 2, 3$ in number and variants $N_V = 2, 3, 4, 6$ in number, have been scaled using the Barsch and Krumhansl (BK) scaling procedure. This yields scaled Landau minima that fall on the corners of regular polyhedra inscribed in a sphere, that has unit radius at the Landau transition [33].

The transition-specific scaled free energies can be truncated to these polyhedra corners in the order parameter space [33]. This procedure induces N_{OP}-component *pseudospins* $\{\vec{S}(\vec{r})\}$ of unit magnitude $\vec{S}^2(\vec{r}) = 1$, pointing to N_V *corners*; and to the *centre* $\vec{S}(\vec{r}) = \vec{0}$, of a regular polyhedron. The free energies induce 'clock-zero' or $\mathbb{Z}_{N_V+1}$ Hamiltonians $H(\{\vec{S}(\vec{r})\})$ that are like Blume-Capel models [31, 45], but now with power-law anisotropic interactions $U(\vec{R}) \sim 1/R^d$, where d is the dimensionality. Since $\vec{S}^6 = \vec{S}^4 = \vec{S}^2 = 0$ or 1, the free energy nonlinearities collapse to give pseudospin Hamiltonians that are *bilinear* in the spins, and diagonal in Fourier space. They are not harmonic oscillators in $\vec{S}(\vec{k})$, since discrete spin flips are in $\vec{S}(\vec{r})$; however the models are closest in spirit to the inhomogeneous oscillator models of Garriga and Ritort [24]. For the simplest, scalar $N_{OP} = 1$ pseudospins $S(\vec{r})$ on a reference lattice $\{\vec{r}\}$ of unit spacing, and with $K_0 \propto E_0$, the elastic energy per cell, the Hamiltonian is

$$H = \frac{1}{2} K_0 \sum_{\vec{k}} \epsilon(\vec{k}) |S(k)|^2, \tag{1.1}$$

where $\epsilon(\vec{k}) \equiv \xi^2 \vec{K}^2(\vec{k}) + g_L + \frac{1}{2} A_1 U(\vec{k})$. Here ξ^2 is a length scale induced by the domain wall width in the strains; $g_L(\tau)$ is proportional to the Landau free energy, with scaled temperature $\tau(T) = (T - T_c)/(T_0 - T_c)$; and A_1 is stiffness constant related to the elastic anisotropy. Here $U(\vec{k}) \sim \cos^2 2\theta > 0$ is the kernel of the St.Venant interaction that is zero, in preferred $\theta = \pm\frac{\pi}{4}$

diagonal directions; and $\vec{K}_\mu \equiv 2\sin(k_\mu/2)$ is the Fourier space difference operator in the Ginzburg term, of nearest-neighbour 'ferromagnetic' interactions. Domain wall *microstructures* emerge, from the competition between nearest-neighbour and power-law anisotropic interactions.

These discrete-strain pseudospin clock-zero models can be studied using *local meanfield* approximations [33, 34], that yield microstructures similar to continuous-variable simulations [26–30], and experiments [4]. Thus, the reduced pseudospin description is *faithful*.

Uniform austenite or $\{S(\vec{r}) = 0\}$ for all $\vec{r}$ has *zero* energy. Since $g_L < 0$ below the Landau transition T_0, the scaled spectrum $\epsilon(\vec{k})$ will change sign to be negative for small $\vec{k}$, defining the edge of a '*golf hole*' $\epsilon(\vec{k}) = 0$. This negative energy region in Fourier space changes size with temperature, with a funnel-like behaviour inside. Golf holes and funnels are concepts borrowed from protein folding [19, 20].

1.3.2 Metropolis algorithm

Monte Carlo (MC) simulations have been used extensively in the study of discrete-variable models in statistical mechanics. The Metropolis algorithm is an importance sampling technique, that has been used in physics, biology, social sciences and finance [35].

Using this algorithm, we can construct a Markov chain of microstates using a transition probability which depends on the energy difference between the initial and trial states. The evolution of the system with time can be described by a Master Equation [35],

$$\frac{\partial P_n(t)}{\partial t} = -\sum_{n \neq m} [P_n(t) W_{n\to m} - P_m(t) W_{m\to n}] \tag{1.2}$$

where $P_n(t)$ is the probability of the system being in state n at time t, and $W_{n\to m}$ is the transition rate for $n \to m$. In equilibrium, $\frac{\partial P_n(t)}{\partial t} = 0$ gives a

detailed balance condition,

$$P_n(t)W_{n\to m} = P_m(t)W_{m\to n}. \tag{1.3}$$

The probability of the nth state occuring in a classical system is given by

$$P_n(t) = \frac{e^{-E_n/k_BT}}{Z}, \tag{1.4}$$

where Z is the partition function. This probability is usually not fully known because of the denominator; however one can avoid this difficulty by generating a Markov chain of states, i.e., generate each new state directly from the previous state. If the n-th state is generated from the m-th state, then the relative probability is the ratio of the individual probabilities, and the denominator cancels. As a result, only the energy difference ΔE between the two states is needed [35],

$$\Delta E = E_n - E_m. \tag{1.5}$$

Any transition rate which satisfies the detailed balance is acceptable, e.g.

$$W_{n\to m} = {\tau_0}^{-1} \exp(-\Delta E/k_BT), \quad \Delta E > 0 \tag{1.6a}$$

$$= {\tau_0}^{-1}, \quad \Delta E < 0 \tag{1.6b}$$

where τ_0 is the time required to flip a spin. Often, this time unit is set equal to unity. The Metropolis algorithm [35] implementation is as follows:

1. Consider an initial state C_i and calculate the energy E_n.
2. Construct a trial state C_t, by picking a site randomly, and flipping its spin.
3. Calculate the energy E_t of C_t and the change $\Delta E = E_t - E_i$.
4. Generate a random number r such that $0 < r < 1$.
5. If $r < \exp(-\Delta E/k_BT)$, accept the flip.

6. Otherwise, restore the spin and go to step 2.

The N sites are labelled with random numbers and arranged in an increasing-value chain, so sequentially visiting every site in the chain means every site is visited randomly, but once and only once, in 1 MC 'sweep' (MCS) over N sites, that then corresponds to 1 MC flip per spin. Here, the flips explore *all* $N_V + 1$ pseudospin values. The standard measure of Monte Carlo time 't' is the serial number of the Monte Carlo sweep [35].

In continuous strain $e_2(\vec{r}, t)$ simulations, there are barrier traversals of unit cells from one Landau minimum; and for longer times there are also motions of interacting domain walls separating variants. In the reduced, and more economical pseudospin description, the local unit cell barrier-traversing time collapses into the single, local pseudospin-flip, enabling a focus on the global domain-wall diffusion time. The unit MC time of a spin flip is proportional to the time for an austenite unit cell to distort to martensite unit cell.

In this thesis, we study microstructural evolutions in different ferroelastic transitions in 2- and 3-dimensions using Monte Carlo simulations under systematic quenches *without extrinsic disorder*; and investigate the distinction between athermal and isothermal martensites; the puzzling conversion-delay tails in athermal martensites; and the dependence of textural evolution on initial conditions. In the athermal martensite regime, for deep temperature quenches, we study partial equilibration energy surfaces, golf holes and entropic channels and effective temperatures, to understand the re-equilibration process. Our results [54–57] are summarized below.

1.4 The present work and structure of the thesis

The thesis is divided into eight Chapters. We outline the strain-pseudospin or clock-zero models in Chapters 2 and 5 drawing on previous work in the literature. We present our own results in Chapters 3, 4, 6 and 7, with a summary in Chapter 8. Results published so far are given later. In a chain of argument, each Chapter answers a primary question, and raises another, that is answered in the next Chapter and so on. There is some (deliberate) repetition, to make the Chapters readable by themselves.

Question:What are pseudospin Hamiltonians and how are they obtained ?

Chapter 2 (Strain and pseudospins in 2D): This Chapter introduces the concept of strain, and outlines the previously derived strain-pseudospin model Hamiltonians (with power-law anisotropic potentials) in 2D [33].

Question: Can any one of these discrete-strain or pseudospin models, help us to understand the materials science issues mentioned ?

Chapter 3 (Square-rectangle transition in 2D: Conversion-delays tails): In this Chapter, we present our results [54–56] of systematic Monte Carlo temperature-quench simulations on the simplest, 3-state, discrete-strain, pseudospin model ($S = 0, \pm 1$) for a scalar-OP ($N_{OP} = 1, N_V + 1 = 3$), corresponding to the *square-rectangle* ferroelastic transition. In different material parameter regimes, the same model shows both isothermal behaviour, and athermal behaviour with rising tails, as in Figure 1.2. The tails flatten towards a classical athermal boundary, for increasing stiffness constants A_1.

Domain wall phases and droplet parametrizing of textures: In this model system, the *domain walls* are the 'inherent structures', using the terminology of glasses [18]. After a given quench to a temperature τ, a domain wall *'vapour'* of martensitic droplets in an austenite background *converts* to a fluctuating domain wall *'liquid'* (with austenite bubbles) at a martensitic time $t_m(\tau)$; and later, that *orients* to a twinned domain wall *'crystal'* after a time $t_C(\tau)$. The small martensite fraction $n_m(t) = \frac{1}{N}\sum_{\vec{r}} S^2(\vec{r},t) = \frac{1}{N}\sum_{\vec{k}} |S(\vec{k},t)|^2$ shows *incubation*, with almost flat behaviour, till it sharply rises through 50%. This defines the conversion time t_m from $n_m(t_m) = 1/2$.

The complex textures can be parametrized in terms of the simple energies of *effective droplets* [56]. A parameter $R(t)$ appears, that has also a geometrical meaning for early times as a square-droplet side, but is essentially an energy parameter, that can go negative for longer times, as the energy goes negative. The complex textural energy $H/N = \frac{K_0}{2N}\sum_{\vec{k}} \epsilon(\vec{k})|S(\vec{k})|^2$ is set equal to sum of bulk and surface terms $4\xi^2 R(t) + (g_L + \frac{1}{2}A_1[U])R^2(t)$ where $[U] \simeq 0.29$ is an average over the Brillouin zone. A characteristic length scale $R_c(\tau) = -2\xi^2/(g_L + \frac{A_1}{2}[U]) > 0$ emerges naturally, that is finite, and well below its divergence temperature. The scaled textural energies H/N versus $R(t)/R_c(\tau)$ fall on an inverted parabola. The parameter ratio that controls the evolutions is the initial value $R(0)/R_c(\tau)$, where $R(0)$ is related to the seed size, and is set equal to unity $R(0) = 1$ for unit seeds. The peak of the inverted parabola is at $R(0)/R_c(\tau) = 1$, and other special values are $R(0)/R_c(\tau) = 2, 1/2$, and 0. Through the droplet parametrization, an athermal/isothermal 'regime diagram' is obtained in material parameters $(1 - \frac{T_c}{T_0})$ versus A_1, with boundaries that are in good agreement with simulation data.

Since for a given unit seed $R(0) = 1$, the ratio depends on τ, the characteristic temperatures for textures can be understood.

Isothermal martensite parameter regime: In this regime, we find the characteristic 'U'-shaped curve in time-temperature-transformation (TTT) plots,

with conversion times t_m showing exponential dependence on the Hamiltonian energy scale E_0, and inverse temperature $1/T$ i.e. $t_m \sim e^{E_0/T}$ [55]. This is the signature of activation over *energy* barriers.

Athermal martensite parameter regime: The TTT curves under systematic quenches in the athermal regime have characteristic temperatures T_1, T_2, T_3, T_4 or corresponding values of scaled temperatures τ_1, τ_2, τ_3, τ_4, or droplet parameter $R(0)/R_c(\tau)$. These temperatures are related to very different evolutions. There is manifestly an explosive growth of seeds for $T \lesssim T_1$ correspond to $R(0)/R_c(\tau) \gtrsim 2$. There is a non-zero but small delay for $T_2 > T > T_1$ or $2 > R(0)/R_c(\tau) > 1$. The delay becomes large for $T_4 > T > T_2$ or $1 > R(0)/R_c(\tau) > 1/2$ and diverges at $T = T_4$, well below the Landau transition temperature T_0 and with $R_c(\tau)$ still finite. There is *no* conversion from seeded austenite to martensite for $T \gtrsim T_4$ ($<< T_0$) or $R(0)/R_c(\tau) \lesssim 1/2$ even though the bulk free energy is negative. On temperature cycling, that sweeps across the characteristic temperatures of the athermal regime TTT phase diagram, there are peaks in acoustic emission variable and latent heat releases.

Incubation-delays and entropy barriers: The incubation tails of Kakeshita et al [9] and Klemradt et al [10] in athermal martensites are found to exist generically, above the temperature of explosive martensitic conversions $\tau > \tau_1$. The conversion times goes as $t_m \sim e^{\frac{1}{|T-T_4|}}$ [54] similar to Vogel-Fulcher behaviour in glassy freezing [18]. So there are no conversions above $\tau_4 (<< T_0)$ as in the null result of Otsuka et al [14]. The temperature τ_1 has a spinodal character (like T_c), but from the austenite bound to domain walls, rather than the bulk spinodal of Planes et al [12].

During the conversions, we find jerkiness [36]; cooperative nucleation [37]; and autocatalytic twinning seen as in Bales and Gooding in 1D strain models [6, 29]. We show that both conversion incubation-delay times, and conversion probabilities are insensitive to Hamiltonian energy scales E_0, suggesting

entropy barrier dominance. Just like a *energetically critical* droplet at the top of an energy barrier, there can be an *entropically critical* droplet at the start of an entropy barrier or search for pathways. Log-normal distributions in conversion delay rates, are seen for $\tau_4 > \tau > \tau_2$, and are characteristic of *rare* pathways [38]. The power-law anisotropic potential plays a central role in the conversion incubations or flatness of $n_m(t)$.

We also find during orientation-incubation, that the high-temperature austenite droplets, that are *spontaneously generated* in local stress regions, can act as *dynamical catalysts* [33, 54] to unlock frozen domain walls, that then orient in preferred directions to form a domain wall crystal. When they die out at low temperatures, there is a glassy freezing of the domain wall liquid states. This dynamical catalyst idea could be relevant for the actual glass transition [18, 33].

We monitor evolutions of OP, and non-OP strain textures; local stresses and stress distributions; and textural thermodynamics of entropy and energy that are flat during conversion and orientation delays. The final scenario of athermal martensite formation and growth is [54]: initial 2% seeds $\rightarrow$ formation of single-variant, entropically critical droplet ('vapour') $\rightarrow$ searches during incubation $\rightarrow$ autocatalytic twinning $\rightarrow$ disordered bidiagonal domain walls ('liquid') $\rightarrow$ ordered monodiagonal domain walls, or twins ('crystal').

Finally, since *uniform* single-variant martensite is the global minimum, why do metastable twins occur at all ? We find the probability of reaching the global-minimum decreases with system size as $1/\sqrt{N}$; with the 'excited-state' energy of sparse twins relavant to the uniform state energy also going as $\sim 1/\sqrt{N}$. Therefore the twinned martensite states, that are exponentially large in number, and almost degenerate with the global minimum, can successfully compete with a single uniform martensite state [55].

Question: Are these results specific to the scalar-OP pseudospin model for

square-rectangle transition considered, or are they generic for vector-OP pseudospin models for transitions in 2D ?

Chapter 4 (Other 2D transitions: Conversion-delay tails): In this Chapter, we present our MC simulations [57] on three discrete-strain models for *vector*-OP ($N_{OP} = 2$) transitions in 2D: triangle-centered rectangle ($N_V+1 = 3$); square-oblique ($N_V+1 = 5$); and triangle-oblique ($N_V+1 = 7$). For these two-component vector-pseudospin transitions, we find similar results in the athermal martensite parameter regime, as in scalar-pseudospin square-rectangle transition. During conversion incubations, we again determine for all three cases, the evolving textures of OP, non-OP, local stresses; stress distributions; and textural thermodynamics of internal energy and entropy.

Therefore, the obtained results are not transition-symmetry specific to the simplest scalar-OP transition, but are seen also in vector-OP transitions in 2D.

Question: Can pseudospin models be also obtained in 3-dimensions ?

Chapter 5 (Strain and pseudospins in 3D): We discuss the strain in 3D, and outline previously obtained discrete-strain pseudospin models including their characteristic power-law anisotropic potentials [33].

Question: Are the results obtained in Chapters 3 and 4 are specific to 2D transitions, or do they carry over for 3D transitions ?

Chapter 6 (3D transitions: Conversion-delay tails): In this Chapter, we present our MC simulations [57] on four discrete-strain pseudospin models in 3D: for the tetragonal-orthorhombic ($N_{OP} = 1, N_V+1 = 3$); cubic-

tetragonal ($N_{OP} = 2, N_V + 1 = 4$); cubic-trigonal ($N_{OP} = 2, N_V + 1 = 5$); cubic-orthorhombic ($N_{OP} = 2, N_V + 1 = 7$)) transitions. In the athermal martensite parameter regime, we find similar results in four 3D transitions as seen in the four 2D transitions.

Therefore, the results obtained in 2D transitions are not dimension-specific, but are generic, for at least in four 3D transitions.

Question: Can we use pseudospin models to illustrate and understand the deeper issues mentioned in nonequilibrium aging systems?

Chapter 7 (Re-equilibration after a temperature quench: searches for Fourier-space golf holes): We now go back to the simplest 3-state pseudospin model for the square-rectangle transition, under systematic temperature quenches. Concepts from protein folding, such as 'golf holes' and 'funnels', are borrowed to understand the re-equilibration process in martensites [19–22, 57]. The evolving entropy and internal energy in Chapter 3 were obtained from the local-meanfield treatment of the pseudospin Hamiltonians [33]. We find that, after a deep temperature quench, the system behaves as "*temporarily microcanonical*" on a constant energy surface as in the ideas of Ritort and colleagues [24]. The conversion incubations are understood from the entropy barriers encountered in searching for rare pathways on a constant-energy surface, and are similar to toy models of protein folding [20], where the entropy barriers arise in the searches for the edge of a golf hole. In our case, the golf hole is anisotropic, and the distributions have to narrow in width and deform, to fit and roll in. One can extract an internally determined, and time-dependent effective temperature, that remains almost flat until the completion of the evolutions of the vapour, liquid, or crystal phases.

We track the evolving Fourier space pseudospin structure-factor $|S(\vec{k})|^2$,

and identify and parametrize, its evolution along paths where Hamiltonian energies are constant or decreasing. The martensite fraction $n_m(t) = \frac{1}{N}\sum_{\vec{k}} |S(\vec{k})|^2$ is the area under the curve. The initial-state uniform structure-factor distribution rapidly becomes an isotropic gaussian, peaked over the golf hole, with Hamiltonian energy $H = 0$, that of austenite. This is the Fourier space version of the critical droplet for entropy barriers mentioned earlier. The martensite fraction is incubated over the time $t < t_m$ ('vapour phase'), until the isotropic distribution searches for a pathway to become anisotropic, as it narrows to the golf hole size. The peak height increases during narrowing such that the area $n_m(t)$ rises sharply, at $t = t_m$. After the narrowing, the anisotropic peak 'rolls down' into the funnel, and there is an emergence of a bidiagonal ('X') profile ('liquid phase'), followed by a further orientation along a symmetry breaking diagonal ('\' or '/') direction beyond $t = t_C$ ('crystal phase').

For $\tau \geq \tau_4$, the golf hole size becomes too small for the incubating gaussians to deform, so the entropy barriers and conversion times diverge, $t_m \to \infty$. With the conversion pathway blocked by this divergent entropy barrier, the zero-energy droplet goes back to its energetically-degenerate parent austenite. On the other hand, for temperature $\tau < \tau_1$, the golf hole is so large that the isotropic gaussian can roll in rapidly in a few MC sweeps as entropy barriers vanish, i.e. droplets show explosive growth.

Thus the coordinate-space martensite formation and growth is understood in Fourier space through the ideas of protein folding [19, 20, 22]; and of searches for rare energy-lowering pathways on constant energy surfaces [23, 24].

Chapter 8 (Thesis summary): In this Chapter we summarize our results.

2

Strain and pseudospins in 2D

In this Chapter, we follow previous work [33] and start with continuous strain variable representation of free energies for ferroelastic transitions [40] in 2-dimensions. We then outline how the Landau part of the free energy produces the discrete-strain 'pseudospins'. The clock-zero model Hamiltonians are then systematically derived from continuous strain free energies for both scalar and vector order parameter ferroelastic transitions in 2D. These will be used in our simulations of chapters 3, 4, and 7.

2.1 Continuous strain representation

In this Section, we discuss distortions, strains and 'no-defect' compatibility constraints. We then outline the Barsch-Krumhansl (BK) procedure [39] for scaling experimental parameters, that is generalized to obtain the strain free energy in terms of *order parameter only*, in the spirit of Landau, for five 2D ferroelastic transitions [33].

2.1.1 Distortions, strains and compatibility condition

Consider a solid material as a homogeneous, anisotropic, and continuous elastic medium. Let us represent the position of a material point, by it's radius vector $\vec{r}$. On cooling or under the action of stress, the solid material exhibits *distortion*. Mathematically, the distortion is described by a displacement vector $u_\mu = r'_\mu - r_\mu$, with $\mu = x, y$ where r'_μ is component of the new position of the point after the deformation. The distortion tensor $D_{\mu\nu}$ or displacement gradient [1, 41] is given by,

$$D_{\mu\nu} = \left(\frac{\partial u_\mu}{\partial r_\nu}\right), \tag{2.1}$$

where μ, ν runs over x, y in 2D. In Fourier space,

$$D_{\mu\nu}(\vec{k}) = i u_\mu(\vec{k}) k_\nu. \tag{2.2}$$

The $\mathbf{D}$ tensor is in general neither symmetric nor antisymmetric under interchange of Cartesian indices, but can be written as a sum of symmetric **(e)** local distortion, and antisymmetric **(w)** local rotation tensor. With T as a transpose,

$$\mathbf{D}(\vec{r}) \equiv \mathbf{e}(\vec{r}) + \mathbf{w}(\vec{r}); \tag{2.3a}$$

$$\mathbf{e}(\vec{r}) \equiv \frac{1}{2}[\mathbf{D} + \mathbf{D}^T]; \tag{2.3b}$$

$$\mathbf{w}(\vec{r}) \equiv \frac{1}{2}[\mathbf{D} - \mathbf{D}^T]. \tag{2.3c}$$

The symmetrized distortion tensor $e_{\mu\nu}$ is henceforth referred as the "*strain*" tensor, and is used as the working variable, in a 'strain representation' [33]. It is distinct from the "*Lagrangian strain*" tensor $E_{\mu\nu}$, which is a derived quantity [41] and is defined in terms of distortion matrix $D_{\mu\nu}$. In order for the free energy to the invariant for *global* rotation [41] it must depend on $(1+D^T)(1+D)^T \equiv 1+2\vec{E}$, where

$$\mathbf{E}(\vec{r}) \equiv \frac{1}{2}\{(1+\mathbf{D})^T(1+\mathbf{D})-1\} = \frac{1}{2}[\mathbf{D}^T+\mathbf{D}]+\frac{1}{2}\mathbf{D}^T\mathbf{D} \equiv \mathbf{e}(\vec{r})+\mathbf{g}(\vec{r}), \quad (2.4)$$

where the "geometric nonlinearity" tensor is $\mathbf{g}(r) \equiv \frac{1}{2}\mathbf{D}^T\mathbf{D}$.

In d-dimensions there are $d(d+1)/2$ components in the symmetric Cartesian strain tensor. *Physical strains* are $d(d+1)/2$ symmetry-motivated linear combinations of these Cartesian components. In 2-dimensions, there are three physical strains e_α, with $\alpha = 1,2,3$, that are the linear combinations of the Cartesian strains ($e_{\mu\nu}$): the compressional or dilatational strain (e_1), the deviatoric or rectangular strain (e_2), and the shear strain (e_3) that are defined as,

$$e_1(\vec{r}) = \frac{c_1}{2}(e_{xx}+e_{yy}), e_2(\vec{r}) = \frac{c_2}{2}(e_{xx}-e_{yy}), e_3(\vec{r}) = \frac{c_3}{2}(e_{xy}+e_{yx}) = c_3 e_{xy}. \quad (2.5)$$

where c_1, c_2, c_3 are temperature-independent constants. The physical Lagrangian strains E_α are similarly defined as,

$$E_1(\vec{r}) = \frac{c_1}{2}(E_{xx}+E_{yy}), \quad E_2(\vec{r}) = \frac{c_2}{2}(E_{xx}-E_{yy}), \; E_3(\vec{r}) = c_3 E_{xy}. \quad (2.6)$$

The constants are chosen for the high-temperature phase; and for square unit cells are $c_1 = c_2 = \sqrt{2}, c_3 = 1$, and for triangular unit cells are $c_1 = c_2 = c_3 = 1$ [33].

In 2-dimensions there must be only two independent displacement degrees of freedom per lattice point (or per unit cell). Hence, there must be one constraint linking the three strains, so that there are also two independent strain

variables. The required constraint is the St.Venant compatibility condition [6], that says no dislocations are generated during the distortion, and that all distorted unit cells fit together in a smoothly compatible way, maintaining lattice integrity. The St.Venant constraint in coordinate and Fourier space is defined, with 'T' as transpose, as:

$$\vec{\nabla} \times [\vec{\nabla} \times \mathbf{e}(\vec{r})]^T = 0; \quad \vec{k} \times \mathbf{e}(\vec{k}) \times \vec{k} = 0. \tag{2.7}$$

The rotations $\mathbf{w}(\vec{r})$ have their own constraint, but since they appear only in the geometric nonlinearity, and since spontaneous rotations do not occur, we set $\mathbf{w}(r) = 0$, and consider strain only. The physical strains are $\{e_\alpha\}$, with the label 'α' divided into Order Parameter (OP) strains with $\alpha = \ell$, and non-OP strains with $\alpha = i$. As first noted by Kartha et al, the compatibility equation of (2.7) can be written in terms of these [6, 33], linking OP strains $\{e_\ell\}$ to non-OP strains $\{e_i\}$.

2.1.2 Strain free energy and Barsch-Krumhansl scaling

The free energy (F) for a ferroelastic transition depends on the Lagrangian strains $\{E_\ell\}$, and is written in terms of free energy densities f [33],

$$F = \sum_r \{f_L(E_\ell) + f_G(\vec{\Delta} E_\ell) + f_{non}(E_i)\}. \tag{2.8a}$$

Here the sum or integral ($\sum_{\vec{r}} \to \int d^d r/a_0$) is over all positions $\vec{r}$, on a computational grid (that could be the crystal lattice of austenite) with a lattice scale a_0 that is set equal to unity later. Gradient operators are written as central finite-difference operators on the grid $\nabla_\mu \to \Delta_\mu/a_0$ as discussed below. The Landau term $f_L(E_\ell)$ is expanded in terms of symmetry-allowed polynomials $\{I_p\}$ of the OP Lagrangian strains that are invariant in discrete point group symmetry operations. The quadratic term contains a harmonic

elastic coefficient $C^{(2)}(T) = (T - T_c)C_0^{(2)}$, which goes to zero at temperature $T = T_c$, but is pre-empted on cooling by the first order transition at a temperature T_0, that is defined later. Hence, with $\sigma_p = \pm 1$ as appropriate signs to yield N_V martensite minima,

$$f_L = C^{(2)}(T)I_2 + \sum_{p=3,\ldots,p_{max}} \sigma_p C^{(p)} I_p(E_l). \tag{2.8b}$$

The Ginzburg term $f_G(\vec{\Delta}E_\ell)$ is quadratic in square-gradient OP Lagrangian strains, and is *defined* in the model as:

$$f_G = \sum_l \frac{b}{a_0^2}[\vec{\Delta}E_l(\vec{r})]^2, \tag{2.8c}$$

with domain-wall cost-parameter 'b'. The physical meaning of the Ginzburg term is that a non-uniform domain wall between two variants costs an elastic bending energy. This is captured on discrete grid, by a discrete squared (central) difference between nearest neighbour sites. Higher order differences would be needed, to approximate a gradient in a continuum. In any case, the actual small-scale elasticity is that of the natural grid of the crystal lattice (See also Chapter 6.). With the essential physics captured by the squared-difference, we avoid needless expenditure of CPU time by retaining the form (2.8c).

The non-OP terms $f_{non}(E_i)$ are harmonic,

$$f_{non} = \sum_i \frac{1}{2} A^{(i)} E_i^2(\vec{r}), \tag{2.8d}$$

and contain elastic stiffness coefficients $A^{(i)}$ [33, 42, 43].

The ferroelastic free energies contain many material-specific coefficients such as elastic coefficients $C_0^{(2)}, T_c, b, A^{(i)}, C^{(p)}$, that need to be fitted from experiments to get (material-specific) free energies [42]. To extract transition-specific, but material-independent forms, Barsch and Krumhansl (BK) proposed a scaling procedure [39] that can make the free energies internally

simpler. Shenoy et al generalized the BK scaling for different ferroelastic transitions, and derived discrete-strain pseudospin Hamiltonians systematically in 2D (as well as in 3D) [33]. We now outline the general scaling procedure that was used in the derivations of pseudospin Hamiltonians [33].

A. General scaling procedure

Following the Barsch-Krumhansl (BK) scaling procedure [39], all Cartesian distortions, $D_{\mu\nu} \rightarrow \lambda D_{\mu\nu}$ or $e_{\mu\nu} \rightarrow \lambda e_{\mu\nu}, w_{\mu\nu} \rightarrow \lambda w_{\mu\nu}$ are scaled in the magnitude λ of the spontaneous strain at the Landau transition; and all energy terms are scaled in E_0, the elastic energy per unit cell; and a Landau transition temperature $T_0 > T_c$ for a first-order transition is defined [33].
The physical Lagrangian strains then change as [33],

$$E_\alpha \rightarrow \lambda E_\alpha(\lambda) \equiv \lambda(e_\alpha + \lambda g_\alpha) \tag{2.9}$$

Henceforth e_α is the *scaled* strain. The free energy of (2.8) changes as

$$F(E_\alpha) \rightarrow F[\lambda E_\alpha(\lambda)] \equiv E_0 \bar{F}[E_\alpha(\lambda)], \tag{2.10}$$

defining a dimensionless $\bar{F}[E_\alpha(\lambda)] = \sum_{\vec{k}} \bar{f}[E_\alpha(\lambda)]$. The scaled dimensionless free energy densities are the sum of Landau, Ginzburg, and non-OP terms,

$$\bar{f}[E_\alpha(\lambda)] \equiv \bar{f}_L[E_\ell(\lambda)] + \bar{f}_G[\vec{\Delta} E_\ell(\lambda)] + \bar{f}_{non}[E_i(\lambda)], \tag{2.11}$$

Here from (2.8) $\bar{f}_L = \sum_p C_{(p)} I_p(E_l)$; $\bar{f}_G = \sum_l \xi^2 [\vec{\Delta} E_l(\vec{r})]^2$; $\bar{f}_{non} = \frac{1}{2} \sum_i A_i E_i^2(\vec{r})$, contain dimensionless scaled coefficients,

$$C_p \equiv C^{(p)} \lambda^p / E_0; A_i \equiv A^{(i)} \lambda^2 / E_0; \xi^2 \equiv b\lambda^2/(a_0^2 E_0). \tag{2.12}$$

A scaled temperature τ absorbs the harmonic-term material dependence [33, 39] and is a central parameter, defined as

$$\tau(T) = (T - T_c) C_0^{(2)} \lambda^2 / E_0 \equiv (T - T_c)/(T_0 - T_c), \tag{2.13}$$

where the transition temperature $T_0 > T_c$ is determined by requiring $\tau(T_0) = (T_0 - T_c)C_0^{(2)}\lambda^2/E_0 = 1$ or

$$T_0 = T_c + E_0/(C_0^{(2)}\lambda^2). \tag{2.14}$$

The martensite minima are degenerate with the austenite minima when the scaled temperature has a value $\tau(T_0) = 1$ at the first-order Landau transition temperature. The metastable austenite minima disappears at lower spinodal temperature T_c, where the scaled temperature has a value $\tau(T_c) = 0$.

To compare with experiment in 3D (Chapter 6), the Voigt elastic constant [43] $C^{'}(\tau) \equiv C_{11} - C_{12}$ that softens at an extrapolated T_c (pre-empted by the first-order transition at T_0), need to be found from sound velocities [44]. The identified OP magnitude λ jump at the same $T = T_0$ needs to be found from crystallographic measurements [1]. See related discussion in Chapter 6.

The material-dependent higher order elastic coefficients $C^{(p)}$, have not disappeared: they are absorbed into an overall external prefactor E_0 in the Landau free energy $f_L = E_0\bar{f}_L$; into the scaled temperature τ; and into the spontaneous strain magnitude λ at transition, that is an internal prefactor of the geometric nonlinearities. The external coefficients of the scaled invariant polynomials, studied case by case, become symmetry-specific but purely *numerical* values in most cases, independent of specific materials [33], circumventing the need for term-by-term, material-specific fits [42].

B. Minimization procedure

A constrained minimization of the scaled free energy $\bar{f}[E_\alpha(\lambda)]$ can be carried out for different ferroelastic transitions. The scaling parameters and compatibility potentials are calculated perturbatively, through a simplifying assumption [33] that the typical spontaneous distortion is small compared to unity, as for most materials, $\lambda \simeq 10^{-1}$, treating

$$\lambda \ll 1. \tag{2.15}$$

Then the scaled physical Lagrangian strains $E_\alpha(\lambda) = e_\alpha + \lambda g_\alpha$ are initially approximated by the scaled physical symmetrized distortions,

$$E_\ell(\lambda) \approx E_\ell(0) = e_\ell; \quad E_i(\lambda) \approx E_i(0) = e_i, \tag{2.16}$$

with the geometric nonlinearities neglected, to leading relative order in λ.

2.2 Discrete-strain pseudospins

Pseudospin variables as a phenomenological description of strains has a long history [32]. However, a systematic reduction procedure was proposed [33] to obtain discrete-strain pseudospin Hamiltonians, by evaluating scaled free energies at their Landau minima. The total free energy evaluated at these minima is then the model Hamiltonian for the scalar/vector pseudospins, that have N_{OP}-component strains, and $N_V + 1$ values. The model coefficients are then not just arbitrary, but are related through the parent free energy, to the scaled temperature τ, to the scaled energy cost of an elastic domain-wall segment ξ^2, and to the scaled bulk stiffness A_1.

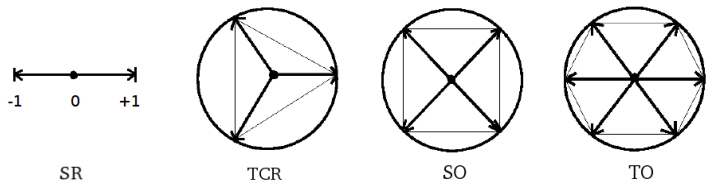

Figure 2.1: *Landau free energy minima:* Positions in OP space of martensitic minima (arrow heads) and austenite minima (dots). (A) square-rectangle (SR); (B) triangle-centered rectangle (TCR); (C) square-oblique (SO); (D) triangle-oblique (TO) transitions.

We outline the derivation of the pseudospin Hamiltonians and compatibility potentials [33] for transitions in 2D: (A) square-rectangle ($N_V = 2$);

(B) triangle-centered-rectangle ($N_V = 3$); (C) square-oblique ($N_V = 4$); and (D) triangle-oblique ($N_V = 6$).

2.2.1 Pseudospin Hamiltonians for 2D transitions

In 2-dimensions, structural transitions have $d(d+1)/2 = 3$ or three distinct physical strains, the compressional (e_1), deviatoric (e_2) and shear (e_3) strains. Of these, N_{OP} are the OP and the remaining $n = 3 - N_{OP}$ are the non-OP strains. We will take the simplest case of square-rectangle transition with ($N_V + 1 = 3, N_{OP} = 1, n = 2$), as a prototype for simulations.

A. Square-rectangle transition ($N_{OP} = 1, N_V = 2, n = 2$)

The square-rectangle transition (SR) has deviatoric strain e_2 as single-component order parameter $N_{OP} = 1$; while the $n = 2$ non-OP strains are the compressional and shear strains, e_1, e_3. The free energy, scaled as in the BK scaling procedure [33], has a sixth-order Landau term $\bar{F}_L(e_2)$; a Ginzburg term quadratic in the OP gradients $\bar{F}_G(\vec{\Delta}e_2)$; and a seemingly innocuous term quadratic in the non-OP strains $\bar{F}_{non}(e_1, e_3)$, that turns out to generate crucial powerlaw anisotropic interactions between the OP at different sites. Thus the free energy with an elastic energy per unit cell E_0 is,

$$F = E_0[\bar{F}_L + \bar{F}_G + \bar{F}_{non}]. \tag{2.17}$$

The Landau polynomial term is $\bar{F}_L = \sum_{\vec{r}} \bar{f}_L(e_2)$. Here $\bar{f}_L(e_2) \equiv [(\tau - 1)e_2^2 + e_2^2(e_2^2 - 1)^2]$ is the Landau free energy density. It has an austenite minimum at $e_2 = 0$, and $N_V = 2$ martensite minima at $e_2 = \pm\bar{\varepsilon}(\tau)$. The magnitude of the Landau minima $\bar{\varepsilon}$, and the scaled temperature τ, are

$$\bar{\varepsilon}^2(\tau) = \frac{2}{3}\{1 + \sqrt{1 - 3\tau/4}\}; \tag{2.18a}$$

$$\tau(T) = \frac{(T - T_c)}{(T_0 - T_c)};\ T = T_c[1 - \frac{\tau}{\tau_0}], \tag{2.18b}$$

where $\tau_0 \equiv \tau(T = 0) = -T_c/(T_0 - T_c)$. Note that the square-rhombus transition has shear e_3 as the OP, and e_1, e_2 as the non-OP, but has the same form of $\bar{f}_L(e_3)$, and the same compatibility potential, so is essentially the same as the square-rectangle transition, with a $\pi/4$ rotation of the grid. The square-rhombus model has been considered extensively by Rao, Sengupta and collaborators [30].

The single OP strains were set to pseudospin values at the $N_V + 1 = 3$ Landau minima [33],

$$e_2(\vec{r}) \to \bar{\varepsilon}(\tau)S(\vec{r}); \quad S(r) = 0, \pm 1. \tag{2.19}$$

The strain pseudospins $S = 0, \pm 1$ represent the single austenite and two martensite minima. Zero spin values are retained at all temperatures, allowing their existence or otherwise, to be determined dynamically.

The pseudospin Hamiltonian $H(S)$ is derived [33] by substituting (2.19) into the total free energy of (2.17), yielding

$$H(S) \equiv F(e_2 \to \bar{\varepsilon}S) = H_L + H_G + H_{compat}. \tag{2.20}$$

The Landau term H_L of (2.20) generates a quadratic pseudospin term in coordinate and Fourier space [33],

$$H_L(S) = E_0\bar{\varepsilon}^2 \sum_{\vec{r}} g_L(\tau)S^2(\vec{r}) = E_0\bar{\varepsilon}^2 \sum_{\vec{k}} g_L(\tau)|S(\vec{k})|^2, \tag{2.21}$$

where $S^6 = S^4 = S^2 = 0, 1$ are used to collapse nonlinearities into bilinear terms [33]. Note that, unlike Ising spins, $S^2 = 0, 1$ is still a statistical variable. Here $g_L < 0$ for the $\tau < 1$, temperatures we will consider, favouring $S^2 = 1$ martensite states, and is,

$$g_L \equiv \tau - 1 + (\bar{\varepsilon}^2 - 1)^2, \tag{2.22}$$

where the scaled Landau free energy is $\bar{f}_L(\bar{\varepsilon}) = \bar{\varepsilon}^2 g_L S^2$. Note that the temperature τ here is the quenched bath temperature, i.e. the Landau term

responds immediately to the quench. The time delays are then due to the domain walls (entering the other terms) relaxing, to finally reach the bath temperature.

The Ginzburg term H_G in coordinate and Fourier space is,

$$H_G(S) = E_0\bar{\varepsilon}^2 \sum_{\vec{r}} \xi^2(\vec{\Delta}S)^2 = E_0\bar{\varepsilon}^2 \sum_{\vec{k}} \xi^2 \vec{K}^2 |S(\vec{k})|^2, \tag{2.23}$$

where $\vec{K}^2 \equiv K_x^2 + K_y^2$ with $K_\mu \equiv 2\sin(k_\mu a_0/2); \mu = x, y$, and a_0 is the lattice scale set equal to 1.

The compatibility term F_{compat} from the harmonic non-OP strains $(A_1/2)e_1^2 + (A_3/2)e_3^2$, is minimized subject to no-defect condition in the later Section 2.2.2, to yield the compatibility potential. With the substitution (2.20) one gets $H_{compat}(S)$.

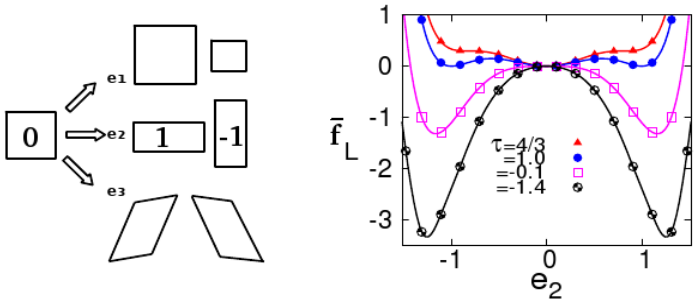

Figure 2.2: *Square-rectangle transition: Left*: Physical strains, showing pseudospin values S of OP e_2. *Right*: Landau free energy density $\bar{f}_L(e_2)$ versus e_2, for various values of the scaled temperature $\tau(T)$.

The total Hamiltonian $H \equiv H_L + H_G + H_C$ in coordinate space is [33]

$$\beta H = \frac{D_0}{2}[\sum_{\vec{r}}\{g_L(\tau)S(\vec{r})^2 + \xi^2(\vec{\Delta}S)^2\} + \sum_{\vec{r},\vec{r}'} \frac{A_1}{2} U(\vec{r}-\vec{r}')S(\vec{r})S(\vec{r}')]. \tag{2.24a}$$

Here $D_0(T) \equiv 2\bar{\varepsilon}^2(\tau)E_0/k_BT$ and the kernel $U(\vec{k})$ of the power-law anisotropic potential $U(\vec{R})$ is given in (2.47) in Section 2.2.2 later. The potential goes as

$$U(\vec{r}) \sim \frac{\cos^2 2\theta}{R^d}, \tag{2.24b}$$

where $d = 2$ is the space dimensionality and the *anisotropic* numerator has the 4-fold symmetry of the square austenite unit cell.

With $S(\vec{r}) = \frac{1}{\sqrt{N}}\sum_{\vec{k}} S(\vec{k})e^{i\vec{k}.\vec{r}}$, $U(\hat{R}) = \frac{1}{N}\sum_{\vec{k}} U(\vec{k})e^{-i\vec{k}.\vec{r}}$, and periodic boundary conditions, the Hamiltonian is diagonal in Fourier space,

$$\beta H = \frac{1}{2}\sum_{\vec{k}} Q_0(\vec{k})|S(\vec{k})|^2; \quad Q_0(\vec{k}) \equiv D_0[\{g_L(\tau) + \xi^2\vec{K}^2\} + \frac{A_1}{2}U(\vec{k})]. \tag{2.25}$$

The Hamiltonian with $S = 0, \pm 1$ pseudospins is like Spin-1 Blume-Capel model [31], but now with temperature dependence, and powerlaw anisotropic interactions. In this, as in all other pseudospin simulations, the possibility of austenite $\{S(\vec{r}) = 0\}$ values are included at all temperatures, allowing their actual populations to be determined dynamically.

B. Triangle-centered rectangle transition $(N_{OP} = 2, N_V = 3, n = 1)$

The triangle-centered rectangle transition (TCR) has deviatoric and shear strains e_2, e_3 as two-component OP $N_{OP} = 2$, and a single $n = 1$ non-OP strain e_1. The scaled Landau free energy, that describes the first-order phase transition between the single high-symmetry austenite phase and $N_V = 3$ martensite variants, is [33],

$$\bar{f}_L(e_2, e_3) = \tau(e_2^2 + e_3^2) - 2(e_2^3 - 3e_2e_3^2) + (e_2^2 + e_3^2)^2, \tag{2.26}$$

where signs of (2.8b) are chosen $\sigma_3 = -1, \sigma_4 = \sigma_6 = +1$ (Alternatively, one could have $\sigma_3 = -1$ as noted below.). The continuous strains are replaced by discrete-valued pseudospins at $N_V + 1 = 4$ Landau minima [33] with,

$$\vec{e}(\vec{r}) = (e_2, e_3) = |\vec{e}|(\cos\phi, \sin\phi) \to \bar{\varepsilon}(\tau)\vec{S}(\vec{r}) = \bar{\varepsilon}(\tau)(S_2, S_3), \tag{2.27a}$$

$$\bar{\varepsilon}(\tau) = \frac{3}{4}(1 + \sqrt{1 - 8\tau/9}) \tag{2.27b}$$

The ϕ angles are $\phi = \phi_m = 2(m-1)\pi/N_V$, where $m = 1, 2, 3 (= N_V)$. The pseudospin values at $N_V + 1 = 4$ minima are, then

$$\vec{S} = (S_2, S_3) = (0,0), (1,0), (-\frac{1}{2}, \pm\frac{\sqrt{3}}{2}). \tag{2.28}$$

as seen in Figure 2.3 with triangle vertices falling on unit circle. For the alternative $\sigma_3 = -1$ sign choice, the triangle could point to the left with $\vec{S} \to -\vec{S}$ in (2.28). See also Chapter 6.

The Landau polynomials again collapse into a simple bilinear form in the pseudospins with substitution and $\vec{S}^6 = \vec{S}^4 = \vec{S}^2 = 0, 1$, and the Landau term $H_L(e_2, e_3)$ is

$$H_L(\vec{S}) = E_0 \bar{\varepsilon}^2 \sum_{\vec{r}} g_L(\tau) \vec{S}^2(\vec{r}); \quad g_L(\tau) \equiv \tau - 1 + (\bar{\varepsilon} - 1)^2, \tag{2.29}$$

with $g_L(\tau)$ of the TCR case is different from the SR case.
The Ginzburg term H_G is quadratic in OP-gradients is again

$$H_G(\vec{S}) = E_0 \bar{\varepsilon}^2 \sum_{\vec{r}} \xi^2 (\vec{\Delta}\vec{S})^2 = E_0 \bar{\varepsilon}^2 \sum_{\vec{k}} \xi^2 \vec{K}^2 |\vec{S}(\vec{k})|^2. \tag{2.30}$$

The harmonic non-OP term H_{compat} is minimized subject to St.Venant condition, that induces power-law anisotropic potentials between OP strains $U_{\ell\ell'}(\vec{k})$, given in (2.52), (2.53) in the later Section 2.2.2.
In coordinate space the total pseudospin Hamiltonian is,

$$\begin{aligned} \beta H(\vec{S}) = \frac{D_0}{2} [\textstyle\sum_{\vec{r}} \sum_{\ell=2,3} \{ g_L S_\ell(\vec{r})^2 + \xi^2 |\vec{\Delta} S_\ell(\vec{r})|^2 \} \\ + \frac{A_1}{2} \textstyle\sum_{\vec{r},\vec{r}'} \sum_{\ell,\ell'=2,3} U_{\ell\ell'}(\vec{r} - \vec{r}') S_\ell(\vec{r}) S_{\ell'}(\vec{r}')], \end{aligned} \tag{2.31}$$

and is a 'clock-zero' $\mathbb{Z}_{3+1}$ model [33]. It is again diagonal in Fourier space,

$$\beta H = \frac{1}{2} \sum_{\vec{k}} \sum_{\ell,\ell'=2,3} Q_{0,\ell\ell'}(\vec{k}) S_\ell(\vec{k}) S_{\ell'}(\vec{k})^*, \tag{2.32}$$

with $\vec{S}(\vec{k})^* = \vec{S}(-\vec{k})$, as $\vec{S}(\vec{r})$ is real, with pseudospins given in (2.28). Here

$$Q_{0,\ell\ell'}(\vec{k}) \equiv D_0 [\{ g_L(\tau) + \xi^2 \vec{K}^2 \} \delta_{\ell,\ell'} + \frac{A_1}{2} U_{\ell\ell'}(\vec{k})]. \tag{2.33}$$

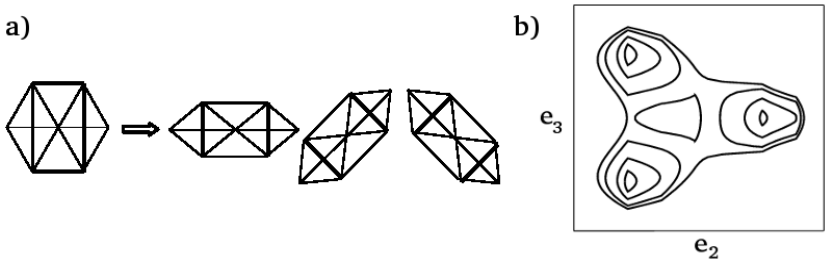

Figure 2.3: *Triangle-centered rectangle transition:* (a). Single austenite (triangle) goes to $N_V = 3$ possible martensite variants (centered rectangles). (b). Contour plot of Landau free energy density $\bar{f}_L(e_2, e_3)$ of (2.26) showing the austenite and martensite minima. An alternative sign choice of the cubic term gives the contour minima position flipped in sign.

C. Square-oblique transition ($N_{OP} = 2, N_V = 4, n = 1$)

The square-oblique transition (SO) also has deviatoric (e_2) and shear (e_3) as two-component $N_{OP} = 2$ OP strains, and a single $n = 1$ non-OP strain (e_1) similar to triangle-centered rectangle transition. The scaled free energy for square-oblique transition with now a material-dependent scaled elastic constant C_4' is [33],

$$\bar{f}_L = \tau(e_2^2 + e_3^2) - (4 - C_4'/2)(e_2^4 + e_3^4) + 4(e_2^6 + e_3^6) - C_4' e_2^2 e_3^2. \tag{2.34}$$

The continuous strains are replaced by pseudospins at $N_V + 1 = 5$ minima [33] with $\bar{\varepsilon}(\tau)$, that is same as in SR transition, given in 2.18,

$$\vec{e}(\vec{r}) = (e_2, e_3) = |\vec{e}|(\cos\phi, \sin\phi) \to \bar{\varepsilon}(\tau)\vec{S}(\vec{r}) = \bar{\varepsilon}(\tau)(S_2, S_3). \tag{2.35}$$

Here the angles of the pseudospin vector-OP $\phi = \phi_m = \frac{(2m-1)\pi}{N_V}$, where $m = 1, 2, 3, 4 (= N_V)$; and the pseudospin values $\vec{S}(\vec{r}) = (S_2, S_3)$ are,

$$\vec{S} = (S_2, S_3) = (0, 0), (\pm\frac{1}{2}, \pm\frac{1}{2}). \tag{2.36}$$

The Landau term H_L becomes

$$H_L(\vec{S}) = E_0\bar{\varepsilon}^2 \sum_{\vec{r}} g_L(\tau)\vec{S}^2(\vec{r}); \quad g_L \equiv \tau - 1 + (\bar{\varepsilon}^2 - 1)^2 \tag{2.37}$$

where $g_L(\tau)$ is as in SR case.
The Ginzburg term H_G is quadratic in the OP-strain gradient, same as in (2.30). The compatibility term H_{compat} is given in (2.51) of Section 2.2.2.

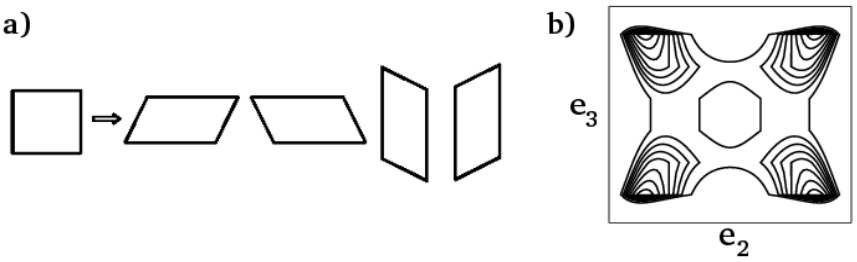

Figure 2.4: *Square-oblique transition:* (a). Single austenite (square) is going to $N_V = 4$ possible martensite variants (oblique). (b). Contour plot of Landau free energy density $\bar{f}_L(e_2, e_3)$ of equation (2.34) showing the austenite and martensite minima.

In coordinate space the total pseudospin Hamiltonian is,

$$\begin{aligned}\beta H(\vec{S}) = \frac{D_0}{2}[\textstyle\sum_{\vec{r}} \sum_{\ell=2,3} \{g_L S_\ell(\vec{r})^2 + \xi^2 |\vec{\Delta} S_\ell(\vec{r})|^2\} \\ + \frac{A_1}{2} \textstyle\sum_{\vec{r},\vec{r}'} \sum_{\ell,\ell'=2,3} U_{\ell\ell'}(\vec{r} - \vec{r}') S_\ell(\vec{r}) S_{\ell'}(\vec{r}')].\end{aligned} \tag{2.38}$$

The square-oblique transition is clock-zero $\mathbb{Z}_{4+1}$ Hamiltonian with $\vec{S}$ having $4+1$ spin directions of (2.36). It is again diagonal in Fourier space and 2×2 kernel $U_{\ell\ell'}(\vec{k})$ is same as TCR case, given in (2.52).

D. Triangle-oblique transition ($N_{OP} = 2, N_V = 6, n = 1$)

The triangle-oblique transition (TO) also has deviatoric (e_2) and shear (e_3) as two-component strains $N_{OP} = 2$, while the single $n = 1$ non-OP is the compressional strain (e_1). The scaled free energy for triangle-oblique transition,

invariant under triangle group symmetries is [33],

$$\bar{f}_L = (\tau - 1)I_2 + I_2(I_2 - 1)^2 + C_6({I_2}^3 - {I_3}^2), \tag{2.39}$$

where $I_2 = \vec{e}^{\,2} \equiv \varepsilon^2$, $I_3 = e_2^3 - 3e_2e_3^2$, and C_6 is a scaled material constant.

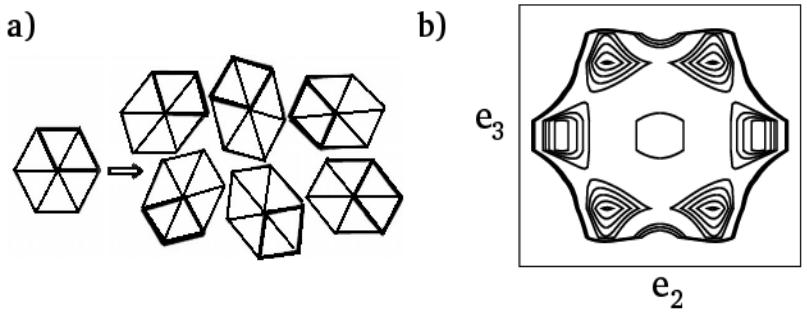

Figure 2.5: *Triangle-oblique transition: Left*: Single austenite (square) is going to $N_V = 6$ possible martensite variants (oblique). *Right*: Contour plot of Landau free energy density $\bar{f}_L(e_2, e_3)$ of (2.39), showing the austenite and martensite minima.

With the usual approximation $\vec{e}(\vec{r}) \to \bar{\varepsilon}(\tau)\vec{S}(\vec{r})$, the pseudospin $\vec{S}(\vec{r})$ has $N_V + 1 = 7$ values, with $\varepsilon = \bar{\varepsilon}(\tau)$ of (2.18),

$$\vec{S} = (S_2, S_3) = (0, 0), (\pm 1, 0), (\pm\frac{1}{2}, \pm\frac{\sqrt{3}}{2}) \tag{2.40}$$

The Landau term becomes,

$$H_L(\vec{S} = E_0\bar{\varepsilon}^2 \sum_{\vec{r}} g_L(\tau)\vec{S}^2(\vec{r});\ g_L(\tau) \equiv (\tau - 1) + (\bar{\varepsilon}^2 - 1)^2. \tag{2.41}$$

where $g_L(\tau)$ is same as the SR case.
The Ginzburg term H_G is given in (2.52), and $H_{compat}(\vec{S})$ with matrix kernel $U_{\ell\ell'}(\vec{k})$ is given (2.51) of Section 2.2.2.
In coordinate space the total pseudospin Hamiltonian is,

$$\begin{aligned}\beta H(\vec{S}) = \frac{D_0}{2}[\textstyle\sum_{\vec{r}} \sum_{\ell=2,3}\{g_L S_\ell(\vec{r})^2 + \xi^2|\vec{\nabla} S_\ell(\vec{r})|^2\} \\ + \frac{A_1}{2} \textstyle\sum_{\vec{r},\vec{r}'} \sum_{\ell,\ell'=2,3} U_{\ell\ell'}(\vec{r} - \vec{r}')S_\ell(\vec{r})S_{\ell'}(\vec{r}')],\end{aligned} \tag{2.42}$$

The triangle-oblique transition is clock-zero $\mathbb{Z}_{6+1}$ Hamiltonian with $\vec{S}$ having $6+1$ spin values of (2.40). The Hamiltonian is diagonal in Fourier space and $U_{\ell\ell'}(\vec{k})$ is given in (2.52) for TCR case.

2.2.2 Compatibility potentials for 2D transitions

We now outline the derivations [33] of the compatibility kernels $U_{\ell\ell'}(\vec{k})$, as stated in previous section. In 2-dimensions, the St. Venant compatibility constraint in terms of Cartesian tensor is $\vec{\Delta} \times [\vec{\Delta} \times \mathbf{e}(\vec{r})]^T = 0$, where 'T' is 'transpose'. In terms of physical strains e_α with $\alpha = 1, 2, 3$,

$$\vec{\Delta}^2 e_1 - (\Delta_x^2 - \Delta_y^2)e_2 - 2\Delta_x\Delta_y e_3 = 0. \tag{2.43}$$

In Fourier space the central difference operator $\Delta_\mu \to K_\mu(\vec{k}) \equiv 2\sin(k_\mu/2)$ and the constraint is $\vec{K} \times \mathbf{e}(\vec{k}) \times \vec{K} = 0$. Hence

$$O_1 e_1(\vec{k}) + O_2 e_2(\vec{k}) + O_3 e_3(\vec{k}) = 0. \tag{2.44}$$

For the square lattice, the compatibility coefficients are $O_1(\vec{k}) = -\frac{1}{\sqrt{2}}\vec{K}^2$, $O_2(\vec{k}) = \frac{1}{\sqrt{2}}({K_x}^2 - {K_y}^2)$, $O_3(\vec{k}) = 2K_xK_y$, while for the triangular case, $O_1(\vec{k}) = -\vec{K}^2$, $O_2(\vec{k}) = ({K_x}^2 - {K_y}^2)$, $O_3(\vec{k}) = 2K_xK_y$.
For the uniform $\vec{k} = 0$ case, the parabolic terms are minimized by zero non-OP strains $e_1, e_3 = 0$. For the nonuniform $\vec{k} \neq 0$ case, the deviatoric strain evolution $e_2(\vec{r}, t)$ could generate some compressional and shear strains e_1, e_3, in exploring energy-lowering pathways. Thus one cannot just set $e_1 = e_3 = 0$, ignoring the non-order parameters to study OP-only models with only $F = F_L(e_2) + F_G(\vec{\Delta}e_2)$: to do so would be to implicitly, and incorrectly assume there are three independent physical strains. One must minimize in non-OP strains, but subject to the constraint. In the displacement representation, for a 2D square lattice there are two independent variables (u_x, u_y) per lattice point (or per unit cell). In the equivalent (symmetric) strain representation,

there are three physical strains e_1, e_2, e_3 and one constraint, so there are again $3-1=2$ independent variables.
We now derive compatibility kernels for transitions in 2D.

A. Square-rectangle transition ($N_{OP}=1, n=2$)

The simplest square-rectangle transition has a single-component OP ($N_{OP}=1$), namely the deviatoric strain e_2; and e_1, e_3 as $n=2$ non-OP strains. The non-OP term in the Hamiltonian is harmonic, and must be minimized. It is

$$\bar{F}_{non}(e_1,e_3)=\sum_{\vec{r},i=1,3}\frac{A_1}{2}e_i^2=\sum_{\vec{k},i=1,3}\frac{A_1}{2}|e_i(\vec{k})|^2. \tag{2.45}$$

Inserting a $\vec{k}\neq 0$ direct solution $e_1=-(O_2e_2+O_3e_3)/O_1$ into (2.45), and minimizing freely in e_3, yields the compatibility term

$$H_{compat}(e_2)=\sum_{\vec{k}}\frac{A_1}{2}U(\vec{k})|e_2(\vec{k})|^2, \tag{2.46}$$

where $A_1U(\vec{k})=\nu(\vec{k})O_2^2/[\{O_1^2/A_1\}+\{O_3^2/A_3\}]$. Explicitly, the kernel is,

$$U(\vec{k})=\nu(\vec{k})(K_x^2-K_y^2)^2/[K^4+(8A_1/A_3)(K_xK_y)^2]. \tag{2.47}$$

Here we insert a prefactor $\nu(\vec{k})\equiv 1-\delta_{\vec{k},0}$ since the optimum non-OP strains are zero in the uniform case, as mentioned. For long wavelengths, the kernel is manifestly independent of $|\vec{k}|$ and depends only on the direction $\hat{k}$ in the Brillouin zone $U(\vec{k})\simeq U(\hat{k})\sim\cos^2 2\theta$. In minimizing, the non-OP strains are eliminated in favour of the OP in Fourier space as before, with

$$e_1(\vec{k})=B_{12}e_2(\vec{k}),\quad e_3=B_{32}e_2(\vec{k}); \tag{2.48a}$$

$$\text{where}\quad B_{12}=\frac{-O_1O_2}{A_1[\frac{O_1^2}{A_1}+\frac{O_3^2}{A_3}]};\ B_{32}=\frac{-O_3O_2}{A_3[\frac{O_1^2}{A_1}+\frac{O_3^2}{A_3}]}. \tag{2.48b}$$

Hence, given an OP texture $e_2(\vec{k})$, one can calculate the corresponding non-OP strains $e_1(\vec{k}), e_3(\vec{k})$. Of course, substituting this back into (2.45) also

recovers the kernel $U \sim O_2^2$. At the optimum orientation $k_x = \pm k_y$, the compatibility potential vanishes, and the non-OP strains are expelled. As seen in Chapter 3 this also corresponds to a vanishing of internal local stresses.

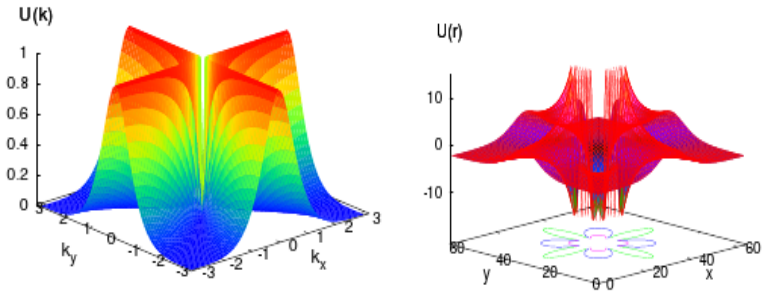

Figure 2.6: *Compatibility-induced effective interaction for square-to-rectangle transition: Left*: Fourier kernel $U(\vec{k})$ versus k_x, k_y. *Right*: Powerlaw anisotropic potential $U(\vec{r})$ versus x, y . Note 4-fold symmetry from square-lattice austenite, in both cases.

Figure 2.6 shows the compatibility potential in Fourier and coordinate space. From (2.25), and (2.47), droplets of same-sign variants at a given separation will repel, except along diagonals $\theta = \pm\pi/4$, where they are non-interacting, so for both variants present, there is a natural tendency to form tweed-like chessboards [4, 55] and as in Bratkovsky et al [26]. If same-sign variant droplets in tweed expand diagonally to merge into parallel slabs, one gets oriented twins. Clearly, this Fourier-component solution

$$S(k_x, k_y) = \delta_{k_x, \pm k_y} \bar{S}(k_x, \pm k_x), \tag{2.49}$$

is preferred, since then the compatibility kernel takes on its smallest value of zero, $U(k_x, \pm k_x) = 0$. The optimum domain wall angles are then $\pm\pi/4$, and *random* deviations cost energy. A diagonal $+\pi/4$ domain-wall can escape only through almost zero-cost, but *improbable* 'hairpin' deviations, with segments

along $-\pi/4$, $+\pi/4$, $-\pi/4$, extending in time: the domains are thus locked in place by *entropy barriers*.

B. Triangle-centered rectangle, square-oblique, triangle-oblique transitions ($N_{OP}=2, n=1$)

The triangle-centered rectangle, square-oblique and triangle-oblique transitions have e_2, e_3 as two-component OP strains ($N_{OP}=2$) and a single $n=1$ non-OP strain that is the compressional e_1. They all have the *same* compatibility kernel. The non-OP term in all cases is simply harmonic,

$$\bar{F}_{non}(e_1) = \frac{A_1}{2}\sum_{\vec{r}} e_1^2(\vec{r}) = \frac{A_1}{2}\sum_{\vec{k}} |e_1(\vec{k})|^2. \tag{2.50}$$

Substitution of the compatibility solution $e_1(\vec{k}) = -(O_2 e_2 + O_3 e_3)/O_1$ in (2.50), yields the St Venant term $H_{compat}(e_2, e_3)$ in terms of the OP,

$$H_{compat} = \sum_{\vec{k},\ell,\ell'=2,3} \frac{A_1}{2} U_{\ell\ell'}(\vec{k}) e_\ell(\vec{k}) e_{\ell'}(\vec{k})^*. \tag{2.51}$$

The compatibility potentials in Fourier space is,

$$U_{\ell\ell'}(\vec{k}) = \nu(\vec{k}) O_\ell O_{\ell'}/O_1^2, \tag{2.52}$$

or explicitly the kernels are,

$$U_{22}(k) = \nu\frac{(K_x^2-K_y^2)^2}{K^4}; U_{33}(k) = \nu\frac{(2K_xK_y)^2}{K^4}; U_{23} = \nu\frac{2K_xK_y(K_x^2-K_y^2)}{K^4} = U_{32}. \tag{2.53}$$

for all three transitions, that of course still differ in their N_V characteristic values of the pseudospins $\vec{S}$.

In this Chapter, we have discussed the continuous strain representation for ferroelastic martensites, and outlined the derivation of discrete-strain pseudospin Hamiltonians for four transitions in 2D [33], that include power-law anisotropic potential, induced from the no-defect constraint.

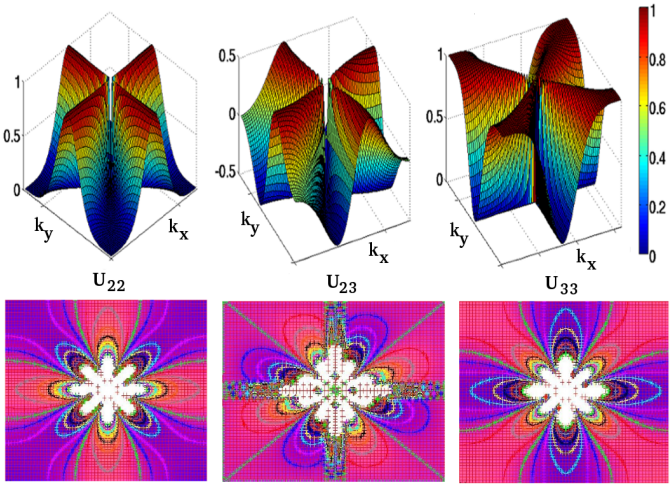

Figure 2.7: *Compatibility-induced anisotropic interactions between OP strains for TCR, SO, TO transitions:* First row is showing the kernels $U_{22}(\vec{k}), U_{23}(\vec{k}), U_{33}(\vec{k})$; and second row is showing contours of $U_{22}(\vec{r}), U_{23}(\vec{r}), U_{33}(\vec{r})$ anisotropic potentials respectively.

Question: Can we use these pseudospin models to understand the issues in materials science, mentioned earlier ?

3

Square-rectangle transition in 2D: Conversion-delay tails

In this Chapter, we present the Monte Carlo dynamics of microstructural evolutions in the simplest three-state, strain-pseudospin model for the scalar-order parameter square-rectangle transition [54–56]. We find athermal and isothermal martensite regimes, for different material parameters in the same model. In the isothermal martensite regime, we find conversion times have U-shaped curves in time-temperature plots, that are understood from activation over energy barriers. We show that the U-shaped TTT conversion curves with initial smaller martensite seeds transform to athermal curves, that have delay tails. For larger (but fewer) seeds, we recover pre-

vious trends of Pati and Cohen of isothermal curves changing to athermal curves for larger seeds [16]. We also find the isothermal U-shaped TTT curves change to athermal on changing material parameters. In the athermal martensite regime, above an 'spinodal' temperature for austenite bound on martensite domain-walls, there are conversion delay tails as in experiment. We reconcile three results as mentioned earlier. We show that the conversion-delay tails have Vogel-Fulcher divergences and Log-normal distributions, near the transition to austenite. This is understood as coming from entropy barrier dominance, in finding rare conversion channels or energy-lowering pathways. The Temperature-Time-Transformation phase diagram and crossover temperatures are understood through the parametrization of complex-texture energies in terms of effective droplet energies. We find peaks in acoustic emission variable and latent heat releases on temperature cycling. Finally, by switching off the compatibility term, we show that the power-law anisotropic interactions are as central to the evolution dynamics, as to the final statics.

3.1 Textural diagnostics

The strain pseudospin model Hamiltonian for square-rectangle transition (SR) is like spin-1 Blume-Capel model [31, 45] with temperature dependent coefficients and power-law interactions [33, 34] as mentioned in (2.24) of the previous Section. The total Hamiltonian $H \equiv H_L + H_G + H_C$ in coordinate and Fourier space is, with $D_0(T) \equiv 2\bar{\varepsilon}^2(\tau)E_0/k_BT$,

$$\beta H = \frac{D_0}{2}[\sum_{\vec{r}}\{g_L(\tau)S(\vec{r})^2 + \xi^2(\vec{\Delta}S)^2\} + \sum_{\vec{r},\vec{r'}}\frac{A_1}{2}U(\vec{r}-\vec{r'})S(\vec{r})S(\vec{r'})]; \quad (3.1)$$

$$\beta H = \frac{D_0}{2}\sum_{\vec{k}}\{g_L(\tau) + \xi^2\vec{K}^2\} + \frac{A_1}{2}U(\vec{k})\}|S(\vec{k})|^2. \quad (3.2)$$

To study martensitic kinetics after systematic temperature quenches, we do Monte Carlo (MC) pseudospin simulations [54–56] on a $d = 2, N = L^2$ square lattice. Fast Fourier Transforms are used to find energy changes, after random spin flips, over all $N_V + 1$ pseudospin values, of equal probability. To focus on domain-wall dynamics, it is computationally convenient to exclude the strictly zero $\vec{k} = 0$ point, while including all other wave vectors, with the smallest $k_{x,y} \sim 1/L$, as is justified for large systems in Section 3.6. Randomly located 2% sites of both variants in austenite, are quenched at $t = 0$ to a fixed $\tau << 1$ well below the Landau transition, holding at that temperature for $t \leq t_h$ MC sweeps. Parameters are typically $T_0 = 1; T_c/T_0 = 0.9 - 0.5, \xi = 1; A_1 = 1, 4, 10; 2A_1/A_3 = 1; L = 64;\ E_0 = 3, 4, 5, 6; t_h \leq 20,000$ sweeps, and conversion runs over $N_{runs} = 100$ different seeds. Here temperatures and energies are scaled in T_0 and $k_B T_0$, and scaled stiffnesses [33] are related to Voigt elastic constants e.g. $A_1 \sim (C_{11} + 2C_{12})/(C_{11} - C_{12})$ proportional to the elastic anisotropy parameter $2C_{44}/(C_{11} - C_{12})$. In calculating average times, computational durations depend on the space-time volumes $V_{comp} = L^d t_h N_{runs}$. With $L = 64, t_h = 20,000, N_{runs} = 100$ we have $V_{comp} = 10^{10}$. In fact, $L = 64$ is sufficient, and results are insensitive to larger L, since as we will see, there is a divergent time without a divergent length.

Since both martensite variants have $S^2 = 1$, while austenite is $S^2 = 0$, the austenite-martensite conversion diagnostic is the bulk martensite fraction n_m where

$$n_m(t) \equiv \frac{1}{N} \sum_{\vec{r}} S(\vec{r}, t)^2 = \frac{1}{N} \sum_{\vec{k}} |S(\vec{k}, t)|^2 \leq 1. \tag{3.3}$$

Here $n_m = 0$ or 1, in austenite or the martensite phase, respectively.

Since costs of non-uniformity are in the Ginzburg term, a wave-vector diagnostic is k_m where

$$h_G(t) \equiv {k_m}^2 = \sum_{\vec{k}} \vec{K}^2 |S(\vec{k}, t)|^2 / \sum_{\vec{k}} |S(\vec{k}, t)|^2. \tag{3.4}$$

Here $k_m \neq 0$ in textured states.

Since the St Venant compatibility contribution vanishes at preferred wall orientations, an orientation diagnostic is $n_C(t) \equiv 1 - h_C(t)$, where

$$h_C(t) \equiv \sum_{\vec{k}} U(\vec{k})|S(\vec{k},t)|^2/[U] \sum_{\vec{k}} |S(\vec{k},t)|^2; \tag{3.5}$$

and $[U] \equiv \sum_{\vec{k}} U(\vec{k})/N$, is the average of the kernel over the Brillouin zone. For $2A_1/A_3 = 1$ as taken by Kartha et al [6] in FePd alloys, one finds $[U] \simeq 0.3$. Here $n_C = 1$ or $h_C = 0$ in the crystal or oriented twin state of (2.49). From (2.45), and (2.48), the vanishing of $h_C = 0$ implies the non-OP strains e_1, e_3 are expelled in twin states. Since the total compatibility term of (3.2) vanishes, this implies that for optimum orientations, the intersite interactions $\vec{r} - \vec{r}\,' \neq 0$ will cancel the self-energy $\sim [U]$ contributions.

The Hamiltonian of (3.2) can be written in terms of the diagnostics $H = H(n_m, k_m, n_C)$ as

$$\beta H = (ND_0/2)n_m[g_L + \xi^2 {k_m}^2 + \frac{A_1[U]}{2} h_C]. \tag{3.6}$$

Since Ginzburg and St Venant costs are positive, uniform martensite is the global minimum, with (Landau) energy $NE_0\bar{f}_L(\bar{\varepsilon})$, negative below $\tau = 1$. Thus the energy excess per site due to textures is

$$\delta_H(t) \equiv \{H(\vec{S}(\vec{r},t)) - NE_0\bar{f}_L(\bar{\varepsilon})\}/N \tag{3.7}$$

This diagnostic is used in Section 3.6, to understand why twins can compete with the uniform global minimum.

The post-quench phase ordering from austenite to twinned martensite involves both conversion and orientation delays. For both athermal and isothermal regimes considered later, we specify the sweep index or 'time' $t = t_m$ for passage to martensite as when the martensitic fraction rises to 50% or

$$n_m(t_m) = \frac{1}{2}. \tag{3.8a}$$

The austenite fraction $n_0(t) = 1 - n_m(t)$ correspondingly, falls to 50%

$$n_0(t_m) = \frac{1}{2}. \tag{3.8b}$$

Figure 3.1 shows single-seed runs of $n_m(t)$ versus time t after quenches to various $\Delta\tau \equiv \tau - \tau_4 < 0$. Here the transition temperature $\tau_4 \equiv \tau(T_4)$ is operationally defined as where 100 runs all give austenite, and also agrees with an independently defined value in Figure 3.10, as where conversion times diverge [54]. Figure 3.1a shows that $n_m(t)$ rises rapidly at low temperatures to nearly unity, but for high temperatures, shows *incubation* behaviour, with no apparent change followed by sharp rises at t_m. (As seen in Section 3.5.4 and 4.3.4 during this essentially flat incubation of macro variables like n_m, t_m, the microstructure is like an evolving embryo, in an egg.) The transition is 'fuzzy' : on approaching τ_4, there is a smooth fall, rather than a step-like drop, in the fraction Φ_m of successful runs that go to martensite as in the later Figure 3.12. This *success fraction* is insensitive to the holding time t_h: longer waitings do not results in more conversions. The orientation time $t = t_C$ is similarly specified in Figure 3.1b, as when the oriented fraction

$$n_C(t_C) \equiv 1 - h_C(t_C) = 0.99. \tag{3.9}$$

After a quench in a macroscopic volume, different regions have different martensite fluctuation seeds in an austenite background. To define a typical conversion time $\bar{t}_m$ we must average suitable time-related variables over these many regions in the volume; or equivalently, average over many random-seed runs (N_{runs}) in a single simulated region (of size L^d). If the slowest conversion time inhibits the conversion of the whole volume, then the the largest time dominates (like resistors in series) and we must average over times t_m. However if a successful local martensite conversion can rapidly propagate to other regions, as is the case [16], then the shortest conversion

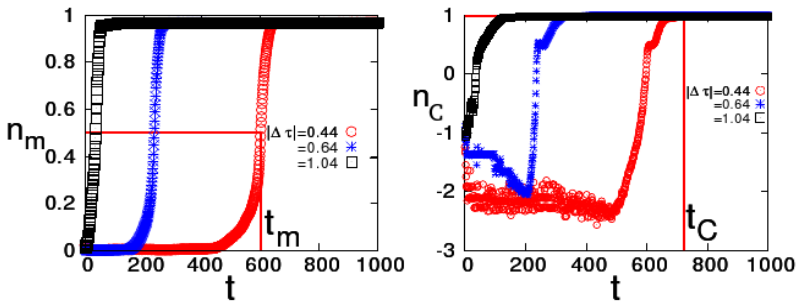

Figure 3.1: *Definition of incubation times* t_m, t_C*: Left*: Martensite fraction $n_m(t)$ versus time t, for $T_c/T_0 = 0.9$, fixed stiffness $A_1 = 4$ and various $\Delta\tau \equiv \tau - \tau_4 < 0$, showing the 50% conversion definition of t_m. Note flat incubation regions for $t < t_m$. *Right*: Orientation parameter $n_C(t) \equiv 1 - h_C(t)$ versus time t, showing the 99% orientation definition of t_C.

time or largest rate dominates (like resistors in parallel), and we must average over *rates* $r_m \equiv 1/t_m$. Here the fastest rate is conversion in a single step, while if there is no conversion over the holding time, we set $r_m = 1/t_h$, so $1 \geq r_m \geq 1/t_h$. We define [54–56] a mean conversion *rate*

$$< r_m >=< 1/t_m >, \tag{3.10}$$

arithmetically averaged over $N_{runs} = 100$ different seeds. Then a typical conversion time is *defined* as the inverse mean rate

$$\bar{t}_m \equiv 1/ < r_m > . \tag{3.11}$$

The results turn out to be similar to an average $< t_m >$ restricted to successful martensite runs only, but with better statistics. Similarly, the mean orientation rate is

$$r_C \equiv 1/t_C, \tag{3.12}$$

with $\bar{t}_C \equiv 1/ < r_C >$. We average over $N_{runs} = 10$, in this case.

We now consider broad concepts useful in further analysis.

3.2 Quenches, Times and Barriers

Steels have been studied under cooling ramps from an initial to final temperature, after which there is 'annealing' at a fixed temperature. In TTT diagrams plotted with temperature T (y-axis) versus time t (x-axis), the cooling curve is a line of negative slope and isothermal transformation curves are C-shaped [2, 8]. However, this sweeping of temperature means the evolving intervening states at intermediate values are swept along with the final states, carrying this thermal history and cooling rate dependence. We consider *quenches* instead, with a focus on the internal re-equilibration of states to the new final temperature, avoiding history effects. The TTT diagrams are plotted with *quench* temperature T (x-axis) versus time t (y-axis), and isothermal curves are U-shaped.

After a quench to a bath temperature T, the initial configuration faces a set of possible free energy barriers $\{\Delta F = \Delta U_{ener} - T\Delta S_{entr}\}$ in reaching the equilibrated final configuration where $\Delta U > 0$, and $-\Delta S_{entr} = |\Delta S_{entr}| > 0$ are energy and entropy barriers. These cause equilibration delays $\{\bar{t} \sim e^{\Delta F/T} = e^{|\Delta S_{entr}|} e^{\Delta U_{ener}/T}\}$, with the exponent in general having both energy barrier $\Delta U_{ener}/T$ and entropy barrier $|\Delta S_{entr}|$ contributions. The energy barriers involve traversing abundant paths from low to high energies, and waiting for sufficiently large $k_B T$ thermal kicks from the bath; whereas the entropy barriers involve traversing rare paths from high to low entropies waiting for successful searches for channels. Note the cancelation of T in the latter case and the negative sign in $\Delta S_{entr} = -|\Delta S_{entr}|$, for more probable states going to less probable. With a Hamiltonian energy scale E_0, the energy barrier contributes activated times $\sim e^{E_0/T}$, exponentially sensitive to E_0.

For *deep* quenches $E_0/T >> 1$, energy barriers above a landscape-slice of some constant U_{ener} are insurmountable, as $e^{\Delta U_{ener}/T} >> 1$. The system therefore search on a constant-energy configurational subspace $\Delta U_{ener} \simeq 0$

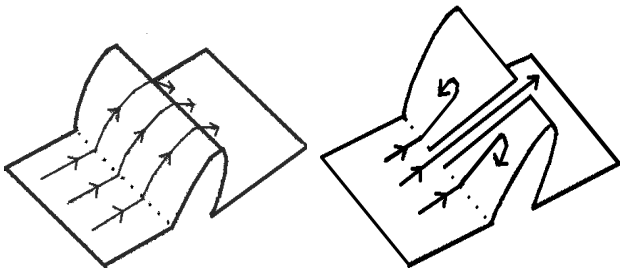

Figure 3.2: *Schematic of energy/ entropy barriers: Left*: Energy barrier of scaled height $\beta E_0 \sim 1$. *Right*: Entropy barrier as a search for a narrow channel (on a constant energy surface), cutting through deep-quench $\beta E_0 >> 1$ energy barriers on either side. Transverse Brownian wanderings are not shown.

of relaxation pathways, with delays $\{\bar{t} \sim e^{|\Delta S_{entr}|}\}$ dominated by *entropy* barriers [23]. These are non-activated, and insensitive to E_0, since increasing E_0 merely deepens the channels without affecting this rarity. The entropy barrier is like threading a needle or putting a ball into a golf hole. The delays from entropy barriers are not because of any blockings, but because there are many ways of being wrong, and only a few ways of being right.

The constant-energy searches are on the 'partial equilibration' surfaces considered by Ritort [24]. As we will see in later Section of this Chapter as well as in Chapter 7, this 'temporarily microcanonical' evolution has almost flat U_{ener} or Hamiltonian energies, and search paths on partially equilibrated constant energy surfaces are explicitly identified and parametrized.

Figure 3.2 shows schematics distinguishing between the limiting cases of pure energy and pure entropy barriers.

Figure 3.3 is a schematic picture of a rugged *energy* landscape βU_{ener} with entropic pathways (see Figure 3.2), in the athermal regime. A similar picture in the isothermal regime would include hops over energy barriers. The

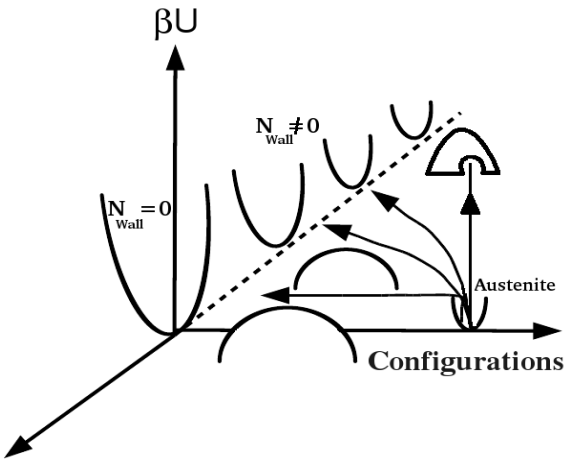

Figure 3.3: *Schematic of energy landscape:* Scaled internal energy βU_{ener} in configuration space, in the non-activated regime. See text.

configuration point after a deep quench avoids insurmountable high barriers, moving through a network of interconnecting rare transition pathways in the vapour and liquid regions, towards the competing N_{wall} crystal states. A trapping in an 'igloo' is shown, corresponding to a closed channel or an infinite entropy barrier, along that path. Sequential external stress and heat treatments could channel the system into desired, and functionally useful, textural patterns, as empirically found in steels [2, 8, 16].

3.3 Athermal and isothermal martensites

Martensitic materials are classified as '*athermal*' martensites, with apparently instantaneous conversions on cooling below a martensite start temperature M_s; and '*isothermal*' martensites, with time delays before martensitic conversions. The athermal or isothermal martensites [2, 8, 15, 16] supposedly have fixed, material-specific *energy* barriers that are very small or very large, respectively.

The traditional calssification of martensites became questionable, as there are apparently three different results that have been reviewed as discussed clearly in Chapter 1 and Section 1.2.1. One needs to reconcile these results [9, 10, 12, 14, 15], schematically summarized in Figure 1.2 previously.

We show that pseudospin MC simulations can provide an understanding of the athermal/ isothermal classification, and that all three results are relevant in different parameter regimes; and we also recover previous literature results on isothermal/athermal crossover with fixed austenitic grain size, but for different initial embryo sizes [16]. Our model depends on four material constants $T_c/T_0, A_1, E_0, \xi^2$, and shows both isothermal and quasi-athermal behaviour, depending on parameters; and also athermal/isothermal or vice versa crossover on changing material parameters. Experiments have shown such crossover but under high magnetic field and hydrostatic pressure [16].

Figure 3.4 shows Temperature-Time-Transformation curves [54] of $\bar{t}_m$ vs τ for different materials $A_1 = 1, 4, 10$ and $T_c/T_0 = 0.9$, under systematic quenches to τ with 2% initial random seeds of both variants. The curves show rapid conversions followed by *rising delay tails*, as in experiment [9, 10]. Moving down from τ_4, the times fall to $\bar{t}_m \sim O(10)$ sweeps at τ_2 as marked, and after a flat region become explosive $\bar{t}_m \sim O(1)$ below τ_1, that has a spinodal character. A rough conceptual connection to Figure 3.2 is then [54] $T_2 \sim$ "M_s" and $T_1 \sim$ "T_c". The inset of Figure 3.4 shows that for stiffer materials, the incubation tails flatten; the rising curves, squeezed into a narrowing region below τ_4 will start looking more like the classical athermal picture of Figure 3.2.

The main Figure 3.4 also shows for $T_c/T_0 = 0.63, A_1 = 4$, an isothermal U-shaped curve [2, 8, 16]. It has been suggested that the athermal curves emerge when isothermal U-curves move down to the temperature axis, for some materials [2, 15].

Figure 3.5 shows such crossovers within this model, for fixed $A_1 = 4$

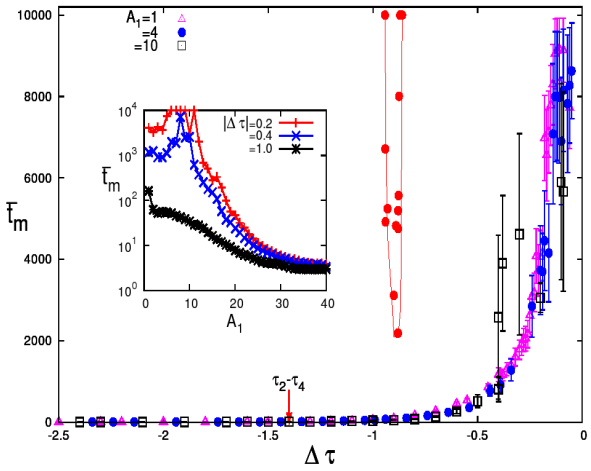

Figure 3.4: *Conversion times:* TTT plot of conversion delay $\bar{t}_m$ versus $\Delta\tau$ deviation from transition. Rapid conversions are followed by rising delay tails as shown, for $T_c/T_0 = 0.9$, and $A_1 = 1, 4, 10$ and $E_0 = 3$. Here τ_2 is marked, where $\bar{t}_m \sim 10$, but a lower spinodal τ_1, where $\bar{t}_m \sim O(1)$, is not shown. The isothermal U-curve shown has $T_c/T_0 = 0.63, A_1 = 4$. *Inset:* Complementary curves of $\bar{t}_m$ vs A_1 for fixed $|\Delta\tau| = 0.2, 0.4, 1$ showing that tails flatten, for increasing A_1, approaching the classical athermal boundary as shown in Figure 1.2. See text.

and increasing T_c/T_0; and for fixed $T_c/T_0 = 0.63$ and decreasing A_1. The isothermal U-curve has a low-temperature rise from the $e^{1/T}$ dependence, that first comes down to intersect the vertical time axis in intermediate curves; and these collapse towards very short, explosive times, on emergence of an athermal curve.

Figure 3.6 is a phase diagram in $(1 - \frac{T_c}{T_0})$ versus A_1, for athermal, isothermal regimes, and austenite. The lower right athermal regime for A_1 corresponds to values of the Figure 3.4 inset. Data of Figure 3.5 that give isothermal and athermal curves are included. For other parameters, rather

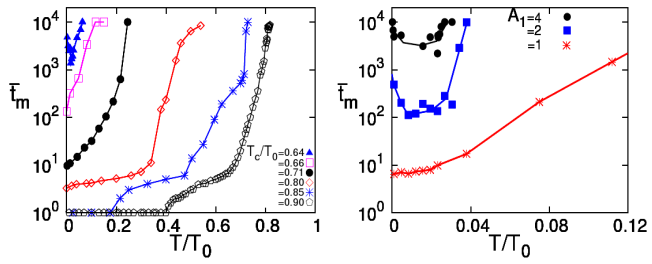

Figure 3.5: *Isothermal/athermal crossover:* TTT plots of time $\bar{t}_m$ versus temperature T/T_0, for $E_0 = 3$. *Left*: Fixed $A_1 = 4$ and T_c/T_0 increasing from 0.64 to 0.9. *Right*: Fixed $T_c/T_0 = 0.63$ and decreasing $A_1 = 4, 2, 1$. See text.

than similarly (and tediously) checking the shape of the curves in each case, we simply assign points on the phase diagram to be 'athermal' if they give rapid conversions within $t = 10$ sweeps, while the 'isothermal' points have no such rapid conversions. 'Austenite' points have no conversions at all, for holding times up to $t_h = 10^3$. The 'isothermal' points fall in a narrower region than material parameters for athermal martensites.

The non-activated athermal region is generically for *smaller* values of $(1 - \frac{T_c}{T_0})$, as can be heuristically understood. For activated processes, the Boltzmann factor $\sim e^{\frac{1}{T}}$ is exponentially sensitive to temperature T variations. However, from (2.18), $T = T_c + (T_0 - T_c)\tau$. Thus for $(1 - \frac{T_c}{T_0})$ small and quenches into a range of temperatures τ such as $\tau_2 < \tau < \tau_4$, the τ-dependence in the Hamiltonian dominate the τ-dependence of the (almost constant) Boltzmann factor temperature $T \simeq T_c$. This control of rates by the τ-dependence of H is a signature of athermal behaviour, that thus dominates for $(1 - \frac{T_c}{T_0}) << 1$ in Figure 3.6.

The solid lines are from a droplet model parametrization of textural energies, discussed later in Section 3.5.3. Sketching the argument to follow, athermal /isothermal/ austenite phase boundaries can be estimated

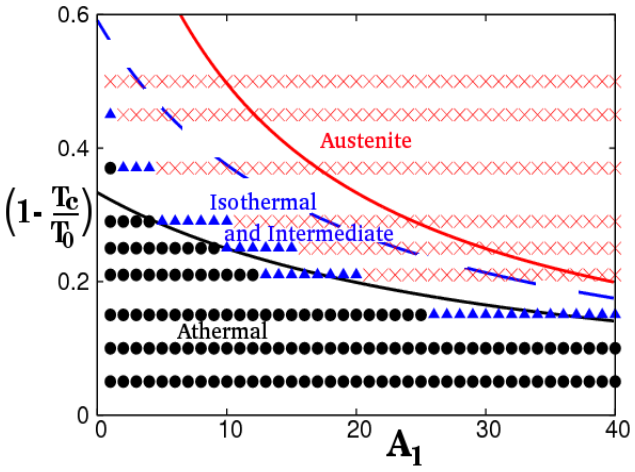

Figure 3.6: *Athermal/isothermal phase diagram:* Data of athermal/ isothermal behaviour as seen in simulations, in a phase diagram of T_c/T_0 versus A_1, for fixed $E_0 = 3$. Solid lines: Simple estimate of isothermal boundaries, from an effective droplet model of Section 3.5.3.

from material-dependent crossover temperatures $T_{1,2,4}(A_1)$, obtained from the droplet parametrization. For the isothermal case, stiffnesses must be large enough to drive the explosive-onset temperature to below zero, so $T_1(A_1) < 0$. On cooling, the fall in times is at least up to a flattening region near $T_2(A_1) > 0$, when the $1/T$ rise can take over giving a 'U'-curve characteristic of isothermal martensites. In terms of scaled temperatures, the isothermal region is then $\tau_2(A_1) > \tau_0 > \tau_1(A_1)$, where from (2.18), $\tau_0 \equiv -T_c/(T_0 - T_c)$, giving boundaries in T_c/T_0 versus A_1. The austenite region is where the transition itself is driven to zero, $T_4(A_1) < 0$ or $\tau_4(A_1) < \tau_0$. These simple boundary estimates work surprisingly well, as shown in Figure 3.6.

3.4 Isothermal martensite regime

We show the data from Monte Carlo simulations [56], that can make contact with the early martensite literature [2, 16]. Their qualitative similarity suggests that even such a simple statistical mechanics model in 2D, can capture some of the complex materials science in 3D.

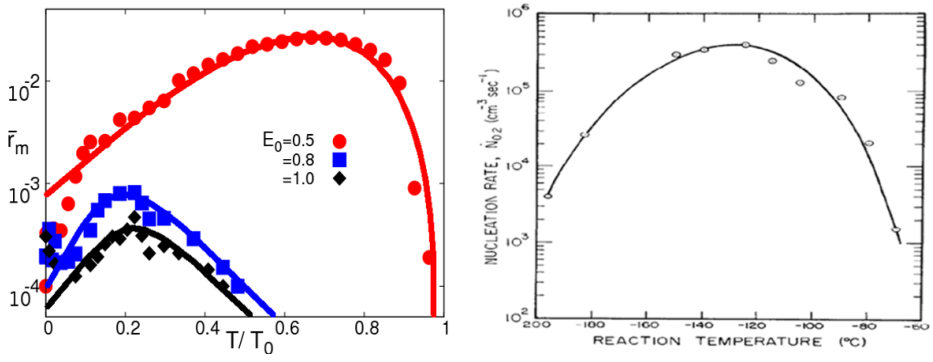

Figure 3.7: *Isothermal nucleation rates: Left:* Conversions rates $\log(\bar{r}_m)$ peaking with temperature T/T_0 for various dimensionless energies E_0. Solid lines are guide to the eye. *Right:* Measured nucleation rate versus reaction temperature in Ni-Mn alloy [16].

Pati and Cohen [16] have measured and modeled the conversion kinetics of Fe-Ni-Ga alloys, with a conversion-time criterion of 2% (rather than our 50%). They find isothermal conversion rates are peaked in temperature as mentioned. They also calculated conversion times for 2% of transfromation as a function of reaction temperatures in Ni-Mn alloy for austenitic grain size of 0.025mm and showed that, isothermal C-shaped curves with smaller embryo size can transform for larger embryo sizes to athermal fast conversions, with delay tails [16]. We will use the term 'isothermal' for curves with thermal activation at low temperatures, and 'athermal' for curves with low-temperature explosive growth, of a few MC sweeps.

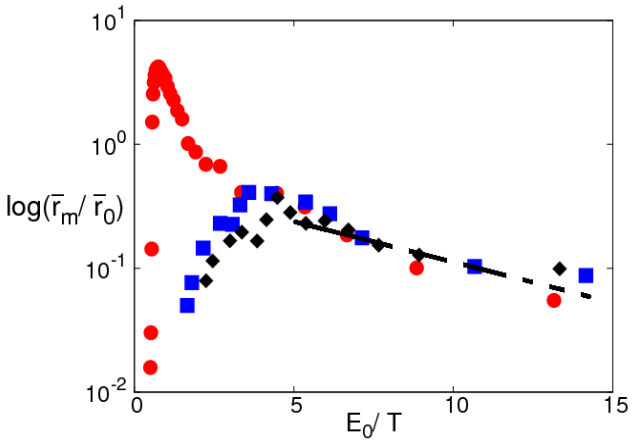

Figure 3.8: *Isothermal behaviour:* Plot of $\log(\bar{r}_m(T, E_0)/\bar{r}_0(E_0))$ versus activation parameter E_0/T for various E_0. Here the scaling rates $\bar{r}_0(E_0)$ are from the backward extrapolations of linear portions of unscaled plots. Note data clustering for large E_0/T, along a guide to the eye dashed line, a signature of activation over energy barriers.

Figure 3.7 (Left) shows that for $T_c/T_0 = 0.63, A_1 = 4$, a log-linear plot of the mean rate $\bar{r}_m(T, E_0)$ versus temperature T/T_0 is peaked, with smaller rates for larger dimensionless energy scales E_0. Figure 3.7 (Right) shows that simulations qualitatively match with experiments of Pati and Cohen [16].

Figure 3.8 shows that on the low temperature side, the logarithm of the scaled rates is linear in the activation variable E_0/T, as a signature of *energy barriers*.

Figure 3.9 (Left) shows the simulation data for fixed martensitic fraction $n_m(0) = 0.02$ and material parameters $A_1 = 4, E_0 = 3, \xi^2 = 1$, but different initial seed sizes $R(0)$. In a temperature-time plot, the isothermal C-shaped TTT curve for $R(0) = 1$ transforms to fast athermal conversions, that have delay tails for larger seeds sizes $R(0) > 1$. Figure 3.9 (Right) shows the calculated TTT curves for experimental data in Ni-Mn alloy with fixed

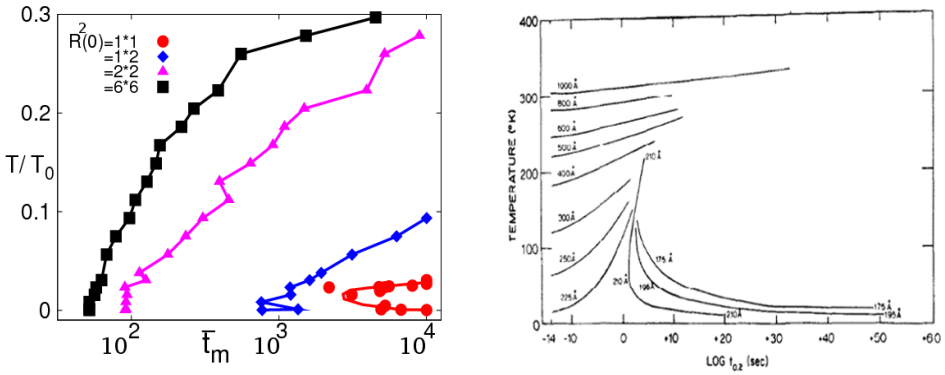

Figure 3.9: *isothermal/athermal crossover: Left:* TTT curves for fixed material parameters $A_1 = 4, E_0 = 3, T_c/T_0 = 0.63$, and fixed $n_m(0) = 0.02$, showing evolution of larger (and fewer) seeds of volume $R(0)^2$. *Right:* Plot of temperature versus transformation time measured in Ni-Mn alloy [16]. Compare Figure 3.5. See text.

austenitic grain size 0.025mm and for larger embryo sizes [16]. Simulations again qualitatively match with the calculations from experimental data.

3.5 Athermal martensite regime

We now focus on the non-activated athermal regime of Figure 3.6.

3.5.1 Conversion incubation times

The temperature dependence of conversion times [54], for various stiffnesses $A_1 = 1, 4, 10$ and different holding times $t_h = 1, 2, 5, 20 \times 10^3$ MCS with $N_{runs} = 100$ are shown in as $1/\ln \bar{t}_m$ vs τ in Figure 3.10. Times are cutoff-independent in the linear regions, where data points actually superpose, but then have t_h dependent peeloffs at times $\sim 0.8 t_h$. The linear portions are extrapolated to intersect the τ axis at temperatures defined as

$\tau_4(A_1)$. These decrease almost linearly with stiffness (see also Figure 3.21 below), and reassuringly agree with the previous operationally defined τ_4.

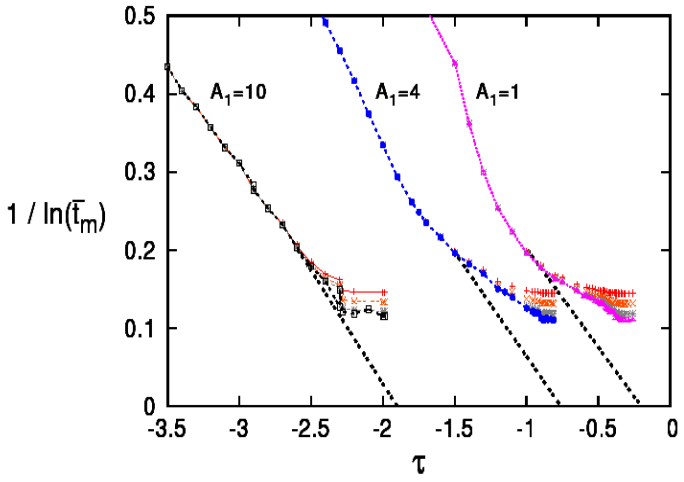

Figure 3.10: *Singular divergence of conversion-incubation times:* The transition temperature $\tau_4(A_1)$ is found from extrapolations to the axis, of inverse log time $1/\ln \bar{t}_m$ vs τ. Data have fixed A_1, and holding times $t_h = 1, 2, 5, 10 \times 10^3$.

A. Divergences

The main Figure 3.11 shows that $\log \bar{t}_m$ versus $\Delta\tau$ is essentially a hyperbola, with $\Delta\tau = 0$ as a vertical asymptote. Data include points extracted from the cutoff-dependent flattenings of the Figure 3.10 through 'finite-time scaling' in $1/t_h \to 0$. This is the Vogel-Fulcher behaviour familiar in (fragile) glasses [18], with times exponentially singular as the transition is approached. Marked temperatures are τ_1 (where $\bar{t}_m \sim 1$) and τ_2 is near the turn of the hyperbola (where $\bar{t}_m \sim 10$). The curve is

$$\bar{t}_m = t_0 exp[b_0|\tau_1 - \tau_4|/|\{\tau - \tau_4\}|], \tag{3.13}$$

with $t_0 = 1, b_0 = 0.88$, for these data. For fixed $E_0 = 3$ and $A_1 = 1, 4, 10$, the data [54–56] cluster on the curve, with a fall-off at the austenite-droplet spinodal τ_1. However Figure 3.11 also shows that clustering persists, for $A_1 = 4$ and *different* $E_0 = 4, 5, 6$: the times are *insensitive to energy scales*, so the athermal delays cannot be from energy barriers, but are dominated by *entropy barriers*.

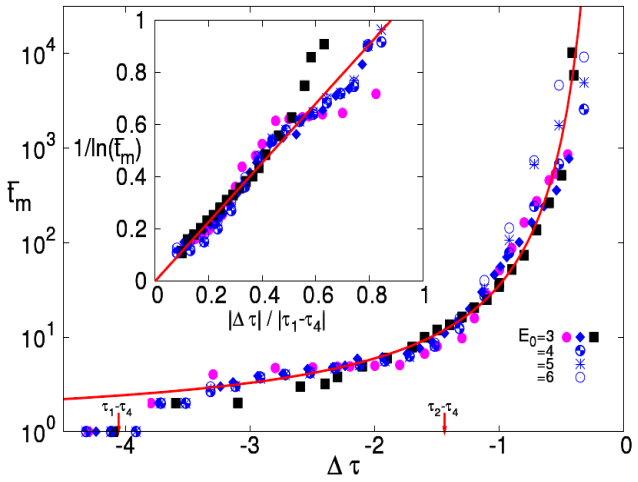

Figure 3.11: *Vogel-Fulcher behaviour of conversion times:* Plot of $\log(\bar{t}_m)$ versus $\Delta\tau = \tau - \tau_4$ with Vogel-Fulcher hyperbola as guide to the eye. Data are for fixed $T_c/T_0 = 0.9$ and $E_0 = 3, A_1 = 1, 4, 10$ as well as for $E_0 = 4, 5, 6$ and $A_1 = 4$. *Inset:* Plots of $1/\ln \bar{t}_m$ vs $|\Delta\tau|/|\tau_1 - \tau_4|$. They all fall on a (common) line to the origin. Compare with data 3D simulations and experiment in Chapter 6, Figire 6.6 and Figure 6.7 respectively.

Another way of showing the divergence is to plot $1/\ln \bar{t}_m$ versus $\gamma \equiv |\Delta\tau|/|\tau_1 - \tau_4|$, that is linear as $|\Delta\tau|$ goes to zero :

$$1/\ln \bar{t}_m = (\gamma/b_0)/[1 + (\gamma/b_0)\ln t_0]. \tag{3.14}$$

The inset of Figure 3.11 shows such a plot of the same data of main Figure 3.11, for different A_1, E_0 falling on the solid line of (3.14) over almost four orders of magnitude, with deviations as expected, near τ_1. The linearity close to transition again shows the behaviour is of the Vogel-Fulcher form.

A heuristic derivation of Vogel-Fulcher behaviour is as follows. The energy decrease for model relaxations of many non-interacting harmonic oscillators, is slow because of *only* entropy barriers, in repeated searches for remaining, and increasingly rare unrelaxed oscillators [23, 24]. The time dependence from analytic MC methods has been found to be [23, 24] $E(t) \sim 1/\ln t$. We assume a similar expression holds when entropy barriers dominate, for our model, that is diagonal and 'harmonic' in Fourier components. After a quench to τ, the energy approaches $H(\tau)$ from above, so $E(t) = H(\tau) + (D_0/2)B/\ln t$, where B is a coefficient. For incubation time $t = \bar{t}_m(\tau)$, this gives $E(\bar{t}_m) = H(\tau) + (D_0/2)B/\ln \bar{t}_m$. Now at a special temperature τ_4, we need $\bar{t}_m(\tau_4)$ to diverge, and the energy $E(\bar{t}_m)$ to become $H(\tau_4)$. A solution of these constraints is $H(\tau_4) = H(\tau) + (D_0/2)B/\ln \bar{t}_m(\tau)$. Linearizing the Hamiltonian difference $\sim g_L(\tau_4) - g_L(\tau)$ close to τ_4, one gets $-(\tau - \tau_4) \simeq B/\ln \bar{t}_m(\tau)$, implying Vogel-Fulcher times. The coefficient B can also be estimated: if at $\tau = \tau_1$ the conversion time is a few sweeps or $log\bar{t}_m(\tau_1) \sim O(1)$, then very roughly, $B \sim -(\tau_1 - \tau_4)$. Hence $|\tau - \tau_4|/|\tau_1 - \tau_4| \sim 1/\ln \bar{t}_m$, and the incubation time then is $\bar{t}_m \sim \exp(|\tau_1 - \tau_4|/|\Delta\tau|)$, as in Figure 3.11.

In summary, the Vogel Fulcher behaviour in simulations is seen over more than four orders of magnitude in time; at temperatures even far from transition; and with insensitivity in scaled variables to different material parameters. The insensitivity of times to E_0 implies that the Vogel Fulcher singularity comes from a non-activated regime of *entropy* barriers, with $\bar{t}_m \sim e^{|\Delta S_{entr}|}$, rather than from energy barriers with activated $\bar{t}_m \sim e^{E_0/T}$. The log-linear times $\bar{t}_m$ TTT curve of Figure 3.11 is thus effectively a plot of the vapour-to-liquid entropy barrier $|\Delta S|$ versus temperature $\Delta\tau$. The entropy barriers

diverge at τ_4, and vanish at τ_1.

$$|\Delta S_{entr}(\tau \to \tau_4)| \to \infty. \tag{3.15a}$$

$$|\Delta S_{entr}(\tau \to \tau_1)| \to 0. \tag{3.15b}$$

What does it mean to have a divergent entropy barrier ? If pathways are becoming rarer and rarer, then successful conversions become fewer and fewer. If the pathways are closed, then there are no conversions even waiting for long holding times t_h. Then there is 'broken ergodicity' for going from the 2% initial seeds to the (lower energy) 100% martensite state.

In the athermal regime and $\tau < \tau_1$, the fraction Φ_m of 100 runs that successfully convert to martensite is unity $\Phi_m = 1$. However, for $\tau > \tau_2$, not all runs can successfully convert, and Figure 3.12 shows that Φ_m starts decreasing at τ_2, to vanish at $\tau = \tau_4$ [54–56]. The rarity of conversions is not a finite-time effect that can be overcome by waiting longer: data for smaller $1/t_h$ (longer holding times also) fall on the same curve. Moreover Φ_m is insensitive to E_0, suggesting that energy barriers are not the cause of the delays. Since free energy barriers $\frac{\Delta F}{T} = \frac{\Delta U_{ener}}{T} - \Delta S_{entr}$ are a sum of energy barriers and *entropy barriers*, this again means the latter play a dominant role, as noted in Section 3.2. Thus the seemingly different results [15] of Figure 1.2 are all seen [54] to be relevant, in different parameter regimes [56]. The athermal regime indeed has delay tails as found by Kakeshita et al and Klemradt et al [9, 10]. The temperature separating explosive conversions from these tails indeed has a spinodal character, as modelled by Planes [12, 13] (so τ_1 is like T_c), but here from release of residual austenite droplets in martensite, rather than a bulk spinodal. See Figure 3.16 and discussion, in Section 3.5.2 below. The rise in times becomes detectable at τ_2, that is like M_s. The time divergence at a temperature T_4 well before the Landau temperature T_0 could explain the absence of conversions even for long annealing, of Otsuka [14].

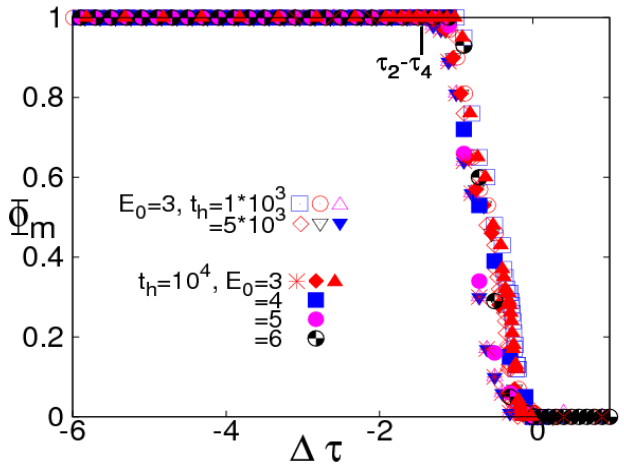

Figure 3.12: *Successful conversion fractions:* Successful-conversion fraction Φ_m versus $\Delta\tau \equiv \tau - \tau_4$, showing conversion become rarer, towards τ_4. Arrow marks $\tau_2 - \tau_4$. The curve is insensitive to holding times t_h, energies E_0, and stiffnesses A_1. The clustered data includes $E_0 = 3$ and $A_1 = 1, 4, 6$; $A_1 = 4$ and $E_0 = 4, 5, 6$; and different holding times, $t_h = 1000$, 5000, and $10,000$.

B. Distributions

We have considered the arithmetic mean $< r_m >$ that determines $\bar{t}_m$, with $1/t_h < r_m < 1$. The variance in the rates is ${\sigma_r}^2 =< (r_m - < r_m >)^2 >$. The *distributions* or probability densities $P(r_m)$ versus r_m are shown in the Figure 3.13, as histograms for different temperatures. For each histogram of N_{hist} data points, the Scott optimized bin size [49] is used, of $dr_m = 3.5\sigma_r/[N_{hist}]^{1/3}$. The histograms narrow sharply, below τ_2 of Figure 3.4 as shown by the delta-function-like peak on the right.

The temperature τ_2 thus has a physical meaning. Firstly, the fraction of successful runs Φ_m decreases falling below unity at τ_2 to become zero at τ_4 as shown in Figure 3.12. Increasing the holding times does not affect this: it is the *pathway* that become intrinsically rarer. Secondly, the sharp rate

distribution start becoming log-normal at τ_2, which is the 'onset of rarity'.

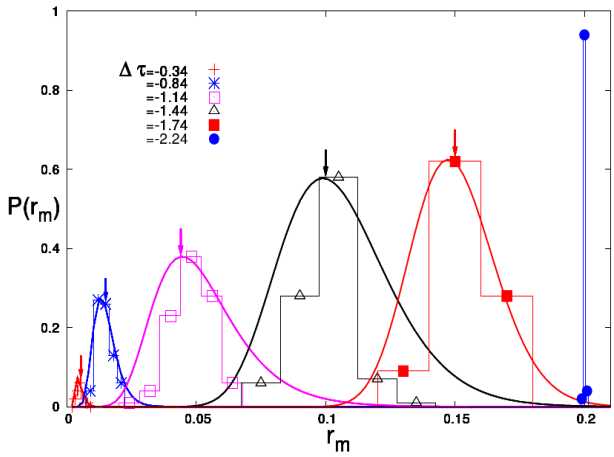

Figure 3.13: *Probability distribution of conversion-rates :* Plot of rate histograms $P(r_m)$ versus rates r_m for various temperatures $\Delta\tau$ and $A_1 = 4$. Arrows mark $< r_m >$ from data. Solid lines are log-normal curves.

Approaching transition at τ_4, the mean rate, (averaged over runs), can decrease in two limiting ways: the rates themselves can decrease with temperature, with all runs successfully converting; or, rates can be temperature-independent, with fewer and fewer runs successfully converting. Figure 3.13 shows that *both* effects occur. The rates clearly decrease approaching transition, with histograms moving to the left. But the histogram heights of successful runs also decrease, with unsuccessful conversions contributing to a spike at $r_m = 1/t_h$ (not shown). Clearly the histograms are not symmetric about the marked $< r_m >$ e.g. are not gaussians. Log-normal curves [38] shown as solid lines, are closer matches.

The log-normal probability *density* [38] for rate is a gaussian in the logarithm of rate $x \equiv \ln r_m$, with mean $< x >$, variances $\sigma_x^2 =< (x - < x >)^2 >$. The density-intervals are related by $dx = dr_m/r_m$, contributing a factor $1/r_m$

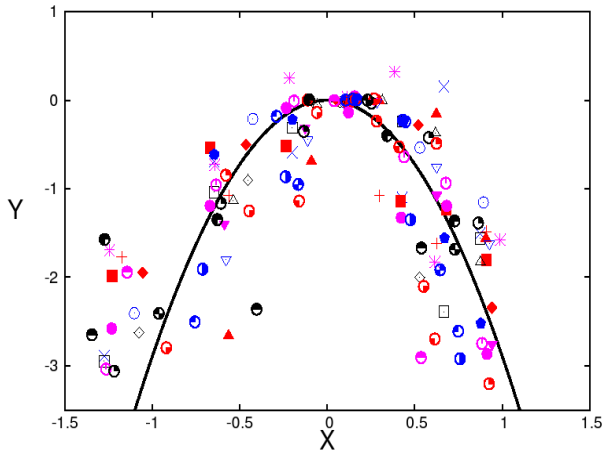

Figure 3.14: *Scaled log-normal distribution of conversion-rates:* Plot from data, of $Y = \ln[P(r_m)/P_0]$ versus $X = (x - < x >)/\sqrt{2}\sigma_x$, where $x \equiv \ln r_m$. Data are from Figure 3.11, with $E_0 = 3$ and different temperatures and stiffnesses. Solid line is the theoretical scaling curve of (3.17).

to the distribution written in terms of r_m, so

$$P(r_m) = P_0\, e^{[-\frac{(x-<x>)^2}{2\sigma_x^2}]}; \quad P_0 = \frac{1}{r_m(\sqrt{2\pi}\sigma_x)}. \tag{3.16}$$

Figure 3.14 shows that the data for $\tau_2 < \tau < \tau_4$ and $A_1 = 1, 4, 10$ all cluster around a scaled log-normal parabola,

$$Y = -X^2 \tag{3.17}$$

where $Y \equiv \ln[P(r_m)/P_0]$, $X \equiv (x - < x >)/\sqrt{2}\sigma_x$.

Kolmogorov has argued that the size-distribution of rock fragments produced by sequential and random splittings, should be log-normal [38]. The rate distribution can be similarly understood, heuristically. If entropy barriers dominate, $r_m \sim e^{\Delta S_{entr}}$ is controlled by rare transition pathways formed from steps $1, 2, 3..$ of probability $p_1, p_2, p_3....$ The *pathway* probability is the

product of these step probabilities, and is proportional to the fraction of states Ω that channel to conversion, or $\Omega \sim [p_1 p_2 p_3 ...]$. The entropy is $\Delta S_{entr} \sim \ln \Omega$, and hence the rate $r_m \sim \Omega$. It is the *logarithm* of the rate, $lnr_m \sim \ln \Omega = \sum_i \ln p_i$, that is the sum of a large number of independent, identically-distributed stochastic variables, and by the central limit theorem it is this logarithm that will have a gaussian distribution [38]. In an interesting paper, Bhattacharjee and co-workers have noted that such a log-normal distribution is relevant for the probability of rare events in turbulence, work fluctuations, and coin-tosses [38]. It is thus reasonable for entropy barriers $|\Delta S_{entr}| \sim |lnr_m|$ from increasingly rare search pathways, to have the distribution of (3.16, 3.17) and of Figures 3.13, 3.14.

3.5.2 Temperature-Time-Transformation phase diagram

An equilibrium phase diagram indicates static thermodynamic phases, at given temperature and pressure. Similarly, a TTT plot [54, 56] is a *dynamical* phase diagram that indicates the evolving domain-wall phases, at a given temperature and time.

A. Final textures and crossover temperatures

We quench to a temperature $T(<< T_0)$ and then hold, so the t-axis shows the evolutions. After the quench, a domain wall 'vapour' of 2% of martensite droplets converts to a disordered bidiagonal domain wall 'liquid' at a time $t = t_m$ through jerkiness, Ostwald ripening, and autocatalytic twinning. The fluctuating domain wall liquid then orients into a symmetry breaking domain wall 'crystal' at a later time $t = t_C$.

Figure 3.15 shows domain wall phases of 'vapour', 'liquid', 'crystal', 'precursor', and 'glass' for different stiffnesses $A_1 = 4$. As mentioned, the vapour-to-liquid conversion time is t_m, while the liquid-to-crystal orientation time

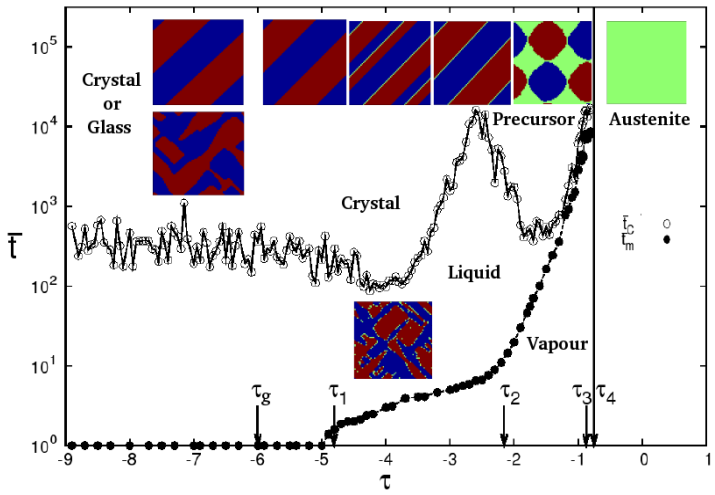

Figure 3.15: *Dynamical phase diagram :* TTT plot of delay times $\bar{t}_C, \bar{t}_m$ versus scaled temperature τ, for $A_1 = 4, T_c/T_0 = 0.9$. Here $\tau_4 = -0.76, \tau_3 = -0.88, \tau_2 = -2.2, \tau_1 = -4.8, \tau_g = -6.0$. Domain wall phases are labelled and characteristic temperatures are marked. Upper pictures show domain wall final states, and lower picture shows an evolving liquid with austenitic dynamic catalysts.

is t_C. Crossover temperatures are marked as $\tau_4 > \tau_3 > \tau_2 > \tau_1$. Here for $A_1 = 4$, phase temperatures are at actual values $\tau_4 = -0.76, \tau_3 = -0.88, \tau_2 = -2.2, \tau_1 = -4.8, \tau_g = -6.0, \tau_0 = -9$; while for other A_1 they would have different values as in a linear relation illustrated later as in Figure 3.21. The upper pictures show the final textures. For $\tau > \tau_4$, there is austenite. For a narrow region $\tau_4 > \tau > \tau_3$ there are tweed-like oscillating chequerboard variants in an austenite sea, discussed later in Subsection 3.5.4. For $\tau_3 > \tau > \tau_1$ there are martensite twins with residual austenite inclusions as seen by the light spots bound to domain walls. Within this region, at a temperature τ_2, the conversion time $\bar{t}_m$ flattens, while the orientation time $\bar{t}_C$ has a rise. For $\tau_1 > \tau$ there are only pure martensite-variant twins without austenite

inclusions. For $\tau_g > \tau$, and different runs, the twins compete with a frozen liquid or a domain-wall 'glass', of equal probability, that requires a separate study.

Figure 3.16 shows behaviour of austenite during successive quenches ending in states of twinned martensite. With the number of static $S = 0$ austenite cells given by $N_0 = N - \sum S^2$, the bulk austenite density $n_0 = N_0/L^2 \equiv 1 - n_m$ falls towards zero at τ_4, with persistent fluctuations down to τ_1. The bound residual austenite has line density N_0/L almost unity below τ_4. It falls to a lower value just above τ_1, and then to zero, as austenite inclusions on walls are released at the onset of pure martensite-martensite twins. Thus τ_1 has a *spinodal-like* character, but from *bound* austenite spots on domain walls, rather than bulk austenite, as mentioned earlier.

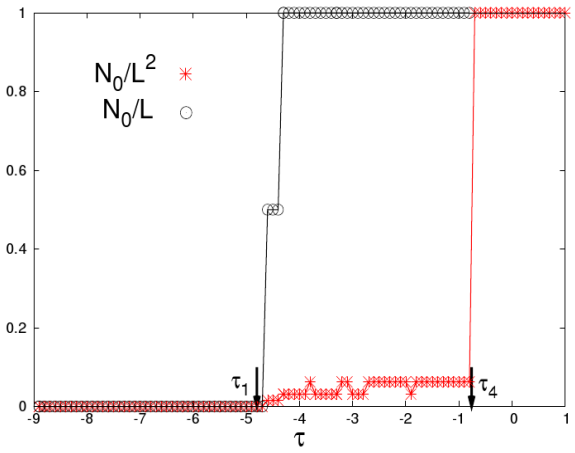

Figure 3.16: *Bound austenite:* Plots of austenite bulk density (N_0/L^2) and line density (N_0/L) versus τ, with τ_1, τ_4 marked.

We now consider parametrization of effective-droplet energies of textures to understand domain-wall phases and crossover temperatures of Figure 3.15.

3.5.3 Parametrization of textures by droplet energies

The classical picture of a droplet [47] for single-variant vapour is a competition between bulk $\sim -R^2$ and surface $\sim +R$ terms, where R is a geometic droplet scale. There is a critical radius $R_c(T)$ that diverges as $1/|T-T_0|$ at the Landau temperature $T = T_0$, where the bulk condensation energy vanishes. The energy barrier profile is an inverted parabola $H(R) \sim R_c[1-(1-R/R_c)^2]$, peaked at R_c, thus defining energetically 'subcritical' ($R/R_c < 1$) and 'supercritical' ($R/R_c > 1$) droplets.

Here we have two variants and the droplets are not independent, but interact through a powerlaw anisotropic potential, as in (2.24b). Nonetheless, at $t = 0$ with a small concentration of random seeds of both variants, the interactions will tend to cancel, as confirmed by simulations, leaving only the self energies $A_1[U]/2$ at each seed. Here $[U]$ is the Brillouin zone average of the kernel of (2.47) and for $2A_1/A_3 = 1$ is $[U] \simeq 0.3$. Then

$$\beta H[S(0)] \simeq \frac{D_0}{2} \sum_{\vec{r}} [g_L S(\vec{r},0)^2 + \xi^2 \{\vec{\Delta} S(\vec{r},0)\}^2 + \frac{A_1[U]}{2} S(\vec{r},0)^2]. \quad (3.18)$$

For an initial fraction $n_m(0) = 0.02$ say, and different-variant square seeds of sides $R(0)$, the simulated initial pseudospin seed energy can be parametrized as a droplet energy $\beta H[S(0)] = \beta H[R(0)]$. Here $\beta H[R(0)] \equiv C_0[\alpha_L g_L R(0)^2 + \alpha_G \xi^2 4R(0) + \alpha_C (A_1[U]/2) R(0)^2]$ with $C_0 \equiv (n_m(0) N D_0/2)$. Thus the $R(0)$ is for a single droplet out of the $n_m(0)L^2$ droplets. We fit the coefficients $\alpha_{L,G,C}$ term-by-term, for different sides $R(0) = 1, 2, 3$, finding $\alpha_L = \alpha_G = \alpha_C = 1$, independent of seed size. See Figure 3.17. Then the initial energy has a droplet-like form $\beta H[R(0)] = C_0 2\xi^2 R_c[1 - (1 - R(0)/R_c)^2]$. Here we define a length

$$R_c(\tau) \equiv \frac{-2\xi^2}{g_L(\tau) + A_1[U]/2}, \quad (3.19)$$

that is positive below a divergence temperature $\tau = \tau_L(A_1)$, where $\frac{1}{R_c(\tau_L)} = 0$. For $A_1 = 0$, $\tau_L = 1$, the Landau temperature.

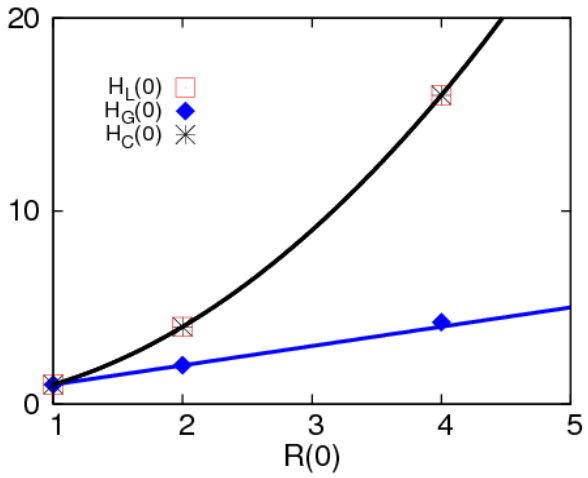

Figure 3.17: *Droplet parametrization:* Behaviour of Landau, Ginzburg and Compatibility terms for different initial seed sizes $R(0)$. Solid lines represents parabolas and a straight line, that are fits to data.

For general time t, the pseudospin and droplet Hamiltonians no longer match term-by term, but we *define* $R(t)$ as parametrizing the whole textural energy through

$$H[S(t)]/H[S(0)] = H[R(t)]/H[R(0)]. \tag{3.20}$$

The energy (ratio) for interacting pseudospins is thus parametrized by the energy (ratio) of a surrogate system of independent droplets. The initially geometric $R(0)$ evolves to an interacting-texture *energetic* parameter $R(t)$, that can even go negative, when $H[S(t)]$ goes negative. Thus

$$\rho(t) \equiv \frac{\beta H[S(t)]}{\beta H[S(0)]} = [1 - (\frac{R(t)}{R_c} - 1)^2]/[1 - (\frac{R(0)}{R_c} - 1)^2]. \tag{3.21}$$

Solving the quadratic, the $R(t)$ evolution is then

$$R(t)/R_c = 1 + \alpha\sqrt{1 - \rho(t)/\rho_c} \tag{3.22}$$

where $\rho_c \equiv [1-(\frac{R(0)}{R_c}-1)^2]^{-1}$, and we take $\alpha = sign(\frac{R(0)}{R_c}-1)$. Here $R(t)=0$ for pure austenite and *also* for martensite droplets where bulk and surface energies balance to give zero energy. These special droplets that are 'critical' for entropy barrier crossing, will appear again in Chapter 7.

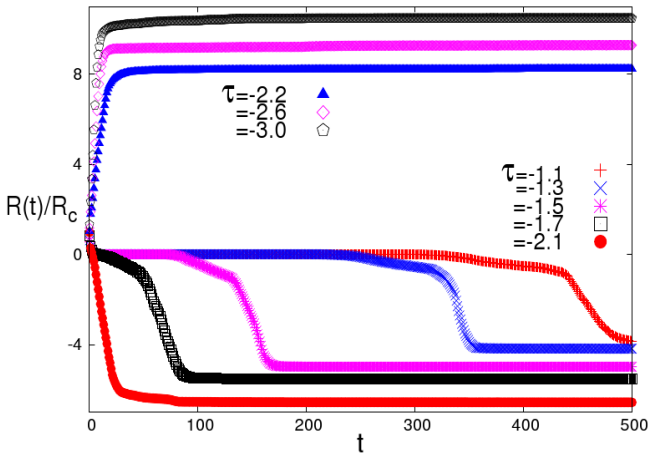

Figure 3.18: *Trajectories:* Energy parameter $R(t)/R_c$ vs t, showing flows are determined by initial $R(0)/R_c(\tau)$ values. Note flat incubations of lower curves, of initial $1 > R(0)/R_c(\tau) > 0.5$, corresponding to $\tau_4 > \tau > \tau_2$. See text.

Figure 3.18 shows the athermal trajectories in a plot of $R(t)/R_c(\tau)$ versus time, with starting values $R(0)/R_c$ determining the $R(t)$ flows. At low temperatures $\tau < \tau_1$, there are rapid rises to final positive values (and negative energies). At higher temperatures $\tau_4 > \tau > \tau_1$, there can be long incubations before falls to final negative values (and negative energies). The relative flatness of the energy parameter $R(t)$ during incubations will re-appear as constant-energy signatures of entropy barriers, in Subsection 3.5.4.

As a consistency test of parametrization, Figure 3.19 shows that the simulated $\rho(t)/\rho_c$ versus $R(t)/R_c$ indeed matches an inverted parabola of (3.21) for all t, and all A_1, and many starting values $R(0)/R_c(\tau)$. The parabola is

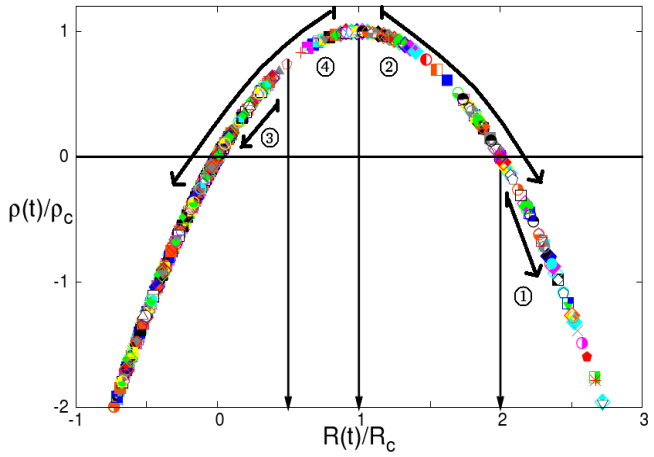

Figure 3.19: *Parametrization and crossover temperatures :* Scaled pseudospin energy $\rho(t)/\rho_c$ versus $R(t)/R_c(\tau)$, showing athermal flows fall on a parabola as a test of parametrization. For $R(0) = 1$ seeds, characteristic initial values $R(0)/R_c$ are ${R_{c1}}^{-1} = 2, {R_{c2}}^{-1} = 1, {R_{c4}}^{-1} \simeq 0.5$ as marked by the initial starting bars of arrows. These correspond to temperatures τ_1, τ_2, τ_4. For initial $R(0)/R_c < 0.5$, flows are to $R = 0$ austenite. The Regions ①,②,③,④ are marked, and used in Chapter 7 later. See text.

divided into four $R(0)/R_c(\tau)$ value regions ①,②,③, and ④, that determine subsequent flows. Flow directions of $R(t)$ in the athermal region are indicated by arrows starting at $R(0)/R_c$, with asymptotic $R(t)$ giving final energies, that are negative in martensite, or zero in austenite. Note that flows to the left can pass through and pause for a long time at $R = 0$ values that corresponding to textures with the same energy as austenite. As discussed in Chapter 7, there is a formation of such a self organized, (entropically) critical droplet, in searches for pathways.

The droplet-energy parametrization can be used to estimate the characteristic temperatures $\tau_{1,2,4}(A_1)$.

i) *Region* ①: For initial $R(0)/R_c \geq 2$ in the ① of Figure 3.19, the seed

energies are already negative, i.e below that of $R = 0$ austenite, going even more negative through explosive martensite growth and austenite expulsion. With initial unit seeds $R(0) = 1$, this determines a temperature $\tau = \tau_1$ through

$$1/R_c(\tau_1) \equiv 1/R_{c1} = 2. \tag{3.23}$$

where $R_c(\tau)$ is defined in (3.12), and its numerical value at τ_1 is $R_{c1} = \frac{1}{2}$.

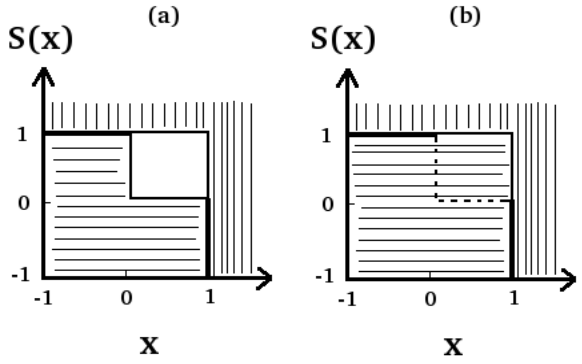

Figure 3.20: *Schematic diagram for zeros on domain walls :* (a) showing two steps from the presence of the austenite (white $S = 0$) on domain walls. (b) single step as there are no zeros on domain walls. Dashed line marks the removed austenite droplet.

The final state for $\tau_g < \tau < \tau_1$ from TTT phase diagram of Figure 3.15 is single diagonal twins of martensite variants. For $\tau < \tau_1$, there can be bound austenite on domain walls. We can directly estimate the binding energy of an austenite $S = 0$ unit cell attached to a stepped diagonal between $S = +1$ and $S = -1$ martensite variants. The schematic is shown in Figure 3.20 with $S = 0$ (white) as austenite unit cell; and $S = +1$ (vertical hatch) $S = -1$ (horizontal hatch) as martensite unit cells. For an austenite/ martensite unit interface, $[\vec{\Delta}S(\vec{r})]^2 = (\pm 1 - 0)^2 = 1$ marked by the light line. The energy of the austenite 4-sided square is $H = H_L + H_G + H_C \sim 0 + 4\xi^2 \times 1 + 0 = 4\xi^2$. For

a martensite/ martensite unit interface, the wall-cost is higher, $[\vec{\Delta}S(\vec{r})]^2 = (1-\{-1\})^2 = 4$ marked by the heavy line. Replacing the $S=0$ austenite square, by martensite the four austenite/ martensite interfaces are replaced by two martensite/ martensite interfaces, and have extra condensation and self-interaction energies, so $H = H_L + H_G + H_C \sim g_L + 2\xi^2 \times 4 + A_1[U]/2$. The difference is the binding energy of the austenite square to the martensite domain wall, $\sim g_L(\tau) + 4\xi^2 + A_1[U]/2 \leq 0$. The austenite binding thus vanishes at the same temperature given in (3.23), and therefore τ_1 has a (local) spinodal character.

ii) *Region* ②: For initial droplets $2 > R(0)/R_c \geq 1$ in the Region ② of Figure 3.19, flows are again to increasingly positive R and decreasing energy. With unit seeds, this determines a temperature $\tau = \tau_2$ through

$$1/R_c(\tau_2) \equiv 1/R_{c2} = 1 \tag{3.24}$$

where the numerical value is $R_{c2} = 1$.

iii) *Region* ③: For $0.5 > R(0)/R_c$ in the Region ③ of Figure 3.19, the above conversion channel closes off for temperatures $\tau > \tau_4$, when flows go only to $R = 0$ austenite.

iv) *Region* ④: For $1 > R(0)/R_c \geq 0.5$ in the Region ④ of Figure 3.19, there is a droplet regime where flows pause for a delay time (as also shown in the R(t) flows of Figure 3.18) at $R(t) \simeq 0$ as mentioned earlier, and then go to increasingly negative R and decreasing energy. These incubations occur up to a temperature $\tau = \tau_4$ where

$$1/R_c(\tau_4) \equiv 1/R_{c4} \simeq 0.5. \tag{3.25}$$

where the numerical value is $R_{c4} = 2$. The austenite/martensite transition at τ_4 can be understood, through a coalescence or cooperative nucleation scenario [37]. A unit seed with $R(0)/R_c(\tau) = 1/R_c < 1$ below the parabolic maximum. But if there is correlated formation of martensite on any of four

next-nearest (diagonal) sites, then one has a larger droplet or new seed of scale 2. Regarding this as a 'fresh start' with "$R(0)$" $= 2$, one can have effective expansion, as $2/R_c(\tau) > 1$ for the new combined droplet, yielding the same τ_4 as above.

The estimated transition temperatures $\tau_i(A_1)$ for $i = 1, 2, 4$ can be obtained. The transition temperatures are at $R_c(\tau_i) = R_{ci}$ where ${R_{c1}}^{-1} = 2, {R_{c2}}^{-1} = 1, {R_{c1}}^{-1} = 0.5$. Using (2.18) and (2.22) to rewrite this as a quadratic in τ_i, the analytic solution is $\tau_i(A_1) = [1 - 3X_i + \sqrt{1 + 2X_i}]/2$ where $X_i \equiv (A_1[U]/2) + (2\xi^2/R_{ci})$. These are the curves of Figure 3.21 (Left), that are essentially linear in A_1. Expected textures are found in the estimated regions, with fuzziness as usual (not shown), at the boundaries. Figure 3.21 (Right) shows the same data of Figure 3.21 (Left) but now in terms of $R(0)/R_c(\tau)$ of (3.23), (3.24), and (3.25). Clearly, the parametrization is in good agreement with the simulation data for different elastic stiffness constants A_1. The divergence temperature of (3.19) where $1/R_c(\tau_L) = 0$ is far above, i.e. $\tau_L > \tau_{1,2,4}$, so the effective droplet scales $R_c(\tau)$ at the boundaries are *finite*.

The analytic results for $\tau_{1,2,4}$ then provide the isothermal region boundaries of the earlier Figure 3.6. From Figure 3.5, for the athermal case both temperatures are positive, $T_2 > T_1 > 0$, or $\tau_2(A_1) > \tau_1(A_1) > \tau_0$. For the isothermal and intermediate curves there must be no explosive onsets, that are driven below zero temperature, so $T_1(A_1) < 0$, or $\tau_1(A_1) < \tau_0$. The isothermal U-curves form easily when the flattening of the TTT curve at τ_2 facilitates the takeover of the slope by the Boltzmann $1/T$, so $T_2 > 0$ or $\tau_2(A_1) > \tau_0$. The combined conditions for isothermal (and intermediate) curves are then

$$[1 - 1/\tau_1(A_1)]^{-1} > T_c/T_0 > [1 - 1/\tau_2(A_1)]^{-1}. \tag{3.26}$$

For $T_2(A_1) < 0$ or $\tau_2 < \tau_0$, distorted intermediate curves are very high,

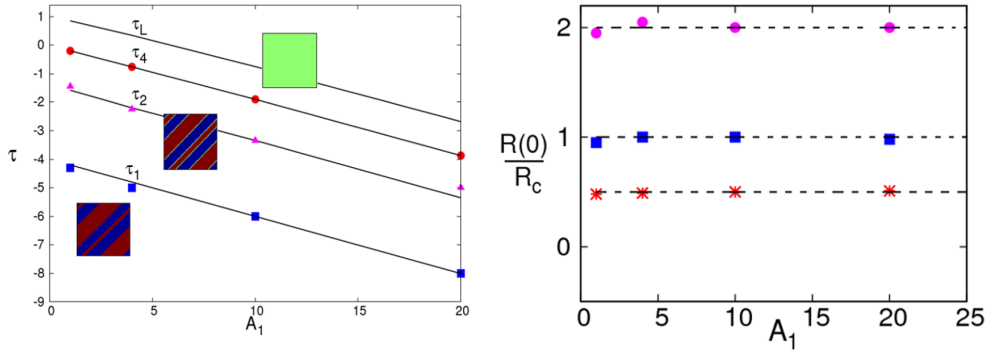

Figure 3.21: *Textural crossover temperatures: Left:* Phase diagram τ versus A_1 for $1 > \tau > \tau_0(= -9.0)$, showing final textures. Theoretical boundaries in τ_1, τ_2, τ_4 are defined by $R_c(\tau_{1,2,4}) = R_{c1,c2,c4}$ of the text. They are all well below the line $\tau_L(A_1)$ where the critical radius diverges, $1/R_c(\tau_L) = 0$. Here the bulk Landau temperature at $A_1 = 0$ is $\tau_L(0) = 1$. *Right:* Comparison of theoretical $R(0)/R_c(\tau) = 1/R_c(i)$ dashed lines with simulation data (symbols), showing good agreement.

and squeezed close to zero temperatures (Figure 3.5). If the austenite-martensite transition itself is driven to zero, $T_4(A_1) < 0$ or $\tau_4(A_1) < \tau_0$, then there is only austenite, for

$$[1 - 1/\tau_4(A_1)]^{-1} > T_c/T_0. \tag{3.27}$$

These rough estimates are the solid and dashed line boundaries of the T_c/T_0 versus A_1 plot of the earlier Figure 3.6, and work surprisingly well.

In fact the parametrization further suggests that a scaled temperature variable

$$\eta(\tau) = -1/R_c(\tau) = \frac{g_L(\tau) + A_1[U]/2}{2\xi^2} \tag{3.28}$$

can be used in the TTT diagram of Figure 3.15, taking on universal crossover values of $\eta(\tau_4) = -0.5, \eta(\tau_2) = -1, \eta(\tau_1) = -2$ for materials of different A_1.

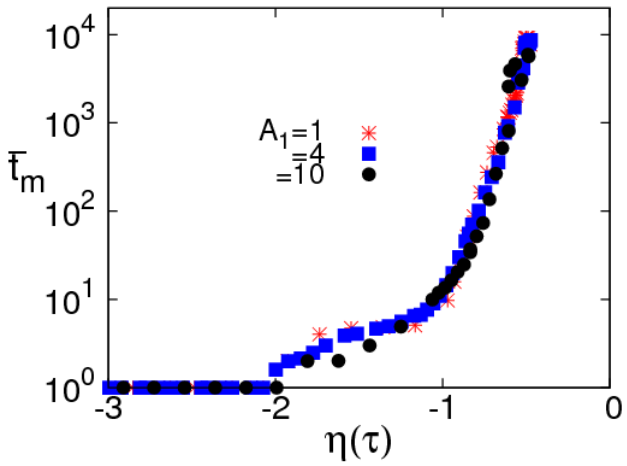

Figure 3.22: *Conversion times and crossover temperatures:* Plot of $\bar{t}_m$ versus scaled temperature variable $\eta(\tau)$ of (3.28) for fixed $E_0 = 3$ and different A_1, showing the data collapse at special values of $\eta(\tau) \simeq -2, -1, -0.5$.

This is confirmed in Figure 3.22, where the data of conversion times versus quench temperatures are strongly clustered.

3.5.4 Development of microstructures during incubations

With the textural crossover temperatures and isothermal/ athermal regimes in hand, we now see how microstructures evolve during macroscopic non-activated incubations in both conversion and orientation, for different temperatures in the athermal parameter regime.

A. Conversion incubations

What goes on, at a textural and thermodynamic level, during *conversion* or vapour-to-liquid incubations t_m ?

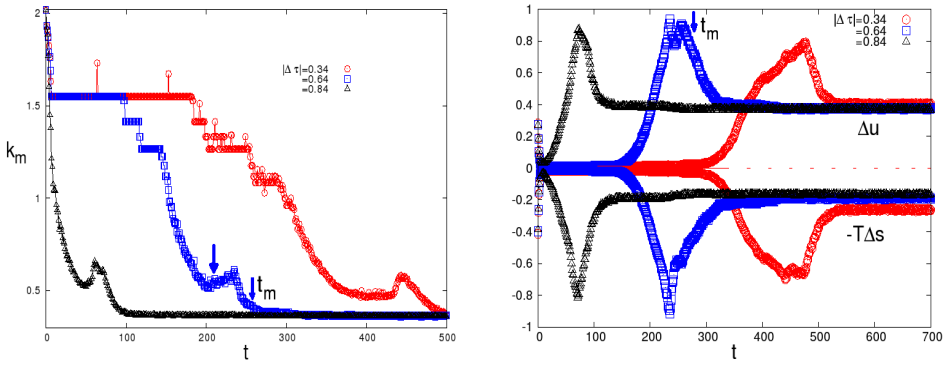

Figure 3.23: *Conversion-case: Wavenumbers and Textural thermodynamics: Left:* Diagnostic $k_m(t)$ versus time during t_m incubation for $A_1 = 4$ and $|\Delta\tau| = 0.34, 0.64, 0.84$. Arrow indicates onset of 'autocatalytic twinning', see text. The later time t_m is also marked. *Right:* Excess internal energy $\Delta U_{ener}(t)$, and negative entropy $-T\Delta S_{entr}(t)$ versus time t, for $|\Delta\tau| = 0.34, 0.64, 0.84$. Note the flat regions during t_m incubation, and asymptotic nonzero values.

For $\tau_3 > \tau > \tau_2$, the vapour-to-liquid incubation dominates the total delay to twins, hence $t_C - t_m << t_C$ as shown in Figure 3.15. For such temperatures, Figure 3.23 shows the wavenumber coarsening in k_m, that is *finite* during incubation delays, decreasing in jerky steps, rising and then finally falling to level off at a nonzero value. The initial 2% random concentration of ± 1 variants quickly transform to a single variant droplet, reminiscent of Ostwald ripening [47]. See Chapter 7. This is shown in the variant imbalance of Figure 3.24 that rises to unity (single variant) before falling to zero ('neutrality'). The droplet then searches for a rare transitional state by sending fluctuating arms along diagonals, through which it sequentially expands in a jerky way, sticking at various sizes. This is reflected both in the $k_m(t)$ steps and also the steps in martensite fraction $n_m(t)$ of Figure 3.24. At a time

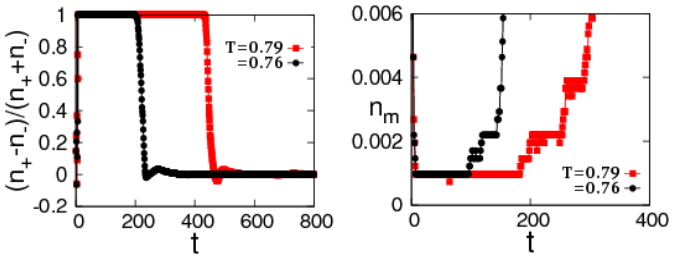

Figure 3.24: *Left: Growth of martensite droplet :* Martensite fraction imbalance between $S = \pm 1$ variants, or $(n_+ - n_-)/(n_+ + n_-)$ versus time for two temperatures in quench region ④. A single-variant droplet (of imbalance) unity forms after a short interval t_{start}, that searches for a path to textures of zero variant imbalance. *Right:* Jerkyness in the 'flat' incubation regions of martensite fraction $n_m = n_+ + n_-$ versus time before autocatalytic rise around the mean conversion time.

marked by the arrow in Figure 3.23 (Left), the expanded droplet generates the other variant by *autocatalytic twinning*, or cooperative droplet formation, as found by Bales and Gooding as in 1D strain dynamics (without no compatibility potential). There is then correlated anisotropic expansion. The twin front extends through the system in the easy directions of the power law anisotropic potential. After the incubation time t_m as indicated, the wavenumber flattens. See movie of martensite formation and growth in the online version of Ref [54, 54].

Thermodynamic functions F, U_{ener}, S_{entr} can be found, as in the thesis Appendix A , in local meanfield approximation [33]. The *excess* thermodynamic functions are the domain wall costs above the corresponding $A_1 = 0$, $\xi = 0$ expressions. Figure 3.23 (Right) shows that the excess internal energy ΔU_{ener} and entropy ΔS_{entr} versus time, indeed are quite flat, decreasing only slowly. (In the Hamiltonian, the large coarsening decreases in the gradient term $\sim k_m^2(t)$, are nicely compensated by correlated increases in the mis-

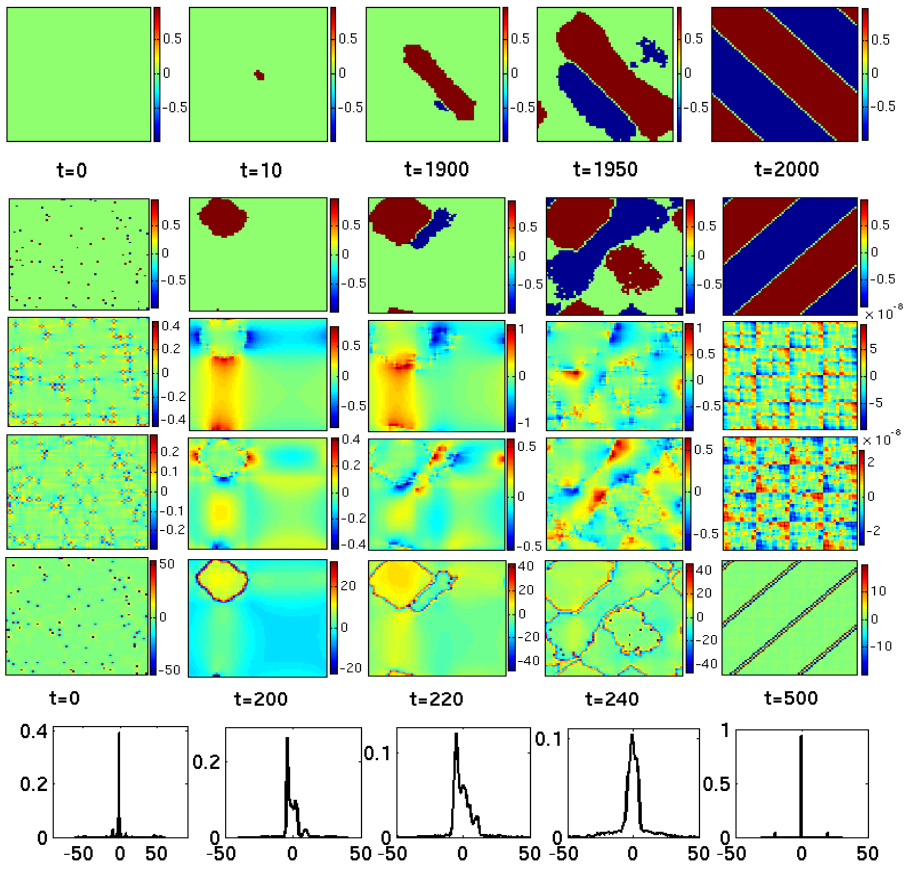

Figure 3.25: *Conversion-case: Textural evolution.* First row: Local *external* stress applied to austenite $\tau > \tau_4$, showing elastic photocopying ending in stress-induced twins. Second row: Time evolution of OP strain e_2 for $\tau < \tau_4$, with snapshots showing that *internal* stress produces an elastic photocopying route to twins. Third, fourth rows: Expulsion of non-OP strains e_1, e_3 respectively. Fifth row: Local *internal* stress $p_2(r)$ showing the *bulk is stress-free*, with trapped stress only along walls. Sixth row: Evolution of stress distribution, to a spike at zero bulk stress, with small peaks on either side. See text.

orientation cost.) In fact the excess *free* energy $\Delta F = \Delta U_{ener} - T\Delta S_{entr}$ is also flat, and almost zero. For long times, there are trapped residual values, reminiscent of glasses.

Textural evolution snapshots are shown in Figure 3.25, with OP e_2 and non-OP strains $e_{1,3}$ from pseudospins S as from (2.48). The first row illustrates the effect of a local, fixed *external* stress $p^{ext}(\vec{r})$ applied to $\tau > \tau_4$ austenite. Snapshots show the externally induced autocatalytic twinning or 'elastic photocopying' as in Lookman et al [29] in $e_2 \sim S$, ending in stress-induced martensite. The discrete pseudospins thus faithfully reproduces the effect seen in continuous variable simulations [29].The second row shows e_2 evolution described above, with autocatalytic twinning, ending in twins with bound residual austenite. The third and fourth rows show expulsion of the corresponding non-OP strains e_1, e_3 with very small final values. The fifth row shows that the dynamic internal local stress $p_2(\vec{r}, t)$ of the thesis Appendix relaxes to zero in the bulk of the system, and is nonzero only on parallel lines of positive/negative trapped stresses along e_2 domain walls. Thus the driving force towards the ordered textures of the domain-wall glass is the expulsion of stresses in the bulk. The sixth row shows evolution of the stress distributions, that fall and then rise to then become symmetric, ending as a delta function at the (bulk) zero stress with small peaks on either side from the trapped wall stresses.

B. Orientation incubations

What goes on, at a textural and thermodynamic level, during *orientation* or liquid to crystal incubations t_C ?

For $\tau_1 > \tau > \tau_g$, the liquid-to-crystal incubation t_C dominates the total delay to twins and $t_C - t_m >> t_m$ as in Figure 3.15. Wavevectors during orientation delays are shown in Figure 3.26 (Left), with flat regions of finite scales during incubations, finally falling to level off to a nonzero wave-vector, as before.

Figure 3.26 (Right) shows the excess internal energy (ΔU_{ener}) and entropy (ΔS_{entr}) are flat during the incubation, with steps at hotspot appearances. The flatness in energy again is a signature of entropy barriers. The free energy is again also flat, but now at nonzero values. Asymptotically, there are trapped residual energies and entropies in the twin states, reminiscent of glasses [18].

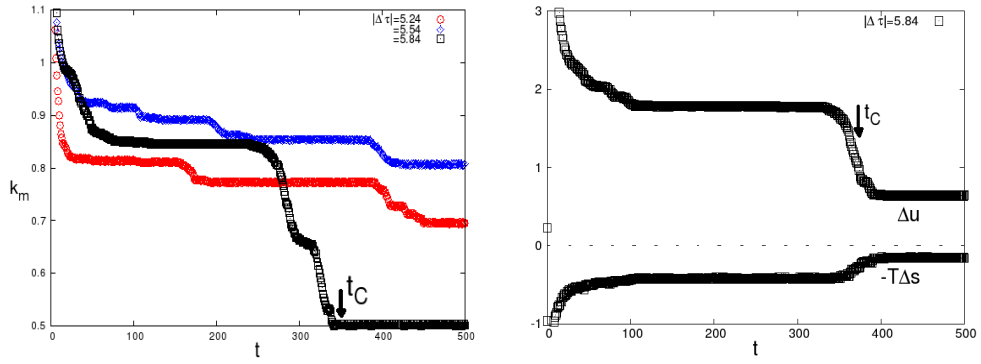

Figure 3.26: *Orientation-case: Wavenumbers and Textural thermodynamics: Left:* Diagnostic $k_m(t)$ versus time during t_C incubation for $A_1 = 4$ and $|\Delta\tau| = 5.24, 5.54, 5.84$. *Right:* Excess internal energy $\Delta U_{ener}(t)$, and negative entropy $-T\Delta S_{ent}(t)$ versus time t, for $|\Delta\tau| = 5.84$. Note flat region during t_C incubation, and asymptotic nonzero values.

Textural evolution snapshots are shown in Figure 3.27. The first row shows evolving domain-wall liquid patterns below τ_1 where austenite inclusions disappear, so all austenite spots are transient fluctuations. The liquid is frozen over large regions, but domain-wall mobilities are enhanced by *transient austenitic hotspots* [33], that are *dynamical catalysts*, acting nonlocally in both space and time. The high temperature austenite droplets are generated in non-OP regions [53, 54], relieving local stresses. See movie of how orientation is induced in the online version of Ref [54, 56] by these high-

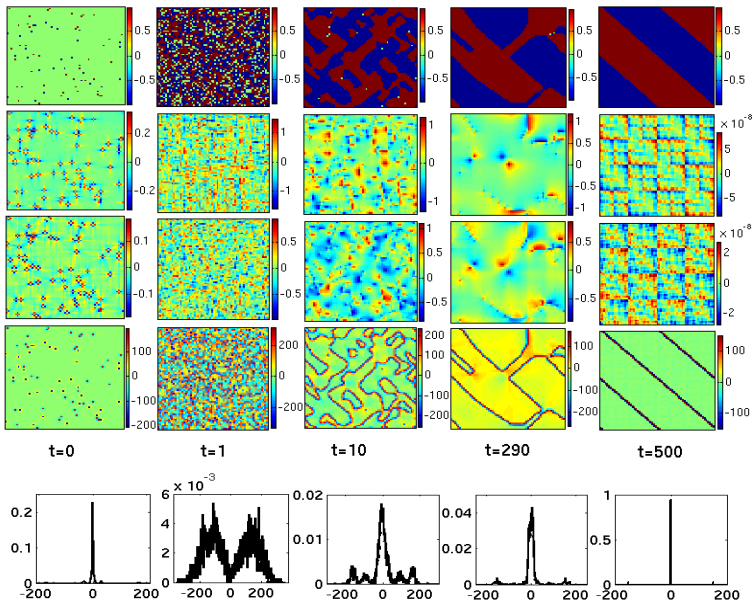

Figure 3.27: *Orientation-case: Textural evolution.* First row: Time evolution of e_2 textures, for $\tau_g < \tau < \tau_1$, with snapshots showing transient hotspot catalysts facilitating twin formation. Second , third rows: Expulsion of non-OP e_1, e_3, respectively. Fourth row: Local internal stress $p_2(\vec{r})$ showing bulk is stress-free, with trapped stress only along walls. Fifth row: Evolution of stress distribution, to a spike at zero bulk stress, with small peaks on either side. See text.

velocity 'dynamical heterogeneities' in the terminology of glasses [18]. The second and third rows again show expulsion of non-OP strains e_1, e_3 of (2.48) to low values, as before. The fourth row shows the local internal stress $p_2(\vec{r})$ of the thesis Apendix A that is expelled from the bulk, existing only as positive/negative trapped stresses in lines along the domain walls. The fifth row shows the stress distribution becomes bi-modal and small, before rising and sharpening to a final delta function at zero, with small peaks on either side from the wall stresses.

In all of the incubations considered, the powerlaw anisotropic potential plays a central role. Section 3.8 shows that for $A_1 = 0$, there are delays, but no incubations or divergences.

C. Intrinsic tweed

Finally, we go back to the precursors of Figure 3.15 that are qualitatively like the tweed seen in experiments and extrinsic disorder simulations [5, 27]. The tweed here is *intrinsic* [26], in a temperature region below τ_4, whose width depends on initial conditions. For a large seed concentration of 1/3 fraction each of $\pm 1, 0$, the tweed occurs up to a temperature τ_3.

Tweed forms because martensite droplets can order under anisotropic interactions into preferred $\theta = \pi/4$ directions where the potential vanishes [26], as discussed in Subsection 2.2.2 (A). The ordered martensite chessboards are analogous to dilute 'Wigner lattices' of interacting martensite 'charges'. Same-variant droplets order along the diagonals, where their repulsive powerlaw interaction vanishes. For both variant droplets each along its own diagonal, this yields an vibrating chessboard. Figure 3.28 shows tweed evolution. The first row shows snapshots of $e_2 \sim S$ droplets forming the chessboard. The second and third rows show that the non-OP e_1, e_3 of (2.48), is appreciable where droplets are closest. The fourth row is the local stress $p_2(\vec{r})$ of the thesis Appendix, that is expelled from the bulk and localized around the vibrating austenite/ martensite habit boundaries. The sixth row is the stress distribution, that starts out tri-modal and small, then rising to a distribution peaked at zero, but now showing wings on either side, unlike Figures 3.25, 3.27. See movie of tweed formation and oscillations in the online version of Ref [54, 56].

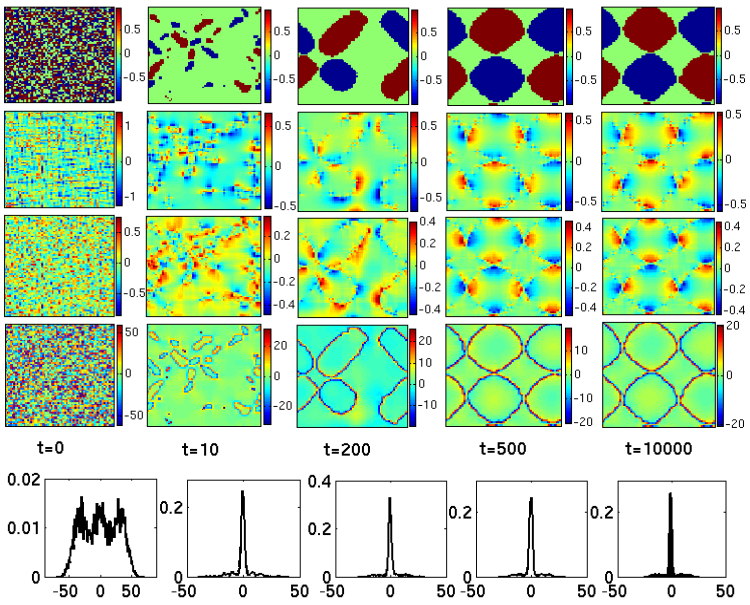

Figure 3.28: *Precursor case: Textural evolution.* First row: Time evolution of e_2 textures for $\tau_3 < \tau < \tau_4$, showing final oscillating chessboards. Second and third rows: Clustering of non-OP strains e_1, e_3 repectively. Fourth row: Local internal stress showing the bulk is stress free, with trapped stress along the austenite/martensite habit boundaries. Fifth row: Evolution of stress distribution to a peak around zero, with wings on either side. See text.

3.6 Why do metastable twins occur ?

How do energies of oriented twins compare with uniform martensite? Consider for simplicity, $\tau < \tau_1$, i.e. no austenite inclusions. The compatibility cost at optimum orientation is zero, and the Landau energy is $\sim N g_L$. For N_{wall} domain walls stretching across the system, the Ginzburg contribution is $\xi^2 \sum (\vec{\Delta} S)^2 \sim N_{wall} L$. The energy is then $H \sim N g_L + \xi^2 N_{wall} L$ and the excess energy diagnostic of (3.7) is $\delta_H \sim (N_{wall}/N) L$.

Now for equally spaced twins arising from surface compatibility poten-

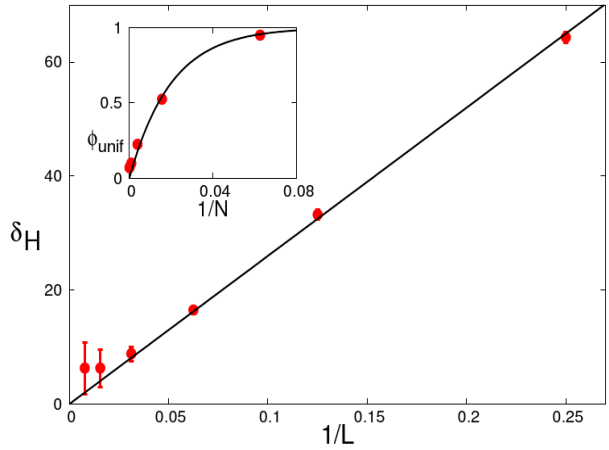

Figure 3.29: *Finite-size dependence of quantities:* Excess energy density δ_H versus $1/L$, showing near-degeneracy of sparse twins with uniform martensite. *Inset :* Fraction of 100 runs ϕ_{unif} that go to uniform martensite (instead of twins), versus $1/N$, showing twins dominate for large systems.

tials, the domain wall separation is found to scale with system size [6] as $w \sim L^{1/2}$, as in experiment. The number of walls is $N_{wall} = L/w = L^{1/2}$. The wall density is sparse rather than intensive, scaling to zero as $N_{wall}/N \sim 1/L^{3/2}$, so the fractional excess energy scales to zero with $\delta_H \sim \xi^2/\sqrt{L}$. The bulk twins of our case are even sparser, with Figure 3.29 showing that $\delta_H \sim 1/L$: in either case, the energy densities of (many possible) twin states are almost degenerate with the single, uniform martensite state. Once formed, the twins are locked into the preferred directions.

For our simulations, as mentioned below (3.2), we had eliminated the strictly $\vec{k} = 0$ state (but allowed the $k \sim 1/L$ states). For $\vec{k} = 0$ now allowed, the inset Figure 3.29 shows that for increasing system size $N = L^2$, the fraction Φ_{unif} of $N_{runs} = 100$ attempts that reach the uniform state becomes negligible. Thus pathways to the many twin states with $N_{wall} \neq 0$ tend to dominate over those to the single, $N_{wall} = 0$ uniform state. It is only for

very small system sizes that the locked-in twins can escape to yield uniform martensite, as in fact we observe.

Thus these 'excited states' of oriented domain walls are almost degenerate with uniform martensite are large in number. Hence the many possible twin states can successfully compete with the single global minimum of uniform martensite.

3.7 Thermal hysteresis and acoustic emissions

In the previous Section, we have considered temperature quenches, followed by long-time fixed-temperature annealing. For temperature *cycling* back and forth on the athermal TTT phase diagram, between a maximum (minimum) temperature τ_{max} (τ_{min}), there is a criss- crossing through phases of different effective stiffnesses, and different entropies. These should show up in the martensitic fraction n_m, latent heat TS_{entr}, and acoustic emission σ_{AE}.

A sawtooth sweep $T(t)$ has constant sweep-rate throughout each linear segment, but there is a rate-jump at cooling/ heating reversal. A smoother alternative is a cosine or *ac* sweep, $\tau(t) = 0.5(\tau_{max} - \tau_{min}) \cos \nu t + 0.5(\tau_{max} + \tau_{min})$. This has a continuous, albeit time-varying, sweep rate, slowing to zero-rate at the ends of the cycles. We show the tenth cycle for all variables, averaged over 10 runs.

Figure 3.30 (Left) shows hysteretic behaviour in n_m versus τ, with the TTT temperatures τ_2, τ_1 are marked, and snapshots of textures. Note ragged and broadening austenite inclusions on the domain walls of the warming branch, that goes up to transition. This is trimmed inwards, for added extrinsic disorder (not shown).

Figure 3.30 (Right) shows entropy or latent heat hysteresis. The specific heats are the slopes, and clearly show changes most between τ_1 and τ_2,

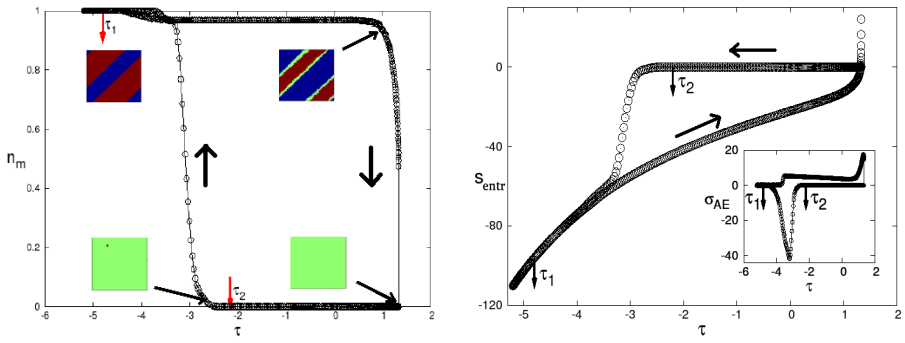

Figure 3.30: *Thermal hysteresis of martensite fraction: Left:* Martensite fraction $n_m(t)$ versus cycled τ, showing textural snapshots. Temperatures τ_1, τ_2 of Figure 3.15 are marked. *Right:* The entropy S_{entr} versus swept τ, with cooling and heating directions indicated. *Inset*: Acoustic emission parameter σ_{AE} versus swept τ, with sign-flipped cooling curves, showing peaks. Temperatures τ_1, τ_2 of Figure 3.15 are marked.

especially on the cooling branch. Extrinsic disorder would modify the curves.

Acoustic bursts in martensite formation have been analysed through binning of hits above an intensity threshold [7], and disorder may play a role. We do not pursue this, but simply take the phonons or displacement fluctuations (such as enter the Debye-Waller factor), as a measure of acoustic emissions: $\sigma^2_{AE} = \sum_{\vec{r}} \vec{u}(\vec{r})^2 = \sum_{\vec{k}} |\vec{u}(\vec{k})|^2$.The strains are related to displacements in Fourier space by $e_{1,2} = i(K_x u_x \pm K_y u_y)/\sqrt{2}$, so u_x, u_y can be written in terms of e_1, e_2. Using (2.48) for e_1, and going over to a pseudospin description $e_2 \to \bar{\varepsilon} S$, the diagnostic $\sigma_{AE}(t)$ is determined from $|S(\vec{k}, t)|^2$.

$$\sigma^2_{AE} = C_{12}|S(\vec{k})|^2[1 - \{\delta_{k_x,k_y} + \delta_{k_x,-k_y}\}|S(\vec{k})|^2]\ \bar{\varepsilon}^2, \tag{3.29}$$

where the coefficients, $C_{12} = \frac{(B_{12}+1)}{2K_x^2} + \frac{(B_{12}-1)}{2K_y^2}$, and B_{12} is defined in (2.48).

We find that after a quench, $\sigma_{AE}(t)$ versus time has bursts up to t_m, settling to a small nonzero background in the liquid phase, that finally drops

to zero at the crystal onset t_C (not shown). This onset of acoustic silence could serve as an experimental probe of twin onsets. The inset of Figure 3.30 (Right) shows σ_{AE} under $\tau(t)$ cycling, For clarity [7], cooling (warming) branches are shown as flipped (unflipped) in sign. Acoustic emissions show peaks between τ_1 and τ_2, with a rise on the warming branch just below τ_4, when trapped twins sublimate to austenite.

3.8 Textures and delays in zero stiffness limit

What happens if we switch off the St.Venant interactions ? The pseudospin Hamiltonian of (3.1) *without* power law anisotropic interactions is like a spin-1 Blume-Capel model [31, 45], with temperature-dependent coefficients. We set $A_1 = 0$ and do simulations in the athermal regime of Figure 3.6, with parameters $T_c/T_0 = 0.9$, $E_0 = 3$, $\xi^2 = 1$.

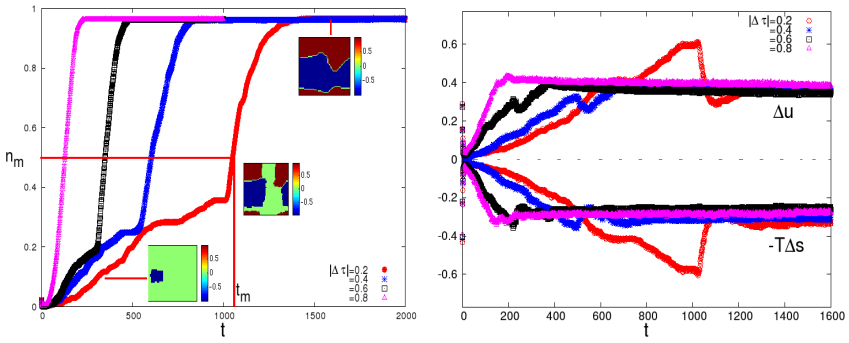

Figure 3.31: *Definition of conversion time t_m : Left*: Martensite fraction n_m versus time t for $A_1 = 0, T_c/T_0 = 0.9, E_0 = 3$ for various $\Delta\tau = \tau - \tau_4$. The definition of t_m is at 50%, as before. Textural snapshots are shown. There are no flat incubation regions such as in Figure 3.1. *Right*: *Textural thermodynamics:* Thermodynamic functions $\Delta U_{ener}(t)$ and $-T\Delta S_{entr}$ vs time t. There is no flat incubation region. Compare Figure 3.23.

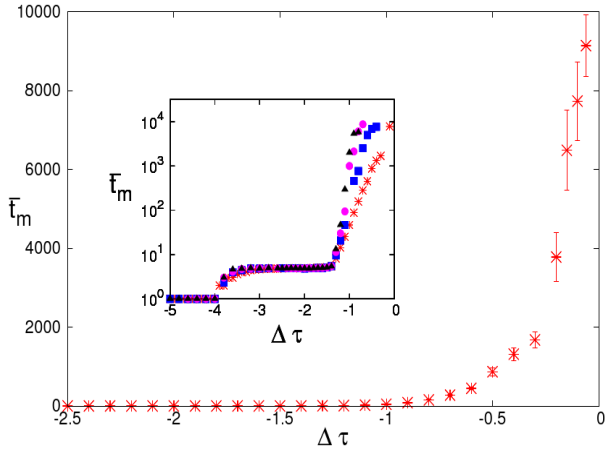

Figure 3.32: *Behaviour of conversion times :* Conversion time $\bar{t}_m$ versus $\Delta\tau$ for $A_1 = 0, T_c/T_0 = 0.9, E_0 = 3$, showing a rising tail. Compare Figure 3.4. *Inset:* Plot of $\log \bar{t}_m$ versus $\Delta\tau$, for $E_0 = 3, 4, 5, 6$, with no apparent divergence, and some contribution from energy barriers. Compare Figure 3.11, that has a Vogel-Fuclher hyperbola.

Figure 3.31 (Left) shows the evolution of $n_m(t)$ has an immediate rise, without the flat incubation as seen in the $A_1 = 4$ case of Figure 3.1. The snapshots show the evolution to final random domain-walls. Note residual austenite on domain walls, as the binding energy argument of Section 3.5.3 carries through.

Figure 3.31 (Right) shows $A_1 = 0$ analogue of Figure 3.23 (Right). The excess internal energy ΔU_{ener} has no initial flat regions, consistent with the lack of incubation in Figure 3.31 (Left). This is like the 'burst' martensite onset seen in some athermal materials [16, 17].

The TTT curve for $A_1 = 0$ shown Figure 3.32 is an analogue of Figure 3.4 for $A_1 \neq 0$. The inset curve of Figure 3.32 is not a Vogel-Fulcher hyperbola as in Figure 3.11, but more like a linear $\log \bar{t}_m \sim \Delta\tau$ and showing E_0 dependence, suggesting entropy barriers are finite up to τ_4 and then divergent, as

channels *close discontinuously*. The absence of Vogel-Fulcher divergence is checked by a plot (not shown) of data in the form of (3.14) showing data do not fall on a line to the origin.

With the (3.19) now given by $R_c(A_1 = 0) = 2\xi^2/|g_L|$, the estimated transition temperatures from the parametrization are $\tau_1 = -4, \tau_2 = -1.4, \tau_4 = -0.14$, close to simulation values of $\tau_1 = -4, \tau_2 = -1.4, \tau_4 = -0.01$.

Thus the $A_1 = 0$ behaviour is quite different from that with nonzero St Venant interactions, that therefore play a central role in incubation processes. Later, in Chapter 7 we will see for $A_1 \neq 0$ golf holes are anisotropic, and incubations arise as the isotropic distribution need to deform to fit in it. Here, for $A_1 \neq 0$, the golf hole is circular, so there is *no* flat incubation.

3.9 Chapter summary

In this Chapter, we presented systematic temperature-quench MC simulations without extrinsic disorder, on the pseudospin Hamiltonian with three pseudospin states, corresponding to the square-rectangle transition, to gain insights into martensitic kinetics. Textural pathways and final states are surprisingly rich. Simulation results include the following.

- After a quench, a domain wall vapour phase converts to a disordered domain wall liquid phase at a conversion time $t = t_m$, that then orients into preferred directions at a later time $t = t_C$, where the anisotropic potential term vanishes.

- We find both isothermal and athermal martensite regimes for different material parameters in the same model, suggesting athermal/ isothermal martensite classification is a matter of material parameters. We obtain athermal/ isothermal/ austenite regime diagram in material paramters.

- The isothermal U-shaped TTT curves for smaller seeds of initial fixed martensite fraction changes to athermal TTT curves (that have delay tails) for larger (hence fewer seeds) seeds. We also find that the isothermal TTT curves transform to athermal TTT curves (that have delay tails) or vice versa on changing material parameters T_c, A_1. Thus, we eventually recover previous experimental literature results on isothermal/ athermal crossover.

- Focusing on the isothermal martensite parameter regime, we find the isothermal TTT conversion rates show dependence on activation variable E_0/T and hence the delays are understood from the dominant energy barriers.

- In the athermal martensite parameter regime, we reconcile recent puzzling experimental results on conversion delays that questioned the traditional classification of martensites. We find fast conversions below an austenite spinodal temperature (here, from the release of bound austenite on domain walls) and delay tails above it, as in experiment. The delays rise to diverge at another temperature, above which there are no conversions even for long holding times, as in experiment.

- These delay divergences have a Vogel-Fulcher form, with Log-normal distributions. The athermal regime is dominated by entropy barriers, with signatures of insensitivity to Hamiltonian energy scale E_0, and temporarily flat energies. The athermal regime conversion fractions are also insensitive to E_0 and for long holding times, again in the signatures of entropy barriers for finding rare energy-lowering pathways that closes off at the divergence.

- Incubation delays are searches for *finite*-scale rare transitional textures during conversion, and orientation. The conversion incubations are

waits for cooperative droplet formation and driven evolution, with entropy barriers diverging at transition. The orientation incubations are waits for local dynamical heterogeneities or austenitic catalysts, to facilitate unlocking of trapped stresses to allow twin formation, with entropy barriers typically finite.

- The Temperature-Time-Transformation phase diagrams of the evolving domain wall phases or inherent structures has characteristic crossover temperatures marking a change in the domain wall dynamics and are understood through the parametrization of complex textures by their effective droplet energies.

- Tweed-like precursors can form above twin regions, as oscillating chessboards, even without extrinsic disorder.

- On temperature cycling, there are hysteresis peaks in the acoustic emission variable and latent heat releases.

- We find that the powerlaw anisotropic potentials induced by no-defect compatibility constraint play an important role in the incubation and orientation dynamics.

Question: Are the results obtained in this Chapter specific to the simplest 3-state scalar-OP pseudospin model for square-rectangle transition ?

4

Other 2D transitions: Conversion-delay tails

In this Chapter, we show that the results obtained in Chapter 3 are not specific to scalar-OP ($N_{OP} = 1$) square-rectangle (SR) transition, but also occur in vector-OP ($N_{OP} = 2$) cases: triangle-centered rectangle (TCR), square-oblique (SO), and triangle-oblique (TO) transitions. We also present microstructural evolutions during conversion-incubation, and final microstructures in all three vector-OP transitions.

4.1 Textural diagnostics

The strain-pseudospin or clock-zero $\mathbb{Z}_{N_V+1}$ Hamiltonians [33] for TCR, SO, TO are given in Chapter 2 and are diagonal in k-space as in the SR transition, but now with three anisotropic kernels from (2.53) between the OP (e_2, e_3) is,

$$\beta H = \frac{1}{2}\sum_{\vec{k}}\sum_{\ell,\ell'=2,3} Q_{0,\ell\ell'}(\vec{k})S_\ell(\vec{k})S_{\ell'}(\vec{k})^*, \tag{4.1}$$

with $\vec{S}(\vec{k})^* = \vec{S}(-\vec{k})$, as $\vec{S}(\vec{r})$ is real, with pseudospins of (2.28), (2.36), (2.40) for TCR, SO, TO transitions respectively. Here

$$Q_{0,\ell\ell'}(\vec{k}) \equiv D_0[\{g_L(\tau) + \xi^2\vec{K}^2\}\delta_{\ell,\ell'} + \frac{A_1}{2}U_{\ell\ell'}(\vec{k})]. \tag{4.2}$$

$D_0(T) \equiv 2\bar{\varepsilon}^2(\tau)E_0/k_BT$; and g_L is in (2.29), (2.37), (2.41) for TCR, SO, TO transitions respectively.

We carry out the Monte Carlo (MC) simulations following the same procedure as in Chapter 3, on three vector-OP pseudospin Hamiltonians under systematic temperature quenches, to study the kinetics of microstructural evolutions on $d = 2, N = L^2$ square lattice [57]. Parameters are typically $T_0 = 1; T_c/T_0 = 0.9 - 0.5, \xi = 1; A_1 = 1, 4, 10; 2A_1/A_3 = 1; L = 64$; $E_0 = 3, 4, 5, 6; t_h \leq 10,000$ and $N_{runs} = 100$.

The textural diagnostics are as before, but now for *vector* pseudospins. The diagnostic for austenite-martensite conversion is the martensite fraction $n_m(t)$ where martensite variants have $\vec{S}^2 = 1$, while austenite is $\vec{S}^2 = 0$ and is defined as,

$$n_m(t) \equiv \frac{1}{N}\sum_{\vec{r}} \vec{S}(\vec{r},t)^2 = \frac{1}{N}\sum_{\vec{k}} |\vec{S}(\vec{k},t)|^2 \leq 1. \tag{4.3}$$

Here $n_m = 0$ in the austenite and $n_m = 1$ in the martensite phase.

A wave-vector diagnostic is k_m that shows the costs of non-uniformity in

the Ginzburg term and is defined as,

$$h_G(t) \equiv {k_m}^2 = \sum_{\vec{k}} K^2 |\vec{S}(\vec{k},t)|^2 / \sum_{\vec{k}} |\vec{S}(\vec{k},t)|^2. \tag{4.4}$$

Here $k_m \neq 0$ in textured states.

After a temperature quench, we define a conversion time t_m, where the martensite conversion fraction $n_m(t) = 1/2$ or 50%, similar to SR transition. As before, we define a mean conversion time [54] as the inverse mean rate $\bar{t}_m \equiv 1/ < r_m >$ where mean conversion rate $< r_m > = < 1/t_m >$, that is arithmetically averaged over $N_{runs} = 100$ different seeds.

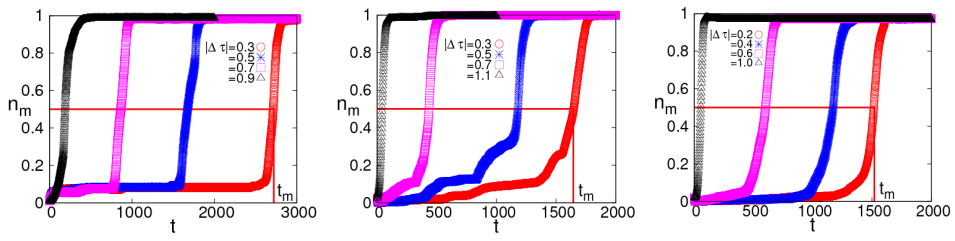

Figure 4.1: *Definition of conversion incubation time (t_m):* Martensite fraction $n_m(t)$ versus time t, for fixed $A_1 = 4, E_0 = 3$ and various $|\Delta\tau| \equiv |\tau - \tau_4|$, showing the 50% conversion definition of t_m. *Left:* TCR transition; *Middle:* SO transition; *Right:* TO transition.

After quenching below a temperature $\tau_4 (<< \tau_0)$ as in the SR case of Figure 3.1, the martensite conversion fraction $n_m(t)$ is flat during incubation, that is followed by step-like jerky behaviour [36] to rise sharply at $t = t_m$ as shown in Figure 4.1 for all three transitions. The incubation delays decrease to become rapid explosive conversions below a temperature $\tau = \tau_1$.

4.2 Athermal and isothermal martensites

In Chapter 3, we presented MC simulations under systematic temperature quenches on a simplest scalar-OP SR transition, and suggested that martensites classification is a matter of parameters; obtained athermal/ isothermal/ austenite regime diagram in material parameters; and crossover of athermal/ isothermal TTT curves on changing material parameters. We need to determine if similar behaviour occurs, in other 2D transitions with vector-OP.

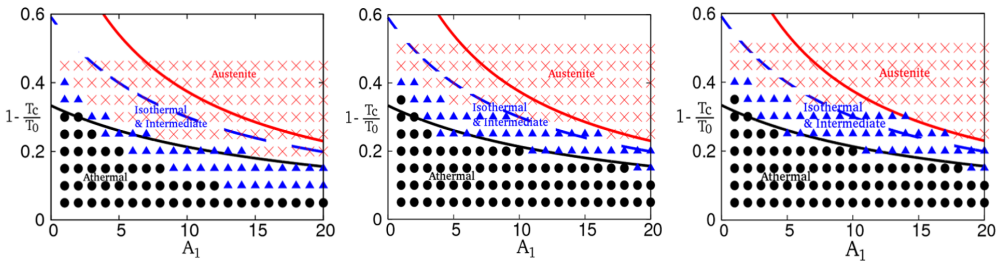

Figure 4.2: *Athermal/isothermal/austenite regime diagram:* Data of athermal (•) intermediate (▲) and austenite (×) behaviour as seen in simulations, in material parameters $(1-\frac{T_c}{T_0})$ versus A_1, with $E_0 = 3$ and $T_c = 0.9$ for *Left:* TCR transition; *Middle:* SO transition; *Right:* TO transition. See text.

Figure 4.2 shows athermal, isothermal (and intermediate), and austenite regimes in a plot of $(1-\frac{T_c}{T_0})$ versus A_1. Both isothermal and athermal regions occur. Compare with Figure 3.6 of SR transition. Solid lines in Figure 4.2 are obtained from the droplet parametrization discussed later in Section 4.3.3. After quenching below a temperature $\tau < \tau_2$, the criterion for 'athermal' is conversion times $\bar{t}_m \lesssim 10$ MCS; 'isothermal' and intermediate for $10 < \bar{t}_m \lesssim 10^3$ MCS; and 'austenite' if there is no conversion even for $t_h = 10^3$ MCS. The data from MC simulations are in good agreement with the rough estimation of boundaries.

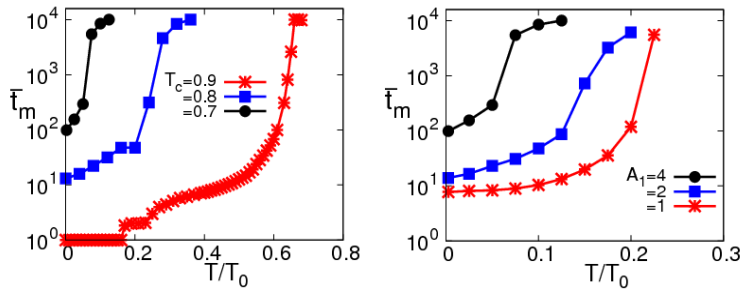

Figure 4.3: *Fast/slow conversions crossover in TCR transition:* Conversion times ($\bar{t}_m$) versus temperature (T/T_0) with $E_0 = 3$, *Left:* for fixed $A_1 = 4$, and different T_c and *Right:* for fixed $T_c = 0.7$ and various A_1.

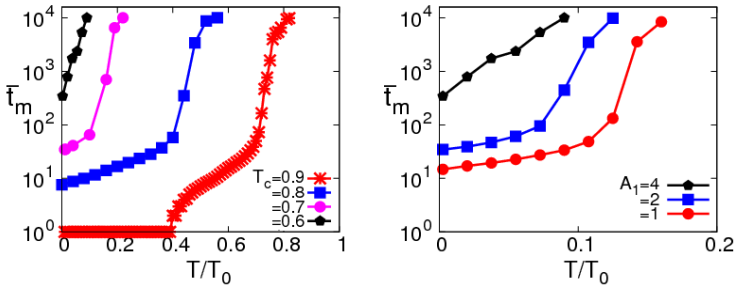

Figure 4.4: *Conversions crossover in SO transition:* Conversions ($\bar{t}_m$) versus temperature (T/T_0) with $E_0 = 3$, *Left:* for fixed $A_1 = 4$, and different T_c and *Right:* for fixed $T_c = 0.7$ and various A_1.

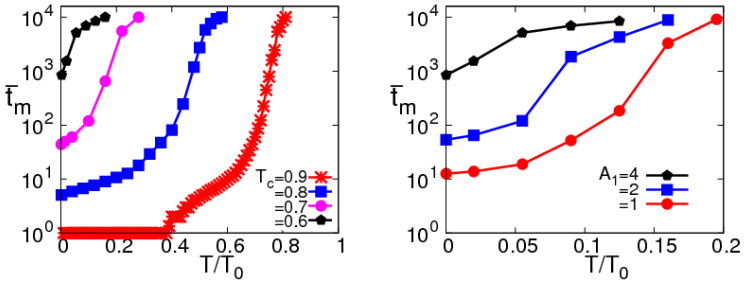

Figure 4.5: *Fast/slow conversions crossover in TO transition:* Conversions with $E_0 = 3$, *Left:* for fixed $A_1 = 4$ and different T_c, and *Right:* for fixed $T_c = 0.6$ and various A_1.

The athermal/isothermal/austenite material parameter phase diagrams in Figure 4.2, suggest that one can change from athermal martensite regime, where there are fast conversions, to an isothermal/intermediate regime that have slow conversions, either by decreasing T_c for a fixed A_1; or by increasing A_1 for a fixed T_c. Here, instead of getting the complete U-shaped TTT curves for the isothermal case, (that one would get by fixing T_c and changing A_1 or vice versa as in Figure 3.5 of SR case.) we focus on the crossover from fast to slow conversions.

Figures 4.3, 4.4, and 4.5 show such crossover from fast conversions followed by incubation-delays to slow conversions, by decreasing T_c from 0.9 to 0.6 (0.9 to 0.7 in TR case), for a fixed $A_1 = 4$ (Left); and also by increasing A_1 from 1 to 4, for a fixed $T_c = 0.6$ (0.7 in TR case) (Right); or viceversa.

Our simulations show that, athermal/isothermal classification is indeed a matter of parameters of the *same* model as suggested in Figure 4.2 in vector-OP TCR, SO, TO transitions.

4.3 Athermal martensite regime

Systematic MC simulations on single-component SR transition, found with a divergent time occuring well below the Landau transition temperature; conversion-incubation delays with Vogel-Fulcher divergences (that are insensitive to Hamiltonian energy scales E_0), and Log-normal distributions; and find conversion probabilities are also insensitive to E_0 or long holding times. We now check in all three vector-OP transitions to find if their results are similar to SR transition.

4.3.1 Conversion incubation times

The temperature dependence of conversion times for various stiffness constants $A_1 = 1, 4, 10$ and fixed $T_c = 0.9, E_0 = 3$ in TCR, SO, TO transitions is shown in Figure 4.6. As before, there are explosive conversions below a temperature $\tau \simeq \tau_1$ (that is different for different transitions); or in scaled variable $\eta(\tau) \simeq -2$ as shown in Figure 4.10. For $\tau \gtrsim \tau_1$ or $\eta(\tau) \gtrsim -2$, there are conversion delays, that rise at $\tau \simeq \tau_2$ or $\eta(\tau) \simeq -1$, to diverge at a temperature $\tau \simeq \tau_4$ or $\eta(\tau) \simeq -0.5$.

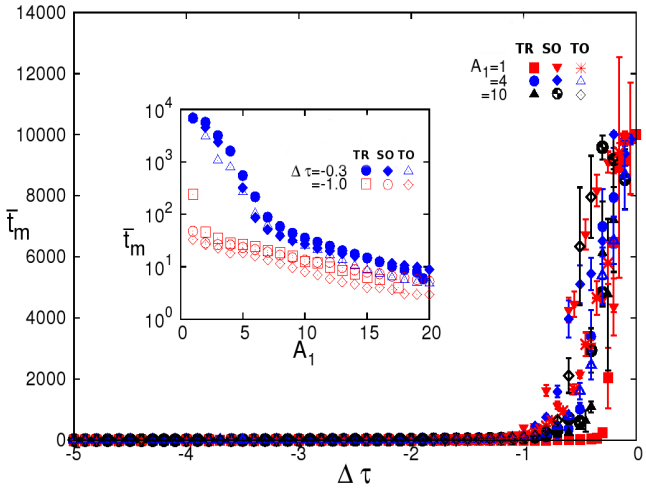

Figure 4.6: *Conversions in TCR, SO,TO transitions:* Plot of conversion times $\bar{t}_m$ versus $\Delta\tau = \tau - \tau_4$, showing fast conversions followed by rising incubation tails for $T_c/T_0 = 0.9, E_0 = 3$, and $A_1 = 1, 4, 10$. *Inset:* Conversion times $\bar{t}_m$ versus A_1 for fixed $\Delta\tau$, showing the delay tail becomes flatter, on increasing A_1. Compare Figure 3.4 of SR case.

As in SR case, the inset of Figure 4.6 shows that, on increasing the stiffness constant A_1, the conversion-delay tails in different transitions decrease to flatten at smaller times $\bar{t}_m < 10$ MCS, that is like the traditional athermal boundary of Figure 1.2.

A. Vogel-Fulcher divergences

Figure 4.7 shows the data of Figure 4.6 for all three transitions, that is for fixed $T_c/T_0 = 0.9$ and various stiffnesses $A_1 = 1, 4, 10$ and $E_0 = 3$; as well as $A_1 = 4$ and $E_0 = 4, 5, 6$ in TCR, SO, TO transitions. Conversion times include both t_h-independent and t_h-dependent data, the latter is extracted through 'finite-time scaling' in $1/t_h \to 0$, as discussed in Chapter 3.

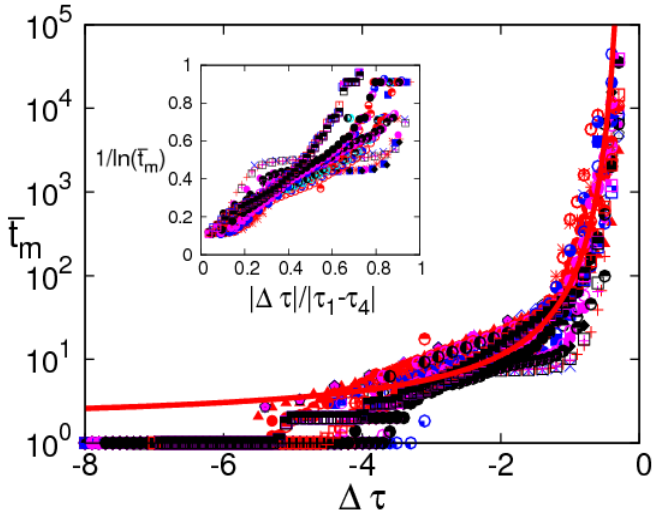

Figure 4.7: *Singular divergence of conversion-incubation times in TCR, SO, TO transitions:* Plot of $\log(\bar{t}_m)$ versus $\Delta\tau \equiv \tau - \tau_4$, with $T_c/T_0 = 0.9$, for $A_1 = 1, 4, 10$ and $E_0 = 3$ as well as $A_1 = 4$ and $E_0 = 4, 5, 6$, showing insensitivity to Hamiltonian energy scales E_0. Solid line is $\log(\bar{t}_m) = \log(t_0) + b_0(\tau_1 - \tau_4)/\Delta\tau$, with $t_0 = 1.6$ and $b_0 = 1.7$. *Inset:* Plot of $1/\ln \bar{t}_m$ versus $|\Delta\tau|/|\tau_1 - \tau_4|$ showing Vogel-Fulcher divergence. Compare Fig 3.11.

Conversion times data in TCR, SO, TO transitions for different A_1 and E_0 fall on a single hyperbola $\ln \bar{t}_m \sim 1/|\Delta\tau|$, suggesting Vogel-Fulcher divergence, that is familiar in glasses [18]. Specifically, $\bar{t}_m = t_0 e^{[b_0|\tau_1 - \tau_4|/|\tau - \tau_4|]}$, with $t_0 = 1.6, b_0 = 1.7$, for these data. These constants are different from

SR case of Figure 3.11. The inset of Figure 4.7 is the same data plotted in another way showing the divergence as a linearity as $|\Delta\tau|$ goes to zero in $1/\ln \bar{t}_m$ versus $|\Delta\tau|/|\tau_1 - \tau_4|$ from (3.14).

In particular, the insensitivity of conversion times to Hamiltonian energy scales E_0 again implies that the Vogel-Fulcher singularity at $\tau \simeq \tau_4$ comes from divergence of entropy (rather than energy) barriers, $\bar{t}_m \sim e^{|\Delta S_{entr}|}$ as in the SR transition, discussed in Chapter 3.

B. Log-normal distributions

Similar to the SR transition, we have considered in TCR, SO, TO transitions the arithmetic mean rate $< r_m > \equiv < 1/t_m >$ that determines $\bar{t}_m = 1/ < r_m >$, with $1/t_h < r_m < 1$. The variance in the rates is ${\sigma_r}^2 = < (r_m - < r_m >)^2 >$. The *distributions* or probability densities $P(r_m)$ versus r_m are shown in the Figure 4.8, as histograms for different temperatures. For each histogram of N_{hist} data points, the Scott optimized bin size [49] is used, of $dr_m = 3.5\sigma_r/[N_{hist}]^{1/3}$. The histograms again narrow sharply, below τ_2, as in the delta-function-like peak on the right. As mentioned in Chapter 3, the Log-normal distribution is a signature of rare events [38]. The successful

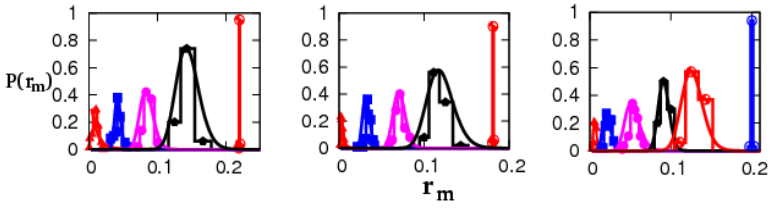

Figure 4.8: *Log-normal distributions of conversion-rates in TCR, SO, TO transitions:* Plot of $P(r_m)$ versus r_m for $\tau_1 > \tau > \tau_4$. Data are from Figure 4.7, with $T_c/T_0 = 0.9, A_1 = 4, E_0 = 3$. Solid lines are the theoretical log-normal distributions with $< r_m >$ and σ_{r_m} from data. *Left:* TCR; *Middle:* SO; *Right:* TO transitions. Compare Fig 3.13. See text.

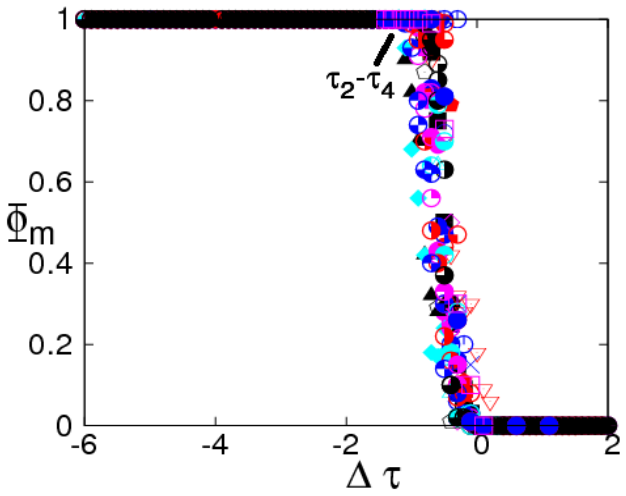

Figure 4.9: *Rare conversion channels in TCR, SO, TO transitions:* Plot of successful conversion fraction Φ_m versus $\Delta\tau$ with $A_1 = 1, 4, 10$ and $E_0 = 3$; and $A_1 = 4$, and $E_0 = 4, 5, 6$ and $t_h = 10^4$ MCS.

conversion fraction Φ_m of 100 runs versus $\Delta\tau$ for different material parametrers A_1, and E_0 is plotted in Figure 4.9. Clearly, the fraction decreases for $\tau < \tau_2$, and becomes zero at τ_4. Compare Figure 3.12 of SR case. The insensitivity to different energy scales E_0 is again a signature of entropy barriers [23].

4.3.2 Temperature-Time-Transformation phase diagram

Figure 4.10 shows TTT phase diagram in conversion times $\bar{t}_m$ versus scaled variable $\eta(\tau) = -1/R_c(\tau)$ for fixed $A_1 = 4, E_0 = 3$ for TCR, SO, TO transitions. As in Figure 3.22 of the SR case there is data clustering, now for all three transitions. The derivation of $\eta(\tau)$ is given in Section 4.3.3.

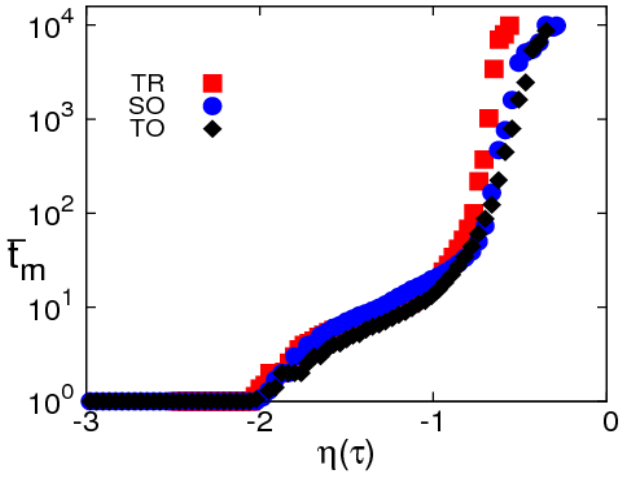

Figure 4.10: *Dynamical phase diagram in TCR, SO, TO transitions:* TTT plot of delay times $\bar{t}_m$ versus scaled variable $\eta(\tau)$, with $A_1 = 4, E_0 = 3, T_c/T_0 = 0.9, L = 64$. Here, the crossover temperatures are at $\eta(\tau) = -2, -1, -0.5$. See Figure 3.22 of SR case.

A. Final textures and crossover temperatures

In Figure 4.10, the characteristic temperatures $\tau_{1,2,4}$ are defined in terms of scaled variable as $\tau = \tau_1$ or $\eta(\tau) = -2$ where $\bar{t}_m \simeq 1$ MCS; $\tau = \tau_2$ or $\eta(\tau) = -1$ where $\bar{t}_m \simeq 10$ MCS; and $\tau = \tau_4$ or $\eta(\tau) \simeq -0.5$ where conversion times diverges.

Figure 4.11 shows final microstructures for all cases. The colorbar for OP strain (e_2, e_3) in the first row represent the variant label V in terms of ϕ. For TCR case in Figures 3.17, 3.22, $V = 0$ for austenite; and $V = 1, 2, 3$ for $\phi = 0, \frac{2\pi}{3}, \frac{4\pi}{3}$ for $N_V = 3$ martensite variants. Similarly, in the SO case in Figures 4.19,4.23 and TO case in 4.21,4.24, the colorbar in the first row represent the austenite with $V = 0$ austenite and non-zero values $V = 1, 2, 3, 4$ from corresponding values $\phi = \frac{\pi}{4}, \frac{3\pi}{4}, \frac{5\pi}{4}, \frac{7\pi}{4}$ and $V = 1, 2, ..6$ for $\phi = 0, \frac{\pi}{3}, \frac{2\pi}{3}, \pi, \frac{4\pi}{3}, \frac{5\pi}{3}$ respectively.

At low temperatures for $\tau << \tau_1$ or $\eta(\tau) << -2$, the domain wall crystal or oriented twins can have vortex-like (or topological defects or charges) behaviour at multi-variant junctions in SO, TO cases, and partially oriented star-like states in TCR case, can compete with a frozen domain wall liquid or 'glass'. For $\tau_1 \lesssim \tau < \tau_2$ or $-2 \lesssim \eta(\tau) < -1$, austenite droplets can appear as

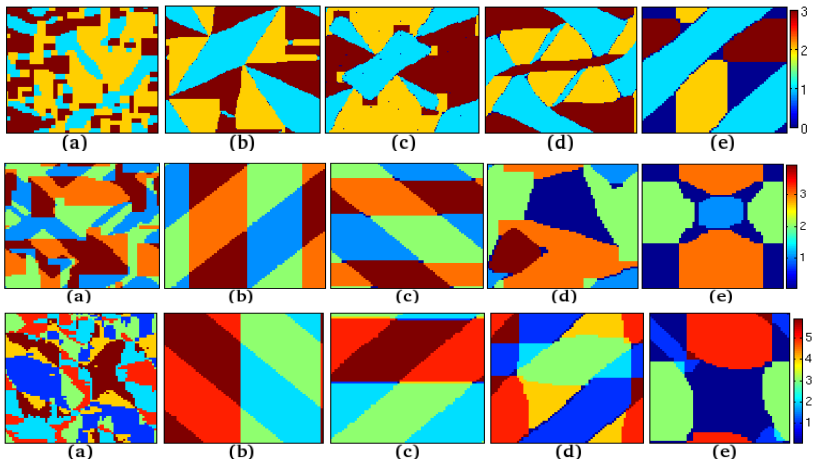

Figure 4.11: *Final 'equilibrium' microstructures in TCR, SO, TO transitions:* Domain wall phases: (a) glass for $\tau << \tau_1$; (b) star-like or martensite twins (no bound austenite) for $\tau_1 \gtrsim \tau \gtrsim \tau_2$; (c) and (d) fan-like and swastika or twins (austenite appears as point or line densities) for $\tau_2 \gtrsim \tau \gtrsim \tau_4$; (e) precursor vibrating phase (bulk-austenite) for $\tau \simeq \tau_4$ for TCR case (first row), SO case (second row), and TO case (third row). The austenite is represented as zero in the colorbar and the number of variants N_V in each transition. Parameters are typically $A_1 = 4, T_c = 0.9, \xi^2 = 1$ and $E_0 = 3, L = 64$. See text.

points at corners, in domain wall crystal or oriented martensite twins (that have topological charges) in SO, TO cases; and also fan-like oriented states in TCR case. For $\tau_2 \lesssim \tau \lesssim \tau_4$ or $-1 \lesssim \eta \lesssim -0.2$, there are again austenite droplets but now appear as lines, in domain wall crystal in SO, TO cases,

and swastika-like states in TCR case. For $\tau > \tau_4$, there is pure austenite. With random initial seeds, there is a vibrating martensite phase, that has bulk austenite in TCR, SO, TO transitions, that could be equivalent of the chequerboard SR case tweed pattern (and becomes less probable closer to $\tau \simeq \tau_4$.) of Figure 3.28.

The microstructure (b) as shown in Figure 4.11 (first row) for TCR transition is not fully relaxed even after $t_h = 10^6$ MCS and could possibly take longer and longer times, to orient fully to a nested star as seen in continuous variable simulations and experiments [4, 28, 29].

The crossover temperatures in TTT phase diagram are again understood through the parametrization of the textures in terms of effective droplet energies in the next Section.

4.3.3 Parametrization of textures by droplet energies

The evolutions of complex microstructures in the simplest 3-state SR transition is parametrized through the effective droplet energies as in classical droplet theory, where a single-variant droplet in the vapour phase has a competition between bulk $\sim -R^2$ and surface $\sim +R$ terms, where R is a geometic droplet scale. There is a critical radius $R_c(T)$ that diverges as $1/|T - T_0|$ at the Landau temperature $T = T_0$, where the bulk condensation energy vanishes. The energy barrier profile is an inverted parabola $H(R) \sim R_c[1 - (1 - R/R_c)^2]$, peaked at R_c. See Chapter 3 and Section 3.5.3. We similarly parametrize the complex textures in these transitions by effective droplet energies as in SR transition.

Here, we have three vector-OP ($N_{OP} = 2, OP = e_2, e_3$) TCR, SO, TO transitions that have $N_V+1 = 4, 5, 7$ number of pseudospins respectively. The complex textural droplets of N_V variants are not independent, but interacting through a powerlaw anisotropic potential of (2.51) that is the same for all

$N_{OP} = 2$ transitions in 2D. At $t = 0$, we consider 2% of seeds of N_V variants, that are randomly sprinkled throughout the lattice. We find again that, the interaction tend to cancel leaving only self-interaction part $A_1[U[/2$ at each seed. So we have the same form as (3.18), with scalar S replaced by a vector $\vec{S}$ that yields,

$$\beta H[\vec{S}(0)] \simeq \frac{D_0}{2} \sum_{\vec{r}} [g_L \vec{S}(\vec{r},0)^2 + \xi^2 \{\vec{\Delta}\vec{S}(\vec{r},0)\}^2 + \frac{A_1[U]}{2} \vec{S}(\vec{r},0)^2]. \quad (4.5)$$

Here, $[U] \simeq 0.5$, is the Brillouin-zone average of $U_{\ell\ell'}(\vec{k})$ of (2.52) in TCR, SO, TO transitions. For an initial martensite fraction $n_m(0) = 0.02$, we have N_V variants square seeds of sides $R(0)$. Once again, the initial pseudospin seed energy is parametrized as $\beta H(\vec{S}(0)) = C_0[\alpha_L g_L R(0)^2 + \alpha_G \xi^2 4R(0) + \alpha_C (A_1[U]/2)R(0)^2]$ with $C_0 \equiv (n_m(0)ND_0/2)$. For different sides $R(0) = 1, 2, 3$, we fit the coefficients $\alpha_{L,G,C}$ term-by-term, finding again $\alpha_L = \alpha_G = \alpha_C = 1$, independent of seed size as shown in Figure 4.12. Then the initial energy has a droplet-like form $\beta H(R(0)) = C_0 2\xi^2 R_c[1 - (1 - R(0)/R_c)^2]$. Here we define a length $R_c(\tau)$ that is positive below a divergence temperature $\tau = \tau_L(A_1)$,

$$R_c(\tau) \equiv \frac{-2\xi^2}{g_L(\tau) + A_1[U]/2}. \quad (4.6)$$

As in the SR case, we define a scaled temperature variable $\eta(\tau)$ from the parametrization

$$\eta(\tau) = -1/R_c(\tau) = \frac{g_L(\tau) + A_1[U]/2}{2\xi^2}, \quad (4.7)$$

and it has universal crossover values of $\eta(\tau_4) = -0.5, \eta(\tau_1) = -1, \eta(\tau_2) = -2$ that mark the change in microstructural dynamics for TCR, SO, TO transitions as shown in the Figure 4.10.

At $t = 0$, the initial seeds have a geometic meaning, and hence the pseudospin Hamiltonian $H(\vec{S}(0))$ and matches the droplet Hamiltonian $H(R(0))$,

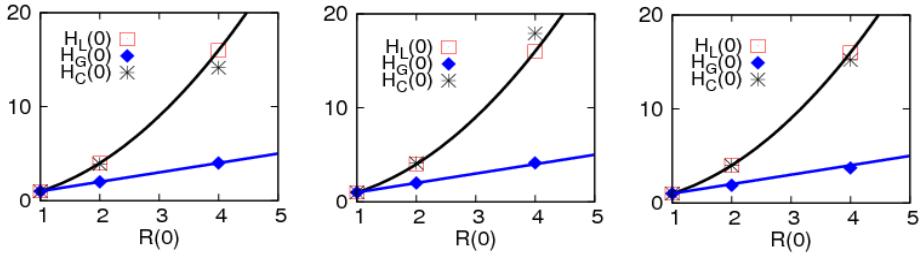

Figure 4.12: *Parametrization in TCR, SO, TO transitions:* Behaviour of Landau H_L, Ginzburg H_G and Compatibility H_C terms for different initial seed sizes $R(0)$. Solid lines represents parabolas and a straight line that are fits to data. See Figure 3.17.

but for general t, these two terms no longer match term-by term. However, as before we define $R(t)$ through $H[\vec{S}(t)]/H[\vec{S}(0)] = H[R(t)]/H[R(0)]$. The energy (ratio) for interacting *vector* pseudospins is parametrized, by the energy (ratio) of a surrogate system of independent droplets. The initially geometric $R(0)$ evolves to an interacting-texture energetic parameter $R(t)$, that can even go negative as the pseudospin energy goes negative. Thus

$$\rho(t) \equiv \beta H(\vec{S}(t))/\beta H(\vec{S}(0)) = [1 - (\frac{R(t)}{R_c} - 1)^2]/[1 - (\frac{R(0)}{R_c} - 1)^2]. \quad (4.8)$$

The $R(t)$ evolution is then once again

$$R(t)/R_c = 1 + \alpha\sqrt{1 - \rho(t)/\rho_c}, \quad (4.9)$$

where $\rho_c \equiv [1 - (\{R(0)/R_c\} - 1)^2]^{-1}$, and we take $\alpha = sign(\{R(0)/R_c\} - 1)$.

Figure 4.13 shows the evolutions of parametrized droplet energy in a plot of $R(t)/R_c(\tau)$ versus time. There are both rapid rises to final positive values and flat-incubations as already seen in the martensite conversion fraction n_m, that goes negative at later times. The flat-incubations are due to the inefficient searches for the rare channels to lower energies. The initial $R(0)/R_c$ values determine the $R(t)$ flows.

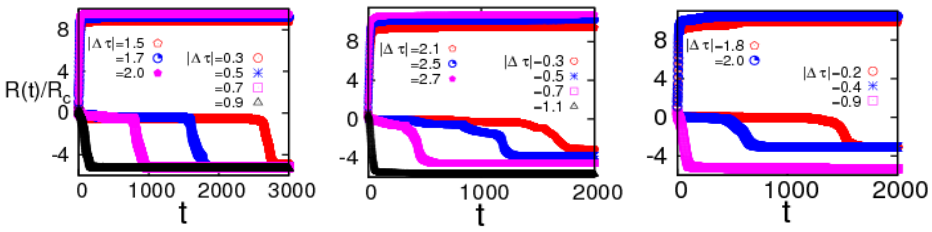

Figure 4.13: *Trajectories in TCR, SO, TO transitions:* Energy parameter $R(t)/R_c$ versus time t, showing flows are determined by initial $R(0)/R_c(\tau)$ values for different $|\Delta\tau|$. Note flat incubations of lower curves, of initial $1 > R(0)/R_c(\tau) > 0.5$, that correspond to $\tau_2 < \tau < \tau_4$. *Left:* TCR; *Middle:* SO; *Right:* TO transitions. See Figure 3.18.

As a consistency test of parametrization, Figure 4.14 shows $\rho(t)/\rho_c$ versus $R(t)/R_c$ indeed matches a parabola, for all t, and all A_1, and many starting values $R(0)/R_c(\tau)$ in TCR, SO, TO transitions. Flow directions of $R(t)$ are indicated by arrows starting at $R(0)/R_c$ for Regions ①,②,③,④, with asymptotic $R(t)$ giving negative final martensitic energies, or zero (going to austenite).

The crossover temperatures $\tau_{1,2,4}$ or $\eta(\tau) = -2, -1, -0.5$ in Figure 4.10 are understood as the change in behaviour of the textural evolutions, through the effective droplet parametrization. Remarkably, the parametrization of textures by their effective droplet energies works well for all three vector-OP transitions as in the scalar-OP transition, of Chapter 3. The flow regions determined by $R(0)/R_c(\tau)$ are as below:

i) *Region ①:* For initial $R(0)/R_c(\tau) > 2$, there are explosive conversions to martensite, this determines a temperature $\tau = \tau_1$ or $1/R_c(\tau_1) = 2$ or in scaled varibale $\eta(\tau) = -2$ with initial unit seeds $R(0) = 1$.

ii) *Region ②:* For initial droplets $2 > R(0)/R_c(\tau) > 1$, the flows are again fast, this determines a temperature $\tau = \tau_2$ where $1/R_c(\tau_2) = 1$ or in scaled variable $\eta(\tau) = -1$.

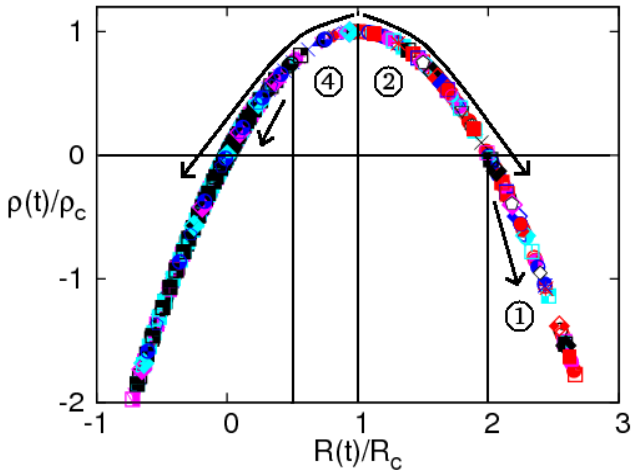

Figure 4.14: *Parametrization and crossover temperatures in TCR, SO, TO transitions:* Scaled pseudospin energy $\rho(t)/\rho_c$ versus $R(t)/R_c(\tau)$, showing flows fall on a parabola as a test of parametrization. For $R(0) = 1$ seeds, characteristic initial values $R(0)/R_c(\tau)$ are ${R_{c1}}^{-1} = 2, {R_{c2}}^{-1} = 1, {R_{c4}}^{-1} \simeq 0.5$ as marked. These correspond to temperatures τ_1, τ_2, τ_4. For initial $R(0)/R_c \lesssim 0.5$, flows are to $R = 0$ austenite. See Figure 3.19. See text.

iii) *Region ③:* For $0.5 \gtrsim R(0)/R_c(\tau)$ or $\eta(\tau) \lesssim -0.5$, the initial droplets are flowing only to $R = 0$ austenite. But, for larger A_1, the droplets can still grow through searches up to $R(0)/R_c(\tau) \simeq 0$ or $\eta(\tau) \simeq 0$, that is well below the Landau transition temperature T_0.

iv) *Region ④:* For $0.5 \lesssim R(0)/R_c(\tau) \lesssim 1$, the initial droplets immediately convert to a single variant droplet, that incubates for long times around $R(t) \simeq 0$ with zero energy $H = 0$ (degenerate with austenite). This entropically critical droplet searches for conversion pathways, and grows through jerky steps and cooperative nucleation. The incubations occur for unit seeds up to a temperature $\tau = \tau_4$ or $1/R_c(\tau_4) \simeq 0.5$ or in scaled variable $\eta(\tau) = -0.5$.

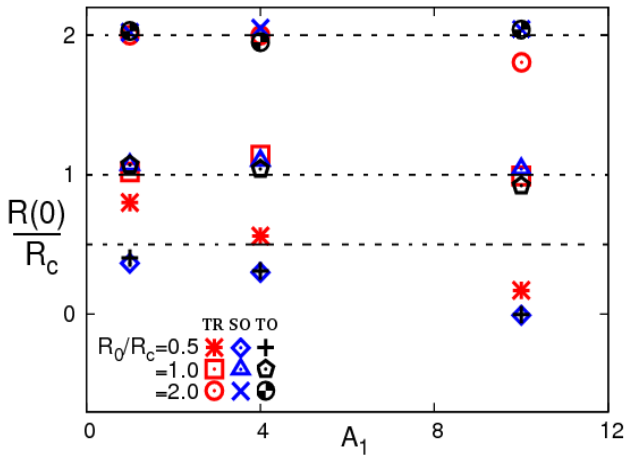

Figure 4.15: *Textural crossover temperatures in TCR, SO, TO transitions:* Plot of R_0/R_c versus A_1 for $1 > \tau > \tau_0(= -9.0)$. Dashed lines are $R_0/R_c(\tau) = 2, 1, 0.5$, are the boundaries that mark the change in textural evolutions of Figures 4.10, 4.14. Compare the SR case of Figure 3.21 (Left).

The boundaries of the athermal, isothermal, and austenite regimes in the phase diagram of Figure 4.2 uses these results of Figures 4.10, 4.14. The estimation of the boundaries in TCR, SO, TO transitions in Figure 4.2, is similar to the procedure used to obtain the boundaries in SR transition, that is discussed in Chapter 3, Section 3.5.3, but here with $[U] \simeq 0.5$.

4.3.4 Development of microstructures during incubation

After a quench into $\tau_4 > \tau > \tau_2$ and holding, we monitor the evolution of OP (e_2, e_3) non-OP (e_1) textures and local internal stresses and their distributions, to understand what happens at the microstructural level, during t_m and n_m incubations at macro level.

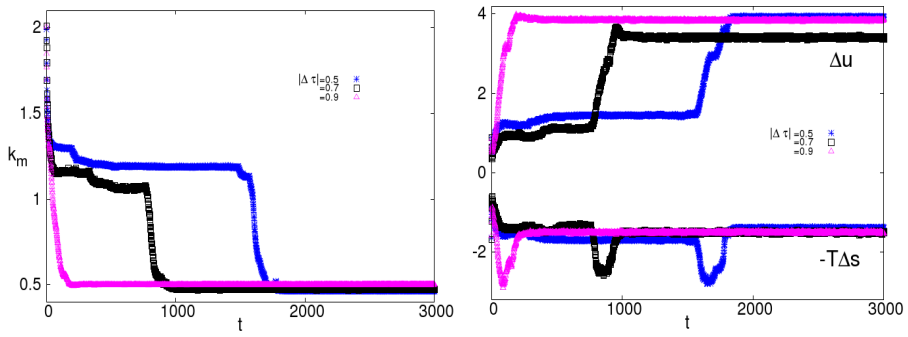

Figure 4.16: *Wavenumbers and textural thermodynamics in TCR transition: Left:* Wavenumbers k_m versus time t during t_m incubation for $\tau_2 < \tau < \tau_4$. *Right:* Excess internal energy $\Delta U(t)$, and negative entropy $-T\Delta S(t)$ versus t, for $|\Delta\tau| = 0.5, 0.7, 0.9$. See text.

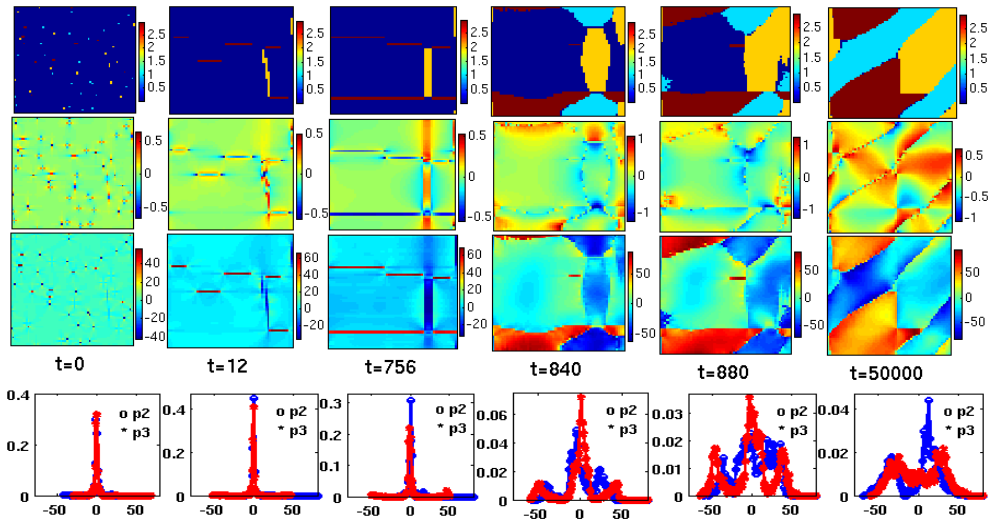

Figure 4.17: *Textural evolution in TCR transition:* First row: Evolution of OP strain (e_2, e_3) in terms of $N_V = 3$ colors indexed by variant label $V = 1, 2, 3$ for $|\Delta\tau| = 0.7$. Second row: non-OP strain e_1. Third row: Local internal stress $p_2(r) + p_3(r)$. Fourth row: Evolution of stress distribution $p_2(r), p_3(r)$ with symbols open circle and star respectively. See text.

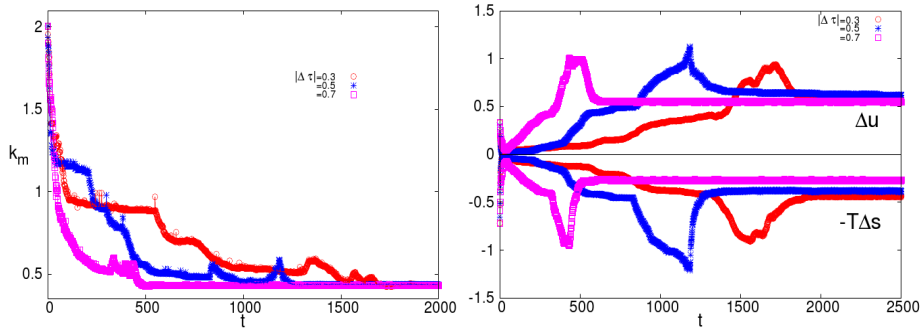

Figure 4.18: *Wavenumbers and textural thermodynamics in SO transition: Left:* Wavenumbers k_m versus t during t_m incubation for $\tau_2 < \tau < \tau_4$. *Right:* Excess internal energy $\Delta U_{ener}(t)$, and negative entropy $-T\Delta S_{entr}(t)$ versus t, for $|\Delta\tau| = 0.3, 0.5, 0.7$.

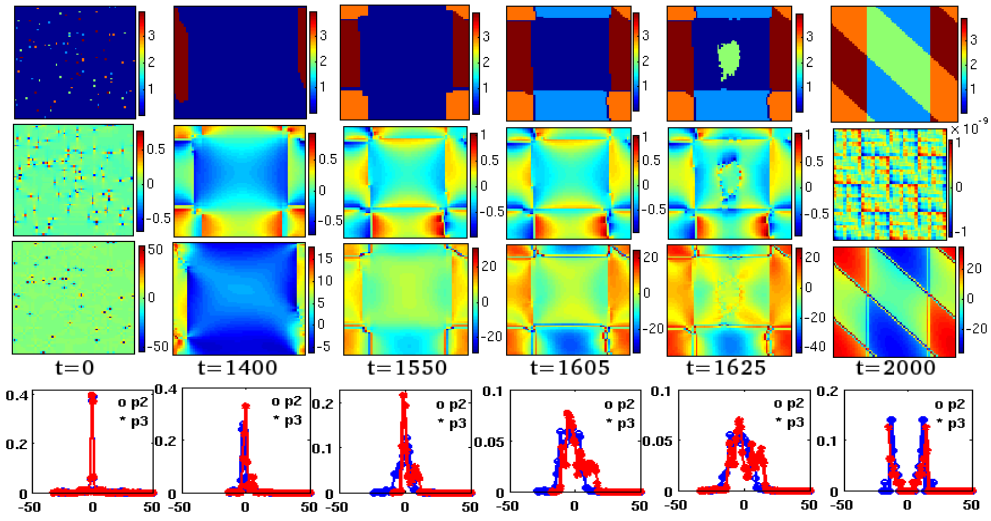

Figure 4.19: *Textural evolution in SO transition:* First row: Evolution of OP strain (e_2, e_3) textures in terms of $N_V = 4$ colors indexed by variant label $V = 1, 2, 3, 4$ for $|\Delta\tau| = 0.5$. Second row: non-OP strain e_1. Third row: Local internal stress $p_2(r)+p_3(r)$. Fourth row: Stress distribution $p_2(r), p_3(r)$ with symbols open circle and star respectively. See text.

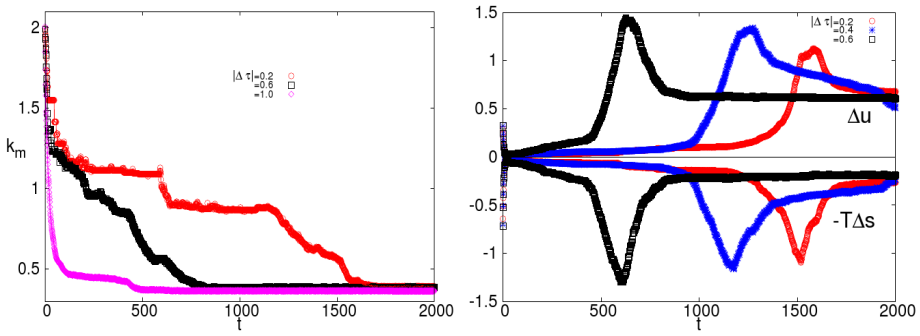

Figure 4.20: *Wavenumbers and textural thermodynamics in TO transition: Left:* Wavenumbers k_m versus t during t_m incubation for $\tau_2 < \tau < \tau_4$. *Right:* Excess internal energy $\Delta U_{ener}(t)$, and negative entropy $-T\Delta S_{entr}(t)$ versus t, for $|\Delta\tau| = 0.2, 0.4, 0.6$.

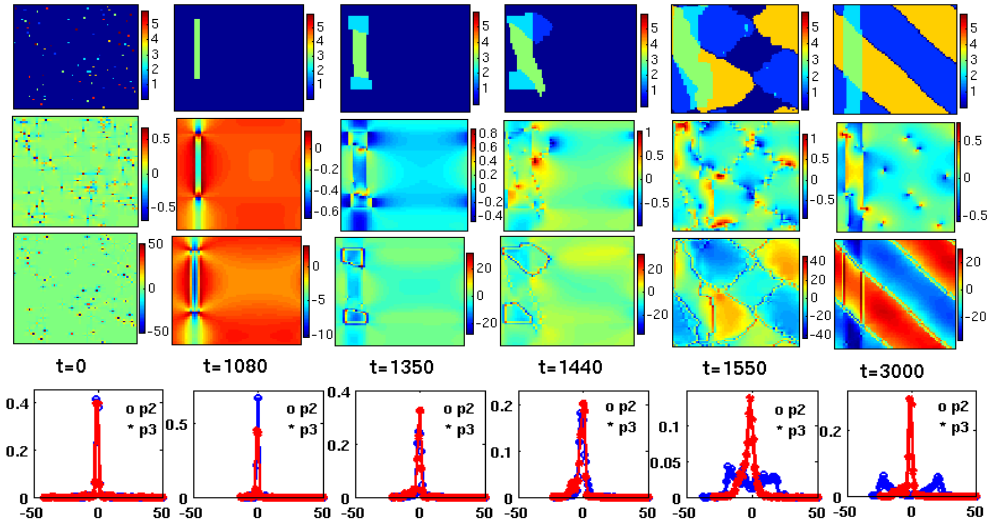

Figure 4.21: *Textural evolution in TO transition:* First row: Evolution of OP strain (e_2, e_3) in terms of $N_V = 6$ colors indexed by variant label $V = 1, 2, ..6$ for $|\Delta\tau| = 0.2$. Second row: non-OP strain e_1. Third row: Local internal stress $p_2(r) + p_3(r)$. Fourth row: Stress distribution $p_2(r), p_3(r)$ with symbols open circle and star respectively. See text.

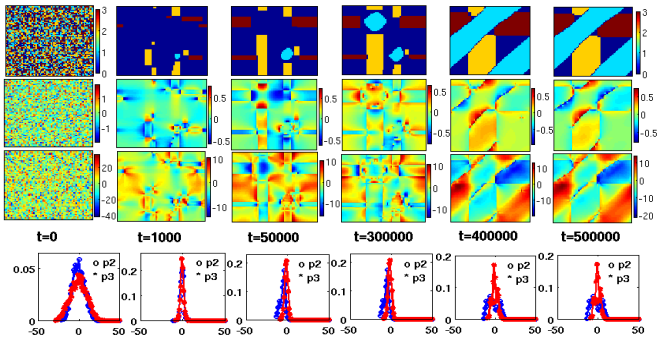

Figure 4.22: *'Precursor' in TCR:* Evolution of OP, non-OP, $p_2(r) + p_3(r)$, distributions of $p_2(r), p_3(r)$ in $1^{st}, 2^{nd}, 3^{rd}$, and 4^{th} rows respectively. See text.

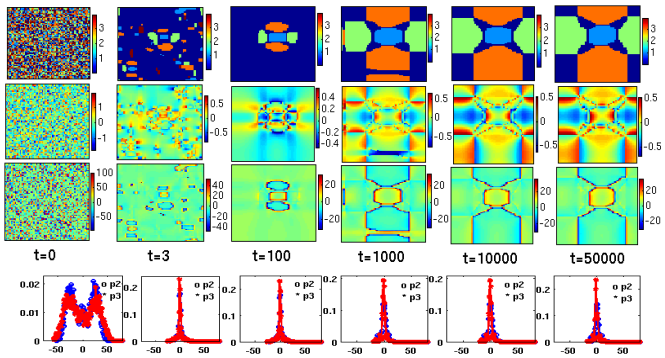

Figure 4.23: *Precursor in SO:* Evolution of OP, non-OP, $p_2(r) + p_3(r)$, distributions of$p_2(r), p_3(r)$ in $1^{st}, 2^{nd}, 3^{rd}$, and 4^{th} rows respectively. See text.

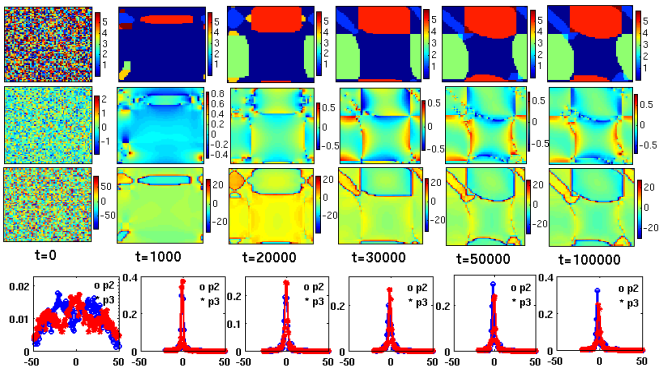

Figure 4.24: *Precursor in TO:* Evolution of OP, non-OP, $p_2(r) + p_3(r)$, distributions of $p_2(r), p_3(r)$ in $1^{st}, 2^{nd}, 3^{rd}$, and 4^{th} rows respectively. See text.

The TCR, SO, and TO cases are in Figures 4.16,4.17,4.22, Figures 4.18,4.19,4.23 and 4.20,4.21 and 4.24 respectively. The V colour representation is as in Figure 4.11. The microstructural evolutions in time are monitored in terms of single 'variant label' V rather than the vector-OP $(e_2, e_3) = (\cos\phi, \sin\phi)$.

The derivations of thermodynamic functions U_{ener}, F, S_{entr} is given in the thesis Appendix A. Thermodynamic functions U_{ener}, F, S_{entr} are calculated by replacing the meanfield local averages at a site $\vec{r}$, by the MC values, $< \vec{S}(\vec{k}) > \rightarrow \vec{S}(\vec{k}, t)$. The excess functions $\Delta U_{ener}, \Delta F, \Delta S_{entr}$ are defined to describe domain wall dynamics during the conversion incubation.

$$\Delta U_{ener} \equiv (U_{ener} - U^{(0)}{}_{ener})/E_0, \tag{4.10a}$$

$$\Delta F \equiv (F - F^{(0)})/E_0, \tag{4.10b}$$

$$\Delta S_{ener} \equiv (S_{entr} - S^{(0)}{}_{entr})/E_0. \tag{4.10c}$$

Here, $U^{(0)}, F^{(0)}, S^{(0)}$ depends only bulk Landau contributions g_L are with $A_1 = \xi^2 = 0$.

In Figures 4.16 (TCR), 4.18 (SO), 4.20 (TO), the wavenumber k_m shows a quick fall that correspond to the formation of single-variant droplet. Note flat regions and step-like jerkiness [36] during t_m, n_m incubation, and asymptotic nonzero values The excess thermodynamic functions, internal energy ΔU and entropy $-T\Delta S$ also show the similar behaviour as in k_m. There are huge dumps in entropy as well as energy dumps close to $t = t_m$. Compare the SR case of Figure 3.23.

After a quench and hold into $\tau_4 > \tau > \tau_2$, the random initial 2% martensite variants at $t = 0$ quickly form a single-variant droplet as shown in Figures 4.17 (TCR), 4.19 (SO), 4.21 (TO). The single-variant droplet expands through searches in finding rare energy-lowering conversion-pathways. The expanded droplet then generate the other variant by autocatalytic twinning of Bales and Gooding [29]. See movies in the attached CD [57].

In the second row of Figures 4.17 (TCR), 4.19 (SO), 4.21 (TO), the

non-OP strain $e_1(\vec{r})$ is generated during the formation and expansion of the droplet, that is then slowly reduced to zero as domain walls orient in preferred directions. The third row shows the large values of local internal stresses represented as $p_2(\vec{r}) + p_3(\vec{r})$ that decrease to zero in the bulk, but have $(\pm)$ finite values at the trapped domain walls in the final oriented state as in the SR case of Figure 3.25.

The precursor from random pseudospin values of $1/(N_V + 1)$ probabilities (including austenite) are shown in Figures 4.22 (TCR), 4.23 (SO), 4.24 (TO) respectively. The oscillations are particularly interesting as they occur only at martensite/austenite interfaces and not at martensite/martensite interfaces. (Compare SR case of Figure 3.28 where the interfaces are also austenite/martensite only.) See all movies in the attached CD of the thesis. The second and third rows are self-explanatory. In the fourth row of Figures 4.22, 4.23, and 4.24, the stress distributions $p_2(\vec{r}), p_3(\vec{r})$ at $t = 0$ are broad with small values, peaking around zero in the TCR case, bi-modal in SO case and tri-modal in TO case. At later times, the distributions becomes sharply peaked around zero with large values in the final oscillating phase. In the fourth row, the local stress distributions $p_2(\vec{r}), p_3(\vec{r})$ are shown. At $t = 0$, the stress distributions are sharply peaked around zero with large values, that generate wings on both sides of the peak during autocatalytic twinning. In the final oriented state, only the wings remain, that correspond to the trapped stress values along the domain-walls (except in TO case, where $p_3(\vec{r})$ is sharply peaked around zero).

4.4 Textures and delays in zero stiffness limit

MC simulations are carried out on the vector-OP pseudospin clock-zero models for TCR, SO, TO transitions without the compatibilty term i.e. setting $A_1 = 0$ to understand the role of power-law anisotropic potential in the

incubation kinetics, as for the SR case of Section 3.8.

Figure 4.25 shows the evolution of $n_m(t)$ has an immediate rise, without the flat incubation as seen in the $A_1 = 4$ case of Figure 4.1. The snapshots show the evolution to final random domain-walls. Note residual austenite on domain walls. Here also in all three vector-OP cases, there are delays, but *no incubations* as in $A_1 \neq 0$ case.

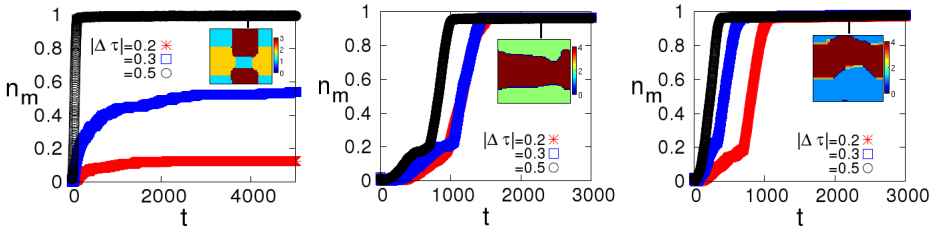

Figure 4.25: *Conversions with $A_1 = 0$ in TCR, SO, TO transitions:* Martensite conversion fraction $n_m(t)$ versus time t for different $|\Delta\tau|$, showing *no* flat-incubations. *Left:* TCR case , *Middle:* SO case, *Right:* TO case. Final microstructures are also shown.

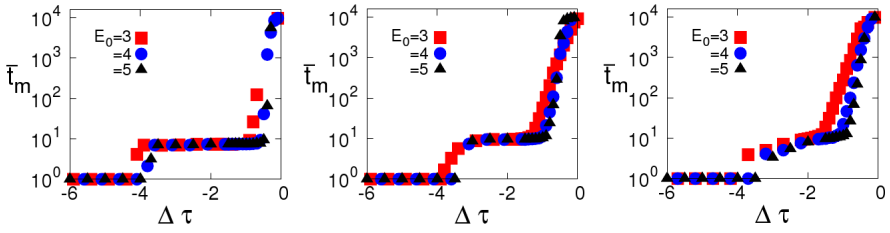

Figure 4.26: *Conversion times with $A_1 = 0$ in TCR, SO, TO transitions:* Conversion times $\bar{t}_m$ versus $\Delta\tau$. Note linear rises instead of a Vogel-Fulcher hyperbola. *Left:* TCR case, *Middle:* SO case, *Right:* TO case.

Figure 4.26 shows the $A_1 = 0$ analogue of Figure 4.7, with $E_0 = 3$. The plot of $\ln \bar{t}_m$ versus $\Delta\tau$ includes data for $E_0 = 3, 4, 5, 6$. There is some E_0

dependence of the slope, so now there could be some role of energy barriers. The curve is not a Vogel-Fulcher hyperbola as in Figure 4.7, but more like a linear $\ln \bar{t}_m \sim \Delta\tau$, suggesting entropy barriers are finite. Thus the $A_1 = 0$ behaviour is quite different from that with nonzero St Venant interactions, that therefore play a central role in incubation processes, for the TCR, SO, TO transitions.

4.5 Chapter summary

In this Chapter, we have presented the systematic temperature quench MC simulations without extrinsic disorder, on the pseudospin Hamiltonians with $N_{OP} = 2, N_V = 3, 4, 6$, corresponding to the TCR, SO, and TO transitions to understand microstructural dynamics [57].

Our MC simulations suggest that, the results in Chapter 3 for scalar-OP square-rectangle (SR) transition also do occur at least in three vector-OP triangle-centered rectangle (TCR), square-oblique (SO), triangle-oblique (TO) transitions.

Question: Are there pseudospin models for ferroelastic transitions in 3D ?

5

Strain and pseudospins in 3D

In this Chapter, we discuss strain and distortions in 3-dimensions. We then outline the discrete-strain pseudospin Hamiltonians and compatibility potentials for tetragonal-orthorhombic, cubic-tetragonal, cubic-trigonal, and cubic-orthorhombic transitions [33] . These will be used in our simulations in Chapters 6 and 7.

5.1 Continuous strain representation

In this Section, we discuss 3D strain under distortions of a material through external stress or on cooling. We outline continuous-variable strain free energies in terms of the order parameter (OP) using Barsch and Krumhansl

(BK) scaling procedure, that was generalized to different transitions in 3D [33]. We then outline the compatibility potentials, that are induced by the St.Venant no-defect condition [33].

5.1.1 Distortions, strain and compatibility condition

For 3D cubic unit cells as the austenite phase, with six Cartesian strain components, the physical strains e_α with $\alpha = 1, 2, ..., 6$ are the compressional (e_1), deviatoric (e_2, e_3), and shear (e_4, e_5, e_6) symmetrized distortions. For the cubic lattice, with X, Y, Z transforming as 3D Cartesian coordinates, the physical strains transform as $e_1 \sim X^2 + Y^2 + Z^2, e_2 \sim X^2 - Y^2, e_3 \sim X^2 + Y^2 - 2Z^2, e_4 \sim XY, e_5 \sim ZX, e_6 \sim XY$, and are defined as [33],

$$\begin{aligned} e_1(\vec{r}) = \frac{1}{\sqrt{3}}(e_{xx} + e_{yy} + e_{zz}), e_2(\vec{r}) = \frac{1}{\sqrt{2}}(e_{xx} - e_{yy}), \\ e_3(\vec{r}) = \frac{1}{\sqrt{6}}(e_{xx} + e_{yy} - 2e_{zz}), e_4(\vec{r}) = 2e_{yz}, \\ e_5(\vec{r}) = 2e_{zx}, e_6(\vec{r}) = 2e_{xy}. \end{aligned} \tag{5.1}$$

For the 3D tetragonal unit cells as the austenite phase, the strains are [33],

$$\begin{aligned} e_1(\vec{r}) = \frac{1}{\sqrt{3}}(e_{xx} + e_{yy}), e_2(\vec{r}) = \frac{1}{\sqrt{2}}(e_{xx} - e_{yy}), e_3(\vec{r}) = e_{zz}, \\ e_4(\vec{r}) = 2e_{yz}, e_5(\vec{r}) = 2e_{zx}, e_6(\vec{r}) = 2e_{xy}. \end{aligned} \tag{5.2}$$

The physical Lagrangian strains E_α are similarly defined [33].

The OP is a subset of the physical strains, directly related to crystallographic lattice vector distortions, as discussed in Chapter 6.

In the displacement representation, for a 3D cubic lattice there are three independent variables (u_x, u_y, u_z) per lattice point (or per unit cell). In the equivalent (symmetric) strain representation, there are six physical strains $e_1, .., e_6$. There must be three constraints linking these 6 physics strain, so

that at the end there are again $6-3=3$ independent variables. The needed constraint is the St.Venant condition, that says all the distorted unit cells fit together smoothly without introducing any dislocations into the system. As before, we work with periodic boundary conditions. The constraint is,

$$\vec{\nabla} \times [\vec{\nabla} \times \mathbf{e}(\vec{r})]^T = 0; \quad \vec{k} \times \mathbf{e}(\vec{k}) \times \vec{k} = 0. \tag{5.3}$$

5.1.2 Strain free energy and Barsch-Krumhansl scaling

In Chapter 2, we outlined the derivations of strain free energies for ferroelastic transitions in 2D. Similarly, in 3D, the strain free energy for ferroelastic transitions is written in terms of free energy densities following the BK scaling procedure,

$$F = E_0 \sum_r \{\bar{f}_L(E_\ell) + \bar{f}_G(\vec{\Delta} E_\ell) + \bar{f}_{non}(E_i)\}. \tag{5.4}$$

where we use a central-difference operator on a (3D cubic) lattice, as for the 2D cases. A constrained minimization of the last term yield a St.Venant OP-OP interactions $\bar{f}_C(E_\ell)$.

5.2 Discrete-strain pseudospins

In this Section, we outline the derivations [33] of pseudospin Hamiltonians from continuous-variable strain free energies for tetragonal-orthorhombic, cubic-tetragonal, cubic-trigonal and cubic-orthorhombic transitions, that have $N_{OP} = 1, 2, 3, 2$ and $N_V = 2, 3, 4, 6$ martensite variants respectively.

5.2.1 Pseudospin Hamiltonians for 3D transitions

The discrete-strain pseudospin Hamiltonians are systematically derived by Shenoy et al [33] for four 3D transitions as mentioned above. Here, we

outline the pseudospin clock-zero Hamiltonians, that we later apply to study microstructural kinetics in ferroelastic martensites using Monte Carlo simulations in Chapter 6.

A. Tetragonal-orthorhombic transition ($N_{OP} = 1, N_V = 2, n = 5$)

The physical strains are in (5.2). There are two variants, $N_V = 2$ for tetragonal-orthorhombic transition similar to SR transition, and the single OP, $N_{OP} = 1$ is the deviatoric strain, e_2. The remaining dilatational, e_1, deviotoric e_3, and shears e_4, e_5, e_6 are the $n = 5$ non-OP strains. The strain free energy for tetragonal-orthorhombic written in terms of the OP strain e_2, contains triple-well Landau term $\bar{f}_L$ for the first order transition; and a domain wall cost Ginzburg term $\bar{f}_G$; and a compatibility term $\bar{f}_C$, that contains powerlaw anisotropic interactions induced from no-defect condition [33].

The single OP strain values at the $N_V+1 = 3$ Landau minima are replaced by discrete pseudospin values [33],

$$e_2(\vec{r}) \to \bar{\varepsilon}(\tau) S(\vec{r}), \tag{5.5}$$

where the discrete-strain pseudospin values are $S(\vec{r}) = 0, \pm 1$. Here $S(\vec{r}) = 0$ represents single austenite, and $S(\vec{r}) = \pm 1$ are two martensite variants.
The total Hamiltonian $H \equiv \{H_L + H_G\} + H_C$ in coordinate space is [33]

$$\beta H = \frac{D_0}{2}[\sum_{\vec{r}} \{g_L(\tau) S(\vec{r})^2 + \xi^2 (\vec{\Delta} S)^2\} + \sum_{\vec{r},\vec{r}'} \frac{A_1}{2} U(\vec{r} - \vec{r}') S(\vec{r}) S(\vec{r}')]. \tag{5.6}$$

Here $D_0(T) \equiv 2\bar{\varepsilon}^2(\tau) E_0 / k_B T$; g_L and $\varepsilon^2(\tau)$ are defined in (2.18), (2.22) in SR cases; and $\vec{r}$ is a 3D lattice taken as cubic for simplicity. With $S(\vec{r}) = \frac{1}{\sqrt{N}} \sum_{\vec{k}} S(\vec{k}) e^{-i\vec{k}.\vec{r}}$ and periodic boundary conditions, the Hamiltonian is diagonal in Fourier space,

$$\beta H = \frac{1}{2} \sum_{\vec{k}} Q_0(\vec{k}) |S(\vec{k})|^2; \tag{5.7}$$

$$Q_0(\vec{k}) \equiv D_0[\{g_L(\tau) + \xi^2 \vec{K}^2\} + \frac{A_1}{2} U(\vec{k})]. \tag{5.8}$$

The compatibility kernel $U(\vec{k})$ for the 3D tetragonal-orthorhombic transition is given in (5.27). This Hamiltonian is like Spin-1 Blume Capel model in 3D, but with temperature dependent coefficients and powerlaw anisotropic interactions.

B. Cubic-tetragonal, and cubic-orthorhombic transitions

$(N_{OP} = 2, N_V = 3, 6, n = 4)$

The Landau free energy for cubic-tetragonal transition has been considered by Barsch and Krumhansl and others [33, 39]. Both cubic-tetragonal and cubic-orthorhombic transitions have two deviatoric strains $\vec{e} = (e_3, e_2)$ as OP $N_{OP} = 2$ and the $n = 4$ non-OP strains are one dilatational, e_1, three shears, e_4, e_5, e_6. There are three martensite variants, $N_V = 3$ for the cubic-tetragonal transition as shown in Figure 1.1 and $N_V = 6$ for the cubic-orthorhombic transition as shown in Figure 5.1.

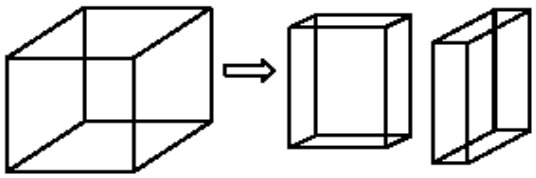

Figure 5.1: *Cubic-orthorhombic transition:* Single cubic austenite unit cell and two (of six) orthorhombic martensite unit cells.

The Landau free energy for the cubic-tetragonal case has a cubic invariant $I_3 = e_3^3 - 3e_3e_2^2$ that in OP-space spherical polar coordinates goes as $-\cos 3\phi$, generating $N_V = 3$ minima at $\phi = \phi_m = 0, \frac{2\pi}{3}, \frac{4\pi}{3}$.

The continuous-variable strain free energy [33, 39] is discretized by choosing its values only at the $N_V + 1 = 4$ Landau minima [33],

$$\vec{e}(\vec{r}) = |\vec{e}|(\cos\phi, \sin\phi) \to \bar{\varepsilon}(\tau)\vec{S}(\vec{r}) \tag{5.9}$$

where the pseudospin values $\vec{S}(\vec{r})$, for cubic-tetragonal are same as TCR transition given in (2.28).

The Landau free energy for the cubic-orthorhombic case has sixth order invariant $I_6 = I_3^2$ that goes as $\cos^2 3\phi \sim \cos 6\phi$, generating $N_V = 6$ minima at $\phi = \phi_m = 0, \frac{2\pi}{6}, ...\frac{7\pi}{6}$. For cubic-orthorhombic case the pseudospin values are same as TO transition given in (2.40).

The total pseudospin Hamiltonian in coordinate space is

$$\begin{aligned} \beta H(\vec{S}) \quad &= \frac{D_0}{2}[\textstyle\sum_{\vec{r}}\sum_{\ell=2,3}\{g_L\vec{S}_\ell(\vec{r})^2 + \xi^2|\vec{\nabla}\vec{S}_\ell(\vec{r})|^2\} \\ &+\frac{A_1}{2}\textstyle\sum_{\vec{r},\vec{r}'}\sum_{\ell,\ell'=2,3}U_{\ell\ell'}(\vec{r}-\vec{r}')\vec{S}_\ell(\vec{r})\vec{S}_{\ell'}(\vec{r}')], \end{aligned} \tag{5.10}$$

and is a clock-zero $\mathbb{Z}_{6+1}$ model [33] , with $\vec{S}$ having $6+1$ values of (2.28), (2.40) and with a compatibility kernel $U_{\ell\ell'}(\vec{k})$ for cubic-tetragonal and cubic-orthorhombic transitions are given in (5.28). It is again diagonal in Fourier space,

$$\beta H = \frac{1}{2}\sum_{\vec{k}}\sum_{\ell,\ell'=2,3} Q_{0,\ell\ell'}(\vec{k})S_\ell(\vec{k})S_{\ell'}(\vec{k})^*, \tag{5.11}$$

with $\vec{S}(\vec{k})^* = \vec{S}(-\vec{k})$, as $\vec{S}(\vec{r})$ is real. Here

$$Q_{0,\ell\ell'}(\vec{k}) \equiv D_0[\{g_L(\tau) + \xi^2\vec{k}^2\}\delta_{\ell,\ell'} + \frac{A_1}{2}U_{\ell\ell'}(\vec{k})]. \tag{5.12}$$

The coefficients g_L and $\varepsilon^2(\tau)$ for cubic-tetragonal is same as the TCR transition in (2.29), (2.27); and for cubic-orthorhombic is same as the SR transition in (2.22), (2.18).

C. Cubic-trigonal transition ($N_{OP} = 3, N_V = 4, n = 3$)

The order parameter strains, $N_{OP} = 3$ are three shears, $\vec{e} = (e_4, e_5, e_6)$, and remaining strains are $n = 3$ non-OP: one dilatational, e_1 and two deviatoric, e_2, e_3 [33]. There are four martensite variants, $N_V = 4$ for cubic-trigonal transition. The continuous strain free energy in OP is discretized by

choosing its values only at the $N_V + 1 = 5$ Landau minima. The continuous-variable strains at minima are replaced by pseudospins [33], $\vec{e}(\vec{r}) \to \bar{\varepsilon}(\tau)\vec{S}(\vec{r})$. The pseudospin values $\vec{S}(\vec{r}) = (S_4, S_5, S_6) = (\sin\theta_m \cos\phi_m, \sin\theta_m \sin\phi_m, \cos\theta_m)$ with $\cos\bar{\theta} = 1/\sqrt{3}$,

$$\phi_m = \frac{\pi}{4}, \frac{5\pi}{4},\ \theta_m = \bar{\theta}; \quad \phi_m = \frac{3\pi}{4}, \frac{7\pi}{4},\ \theta_m = \bar{\theta} + \pi. \tag{5.13}$$

Explicitly, the pseudospin values are [33],

$$(S_4, S_5, S_6) = (0,0,0), (\pm\frac{1}{\sqrt{3}}, \pm\frac{1}{\sqrt{3}}, \frac{1}{\sqrt{3}}), (\pm\frac{1}{\sqrt{3}}, \mp\frac{1}{\sqrt{3}}, -\frac{1}{\sqrt{3}}). \tag{5.14}$$

These point to the four corners of a tetrahedron in $N_{OP} = 3$ component OP-space.

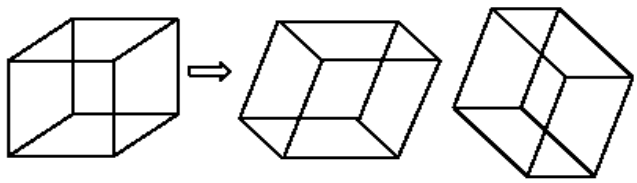

Figure 5.2: *Cubic-trigonal transition:* Cubic unit cell is for austenite and two (of four) trigonal unit cells shown are for martensite variants.

In coordinate space the total pseudospin Hamiltonian is,

$$\begin{aligned} \beta H \quad &= \frac{D_0}{2}[\textstyle\sum_{\vec{r}} \sum_{\ell=4,5,6} \{g_L \vec{S}_\ell(\vec{r})^2 + \xi^2 |\vec{\nabla}\vec{S}_\ell(\vec{r})|^2\} \\ &+ \frac{A_1}{2} \textstyle\sum_{\vec{r},\vec{r}'} \sum_{\ell,\ell'=4,5,6} U_{\ell\ell'}(\vec{r}-\vec{r}')\vec{S}_\ell(\vec{r})\vec{S}_{\ell'}(\vec{r}')], \end{aligned} \tag{5.15}$$

and is a clock-zero $\mathbb{Z}_{4+1}$ model [33] , with $\vec{S}$ having $3+1$ values of (6.64) and with a compatibility kernel of (5.31). It is again diagonal in Fourier space,

$$\beta H = \frac{1}{2} \sum_{\vec{k}} \sum_{\ell,\ell'=4,5,6} Q_{0,\ell\ell'}(\vec{k}) S_\ell(\vec{k}) S_{\ell'}(\vec{k})^*, \tag{5.16}$$

with $\vec{S}(\vec{k})^* = \vec{S}(-\vec{k})$, as $\vec{S}(\vec{r})$ is real. Here

$$Q_{0,\ell\ell'}(\vec{k}) \equiv D_0[\{g_L(\tau) + \xi^2\vec{k}^2\}\delta_{\ell,\ell'} + \frac{A_1}{2}U_{\ell\ell'}(\vec{k})]. \tag{5.17}$$

The temperature dependent coefficients g_L and $\varepsilon(\tau)$ are defined in (2.28), (2.29), same as in TCR transition.

5.2.2 Compatibility potentials for 3D transitions

In three dimensions, the compatibility condition of (2.7) in Fourier space for Cartesian distortions is a vanishing of the Incompatibility $Inc(\mathbf{e}) = \vec{K} \times \mathbf{e}(\vec{K}) \times \vec{K} = 0$. This is written [33] as three equations from diagonal components of Incompatibility, $Inc(e)_{xx} = 0$, and three equations from off-diagonal components $Inc(e)_{yz} = 0$ that are identically satisfied from the first three.

In the displacement representation, for a 3D cubic lattice there are three independent variables (u_x, u_y, u_z) per lattice point (or per unit cell). In the equivalent (symmetric) strain representation, there are six physical strains $e_1, .., e_6$ and three constraints, so there are again $6 - 3 = 3$ independent variables. The St Venant constraints in Cartesian strains can be written in terms of the Cartesian distortions,

$$O_1^{(s)}e_1 + O_2^{(s)}e_2 + O_3^{(s)}e_3 + O_s^{(s)}e_s = 0, \tag{5.18}$$

using the relation,

$$\begin{aligned} e_{xx} &= \frac{1}{\sqrt{3}}e_1 + \frac{1}{\sqrt{2}}e_2 + \frac{1}{\sqrt{6}}e_3; \\ e_{yy} &= \frac{1}{\sqrt{3}}e_1 - \frac{1}{\sqrt{2}}e_2 + \frac{1}{\sqrt{6}}e_3; \\ e_{zz} &= \frac{1}{\sqrt{3}}e_1 - \frac{2}{\sqrt{6}}e_3. \end{aligned} \tag{5.19}$$

The three shear components e_s labelled $s = 4, 5, 6$, are related to three non-shears e_1, e_2, e_3 as,

$$e_s = -\sum_{\alpha=1,2,3} \bar{O}_\alpha^{(s)} e_\alpha. \tag{5.20}$$

where $\bar{O}_\alpha^{(s)}$ is defined as,

$$\bar{O}_\alpha^{(s)} \equiv O_\alpha^{(s)}/O_s, \tag{5.21}$$

The cubic-lattice compatibility coefficients $O_\alpha^{(s)}$ of (5.18) are evaluated [33],

$$\begin{gathered}
O_1^{(4)} = \frac{-1}{\sqrt{3}}(K_y^2 + K_z^2),\ O_2^{(4)} = \frac{1}{\sqrt{2}}K_z^2,\ O_3^{(4)} = \frac{1}{\sqrt{6}}(2K_y^2 - K_z^2); \\
O_4^{(4)} \equiv O_4 = K_y K_z,\ O_1^{(5)} = \frac{-1}{\sqrt{3}}(K_z^2 + K_x^2),\ O_2^{(5)} = \frac{-1}{\sqrt{2}}K_z^2; \\
O_3^{(5)} = \frac{1}{\sqrt{6}}(2K_x^2 - K_z^2),\ O_5^{(5)} \equiv O_5 = K_z K_x,\ O_1^{(6)} = \frac{-1}{\sqrt{3}}(K_x^2 + K_y^2); \\
O_2^{(6)} = \frac{1}{\sqrt{2}}(K_x^2 - K_y^2),\ O_3^{(6)} = \frac{-1}{\sqrt{6}}(K_x^2 + K_y^2),\ O_6^{(6)} \equiv O_6 = K_x K_y.
\end{gathered} \tag{5.22}$$

These will be used in the cubic-tetragonal, cubic-orthorhombic, and cubic-trigonal transitions in Chapter 6.

For the tetragonal-lattice physical distortions are from (5.2), and the tetragonal-lattice compatibility coefficients are

$$\begin{gathered}
O_1^{(4)} = \frac{-K_z^2}{\sqrt{2}},\ O_2^{(4)} = \frac{K_z^2}{\sqrt{2}},\ O_3^{(4)} = -K_y^2,\ O_4^{(4)} \equiv O_4 = K_y K_z; \\
O_1^{(5)} = \frac{-K_z^2}{\sqrt{2}},\ O_2^{(5)} = \frac{-K_z^2}{\sqrt{2}},\ O_3^{(5)} = -K_x^2,\ O_5^{(5)} \equiv O_5 = K_z K_x; \\
O_1^{(6)} = \frac{-1}{\sqrt{2}}(K_x^2 + K_y^2),\ O_2^{(6)} = \frac{-1}{\sqrt{2}}(K_x^2 - K_y^2); \\
O_3^{(6)} = 0,\ O_6^{(6)} \equiv O_6 = K_x K_y.
\end{gathered} \tag{5.23}$$

These will be used for the tetragonal-orthorhombic transition in Chapter 6.

A dimensionless variable is defined [33],

$$G_{\alpha\beta} \equiv \sum_{s=4,5,6} (A_s/A_1)\bar{O}_\alpha^{(s)}\bar{O}_\beta^{(s)}, \tag{5.24}$$

where $G_{\alpha\beta} = G_{\beta\alpha}$ is symmetric, and a remainder term is defined through products, that is used in compatibility kernels later,

$$R_{\alpha\beta,\gamma\delta} = G_{\alpha\beta}G_{\gamma\delta} - G_{\alpha\gamma}G_{\beta\delta}. \tag{5.25}$$

Then the kernels for the four 3D transitions are obtained in terms of the $G_{\alpha\beta}$, by a substitution/minimization method similar to 2D.

A. Tetragonal-orthorhombic transition ($n = 5, N_{OP} = 1$)

As mentioned earlier for this transition, the order parameter strain is one of the deviatoric strains, e_2. The non-OP strains, $n = 5$ are one dilatational, e_1, one deviatoric, e_3 and three shear strains e_4, e_5, e_6. The non-OP strains are harmonic $\bar{f}_{non} = (A_1/2)|e_1|^2 + (A_3/2)|e_3|^2 + \sum_{s=4,5,6}(A_s/2)|e_s|^2$, and are minimized subject to the no-defect St.Venant condition, that yield [33],

$$f_{compat}(e_2) = \sum_{\vec{k}} \frac{A_1}{2}\, U(\vec{k}) e_2(\vec{k}) e_2^{'}(\vec{k})^*. \tag{5.26}$$

The compatibility kernel $U(\vec{k})$ for the tetragonal-orthorhombic transition is given [33],

$$A_1 U(\vec{k}) = \nu[(A_3/A_1)G_{22} + T_2]/G_0, \tag{5.27}$$

with $T_2 = (A_3/A_1)R_{22,11} + R_{22,33} + \{G_{22}R_{33,11} - G_{12}R_{33,12} - G_{32}R_{11,32}\}$, $G_0 \equiv [(\{A_3/A_1\} + G_{33})(1 + G_{11}) - G_{13}^2]$, and $R_{\alpha\alpha,\beta\gamma}$ is defined in (5.54).

For $K_z \to 0$, the kernel become essentially the 2D SR case kernel, as expected [33].

B. Cubic-tetragonal, and cubic-orthorhombic transitions $(n = 4, N_{OP} = 2)$

In both transitions, the order parameter strains are the two deviatoric strains, e_3, e_2, and the non-OP strains, $n = 4$ are the remaining one compressional, e_1 and three shear strains, e_4, e_5, e_6. The non-OP term is harmonic $\bar{f}_{non} = (A_1/2)|e_1|^2 + \sum_{s=4,5,6}(A_s/2)|e_s(\vec{k})|^2$, the usual constrained minimization yields the compatibility term [33],

$$f_{non}(e_1) = f_{compat}(e_3, e_2) = \sum_{\ell,\ell'=2,3} \frac{A_1}{2}\, U_{\ell\ell'}(\vec{k}) e_\ell(\vec{k}) e_{\ell'}(\vec{k})^*. \tag{5.28}$$

Here, the compatibility kernels $U_{\ell\ell'}(\vec{k})$ for the cubic-tetragonal and the cubic-orthorhombic transitions is given [33],

$$U_{\ell\ell'}(\vec{k}) = \nu[G_{\ell\ell'} + R_{\ell\ell',11}]/(1 + G_{11}), \tag{5.29}$$

with $R_{\ell\ell',11} \equiv G_{\ell\ell'}G_{11} - G_{\ell 1}G_{\ell' 1}$ and $G_{\ell\ell'}$ is defined in (5.24).

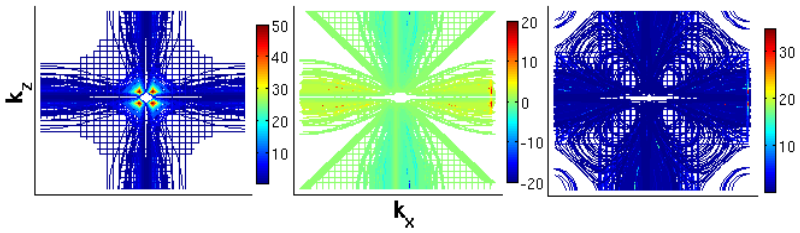

Figure 5.3: *Cubic-tetragonal and cubic-orthorhombic transitions:* Compatability induced anisotropic kernels $U_{22}(\vec{k}), U_{23}(\vec{k}), U_{33}(\vec{k})$ between OP strains.

C. Cubic-trigonal transition $(n = 3, N_{OP} = 3)$

The order parameter (OP) strains are three shears e_4, e_5, e_6, and non-OP strains are one dilatational and two deviatoric strains are e_1, e_2, e_3 respectively. The non-OP strains are harmonic $\bar{f}_{non} = \sum_{i=1,2,3}(A_i/2)|e_i(\vec{k})|^2$, and

are minimized as usual to yield the compatibility term for the cubic-trigonal transition [33],

$$\bar{f}_{non} = \bar{f}_{compat} = \sum_{\ell,\ell'=4,5,6} \frac{A_1}{2}\, U_{\ell\ell'}(\vec{k}) e_\ell(\vec{k}) e_{\ell'}(\vec{k})^*, \tag{5.30}$$

where the compatibility kernels $U_{\ell\ell'}(\vec{k})$ between the OP strains are,

$$A_1 U_{\ell\ell'}(\vec{k}) = \nu \sum_{i=1,2,3;\ \ell,\ell'=4,5,6} A_i N_{i\ell} N_{i\ell'}. \tag{5.31}$$

The elements $N_{14}, N_{15}, N_{16}; ...N_{36}$ in the kernels $U_{\ell\ell'}(\vec{k})$ are given in matrix form [33],

$$\begin{pmatrix} \frac{(K_x^2-K_y^2-K_z^2)}{2\sqrt{3}O_4} & \frac{(K_y^2-K_z^2-K_x^2)}{2\sqrt{3}O_5} & \frac{(K_z^2-K_x^2-K_y^2)}{2\sqrt{3}O_6} \\ \frac{(K_x^2+K_y^2)}{2\sqrt{2}O_4} & -\frac{(K_x^2+K_y^2)}{2\sqrt{2}O_5} & -\frac{(K_x^2-K_y^2)}{2\sqrt{2}O_6} \\ \frac{(2K_z^2+K_x^2-K_y^2)}{2\sqrt{6}O_4} & \frac{(2K_z^2-K_x^2+K_y^2)}{2\sqrt{6}O_5} & -\frac{(2K_z^2+K_x^2+K_y^2)}{2\sqrt{6}O_6} \end{pmatrix}. \tag{5.32}$$

In this Chapter, we have outlined the derivations of discrete-strain pseudospin Hamiltonians for four 3D transitions and compatibility potentials.

Question: Are the results obtained in Chapters 3 and 4 are specific to 2D transitions or do they also occur in 3D transitions ?

6

3D transitions: Conversion-delay tails

In this Chapter, we start by evaluating scaled order parameter (OP) strains from experimental lattice parameters for different materials undergoing 3D structural transitions with N_V martensitic variants, N_{OP} components in the OP. We find that the scaled-OP strains have the values of strain-pseudospins. We show that the results obtained in Chapters 3 and 4 are not specific to 2D transitions, but occur at least in four 3D pseudospin models for tetragonal-orthorhombic (high-T_c superconductors such as $YBaCuO_3$), cubic-tetragonal (shape momory alloys such as $FePd$), cubic-trigonal (Colossal Magnetoresistance Oxides such as $LaSrMnO$), and cubic-orthorhombic (Ferroelectrics such as $BaTiO_3$) transitions. We also present the final twinned microstructures in all four transitions.

6.1 Strain-pseudospins and experimental lattice parameters

In this Section, we evaluate the scaled-OP strains from experiments. One would hope that:
a). Scaled-OP strains should have different values for different variants, and be at least close to pseudospin values. b). The preferred orientations of twin domain walls should be consistent with experiment. b). The scaled non-OP strain values should be the same for all variants. We do not expect the scaled values to be zero as that is for periodic boundary conditions and not free boundary conditions and to leading order in the scaled-OP magnitude, and we ignored uniform non order parameter-order parameter couplings such as $-e_1 \sum_{\vec{r}} e_2^2$.

The evaluations give us the following:
a). Scaled-OP strains are exactly right, suggesting pseudospins are a good description of the OP scaled strains. b). Domain wall orientations are consistent with experiment. c). The scaled non-OP strain values are same for all variants, but for reasons mentioned the values should not be taken too seriously.

The austenite lattice vectors are distorted by a matrix $\mathbf{U}^{'} = \mathbf{1} + \mathbf{D}^{'}$, to martensite lattice vectors. Here, prime denotes the *unscaled* distortions. The distortion matrix $\mathbf{D}^{'}$ is,

$$\mathbf{D}^{'} = \begin{pmatrix} D^{'}_{xx} & D^{'}_{xy} & D^{'}_{xz} \\ D^{'}_{yx} & D^{'}_{yy} & D^{'}_{yz} \\ D^{'}_{zx} & D^{'}_{zy} & D^{'}_{zz} \end{pmatrix} = \mathbf{U}^{'} - \mathbf{1} \tag{6.1}$$

$$D^{'}_{xx} = U^{'}_{xx} - 1; D^{'}_{yy} = U^{'}_{yy} - 1; D^{'}_{zz} = U^{'}_{zz} - 1. \tag{6.2}$$

The unscaled physical distortions for cubic case are [33],

$$e_1^{'} = \frac{D_{xx}^{'} + D_{yy}^{'} + D_{zz}^{'}}{\sqrt{3}}; e_2^{'} = \frac{D_{xx}^{'} - D_{yy}^{'}}{\sqrt{2}}; e_3^{'} = \frac{D_{xx}^{'} + D_{yy}^{'} - 2D_{zz}^{'}}{\sqrt{6}}, \\ e_4^{'} = 2D_{yz}^{'};\ e_5^{'} = 2D_{zx}^{'};\ e_6^{'} = 2D_{xy}^{'} \tag{6.3}$$

Some subset of the physical strains is the OP $\{e_\ell^{'}\}$, and the strain magnitude λ at the Landau transition $T = T_0$ is,

$$\lambda = \sqrt{\sum_\ell (e_\ell^{'})^2} \tag{6.4}$$

The scaled physical strains are then,

$$e_1 = \frac{e_1^{'}}{\lambda}; e_2 = \frac{e_2^{'}}{\lambda}; e_3 = \frac{e_3^{'}}{\lambda}; e_4 = \frac{e_4^{'}}{\lambda}; e_5 = \frac{e_5^{'}}{\lambda}; e_6 = \frac{e_6^{'}}{\lambda} \tag{6.5}$$

We now evaluate the scaled strains for three transitions.

6.1.1 Tetragonal-orthorhombic transition (2 variants)

High-T_c superconductors such as $YBaCuO_3$ undergoes this transition. The distortion matrices or N_V variants, for the tetragonal-orthorhombic transition are given in Bhattacharya's book [1] as,

$$U_1 = \begin{pmatrix} \alpha & 0 & 0 \\ 0 & \beta & 0 \\ 0 & 0 & \gamma \end{pmatrix};\ \ U_2 = \begin{pmatrix} \beta & 0 & 0 \\ 0 & \alpha & 0 \\ 0 & 0 & \gamma \end{pmatrix}, \tag{6.6}$$

where α, β, γ are the ratio of austenite lattice vector a_0 and martensite lattice parameters a, b, c, along cubic axes, $\alpha = a/a_0$, $\beta = b/b_0$, $\gamma = c/a_0$.
The one-component unscaled OP strain is $e_2^{'}$ [33] and its magnitude λ is same for U_1, U_2,

$$\lambda = \sqrt{e_2^{'\,2}} = \sqrt{\frac{(D_{xx}^{'} - D_{yy}^{'})^2}{2}} = \frac{|\alpha - \beta|}{\sqrt{2}}. \tag{6.7}$$

The non-OP strains same for all variants and are 3 shears $e_4^{'} = e_5^{'} = e_6^{'} = 0$, one compressional strain $e_1^{'} = (\alpha + \beta - 2)/\sqrt{2}$, and one deviatoric strain $e_3^{'} = (\gamma - 1)$.
The *scaled*-OP distortions or strains are,

$$e_2(U_1) = \frac{\alpha - \beta}{|\alpha - \beta|}; \;\; e_2(U_2) = \frac{-(\alpha - \beta)}{|\alpha - \beta|}. \tag{6.8}$$

So, the possible scaled-OP strain values for U_1, U_2 are just the pseudospin values.

$$e_2 = \pm 1. \tag{6.9}$$

The scaled non-OP strains, same for both variants, are

$$e_1 = \frac{\alpha + \beta - 2}{|\alpha - \beta|}; \;\; e_3 = \frac{\sqrt{2}(\gamma - 1)}{|\alpha - \beta|}; \;\; e_4 = e_5 = e_6 = 0. \tag{6.10}$$

Table 6.1 shows a material undergoing the above transition [1, 50], the unscaled values α, β; non-OP scaled values e_1, e_3; and shears $e_s, \; s = 4, 5, 6$ e_2 and scaled-OP e_2. The scaled-OP strains are precisely the pseudospin values from minima of the scaled free energies, supporting the pseudospin approximation. The non-OP scaled strains are not zero, for reasons mentioned earlier, but are < 1.

6.1.2 Cubic-tetragonal transition (3 variants)

Shape memory alloys such as $FePd$ exhibit this transition. The distortion matrices or N_V variants, for cubic-tetragonal transition are [1],

$$U_1 = \begin{pmatrix} \beta & 0 & 0 \\ 0 & \alpha & 0 \\ 0 & 0 & \alpha \end{pmatrix}; \;\; U_2 = \begin{pmatrix} \alpha & 0 & 0 \\ 0 & \beta & 0 \\ 0 & 0 & \alpha \end{pmatrix}; \;\; U_3 = \begin{pmatrix} \alpha & 0 & 0 \\ 0 & \alpha & 0 \\ 0 & 0 & \beta \end{pmatrix}, \tag{6.11}$$

where $\alpha = a/a_0, \beta = c/a_0$, with austenite and martensite lattice parameters $a_0; a, c$ respectively.

The two-component unscaled-OP strains are $(e_3^{'}, e_2^{'}) = (\frac{D_{xx}^{'}+D_{yy}^{'}-2D_{zz}^{'}}{\sqrt{6}}, \frac{D_{xx}^{'}-D_{yy}^{'}}{\sqrt{2}})$, and its magnitude λ is same for U_1, U_2, U_3,

$$\lambda = \sqrt{{e_3^{'}}^2 + {e_2^{'}}^2} = \sqrt{\frac{2}{3}}\ |\beta - \alpha|. \tag{6.12}$$

The non-OP strains are same for all variants, and again 3 shears are zero, $e_4^{'} = e_5^{'} = e_6^{'} = 0$; and one compressional strain $e_1^{'} = (2\alpha + \beta)/\sqrt{3}$.
The *scaled*-OP strains for U_1 with $D_{xx}^{'} = \beta - 1,\ D_{yy}^{'} = D_{zz}^{'} = \alpha - 1$ are,

$$(e_3, e_2) = (\frac{e_3^{'}}{\lambda}, \frac{e_2^{'}}{\lambda}) = (\frac{\beta + \alpha - 2\alpha}{\lambda\sqrt{6}}, \frac{\beta - \alpha}{\lambda\sqrt{2}}) = (-\frac{1}{2}, -\frac{\sqrt{3}}{2})sign(\alpha - \beta) \tag{6.13}$$

For U_2 with $D_{yy}^{'} = \beta - 1,\ D_{xx}^{'} = D_{zz}^{'} = \alpha - 1$,

$$(e_3, e_2) = (\frac{e_3^{'}}{\lambda}, \frac{e_2^{'}}{\lambda}) = (\frac{\alpha + \beta - 2\alpha}{\lambda\sqrt{6}}, \frac{\alpha - \beta}{\lambda\sqrt{2}}) = (-\frac{1}{2}, +\frac{\sqrt{3}}{2})sign(\alpha - \beta) \tag{6.14}$$

For U_3 with $D_{zz}^{'} = \beta - 1,\ D_{xx}^{'} = D_{yy}^{'} = \alpha - 1$,

$$(e_3, e_2) = (\frac{e_3^{'}}{\lambda}, \frac{e_2^{'}}{\lambda}) = (\frac{2\alpha - 2\beta}{\lambda\sqrt{6}}, 0) = (1, 0)sign(\alpha - \beta) \tag{6.15}$$

The scaled non-OP strains, for all variants are $e_1 = \frac{\beta+2\alpha}{\lambda\sqrt{3}}$, $e_4 = e_5 = e_6 = 0$. Table 6.2 shows for materials undergoing the above transition [1, 51] the unscaled α, β, γ; the non-OP scaled values e_1, shears e_s $(s = 4, 5, 6)$; and scaled-OP values e_3, e_2. The last OP-value column in the Table 6.2 applies to all the two groups of materials and *both* of the two possible OP triangle orientations of Figure 2.3 appear.

Table 3.1: Scaled strains in tetragonal-orthorhombic transition

Material	α	β	γ	λ	e_1	e_3	e_s	$N_V = 2,\ OP = e_2$
$YBa_2Cu_3O_{7-\delta}$	0.9898	1.0068	0.9887	0.0120	-0.2003	-1.331 (?)	0	U_1: -1.0, U_2: 1.0.

Table 3.2: Scaled strains in cubic-tetragonal transition

Ref.	Material	α	β	λ	e_1	e_s	$N_V = 3,\ OP = (e_3,\ e_2)$
51.a	Fe-7at.%Pd-3	1.0175	0.9660	0.0420	0.0137	0	
51.b	In-32at.%Pb	1.0208	0.9688	0.0424	0.1414	0	
51.c	Fe-24at.%Pt	1.0868	0.8503	0.1931	0.0714	0	$U_1 : (-\frac{1}{2}, -\frac{\sqrt{3}}{2})$
51.d	Fe-7.9at.%Cr-1.1at.%C	1.1176	0.8243	0.2394	0.1434	0	$U_2 : (-\frac{1}{2}, \ \frac{\sqrt{3}}{2})$
51.e	Fe-22at.%Ni-0.8at.%C	1.1083	0.819	0.2362	0.0870	0	$U_3 : (\ 1, \ \ 0\ )$
51.f	Fe-31at.%Ni-0.3at.%C	1.1241	0.8059	0.2598	0.1202	0	
51.g	Fe-7at.%Al-1.5at.%C	1.0946	0.8546	0.1959	0.1290	0	
51.g	Fe-7at.%A1-2at.%C	1.0833	0.8727	0.1719	0.1319	0	
51.h	In-23at.%Tl	0.9889	1.0221	0.0263	-0.0218	0	$U_1 : (\ \frac{1}{2}, \ \frac{\sqrt{3}}{2})$
51.i	Ni-36at.%Al	0.9392	1.1302	0.1559	0.0318	0	$U_2 : (\ \frac{1}{2}, -\frac{\sqrt{3}}{2})$
51.j	Ni-49.4at.%Mn	0.912	1.194	0.2302	0.0451	0	$U_3 : (-1, \ \ 0\ )$

The scaled-OP strains are precisely the pseudospin values supporting the pseudospin approximation. The scaled non-OP strains are non-zero, but relatively small $<<$ 1.

6.1.3 Cubic-trigonal transition (4 variants)

Colossal magnetoresistance oxides such as $LaSrMnO$ exhibit this transition. The distortion matrices or variants N_V, for cubic-trigonal transition are [1],

$$U_1 = \begin{pmatrix} \alpha & \delta & \delta \\ \delta & \alpha & \delta \\ \delta & \delta & \alpha \end{pmatrix}; \quad U_2 = \begin{pmatrix} \alpha & -\delta & -\delta \\ -\delta & \alpha & \delta \\ -\delta & \delta & \alpha \end{pmatrix},$$

$$U_3 = \begin{pmatrix} \alpha & \delta & -\delta \\ \delta & \alpha & -\delta \\ -\delta & -\delta & \alpha \end{pmatrix}; \quad U_4 = \begin{pmatrix} \alpha & -\delta & \delta \\ -\delta & \alpha & -\delta \\ \delta & -\delta & \alpha \end{pmatrix}.$$

The three-component unscaled-OP strains are one compressional and two deviatoric strains and are same for all variants $(e_4^{'}, e_5^{'}, e_6^{'}) = (2D_{yz}^{'}, 2D_{zx}^{'}, 2D_{xy}^{'})$, and its magnitude λ is same for U_1, U_2, U_3, U_4,

$$\lambda = \sqrt{{e_4^{'}}^2 + {e_5^{'}}^2 + {e_6^{'}}^2} = 2\sqrt{3}\delta. \tag{6.16}$$

The unscaled non-OP strains $e_1^{'} = (D_{xx}^{'} + D_{yy}^{'} + D_{zz}^{'})/\sqrt{3}$, $e_2^{'} = (D_{xx}^{'} - D_{yy}^{'})/\sqrt{2}$, $e_3^{'} = (D_{xx}^{'} + D_{yy}^{'} - 2D_{zz}^{'})/\sqrt{6}$, same for all variants.
The *scaled*-OP strains for U_1 with $D_{xy}^{'} = D_{yz}^{'} = D_{zx}^{'} = \delta$ are,

$$(e_4, e_5, e_6) = (\frac{e_4^{'}}{\lambda}, \frac{e_5^{'}}{\lambda}, \frac{e_6^{'}}{\lambda}) = (\frac{2\delta}{2\sqrt{3}\delta}, \frac{2\delta}{2\sqrt{3}\delta}, \frac{2\delta}{2\sqrt{3}\delta}) = (\frac{1}{\sqrt{3}}, \frac{1}{\sqrt{3}}, \frac{1}{\sqrt{3}}) \tag{6.17}$$

For U_2 with $D_{xy}^{'} = -\delta, D_{yz}^{'} = \delta, D_{zx}^{'} = -\delta$,

$$(e_4, e_5, e_6) = (\frac{e_4^{'}}{\lambda}, \frac{e_5^{'}}{\lambda}, \frac{e_6^{'}}{\lambda}) = (\frac{-2\delta}{2\sqrt{3}\delta}, \frac{-2\delta}{2\sqrt{3}\delta}, \frac{2\delta}{2\sqrt{3}\delta}) = (\frac{1}{\sqrt{3}}, \frac{-1}{\sqrt{3}}, \frac{-1}{\sqrt{3}}) \tag{6.18}$$

For U_3 with $D_{xy}^{'} = \delta, D_{yz}^{'} = -\delta, D_{zx}^{'} = -\delta$,

$$(e_4, e_5, e_6) = (\frac{e_4^{'}}{\lambda}, \frac{e_5^{'}}{\lambda}, \frac{e_6^{'}}{\lambda}) = (\frac{2\delta}{2\sqrt{3}\delta}, \frac{-2\delta}{2\sqrt{3}\delta}, \frac{-2\delta}{2\sqrt{3}\delta}) = (\frac{-1}{\sqrt{3}}, \frac{-1}{\sqrt{3}}, \frac{1}{\sqrt{3}}) \tag{6.19}$$

For U_4 with $D^{'}_{xy} = -\delta, D^{'}_{yz} = \delta, D^{'}_{zx} = \delta$,

$$(e_4, e_5, e_6) = (\frac{e^{'}_4}{\lambda}, \frac{e^{'}_5}{\lambda}, \frac{e^{'}_6}{\lambda}) = (\frac{-2\delta}{2\sqrt{3}\delta}, \frac{2\delta}{2\sqrt{3}\delta}, \frac{-2\delta}{2\sqrt{3}\delta}) = (\frac{-1}{\sqrt{3}}, \frac{1}{\sqrt{3}}, \frac{-1}{\sqrt{3}}) \quad (6.20)$$

The scaled non-OP strains, for all variants are $e_1 = \frac{3\alpha-3}{\lambda\sqrt{3}}$, and $e_2 = e_3 = 0$. The scaled-OP strains are exactly the pseudospin values [33] for cubic-trigonal transition in (5.14). Materials undergoing this transition are not given in [1].

6.1.4 Cubic-orthorhombic transition (6 variants)

Ferroelectrics such as $BaTiO_3$ exhibit this transition. The case considered had (e_3, e_2) deviatoric strains as the OP, with lattice vectors along cubic axes. This is simple, but atypical: known materials have a deviatoric strain e.g.(e_3), and a single shear e_4, e_5, or e_6, successively as the second component [1], so the OP would be (e_3, e_2). This requires a separate treatment and will not be pursued here. However, we do simulations on the simplest cubic-orthorhombic model [33]. These pseudospins are same as in TO transition.

6.2 Textural diagnostics

The discrete-strain pseudospin or clock-zero $\mathbb{Z}_{N_V+1}$ Hamiltonians and compatibility potentials for four 3D transitions mentioned above [33] are outlined in Chapter 5.

We perform Monte Carlo (MC) simulations under systematic temperature quenches on $d = 3, N = L^3$ with $L = 16$ cubic lattice, following the same procedure as in Chapters 3 and 4, on these four 3D pseudospin models to understand the athermal/ isothermal martensite classification and the conversion-delays in athermal martensites as discussed in Chapter 1. At $t = 0$, we consider random initial state with 2% of N_V variants. Typical

parameters are $T_0 = 1$; $\xi^2 = 1$; $T_c = 0.81 - 0.97$; $A_1 = 1 - 85$; $E_0 = 3, 4, 5, 6$; $L = 16$; $N_{runs} = 100$; and holding times $t_h = 10^4$ MC sweeps.

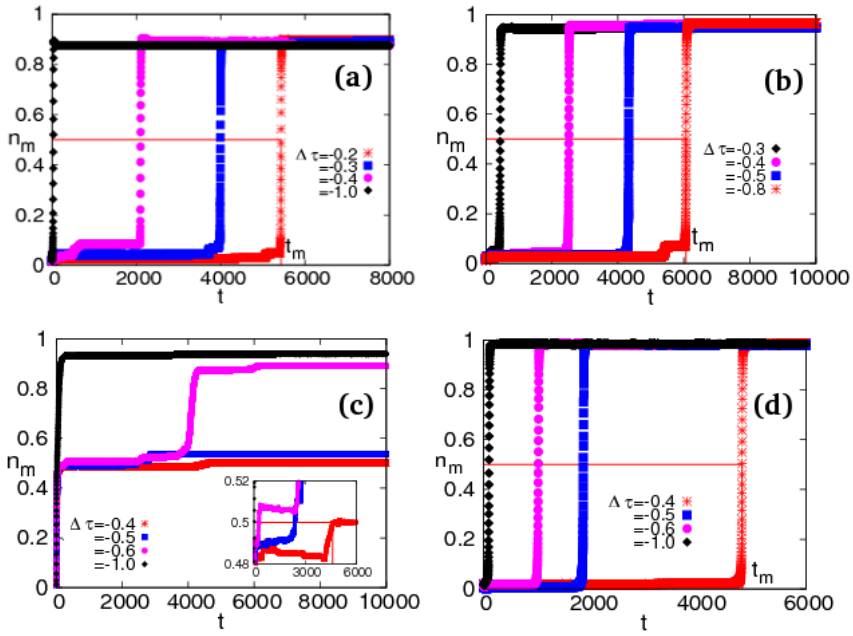

Figure 6.1: *Conversion-incubations and conversion time (t_m) defintion:* Martensite conversion fraction $n_m(t)$ versus time t showing flat incubations for different $\Delta\tau \equiv \tau - \tau_4$ for $E_0 = 3$ in, (a) tetragonal-orthorhombic transition with parameters $T_c = 0.9$, $A_1 = 4$, $A_3 = A_4 = A_5 = A_6 = 2$; (b) cubic-tetragonal transition with parameters $T_c = 0.95$, $A_1 = 4$, $A_6 = 2$; (c) cubic-trigonal transition with parameters $T_c = 0.97$, $A_1 = 4$, $A_2 = A_3 = 2$; (d) cubic-orthorhombic transition $T_c = 0.95$, $A_1 = 4$, $A_6 = 2$. Note jerky steps in n_m, that rises sharply at $t = t_m$. See text.

As before, the diagnostic for austenite-martensite conversion is the martensite conversion fraction $n_m(t)$, and is defined as

$$n_m(t) \equiv \frac{1}{N} \sum_{\vec{r}} S^2(\vec{r}, t) = \frac{1}{N} \sum_{\vec{k}} |S(\vec{k}, t)|^2 \leq 1, \tag{6.21}$$

where $n_m = 0$ in the austenite phase and $n_m = 1$ in the martensite phase.

As before in Chapters 3 and 4, after a temperature quench, we define a conversion time t_m, where the martensite conversion fraction $n_m = 1/2$ or 50%; and a mean conversion time $\bar{t}_m \equiv 1/ < r_m >$, where mean conversion rate $< r_m >=< 1/t_m >$, that is arithmeticallh averaged over $N_{runs} = 100$ different seeds.

Figure 6.1 shows the martensite conversion fraction $n_m(t)$ versus time t for different temperatures $\tau \equiv \tau - \tau_4 (<< T_0)$ in single runs, with the definition of conversion time t_m for all four transitions. There is incubation for long times during which n_m is quite flat, followed by step-like jerkiness to rise sharply at $t = t_m$, except in cubic-trigonal where the incubation is close to $n_m \sim 1/2$.

6.3 Athermal and isothermal martensites

After cooling below the martensite start temperature M_s, martensitic materials are classified as (i) athermal, that have *fast* explosive conversions in *milli seconds*, and sharp conversion boundary at M_s in TTT curves; (ii) isothermal, that have *slow*-delayed conversions in *minutes* or *hours* and C-shaped TTT curves in temperature (y-axis)-time (y-axis) plots. See Figure 1.2. The traditional classification of martensites is questioned as there are three different experimental results, as discussed in Chapter 1.

We find both athermal and isothermal martensite regimes for different material parameters. The athermal TTT curves, that have conversion-delay tails, transform to isothermal U-shaped TTT curves or vice versa on changing material parameters T_c or A_1 as shown in Figures 6.2,6.3,6.4 and 6.5 for tetragonal-orthorhombic, cubic-tetragonal, cubic-trigonal and cubic-orthorhombic transitions respectively.

The athermal regime has fast conversions below a temperature $\tau = \tau_1$

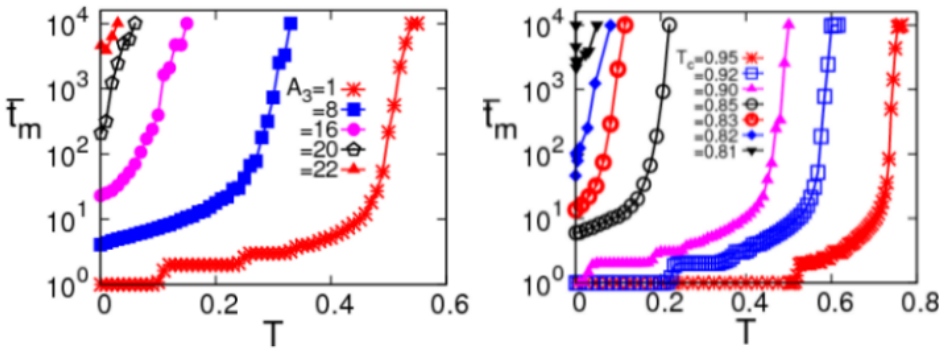

Figure 6.2: *Tetragonal-orthorhombic transition athermal/ isothermal crossover:* Conversion times $log(\bar{t}_m)$ versus temperature T showing crossover from fast athermal conversions with incubation tails to slow isothermal conversions with $E_0 = 3$ for *Left:* fixed $T_c = 0.9$, $A_1 = 4$ and different $A_3 (= A_4 = A_5 = A_6)$; *Right:* fixed $A_1 = 4, A_3 = 2$ $(= A_4 = A_5 = A_6)$ and various T_c.

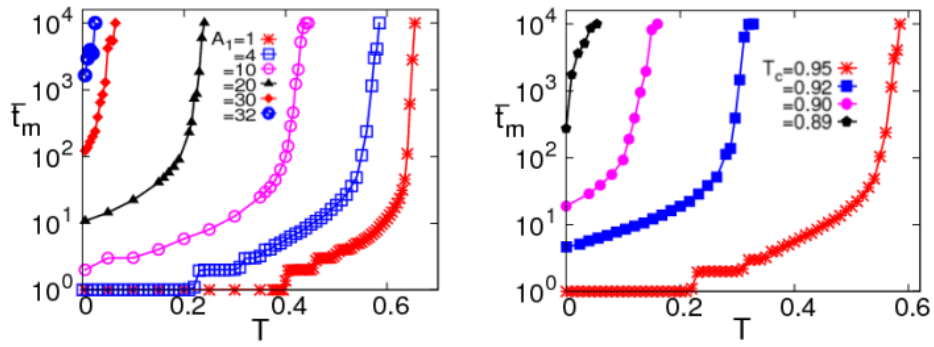

Figure 6.3: *cubic-tetragonal transition athermal/isothermal crossover:* Conversion times $log(\bar{t}_m)$ versus temperature T showing crossover of conversions from fast athermal with delay tails to slow isothermal (intermediate) with $E_0 = 3$ for *Left:* fixed $T_c = 0.95$ and different A_1, $A_6 = A_1/2$; *Right:* fixed $A_1 = 4$, $A_6 = 2$ and various T_c.

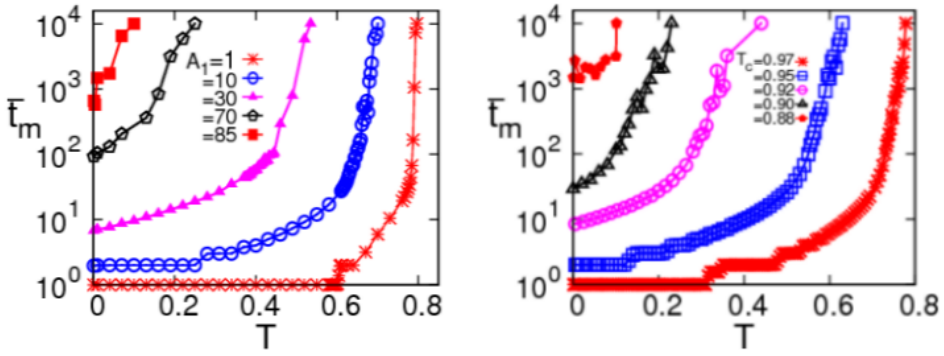

Figure 6.4: *Cubic-trigonal transition athermal/ isothermal crossover:* Plot of conversion times $log(\bar{t}_m)$ versus temperature T showing crossover from fast athermal with delay tails to slow isothermal with $E_0 = 3$ for *Left:* fixed $T_c = 0.97$ and different A_1, $A_2 = A_3 = A_1/2$; *Right:* fixed $A_1 = 4$, $A_2 = A_3 = 2$ and different T_c.

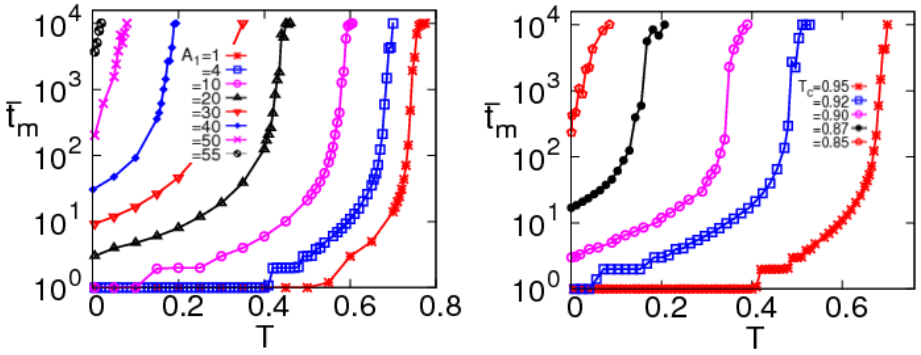

Figure 6.5: *Cubic-orthorhombic transition athermal/isothermal crossover:* Conversion times $log(\bar{t}_m)$ versus T showing crossover of conversions from fast athermal with delay tails to slow isothermal (intermediate) with $E_0 = 3$ for *Left:* fixed $T_c = 0.95$ and different A_1, $A_6 = A_1/2$; *Right:* fixed $A_1 = 4$, $A_6 = A_1/2$ and various T_c.

where $\bar{t}_m \sim 1$ MCS, that rise to $\bar{t}_m \sim 10$ MCS at $\tau = \tau_2$ to become divergent at a temperature $\tau = \tau_4$. So, in the athermal regime, there are conversion-delay tails as found by Kakeshita et al [9] and Klemradt et al [10]. The temperature separating explosive conversions from these tails could indeed has a spinodal character, as modelled by Planes et al [12] (but here from release of residual austenite droplets in martensite as in tetragonal-orthorhombic transition). And a time divergence at a temperature T_4 well before the Landau temperature T_0 might explain the absence of conversions even for long annealing, of Otsuka et al [14].

6.4 Athermal martensite regime

In Chapters 3 and 4, we find similar conversion-delays in athermal martensite regime in four 2D transitions and argued that their emergence could be from the dominant entropy barriers through (i) Vogel-Fulcher behaviour of delay times and their insensivity to Hamiltonian energy scales E_0; (ii) conversion fractions are also insensive to E_0; (iii) Log-normal distributions of rare-events.

In this Section, we focus on the athermal martensite parameter regime of four 3D transitions to find such dominant behaviour if occurs.

6.4.1 Conversion incubation times

The athermal regime conversion times in tetragonal-orthorhombic, cubic-tetragonal, cubic-trigonal, and cubic-orthorhombic transitions are shown in Figure 6.6: there are indications of Vogel-Fulcher behaviour near τ_4.

In experimental data in Ni-Al from Klemradt et al [10], the diagnostic for conversion is different (drop in specular reflection, rather than martensite fraction); the times t are defined differently (and are unaveraged, rather than

inverse of averaged rates); and temperature error bars are large. However a plot of $1/\ln t$ versus temperature T is found to be linear with negative slope, and extrapolation to zero defines a temperature $T_4 = 283$ Kelvin. Then with $\Delta T \equiv T - T_4$, the main Figure 6.7 shows the data, with time in seconds, plotted as an analogue of Figure 3.11. There is clearly a tendency in the main Figure 6.7 for times over two orders of magnitude to fall on a hyperbola, with a fall-off near a T_1-like temperature. The inset of Figure 6.7 shows the data near T_4 fall linearly, suggesting Vogel-Fulcher behaviour. The plots imply that data closer to transition be taken for this, and other athermal martensites, and be suitably averaged, to confirm Vogel Fulcher behaviour.

The linear behaviour in $1/\log(\bar{t}_m)$ versus $|\Delta\tau|/|\tau_1 - \tau_4|$ for different $E_0 = 3, 4, 5, 6$, suggesting the conversion times goes as $\bar{t}_m \sim e^{\{|\tau_1-\tau_4|/|\Delta\tau|\}}$ and are again insensive to E_0. The conversion times $\bar{t}_m$ are obtained for holding times $t_h = 10^4$ MCS. The t_h-dependent data can be extracted through finite-time scaling as $1/t_h \to 0$ as in Chapter 3, to confirm the Vogel-Fulcher behaviour of conversion-delay times.

Figure 6.8 shows the successful conversion fraction Φ_m over 100 runs versus $\Delta\tau \equiv \tau - \tau_4$ for all four transitions. The conversion fraction Φ_m falls from unity close to $\tau \sim \tau_2$ to become zero at $\tau = \tau_4$ and is insensitive to different $E_0 = 3, 4, 5, 6$.

We calculate probability distributions of conversion rates $P(r_m)$ following the same procedure of Scott bin size [49] as in Chapters 3 and 4. As shown in Figure 6.9, the histograms become sharp below $\tau \sim \tau_2$ to become delta-function-like peak in the right. The distributions are clearly non-gaussian. Compare with 2D transitions of Figure 3.13 (SR case) and Figure 4.8 (TCR,SO,TO cases).

In the athermal martensite regime, we find (i) Vogel-Fulcher behaviour of conversion-delays, that are insensitive to E_0; (ii) conversion fractions Φ_m are

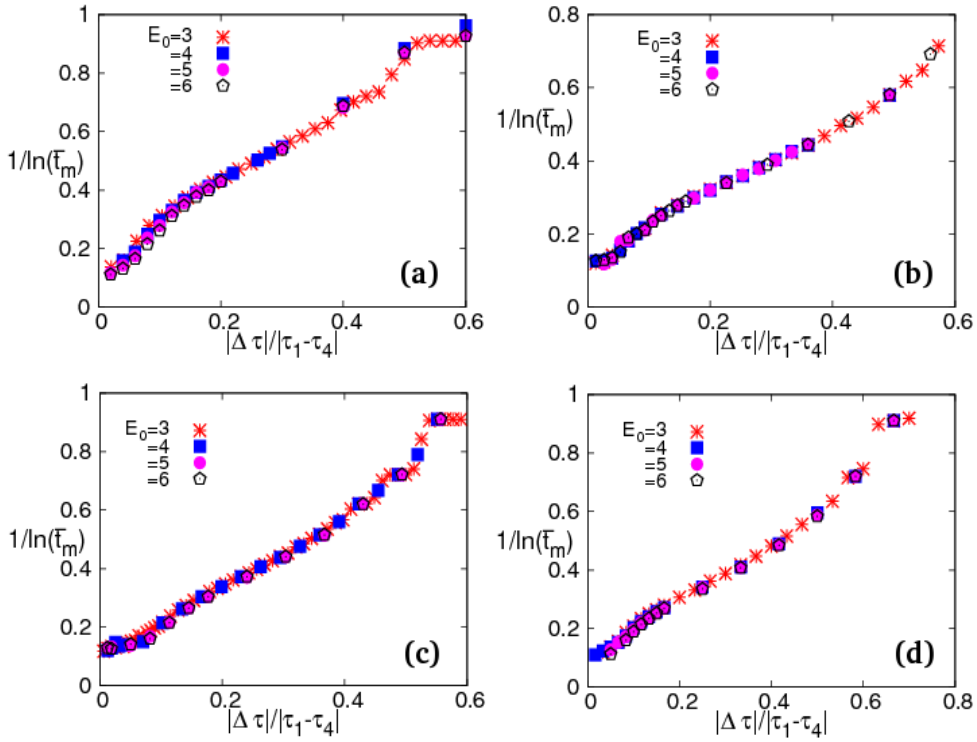

Figure 6.6: *Vogel-Fulcher singular behaviour of conversion delay times:* Plot of $1/\log(\bar{t}_m)$ versus $\Delta\tau \equiv \tau - \tau_4$ showing linearity, that is insensitive to different Hamiltonian energy scales $E_0 = 3, 4, 5, 6$ in (a) tetragonal-orthorhombic transition with $T_c = 0.95$, $A_1 = 4$, $A_3 = 2 (= A_4 = A_5 = A_6)$; (b) cubic-tetragonal transition with $T_c = 0.95$, $A_1 = 4$, $A_6 = 2$; (c) cubic-trigonal transition with $T_c = 0.97$, $A_1 = 4$, $A_2 = A_3 = 2$; (d) cubic-orthorhombic transition with $T_c = 0.95$, $A_1 = 4$, $A_6 = 2$.

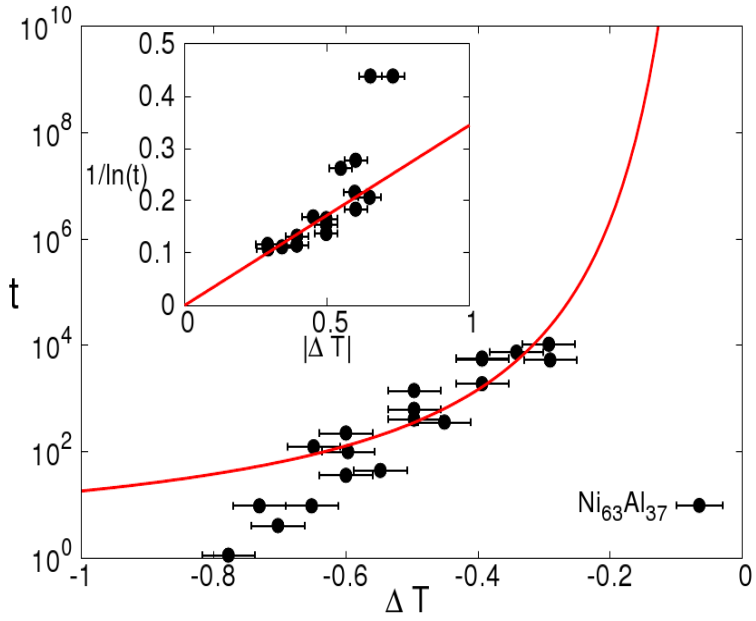

Figure 6.7: *Vogel-Fulcher-like behaviour in measured conversion-delay times:* Conversion times t from Klemradt et al [10] versus temperature T, through a plot of $\ln t$ versus $\Delta T \equiv T - T_4$, and a Vogel-Fulcher hyperbola as a guide to the eye. *Inset:* $1/\ln t$ versus $|\Delta T|$. Data near τ_4 fall on a line to the origin.

also insensitive to E_0; (iii) conversion rates show lognormal distributions as in four 2D transitions. So, we argue that the conversion-delays in athermal regime arise in searching for rare finite fraction pathways facing high entropy barriers on a partially equilibrated constant energy surface.

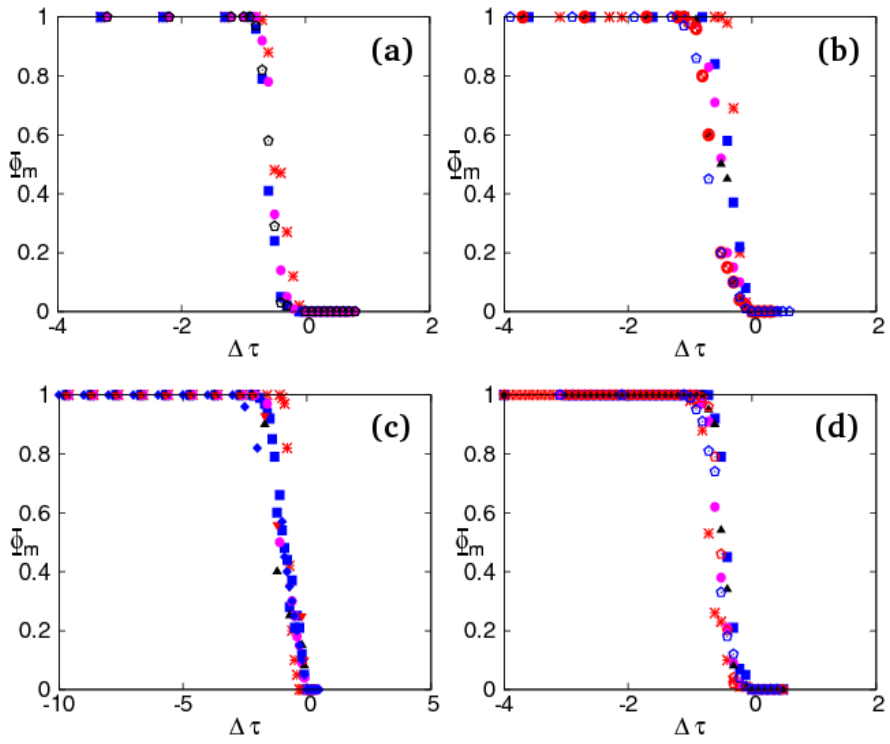

Figure 6.8: *Conversion fractions:* Plot of successful-conversion fraction Φ_m versus $\Delta\tau$ showing insensivity to different Hamiltonian energy scales $E_0 = 3, 4, 5, 6$ and $t_h = 10^4$ MCS in (a) tetragonal-orthorhombic transition with the material parameters of Figure 6.6 (a) ; (b) cubic-tetragonal transition with the parameters of Figure 6.6 (b); (c) cubic-trigonal transition with the parameters of Figure 6.6 (c); (d) cubic-orthorhombic with the parameters of Figure 6.6 (d).

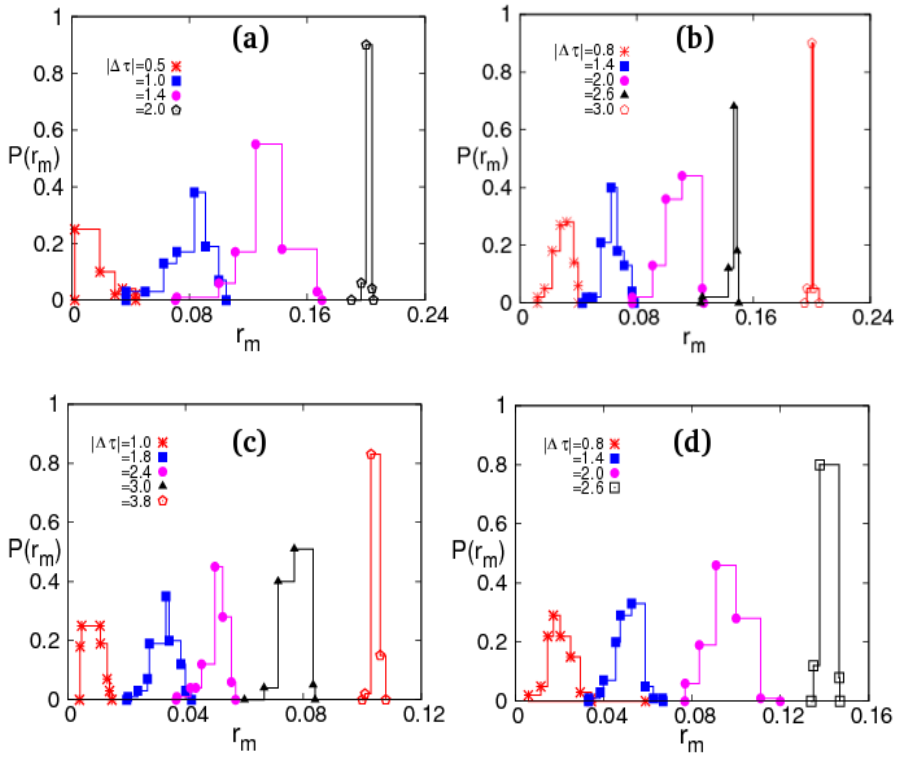

Figure 6.9: *Distribution of conversion rates:* Plot of conversion rate distributions $P(r_m)$ versus r_m for different temperatures τ and $E_0 = 3$. Log-normal distributions in (a) tetragonal-orthorhombic transition; (b) cubic-tetragonal transition; (c) cubic-trigonal transition; (d) cubic-orthorhombic transition. In each case that parameters are for the corresponding cases of Figure 6.6. Compare Figure 3.13 (SR case) and Figure 4.8 (TCR, SO, TO cases).

6.5 Microstructures

A variety of twinned microstructures in tetragonal-orthorhombic, cubic-tetragonal, cubic-trigonal, cubic-orthorhombic transitions from Monte Carlo temperature quench-and-hold simulations are shown in Figures 6.10, 6.11, 6.12, and 6.13 respectively and are oriented along diagonals. The preferred directions from vanishing of compatibility kernels for all four transitions are [1 1 0] and [1 -1 0].

The microstructures are monitored in terms of variant label V as discussed in Chapter 4. So, in the colorbar of Figures 6.11, 6.12, 6.13, $V = 0$ is austenite, and $V = 1, 2, 3$ for $N_V = 3$ variants in cubic-tetragonal, and $V = 1, 2, 3, 4$ for N_V variants in cubic-trigonal, and $v = 1, 2, ..6$ for $N_V = 6$ variants in cubic-orthorhombic transitions respectively.

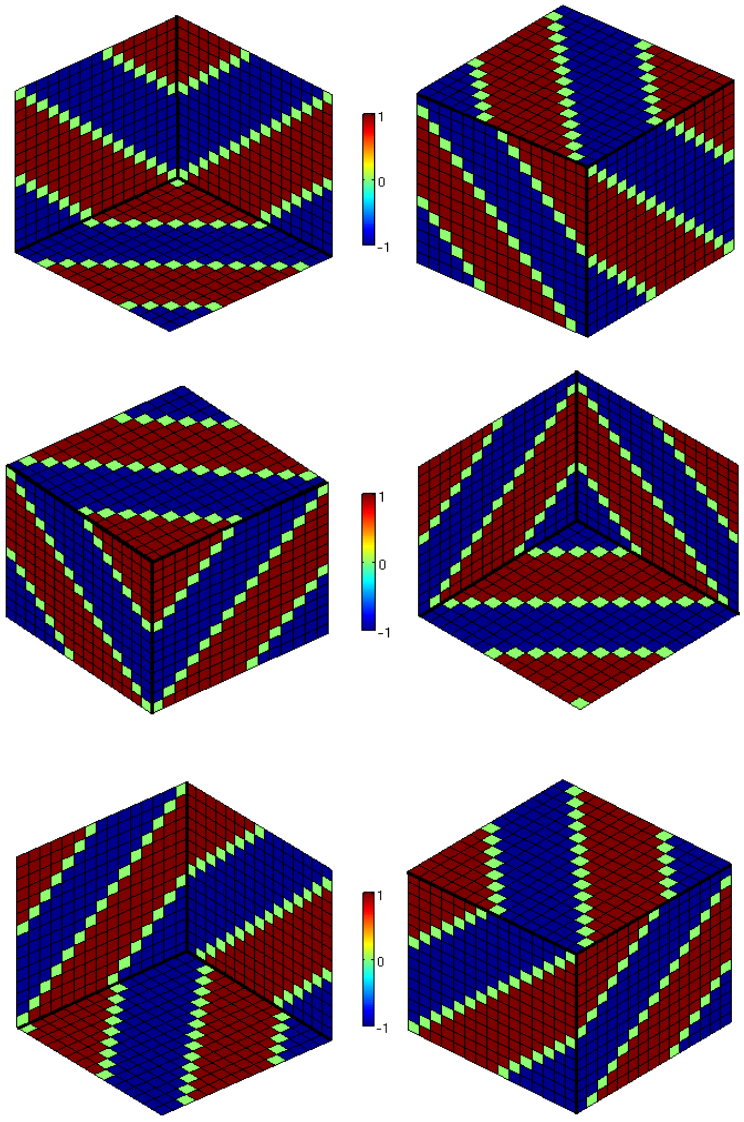

Figure 6.10: *Microstructures in tetragonal-orthorhombic transition:* Orientations of twins in OP strain (e_2) after a quench and holding at temperature $\tau = -4.5$. Parameters are $T_c = 0.9$, $A_1 = 4$, $A_3 = A_4 = A_5 = A_6 = 2$, $E_0 = 3$. Different runs give similar orientations. Colorbar represents the $OP = e_2$ values.

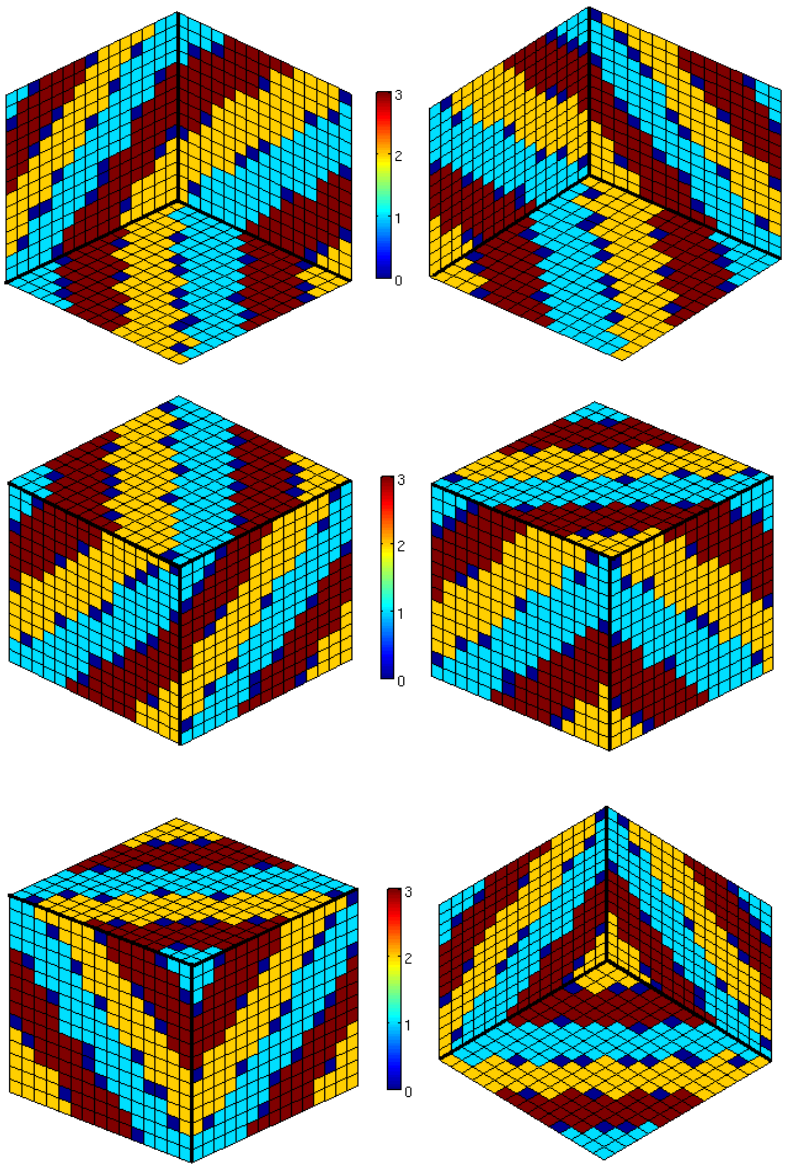

Figure 6.11: *Microstructures in cubic-tetragonal transition:* Orientations of twins in OP strain (e_3, e_2) after quench and hold at temperature $\tau = -14$. Parameters are $T_c = 0.95$, $A_1 = 4$, $A_6 = 2$, $E_0 = 3$. Different runs give similar orientations. Colorbar represents the variant label V. See text.

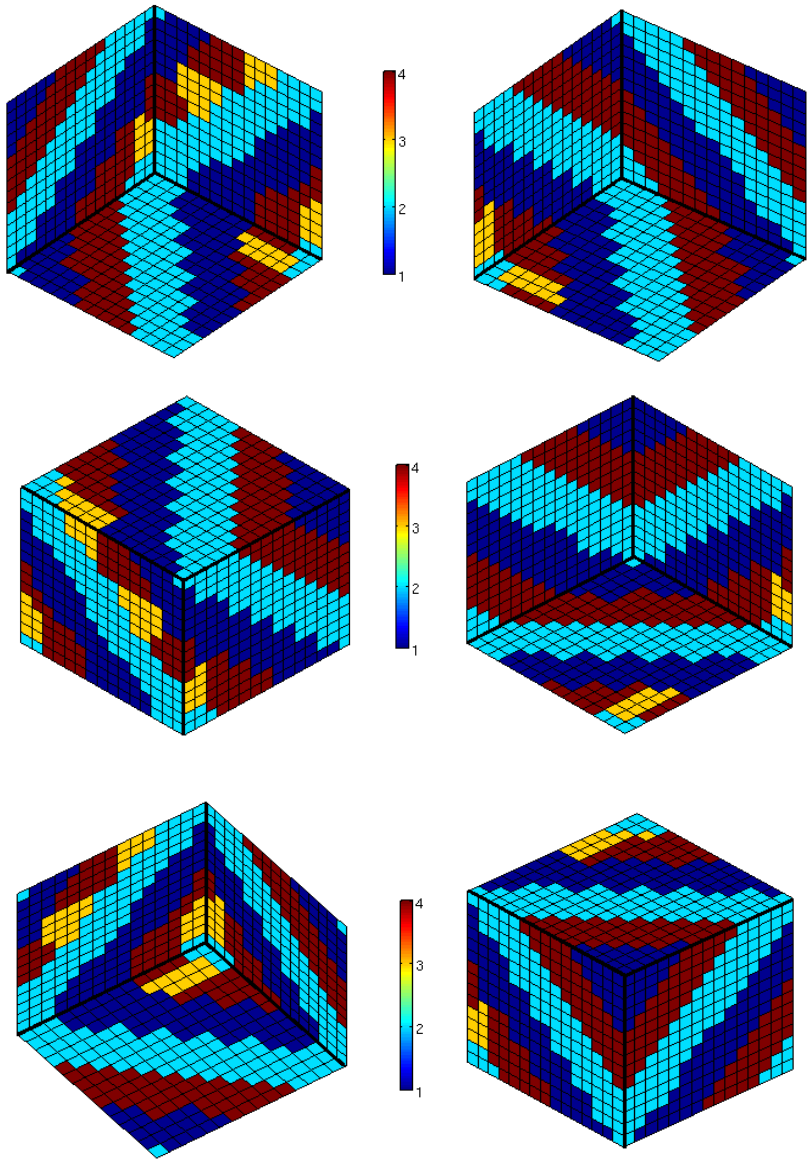

Figure 6.12: *Microstructures in cubic-trigonal transition:* Orientations of twins in OP strain (e_4, e_5, e_6) after quench and hold at temperature $\tau = -20$. Parameters are $T_c = 0.97$, $A_1 = 4$, $A_2 = A_3 = 2$, $E_0 = 3$. Different runs give similar orientations. Colorbar represents the variant label V. See text.

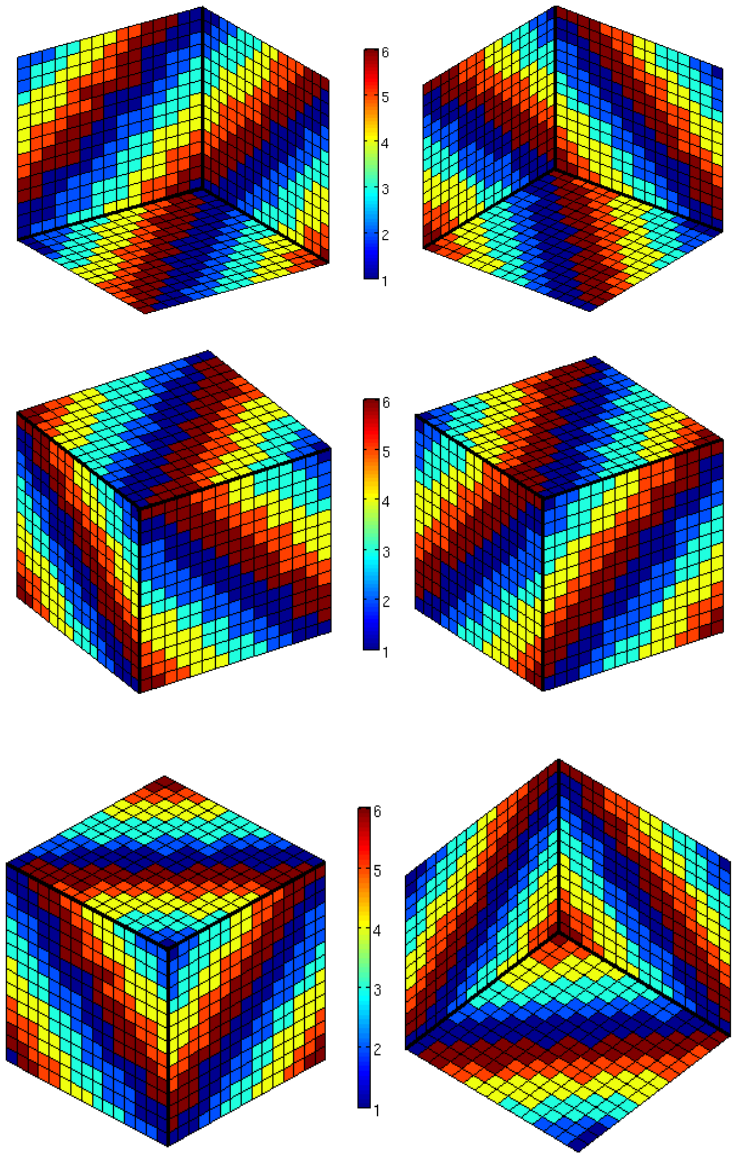

Figure 6.13: *Microstructures in cubic-orthorhombic transition:* Orientations of twins in OP strain (e_3, e_2) after quench and hold at temperature $\tau = -13$. Parameters are $T_c = 0.95$, $A_1 = 4$, $A_6 = 2$, $E_0 = 3$. Different runs give similar orientations. Colorbar represents the variant label V. See text.

6.6 Chapter summary

In this Chapter, we have presented the evaluation of strains and systematic temperature-quench Monte Carlo simulations without disorder on four strain-pseudospin 3D Hamiltonians: tetragonal-orthorhombic, cubic-tetragonal, cubic-trigonal, and cubic-orthorhombic transitions [57]. We summarize our results below.

- Scaled-OP and non-OP strains are calculated for different materials undergoing tetragonal-orthorhombic, cubic-tetragonal transitions and find that the scaled-OP strains are just the strain-pseudospins, from symmetries of the distortion matrices.
- We find both athermal and isothermal martensite regimes in all four transitions, for different material parameters T_c, A_1, A_3.
- The athermal TTT curves change to isothermal U-shaped curves on changing material parameters T_c, A_1, A_3.
- In the athermal martensite parameter regime, we reconcile the three different puzzling results as discussed in Chapter 1.
- In the athermal regime, conversion incubation times show Vogel-Fulcher divergences, that are insensitive to Hamiltonian energy scales E_0; and successful conversion fractions are also insensitive to E_0; and conversion rates show non-gaussian and possibly Log-normal distributions. This supports the idea of dominant entropy barriers.
- We find a variety of twinned microstructures, and orientations that are in good agreement with expectation in all four 3D transitions.

Question: Can we use these pseudospin models to understand the deeper issues in nonequilibrium aging systems ?

7

Re-equilibration after a temperature quench: search for Fourier-space golf holes

In this Chapter, we return to the simplest 3-state strain pseudospin model for square-rectangle (SR) transition, to get insights into re-equilibration process of aging systems after deep temperature quenches [57]. After quenching into different bath-temperature regions of the Temperature- Time- Transformation (TTT) diagram, we monitor evolutions in time of pseudospin structure-factor, energy-occupancy distributions, acceptance fractions, and energy-releases, towards the equilibrium state. The slow formation and

growth of martensite during conversion-incubation, and the ordering of disordered domain walls during orientation-incubation, are understood better in *Fourier space*, rather than coordinate space. We find that, after a temperature quench, the system behaves as 'temporarily microcanonical' or it is *partially equilibrated* on a *constant energy surface*, at a time-dependent *effective temperature*, that shows plateaus in its evolution through domain-wall phases 'vapour','liquid' and 'crystal'. In the TTT region where the conversion-incubation dominates, there is a domain wall vapour, that is partially equilibrated (PE) with almost same ($\sim$ zero) energy of austenite, evolves to a domain wall liquid that is partially equilibrated, and finally reach domain wall crystal that is equilibrated at the bath-temperature. In the TTT region where orientation-incubation dominates the total time, the domain-wall vapour rapidly goes to the domain-wall liquid, and shows fluctuations as the signatures of austenitic dynamical catalysts, to finally reach the domain-wall crystal at the bath-temperature. We describe the evolution of partial equilibration energy surfaces through the pseudospin structure-factor, and identify and parametrize explicit pathways that overcome the entropy barriers, and lower the energy.

We then present for 2D vector-OP cases similar distortions in Fourier space of the $\rho(\vec{k},t) = |\vec{S}(\vec{k},t)|^2$.

7.1 Strain pseudospin model

Although it was given earlier, we repeat the 3-state strain pseudospin model for SR structural transition [33] that involves a square unit cell of austenite spontaneously changing to a rectangle unit cell, along the two axes, variants of martensite. The model has pseudospins at unit-separation sites $\vec{r}$ of a lattice, with values $S = 0$ square unit cell or single austenite state, and $S = \pm 1$ for rectangle unit cells or two martensite variants. The uniform

austenite $S(\vec{r}) = 0$ (for all $\vec{r}$) has *zero* energy. The total hamiltonian is a sum of Landau, Ginzburg and St. Venant compatibility terms, $H \equiv \{H_L + H_G\} + H_C$ and in coordinate space is

$$H = \frac{K_0}{2}[\sum_{\vec{r}}\{g_L(\tau)S(\vec{r})^2 + \xi^2(\vec{\Delta}S)^2\} + \sum_{\vec{r},\vec{r'}}\frac{A_1}{2}U(\vec{r}-\vec{r'})S(\vec{r})S(\vec{r'})]. \quad (7.1)$$

The prefactor $K_0(T) \equiv 2E_0\bar{\varepsilon}^2(\tau)$. (In previous notation of Chapters 2 and 3, $D_0 = K_0/T$).The bath temperature T is related to the scaled temperature $\tau(T)$ by

$$T/T_0 = [1 - \tau/\tau_0](T_c/T_0), \quad (7.2)$$

and $\tau(T)$ is defined in (2.18) where τ_0 is defined as,

$$\tau_0 \equiv \tau(0) = \frac{-T_c}{(T_0 - T_c)}. \quad (7.3)$$

We will discuss the texturing in terms of T, instead of the previous τ. The strain magnitude $\bar{\varepsilon}(\tau)$ as defined in (2.18) is unity at transition $\bar{\varepsilon}(\tau = 1) = 1$; and g_L as defined in (2.18), is related to the Landau free energy density at minima $\bar{f}_L(\bar{\varepsilon})$, that is *negative* below the Landau transition $g_L(\tau = 1) = 0$, favouring $S^2 = 1$ martensite states.

With $S(\vec{r}) = \frac{1}{\sqrt{N}}\sum_{\vec{k}} S(\vec{k})e^{i\vec{k}.\vec{r}}$, $U(\vec{R}) = \frac{1}{N}\sum \vec{k}U(\vec{k})e^{i\vec{k}.\vec{r}}$ and periodic boundary conditions, the Hamiltonian is diagonal and *harmonic* in Fourier coefficients,

$$H = \frac{K_0}{2}\sum_{\vec{k}} \epsilon(\vec{k})|S(\vec{k})|^2; \quad (7.4a)$$

$$\epsilon(\vec{k}) \equiv \{g_L(\tau) + \xi^2\vec{K}^2\} + \frac{A_1}{2}U(\vec{k}). \quad (7.4b)$$

and $K_\mu = 2\sin(k_\mu/2); \mu = x, y$ on the grid of unit spacing. Note that since $g_L < 0$ below the Landau transition, and $U(\vec{k}) > 0$ is bounded, $\epsilon(\vec{k})$ can be *negative* for some regions in the Brillouin zone. The pseudospin structure-factor $|S(\vec{k})|^2$ can have *zero* (Hamiltonian) energies or $H = 0$, (the same as

austenite), corresponding to $S(\vec{r})$ textures where the positive and negative Hamiltonian terms cancel.

The Hamiltonian for SR case in (7.4), is similar in spirit of inhomogeneous oscillator models of Garriga and Ritort [24], but is not quite same. The coefficients $\epsilon(\vec{k})$ are like different spring constants at each point in the Brillouin zone, with squared spring extensions $|S(\vec{k})|^2$ and a dynamical constraint $\sum_{\vec{k}} |S(\vec{k})|^2 = \sum_{\vec{r}} S^2(\vec{r}) = N_m(t) \leq N$. Since $\epsilon(\vec{k})$ can be negative, *uniform* austenite, with all oscillators at rest and $|S(\vec{k})|^2 = 0$, is a nonequilibrium, high-energy state at low temperatures. Our initial state involves a weak $\sim 2\%$ oscillator displacement at $t = 0$. The kernel $U(\vec{k})$ of the power-law interactions is *anisotropic*, and is given in (2.47) of Chapter 2. The kernel vanishes along favoured $k_x = \pm k_y$ diagonal directions, as mentioned earlier in Chapters 2 and 3.

7.1.1 Temperature-Time-Transformation diagram

Systematic Monte Carlo (MC) temperature quench simulations on 3-state pseudospin model are discussed in Chapter 3. After a temperature quench, the evolution of domain wall phases and their kinetics are monitored and shown in a TTT phase diagram, that has crossover temperatures marking the change in dynamics of microstructural evolutions to their final states. The schematic of the TTT phase diagram is depicted again in Figure 7.1 (redrawn from Figure 3.15). The crossover temperatures in the TTT phase diagram are understood through the parametrization of complex textures through effective droplet energies in Section 3.5.3 of Chapter 3. The parametrization shows four Regions ④,③,②,① as shown in Figure 3.19, that are separated by the characteristic crossover temperatures T_4, T_3, T_2, T_1 of Figure 7.1.

To understand how system re-equilibrates after quenching into regions ④,②,① of Figure 7.1, we do MC pseudospin simulations on $d = 2, N =$

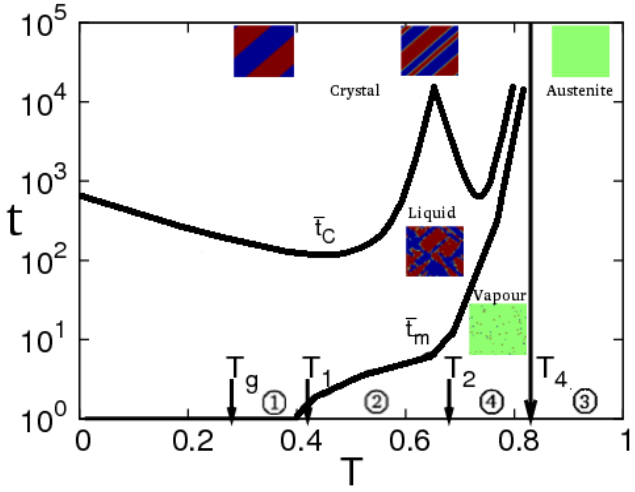

Figure 7.1: *Temperature-Time-Transformation:* Log-linear plots of conversion times $\bar{t}_m$ and orientation times $\bar{t}_C$ versus quench temperatures T for $A_1 = 4, T_c = 0.9, \xi^2 = 1, E_0 = 3, L = 64$. Pictures indicate the time-temperature regimes for domain-wall 'vapour' ($\bar{t}_m > t$), 'liquid' ($\bar{t}_C > t > \bar{t}_m$) and 'crystal' ($\bar{t}_C > t$). Quench regions are indicated: Region ④ with $T_4 > T > T_2$; Region ② with $T_2 > T > T_1$; and Region ① with $T_1 > T > T_g$. The temperature T_3 of tweed precursors just below Region ③ is not shown.

L^2 square lattice with 2% random seeds of both variants. Parameters are typically $T_0 = 1$; $T_c/T_0 = 0.9$, $\xi = 1$; $A_1 = 1, 4, 10$; $2A_1/A_3 = 1$; $L = 64$; $E_0 = 3, 4, 5, 6$; $t_h \leq 10,000$ sweeps, and conversion runs over $N_{runs} = 100$ different seeds. We work in the athermal regime of Figure 3.6.

Note that in austenite Region ③ the initial martensite seeds disappear, even though the bulk Landau free energy $f_L = \bar{\varepsilon}^2 g_L < 0$. A large initial slab of 50% single variant martensite converts, however to 100% martensite. For $T > T_0$, of course, the large initial martensite slab disappears, to give pure uniform austenite. So martensite is not forbidden in Region ③: it is just *inaccessible*, from a sparsely seeded initial state. There is a breaking of

ergodicity, in this sense.

7.1.2 Textural diagnostics

After a temperature quench, we monitor the microstructural evolutions in coordinate space and Fourier space. We define $\rho(\vec{k},t)$, a pseudospin dynamic structure-factor in Fourier space, describing martensite textures, with a martensite fraction normalization,

$$\rho(\vec{k},t) = |S(\vec{k},t)|^2; \quad \frac{1}{N}\sum_{\vec{k}} \rho(\vec{k},t) = n_m(t) < 1. \tag{7.5}$$

(Note this is not to be confused with the Hamiltonian ratio $\rho(s)$ of (4.8).)

We monitor the energy occupancy distribution $W(\epsilon,t)$ [22] and is defined [24] as,

$$W(\epsilon,t) = \frac{\sum_{\vec{k}} \delta_{\epsilon,\epsilon(\vec{k})}|S(\vec{k},t)|^2}{\sum_{\vec{k}}|S(\vec{k},t)|^2}; \tag{7.6a}$$

that by subtracting g_L from ϵ, $\epsilon(\vec{k})$ can be written as

$$W(\tilde{\epsilon},t) = \frac{\sum_{\vec{k}} \delta_{\tilde{\epsilon},\tilde{\epsilon}(\vec{k})}|S(\vec{k},t)|^2}{\sum_{\vec{k}}|S(\vec{k},t)|^2} \tag{7.6b}$$

Here, we define $\tilde{\epsilon}(\vec{k}) \equiv \epsilon(\vec{k}) - g_L(\tau) = \xi^2\vec{K}^2 + \frac{1}{2}A_1U(\vec{k}) > 0$, that depends on domain-wall costs alone.

We also calculate the distributions of energy releases (suitably binned [49]), averaged over runs $N_{runs} = 100$.

$$P(\Delta E,t) = \frac{1}{N_{runs}}\sum_{run=1}^{N_{run}} \Delta E(run,t) \tag{7.7}$$

where $\Delta E = E_{t+1} - E_t$; with MC-sweep label t. Thermodynamic functions, internal energy U_{ener} and entropy S_{entr}, obtained in meanfield approximation [33] as defined in Appendix A are monitored.

7.1.3 Golf holes and funnels

Protein configurations have a complex multivalley energy surface. The folding of proteins, if occuring through random searches, could take astronomically long times, as noted by Levinthal, representing the search by putting a ball into a *golf hole* with unfolded configurations outside, and folded configurations inside. The concept of a guiding *funnel* around the golf hole was introduced to understand the rapid folding [19, 20].

We now analyze the model, drawing on previous work, in particular Bicout and Szabo [20], and Nakagawa [22] (protein folding); and Garriga and Ritort [24] (inhomogeneous harmonic oscillators). The schematic of Figure 7.2 shows a golf hole and funnel, as in models of protein folding [19, 20].

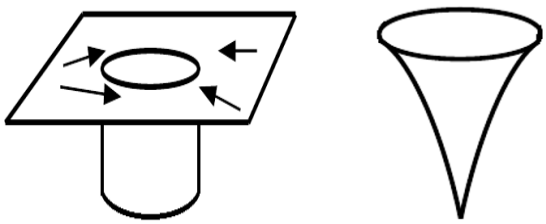

Figure 7.2: *Golf hole and funnel:* Left: Flat surroundings, no funnel. Right: Linear guiding funnel inside the golf hole.

Figure 7.3 shows the (temperature dependent) prefactor $\epsilon(\vec{k})$ in the Brillouin zone with a flat surface at the zero of energy: with $\epsilon(\vec{k}) = 0$ defining the golf hole edge in $\vec{k}$ space. Energies greater than uniform austenite are outside, and lower than austenite are inside the golf hole. The butterfly-like anisotropy reflects the fourfold symmetry of the austenite structure, imbedded in the St.Venant term. The golf hole edge is then

$$\epsilon(\vec{k}) \equiv \{g_L(\tau) + \xi^2 \vec{K}(\vec{k})^2\} + \frac{A_1}{2} U(\vec{k}) = 0, \tag{7.8}$$

in an implicit equation for $\vec{k}$. Note that martensite textures with zero en-

ergy are *degenerate with austenite* with the positive surface term cancelling the negative bulk term. This correspond to the effective droplet energy parameter of Chapter 3 flowing to $R(t) \sim 0$. In a long-wavelength estimate $k^2 \simeq (|g_L| - (A_1/2)\cos^2 2\theta)/\xi^2$, that interpolates between an inner circle of radius $k_< = \sqrt{|g_L|/\xi^2}$ and an outer circle of radius $k_> = \sqrt{(|g_L| - A_1/2)/\xi^2}$. For $A_1 = 0$ (as in Section 3.8), there is a circular golf hole of only one radius $k_< = k_>$. At the Landau transition, $g_L(\tau_L = 1) = 0$, $\epsilon(\vec{k})$ is positive, and there is no golf hole.

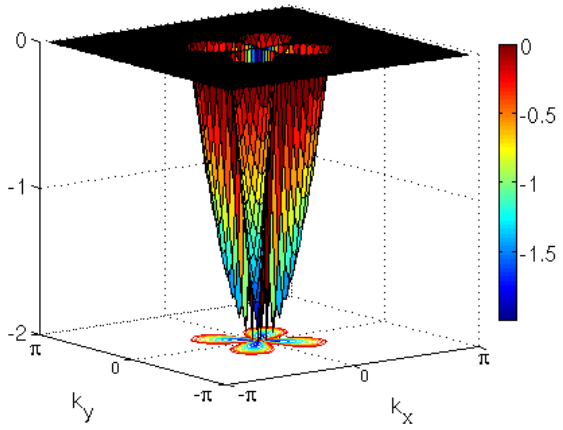

Figure 7.3: *SR case golf hole and funnel in Brillouin zone:* Relief plot of $\epsilon(\vec{k})$ versus $\vec{k}$ for $T = 0.76$, showing golf hole edge and negative-energy anisotropic funnel below austenite energy plane $\epsilon(\vec{k}) = 0$.

Figure 7.4 shows the temperature-dependent golf holes can be *small* near T_4 and hence hard (or impossible) to find, with *slow* conversions; and *large* covering most of the Brillouin zone and easy to find, for *explosive* conversions below T_1. Thus, in the TTT phase diagram of Figure 7.1, the fast or slow conversion times $\bar{t}_m$ can be understood in terms of large or small golf holes in Fourier space. Note that the infinite conversion times occur even before the golf hole closes to zero; and the virtually-zero conversion times occur even

before the golf hole expands to cover the whole Brillouin zone.

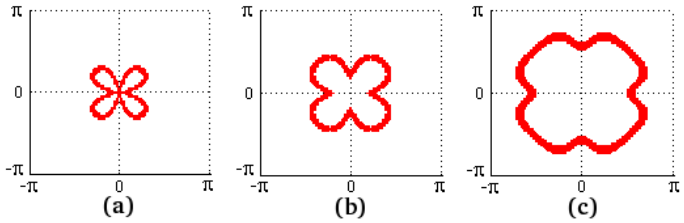

Figure 7.4: *Temperature-dependent golf holes:* Contour plots of golf hole boundary $\epsilon(\vec{k}) = 0$ in (k_x, k_y) Brillouin zone for different quench temperatures (a) $T = 0.76$ in Region ④; (b) $T = 0.55$ in Region ②; and (c) $T = 0.4$ in Region ① of Figure 7.1.

Re-equilibration from a random initial state after a quench below transition, involves not just an internal energy reduction, but also an *entropy* reduction to that of the final ordered state as in protein folding [20]. As noted in Section 3.2, in configuration space, the initial disordered configuration must find its way to the ordered final state by surmounting the intervening configurational free energy barriers $\{\Delta F = \Delta U_{ener} - T\Delta S_{entr}\}$, at rates $\{r \sim e^{-\Delta F/T}\}$. For deep quenches to temperatures T much less than the hamiltonian energy scale E_0, the energy barriers $\Delta U_{ener} \sim E_0$ are insurmountable, and activated rates are negligible $r \sim e^{-E_0/T} << 1$. The configuration must seek out pathways without energy barriers $\Delta U_{ener} \simeq 0$ to reach lower energy and entropy states, at non-activated rates controlled by entropy barriers $\{r \sim e^{\Delta S_{entr}} = e^{-|\Delta S_{entr}|}\}$, that dominate for deep temperature quenches. Delays from entropy barriers $|\Delta S_{entr}|$ can be understood through the repeated attempts required in general to roll a ball into a golf hole, or to thread a needle. There is nothing blocking the trajectories: it is just that there are many ways of failing, and only a few of succeeding. The entropy barrier is the (modulus of) the logarithm of the ratio of successful

pathways to total configurations: it is large or small, for rare or common pathways, respectively.

Note that the conversion and orientation of domain wall textures correspond to changes in *function* $\rho(\vec{k},t)$, and not movement of points [20] at a single $\vec{k}$ in the Brillouin zone. The entropy barriers thus correspond to delays in $\rho(\vec{k},t)$ finding networks of *deformation pathways*, when restricted to energy changes that are either zero, or negative. The search for such rare pathways is an *entropy barrier* delay. When there is a pinch-off of a pathway, the entropy barriers for that pathway is infinite, and the success-fraction Φ_m of conversions starts falling from its low temperature, $T < T_2$ of unity ($\Phi_m = 1$) to its high-temperature value at $T = T_4$, of zero ($\Phi_m = 0$).

7.1.4 Re-equilibration process in Fourier space

We want to describe the martensitic evolutions in terms of distortion of the distribution, or pseudospin dynamic structure-factor $\rho(\vec{k},t) = |S(\vec{k},t)|^2$. The distribution deforms and narrows to match the golf hole for $T \lesssim T_4$ (slow conversion-incubations) followed by a rapid roll-in. For large golf holes, of Figure 7.4 at $T < T_1$, the distribution is already smaller than the golf hole, and the roll-in is rapid (explosive conversions).

A. Microstructural evolutions in Region ④

The initial 2% of randomly located, martensite seeds of both signs $S = \pm 1$, and hence 'neutral', overall. With $n_m \equiv n_+ + n_-$, the normalized imbalance $(n_+ - n_-)/(n_+ + n_-)$ of Figure 3.24 rises from zero to nearly unity, showing the seeds induce the formation of a *single*-variant droplet, that persists for an incubation time t_m, and then falls to zero on autocatalytic twinning to equal, almost 'neutral' variants. The 'flat' martensite fraction during incubation is seen on closer inspection to have a rise that is jerky [30, 36, 54]

in Figure 3.24, reflecting the jerky droplet expansions of the Figure 7.5 snapshots below.

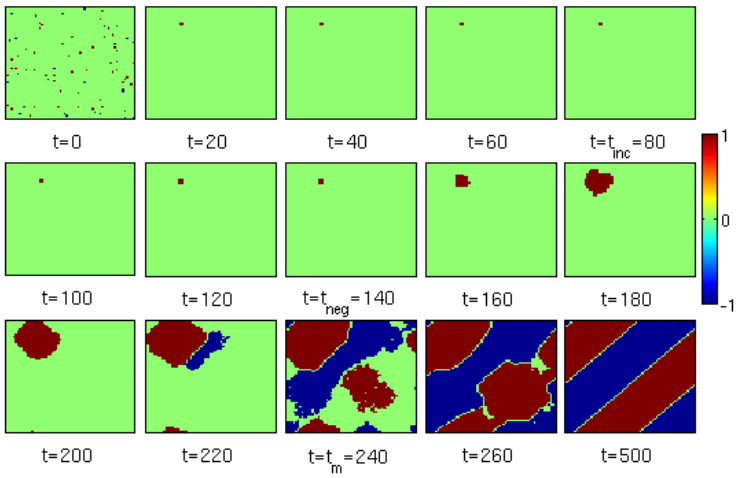

Figure 7.5: *Region ④: Evolution of a droplet in coordinate space:* Snapshots for a fixed temperature $T = 0.76$ and various times, showing the initial 2% random unit-cell seeds of both signs form a single-subcritical droplet of a domain-wall 'vapour', at a time $t = t_{start} \sim 20$. This fluctuates over long times, to find the energy-lowering path, to a domain-wall 'liquid' of both variants at $t = t_m$. The liquid orders and orients to a domain-wall crystal at time $t = t_C$. See text.

Figure 7.5 shows further details of this conversion process as in coordinate space snapshots versus time (shown previously in briefer form, in Figure 3.25.). The initial 2% of random martensite variant seeds at $t = 0$ quickly form at $t = t_{start}$ a single-variant, fluctuating droplet (entropy decreases, but energy increases), whose size depends on the quenched temperature, and whose energy is close to that of zero-energy austenite. After an incubation $t = t_{inc} = 80$, the single variant droplet expands through jerky fluctuations till $t = t_{neg} = 140$ or cooperative nucleation [37] to a size where it gener-

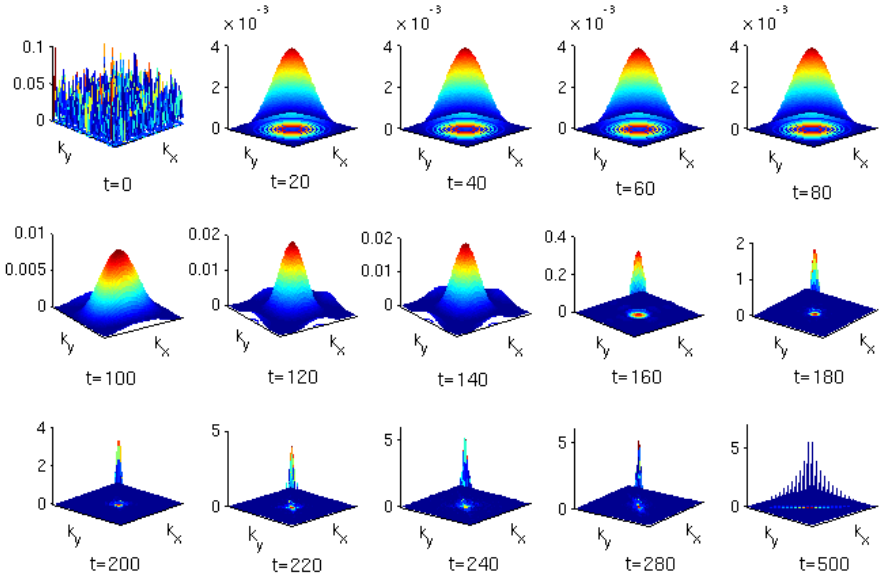

Figure 7.6: *Region ④: Evolution of PE surfaces in Fourier space:* Relief plot snapshots of Fourier coefficients $ln[1 + |S(\vec{k}, t)|^2]$ in the Brillouin zone for fixed temperature $T = 0.76$ and various times, corresponding to the coordinate space textures of Figure 7.5. Note the isotropic gaussian of the 'vapour' phase searches at zero energy $H = 0$, for the onset at $t = t_{incub}$ of anisotropic wings before it goes quickly at $t = t_{neg}$ into the golf hole X-shaped PE surface of the 'liquid' at $t = t_m = 240$. This orients at $t = t_C = 350$ into the single-diagonal inverted fan of the 'crystal'. See text.

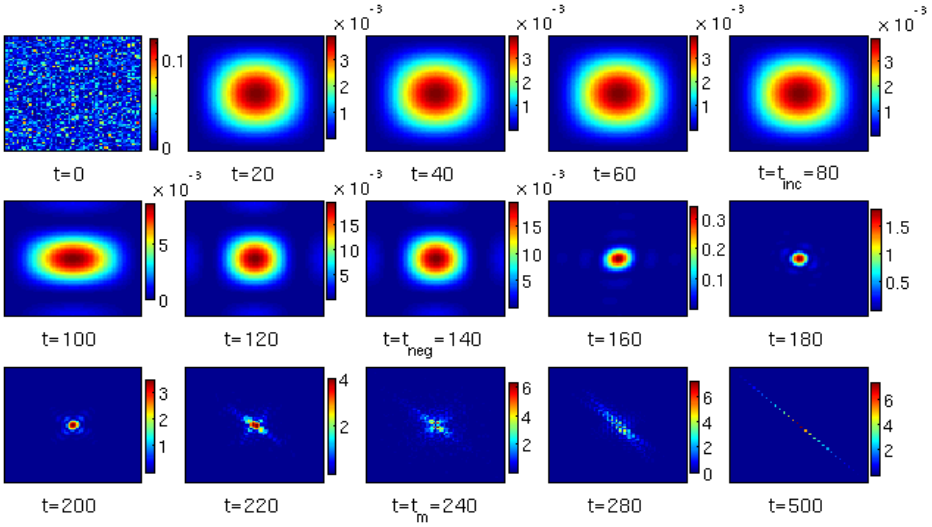

Figure 7.7: *Region ④: Evolution of PE surfaces in Fourier space:* Contour plot version of snapshots Fourier coefficients $ln[1 + |S(\vec{k}, t)|^2]$ of Figure 7.6. Clearly, the three domain wall phases: vapour, liquid, crystal correspond to three PE surfaces: isotropic gaussian (e.g $t = 20$), X-shaped (e.g $t = 240$), single diagonal or fan-shaped (e.g $t = 500$).

ates its *opposite* variant to lower the energy, in a cyclic, autocatalytic, and expanding process. This results, beyond $t = t_m = 240$ in a soup of a disordered domain-wall 'liquid'. At a later time $t = t_C = 500$, the disordered and bidiagonal domain walls orient into a monodiagonal domain wall 'crystal', that has bound austenite droplets, as the temperature is in Region ④. Thus our martensite formation scenario is: random seeds → single-variant 'self-organized' droplet → search delays → autocatalytic twinning → ordered twins.

The $H = 0$ droplet has the energy parameter as $R(t) \simeq 0$, on the left branch of the parabola of Figure 3.19. The self-organized droplet is critical in an *entropy* barrier sense (This is distinct from a droplet at $R(t) \sim 1$, top of the parabola, that is critical in an energy barrier sense.).

Figure 7.6 is the Fourier-space version of Figure 7.5 and the same times. This relief plot shows that for a given run in Region ④ of Figure 7.1, the structure-factor $\rho(\vec{k}, t) = |S(\vec{k}, t)|^2$ in the vapour phase remains for a time $t = t_{inc} = 80$ on an *isotropic* gaussian peaked over the anisotropic golf hole. This distribution is a Fourier space *partial equilibration surface*. After a search delay up to some $t = t_{inc} \simeq 0.3t_m$ corresponding to the incubating droplet of Figure 7.5, a weak, *anisotropic* modulation develops with peaking at the k_x, k_y axes at the Brillouin zone edge. This is *counter* to the diagonal $k_x = \pm k_y$ diagonals of the butterfly shaped golf hole. Thereafter the now-anisotropic peak narrows and rises, at some $t = t_{neg} \simeq 0.6t_m$. There is then rapid roll-down into the golf hole with area $n_m(t)$ under the curve increasing in the liquid phase. There is then a reorientation to a bidiagonal X shape matching the golf hole shape at $t = t_m = 240$, with the anisotropy corresponding to autocatalytic twinning of Figure 7.5. Finally, $\rho(\vec{k}, t)$ evolves to a symmetry-breaking shape of a inverted fan-like, single diagonal ('\' or '/'), crystal phase at $t = t_C = 350$ or twins of Figure 7.5. The diagonal spiking from a fitting to the data is, $\rho(\vec{k}) \sim 1/K_{\pm}^2$, where $K_{\pm} = (K_x + K_y)/\sqrt{2}$. Figure 7.7 is contour

plot version of the Figure 7.6, showing three partial equilibration surfaces (isotropic gaussian, bidiagonal, and single diagonal) corresponding to three domain wall phases, and the sequential deformation mentioned above. See movie in attached CD, of Figures 7.5 and 7.7.

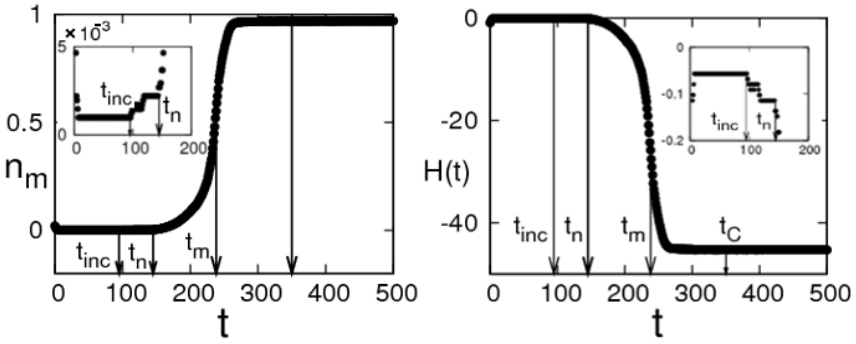

Figure 7.8: *Region ④: Evolution of macro variables: Left:* martensite conversion fraction $n_m(t)$ versus time t; and *Right:* Hamiltonian energy H versus t, showing flat-incubation. The times t_{incub}, t_{neg}, t_m and t_C for $T = 0.76$ are marked. *Insets:* There is a step-like jerkiness [36] in both n_m and H between t_{incub} and t_{neg} in searching for the golf hole edge.

Figure 7.8 shows the martensite fraction $n_m(t)$ and Hamiltonian energy $H(\tau)$ versus time t, with marked times $t = t_{incub} \sim 0.3t_m$ (where the $H = 0$ isotropic gaussian develops wings); $t = t_{neg} \sim 0.6t_m$ (where H goes negative); $t = t_m$ (where n_m rises to 0.5); and $t = t_C$ (where the orientation parameter n_C rises to 0.99).

B. Microstructural evolutions in Region ②

After quenching into Region ② of Figure 7.1, the initial 2% of martensite seeds of domain wall vapour goes rapidly into a disordered bidiagonal domain wall liquid in $t = t_m \simeq 10$ MC sweeps.

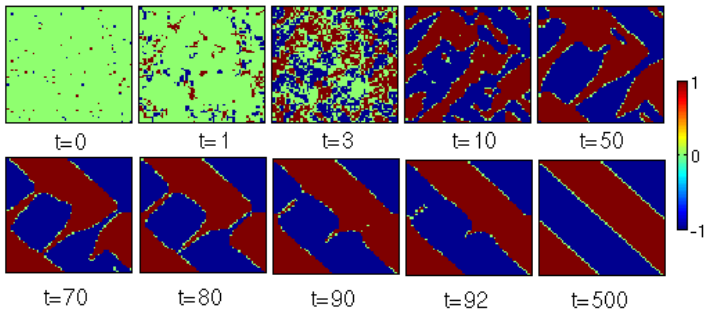

Figure 7.9: *Region ②: Evolution of textures in coordinate space:* Snapshots for a fixed temperature $T = 0.55$ and various times, showing the initial 2% random unit-cell seeds of both signs form domain wall liquid at a time $t = t_m \simeq 10$. This orders at an an orientation time $t = t_C = 500$ to a domain-wall crystal. Note the catalytic role of austenite droplets, from the pre-quench bulk, that survives as bound states on the domain walls.

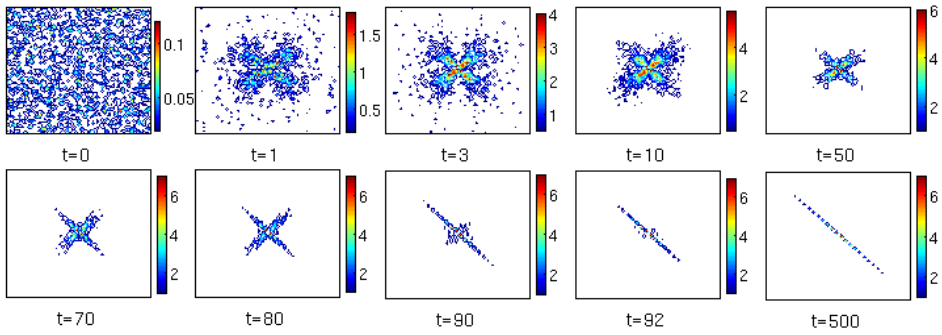

Figure 7.10: *Region ②: Evolution of PE surfaces in Fourier space:* Colour contour plot of Fourier coefficients $ln[1 + |S(\vec{k}, t)|^2]$ in the Brillouin zone for fixed temperature $T = 0.55$ and various times, corresponding to the coordinate space textures of Figure 7.9. Note the vapour phase quickly forms the X-shaped PE surface of the liquid at $t = t_m = 10$. This incubates up to $t \sim 92$ and finally orients at $t = t_C = 500$ into the single-diagonal fan of the crystal.

The austenite droplets $\{S(\vec{r}) = 0\}$, that are from the pre-quench bulk austenite, act as abundant and pre-existing catalysts, in ordering the disordered domain walls into a single monodiagonal domain wall crystal (with bound austenite), at a later orientation time $t = t_C$. The martensite growth and orientation in coordinate space is shown in Figure 7.9.

The microstructural evolutions in coordinate space are also monitored in Fourier space. Figure 7.10 shows the structure-factor version of Figure 7.9. The uniform distrbution at time $t = 0$ is spread over the Brillouin zone, rapidly starts getting X-shaped, (that is broader than the Figure 7.7 of Region ④). At later times, the X-shaped distribution becomes sharp (as the austenite acts catalytically). Finally, the X-shaped distribution becomes a single diagonal ('\' or '/') with inverted fan-like peak falloff shaped in the crystal phase. See movie in attached CD of Figures 7.9 and 7.10.

C. Microstructural evolutions in Region ①

After a quench and hold into Region ①, the initial 2% of martensite seeds explosively form a disordered domain wall liquid at a time $t = t_m \simeq$ 1 MC sweep. Figure 7.11, shows the frozen domain wall liquid waits for austenitic hotspots or dynamical catalysts, that can *spontaneously generate* to reduce high local stresses as shown in Figure 3.27. Once the dynamical catalysts or high-temperature austenite droplets $\{S(\vec{r}) = 0\}$ appear, the domain walls start orienting. The appearance of austenite droplets at one region can affect the other regions, as there are powerlaw interactions. This stochastic process continues, until the disordered domain walls orient into a monodiagonal domain wall crystal, that has *no* bound austenite spots. Figure 7.12 shows the structure-factor $|S(\vec{k}, t)|^2$ is uniform at $t = 0$, that explosively changes to a broad X-shaped PE surface. The X-shaped PE surface becomes sharp, that then remains so for a long time. The frozen X-shaped PE surface changes (as the austenitic hot spots, or dynamical-

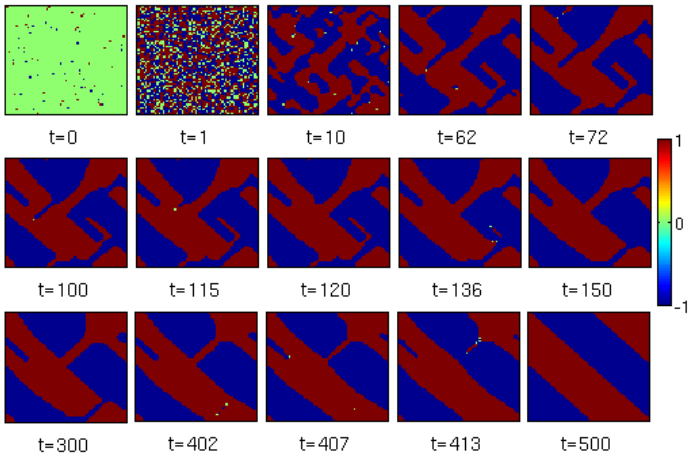

Figure 7.11: *Region ①: Evolution of a textures in coordinate space:* Snapshots for a fixed temperature $T = 0.4$ and various times. See Figure 3.27.

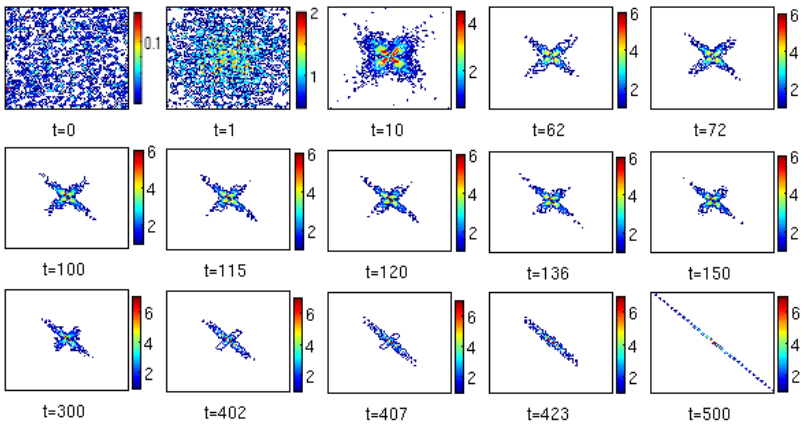

Figure 7.12: *Region ①: Evolution of PE surfaces in Fourier space:* Contour plot of Fourier coefficients $ln[1 + |S(\vec{k}, t)|^2]$ in the Brillouin zone for fixed temperature $T = 0.4$ and various times, corresponding to the coordinate space textures of Figure 7.11. Note the vapour phase quickly forms the X-shaped partial equilibration surface of the liquid at $t = t_m = 10$. This incubates to orient at $t = t_C = 500$ into the single-diagonal fan of the crystal.

catalysts appear), to become fan-shaped peaks on a single diagonal of the domain wall crystal. See movie in attached CD, of Figure 7.11, 7.12.

7.1.5 Acceptance fractions and energy releases

Figure 7.13 shows the Monte Carlo flip-acceptance fractions $A(t)$ versus time t for the three temperatures in the three Regions ④,②,①. In Region ④, $A(t)$ is nearly zero during conversion-incubation delays, with acceptance spiking at conversion and orientation times t_m, t_C, and falling again to zero, in the domain wall crystal phase. In Region ②, $A(t)$ is high initially, accepting most of the flips in the vapour phase, and decreases when the domain wall liquid phase is reached. The acceptance fraction then slowly increases as the austenite droplets, (that remain from the mostly-austenitic pre-quench state) act as dynamical catalysts to orient the disordered domain walls (and remain bound then) in the crystal phase. Sometimes, there can be a second peak in $A(t)$ before $t = t_C$, where austenite droplets are generated to fill the gaps of the bound austenite on the domain walls. Again, in the crystal phase $A(t)$ is zero. Finally, in Region ① , $A(t)$ is again high as the initial 2% martensite droplets of vapour become a disordered liquid very rapidly. It remains almost constant (with strong fluctuations as signatures of catalyst appearances), in the frozen domain wall liquid phase. Then there is a peak in $A(t)$, as a large number of austenite droplets are generated to orient the domain walls. Finally, it is again zero in domain wall crystal phase.

The probability distributions of energy releases $P(\Delta E, t)$ of (7.7) for various times from MC simulation are shown in Figure 7.14, that reflect the microstructural evolutions and acceptance fractions in Regions ④,②,①. The distributions are obtained by averaging over $N_{runs} = 100$. In Region ④, $P(\Delta E, t)$ is large for early times, but restricted to a small-sized window of negative ΔE, reflecting the conversion-incubations. The asymmetric distri-

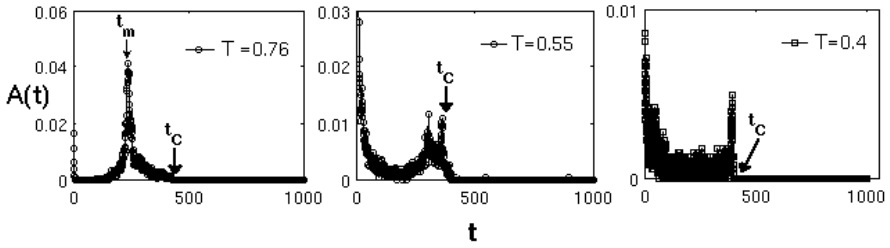

Figure 7.13: *Acceptance fractions:* Plots of (low) acceptance fraction $A(t)$ versus t for three temperatures $T = 0.76, 0.55, 0.4$ in Regions ④,②,① respectively of Figure 7.1, showing spikes at conversion times t_m, and at orientation times t_C.

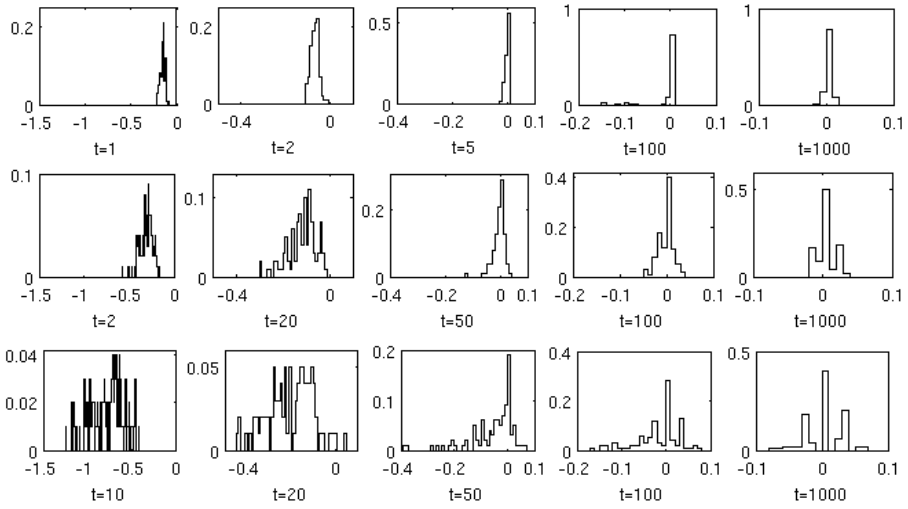

Figure 7.14: *Evolution of energy release distributions :* Plot of $\ln P(\Delta E, t)$ versus ΔE for various times for quench into the three different temperatures in Regions ④,②,① of Figure 7.1 and holding times $t_h = 10^3$. *Top row:* $T = 0.76$ in Region ④. *Middle row:* $T = 0.55$ in Region ②. *Bottom row:* $T = 0.4$ in Region ①. Note the peaking in all cases at negative energy changes of the system (heat releases), evolving to distributions more symmetric around zero, on equilibration.

bution increases sharply as the ΔE window moves down to zero, and finally becomes a symmetric, sharp distribution, peaked around zero.

In Region ②, $P(\Delta E, t)$ is moderate in medium-sized $\Delta E < 0$ window for initial times. At later times, the asymmetric distribution, that has linear tail on the left, rises as the ΔE window moves towards zero. Finally, the linear tail in the distribution vanishes, leaving a symmetric distribution peaked around zero.

In Region ①, $P(\Delta E, t)$ is small, but over a large $\Delta E < 0$ window, as there are explosive conversions for initial times. The distribution again has a linear tail for $\Delta E < 0$, that can persist during waiting of the frozen domain wall liquid for dynamical catalysts. Finally, a symmetric distribution is reached, as the dynamical catalysts are spontaneously generated to orient the domain walls by relieving the trapped local stresses. If the lifetime, or probabilities of the dynamical catalysts vanishes [33], the linear tail in the distribution may remain forever in the glassy phase. In harmonic oscillator models [24], the tails of energy release distributions are used to understand the holding time-dependent *effective temperature* in the aging regime. This cannot be extracted so easily in our model.

7.1.6 Occupancy distributions

We now turn to re-equilibration after a temperature quench to T of the occupancy distributions $W(\tilde{\epsilon}, t)$ of spring-like coupling constants $\tilde{\epsilon}(\vec{k})$, defined in (7.4b). Since the domain walls are sparse, and discrete, the energies are also discrete. Since coupling can be negative inside the golf hole, we define a coupling $\tilde{\epsilon}(\vec{k})$ measured from uniform martensite value of g_L as in the coupling occupancy distribution $W(\tilde{\epsilon}, t)$ is defined in (7.6b) that is just a shift of (7.6a) (to enable log-log plots to be taken).

After equilibration till the holding times $t = t_h$, simulations yields the

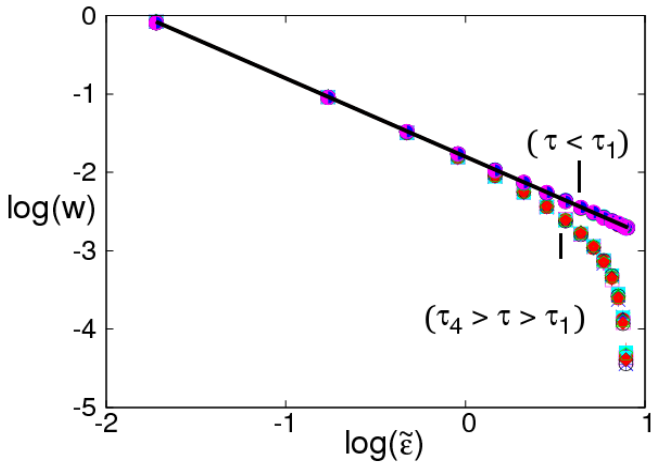

Figure 7.15: *Equilibrium coupling occupancy distributions:* Plot of $log(W(\tilde{\epsilon},t))$ versus $log(\tilde{\epsilon})$ where T is the equilibrium temperature, after long-time equilibration to domain-wall crystal, showing equilibrium $1/\tilde{\epsilon}$ behaviour. Again different energy scales $E_0 = 3, 4, 5, 6$ are shown. Solid line is a straight line $y = mx + c$ with $m = -1.0$ and $c \simeq -1.8$, is fit to the data

result that the final energy occupancies are a power law with exponent equal to unity.

$$W(\tilde{\epsilon},t;T) \to \frac{1}{\tilde{\epsilon}} \quad (t > t_C). \tag{7.9}$$

This is seen in Figure 7.15 for various Hamiltonian energy scales E_0 and anisotropic stiffness constants A_1 and different temperatures in Regions ④,②,①. The energy has an intrinsic upper cut offs $\tilde{\epsilon}(\vec{k}) < Max(8\xi^2, 4\xi^2 + \frac{A_1}{2})$, that for $\xi^2 = 1$, $A_1 = 4$, is $\log(\tilde{\epsilon}(\vec{k})) \lesssim 0.91$.

Figure 7.16 shows the evolution of the *single-run* post-quench nonequilibrium distribution $W(\epsilon,t)$ versus $\epsilon(\vec{k})$, as a histogram with the arrow marking the $\epsilon(\vec{k}) = 0$ surface outside the golf hole. The occupancy distribution reflects the flat incubation in martensite fraction $n_m(t)$ as seen in Figure 3.13 as well as in Figures 7.5, 7.6. The initial flat distribution changes at $t = 10$,

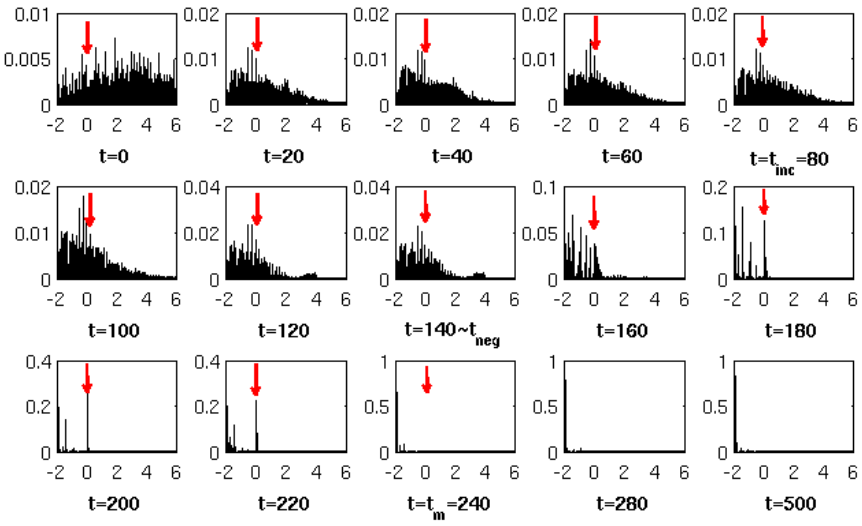

Figure 7.16: *Time evolution of energy occupancy distributions, single run :* Plots of $log(W(\epsilon,t))$ vurses $log(\epsilon)$ for quench into $\tau_4 > \tau > \tau_2$ for a single run, and various times as in Figure 7.15. Note the appearance of a peak at large energies, on the formation of the fluctuating entropically critical droplet.

that corresponds to a single variant droplet as seen in Figure 7.5 or isotropic gaussian distribution in Figure 7.6. During the incubation, there is no change in the distribution a fixed powerlaw-like tail, up to $t = t_{inc} = 80$, after which there is a change in height. A peak appears at $t = t_{neg} = 140$ for higher ϵ values, that corresponds to the cooperative nucleation or an expanded seed in Figure 7.5 and generation of anisotropic wings along axes in Figure 7.6. The peak corresponds to a droplet of Figure 7.14 and appears in many different individual single runs, but at different times, corresponding to different onsets of the droplet. Hence, a time average washes it out, and *single runs preserve this physics* [53]. The peak slowly vanishes as the system finds the golf hole edge $\epsilon(\vec{k}) = 0$, and then rolls into it, by reorienting the anisotropic wings along the preferred diagonal directions. Once the distribution reduces

to fit into the golf hole, and the funnel guides it to roll-in as seen in Figure 7.6, the values of $W(\epsilon, t)$ increase sharply. Finally, the distribution become a monotonically decreasing function with powerlaw falloff $\sim 1/\tilde{\epsilon}$ at $t = 500$.

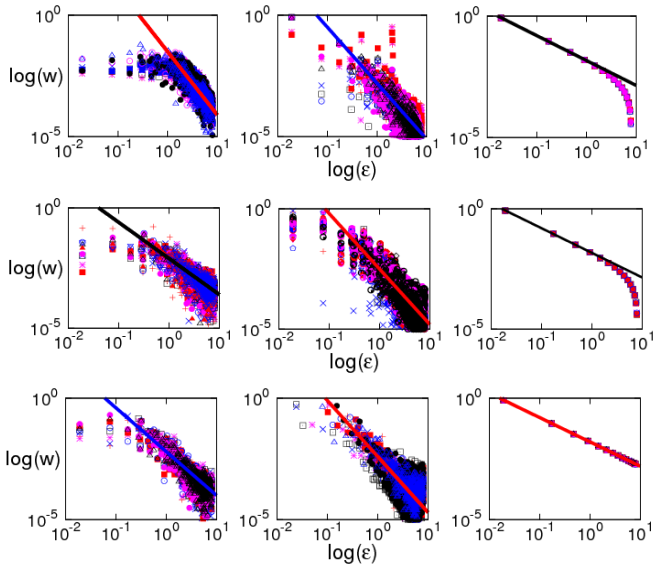

Figure 7.17: Log-log plot of $log(W(\tilde{\epsilon}, t))$ versus $log(\tilde{\epsilon})$ showing slopes in the three phases for different T. *First row:* vapour (Left), liquid (middle) and crystal (right) in Region ④. Similarly, *Second row* for Region ② and *Third row* for Region ①. Note, the slopes α in domain-wall liquid and domain-wall crystal phase are approximately same in Regions ④,②,①.

Figure 7.17 shows the *log-log* plot of the energy occupancy distribution $W(\tilde{\epsilon}, t)$ versus $\tilde{\epsilon}$ with all the different times data simply projected onto the $W - \tilde{\epsilon}$, to give an idea of the evolution. The temperatures are shown in Regions ④ (first row), ② (second row), ① (third row). The last distribution snapshot in all rows correspond to Figure 7.15. *log-log* plots of Figure 7.17 shows exponents as slopes α^{vapour} (first row), α^{liquid} (second row), $\alpha^{crystal}$ (third row) in the vapour, liquid, and the crystal phases respectively.The

exponents are roughly,

$$\alpha^{vapour}(T) \approx 2.6, 1.5, 1.8 \text{ in Regions ④,②,① respectively.} \tag{7.10a}$$

$$\alpha^{liquid}(T) \approx 2.3 \text{ in Regions ④,②,①.} \tag{7.10b}$$

$$\alpha^{crystal}(T) = 1 \text{ in Regions ④,②,①.} \tag{7.10c}$$

7.1.7 Parametrization of partial-equilibrium surfaces in energy

We now seek to parametrize the $\rho(\vec{k}, t)$ of Figure 7.6 distributions describe pathways to get into the golf hole. The initial peak of entropically critical droplet is taken as an isotropic gaussian $\rho \sim e^{-(\vec{K}^2/2\sigma^2)}$, where σ^2 is a variance. The wings along the axes are taken as from a factor of $(1 + \rho_4 \cos 4\theta)$ with parameter $1 > \rho_4 > 1$. The final inverted fan shape (in the crystal) along the $\pm$ diagonals is $W \sim (\eta_\pm / 2K_\pm^2)$ where the parameter $\eta_\pm$ add up $\eta = (\eta_+ + \eta_-)/2$, related to the martensitic fraction. Initially at $t = t_{start}$, when the critical single-variant droplet forms, $\eta_\pm = \rho_4 = 0$, and the martensite fraction is $n_{m0} \equiv n_m(t_{start})$. Putting these elements together in a suitably normalized way, the structure-factor $\rho(\vec{k}, t)$ is parametrized as,

$$\rho(\vec{k}, t) = \frac{n_{m0}(1-\eta)e^{-\vec{K}^2/2\sigma^2}(1 + \rho_r \cos 4\theta)}{\frac{1}{N}\sum_{\vec{k}} e^{-\vec{K}^2/2\sigma^2}(1 + \rho_4 \cos 4\theta)} + \sum_{\pm}(1 - \delta_{k_-,0}\delta_{k_+,0}) \frac{\frac{\eta_\pm}{2}\left[\frac{\delta_{k_\mp,0}}{K_\pm^2}\right]}{\frac{1}{N}\sum_{\vec{k}}\left[\frac{\delta_{k_\mp,0}}{K_\pm^2}\right]} \tag{7.11}$$

Here the 'diagonal' variables are $K_\pm \equiv (K_x \pm K_x)/\sqrt{2}$, and $k_\pm \equiv (k_x \pm k_y)/\sqrt{2}$ so that $K_+^2 + K_-^2 = {K_x}^2 + {K_y}^2$.

The martensite fraction $n_m(t)$ is $\frac{1}{N}\sum_{\vec{k}} \rho(\vec{k}, t) = n_m(t)$ from (7.5). So

$$\eta(t) = \frac{\eta_+(t)}{2} + \frac{\eta_-(t)}{2} = \frac{n_m(t) - n_{m0}}{1 - n_{m0}}; \tag{7.12a}$$

$$\text{or} \quad n_m(t) = n_{m0} + (1 - n_{m0})\eta(t), \tag{7.12b}$$

where the normalizations have been used to evaluate $\sum \rho(\vec{k},t) = n_m N$. Using (7.11) in (7.4a), the parametrized Hamiltonian energy H is evaluated as

$$H/(K_0 N/2) = 2\xi^2 n_m[(1-\eta)(\sigma^2 - {\sigma_0}^2) + \frac{g_L \eta}{2\xi^2 n_{m0}}] \tag{7.13}$$

where ${\sigma_0}^2(\rho_4) \equiv \frac{1}{R_c} - \frac{A_1[U]\rho_4}{8\xi^2}$, and we have used the droplet (3.19) model definition $R_c(T) = -2\xi^2/[g_L(T) + A_1[U]/2]$.

From the simulation results, the $H \simeq 0$ early time incubation is an isotropic gaussian parametrized with variance $\sigma^2 = 1/R_c$ for $t < t_{inc}$, and $\rho_4 = \eta_\pm = 0$. So, $n_m = n_{m0}$ and there is incubation of the martensite fraction. To get into the golf hole, the distribution $\sim \sigma^2$ has to *narrow* its σ^2 at *constant* energy $H = 0$. From (7.13) σ^2 to decrease at constant $H = 0$, the 'wrong' anisotropy cost $\sim \rho_4 A_1$ has to increase, by increasing the distribution along the axes. Thus ρ_4 increases from zero to unity, with $\eta_\pm$ still zero. The normalized distribution falls into the golf hole, reducing the energy to negative values $H < 0$ at $t = t_{neg}$. Then the 'wrong' anisotropy goes into the bidiagonal X-shape of the liquid, and symmetry-breaking reduces the energy further, to a single diagonal of the crystal, since there are the fewer domain-wall segments.

To slide the parameters along the pathway in parameter space, we assume a 'toy dynamics' with parameters at a constant 'velocity' for constant energy; and quadratically $\sim t^2$ at a constant 'acceleration' for decreasing energy. The toy dynamics in terms of ρ_4, σ^2 and $\eta_\pm$ are given below, to match the simulation results discussed previously

$$\rho_4(t) = \begin{cases} 0, & \text{for } t < t_{incub}; \quad \text{(vapour)} \\ \frac{t - t_{incub}}{t_{neg} - t_{incub}}, & \text{for } t_{neg} > t > t_{incub}; \quad \text{(vapour)} \\ 1, & \text{otherwise} \quad \text{(liquid and crystal).} \end{cases} \tag{7.14}$$

$$\sigma^2(t) = \begin{cases} \frac{1}{R_c}, & \text{for } t < t_{incub}; \quad \text{(vapour)} \\ \frac{1}{R_c} - \frac{\rho_4 A_1[u]}{8\xi^2}, & \text{for } t_{neg} > t > t_{incub}; \quad \text{(vapour)} \\ \frac{1}{R_c} - \frac{A_1[u]}{8\xi^2} \equiv \sigma_0^2, & \text{otherwise} \quad \text{(liquid and crystal).} \end{cases} \tag{7.15}$$

$$\eta_{\pm}(t) = \begin{cases} 0, & \text{for } t < t_{incub}; \quad \text{(vapour)} \\ 0, & \text{for } t_{neg} > t > t_{incub}; \quad \text{(vapour)} \\ (\frac{t-t_{neg}}{t^{'}-t_{neg}})^2, & \text{for } t^{'} > t > t_{neg}; \quad \text{(liquid)} \\ [(1 \pm B\ \theta(t-t_c)](\frac{t-t_c}{t_c})^2, & \text{otherwise} \quad \text{(crystal).} \end{cases} \tag{7.16}$$

Here, $\eta = 1$ and $n_m = 1$, in the liquid, so we need $t^{'} > t_m$. We need to have $n_m(t_m) = 1/2$ in between, so using (7.16) in (7.12a) we get $\eta(t_m) = (\frac{t_m - t_{neg}}{t^{'} - t_{neg}})^2 = \frac{\frac{1}{2} - n_{m0}}{1 - n_{m0}}$. This fixes $t^{'}$ in terms of t_m. Thus from simulations, the characteristic times are

$$t_{incub} = 0.3 t_m; \quad t_{neg} = 0.6 t_m; \quad t^{'} = (t_m - t_{neg}) \sqrt{\frac{1 - n_{m0}}{\frac{1}{2} - n_{m0}}}. \tag{7.17}$$

We take t_{incub} and t_C from simulations with $n_{m0} \approx 0.04$ and set B=2. The parametrized pathway is given in Figure 7.18 for different temperatures in Region ④.

The martensite fraction and textural thermodynamics from the simple parametrization is given in Figure 7.19 and follows the data surprisingly closely. Furthermore the structure-factor $\rho(\vec{k})$ from parametrization is shown in Figure 7.20 (relief) and 7.21 (colour contour). Compare with the simulations of Figure 7.6 (relief) and (7.7) (colour contour): the agreement is not only qualitative but even semi-quantitative. Similarly, parametrization in Regions ②,① in Figures 7.22,7.23 gives qualitative agreement. The *equilibrium* occupancy distribution from parametrization is shown in Figure 7.24 and is

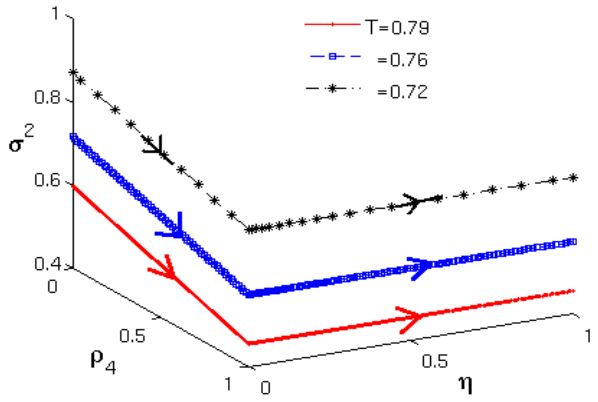

Figure 7.18: *Parameter pathways:* Plot of σ^2 versus ρ_4 and η, for different bath temperatures in Region ④.

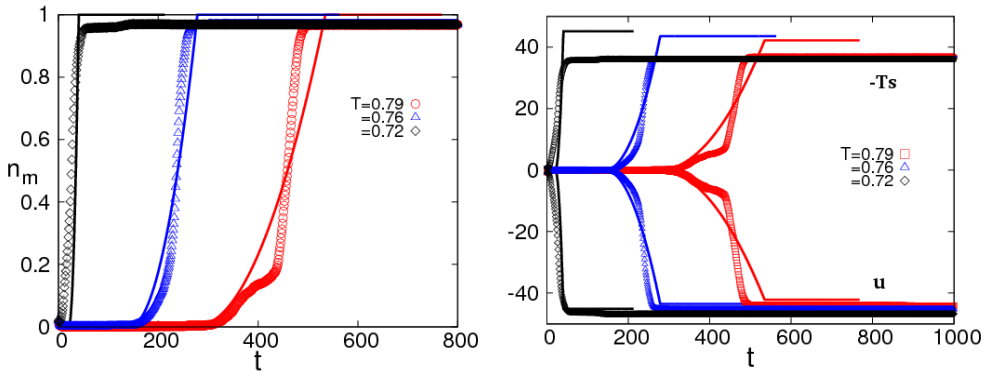

Figure 7.19: *Martensite fraction and textural thermodynamics from parametrization: Left:* Parametrized martensite conversion fraction $n_m(t)$ versus toy time 't' for temperatures T in Region ④ (solid line). Compare data shown, from MC simulations. *Right:* Thermodynamic functions of entropy E_{entr} and energy U_{ener} versus toy time 't' (solid line). Compare with data shown, from MC simulations.

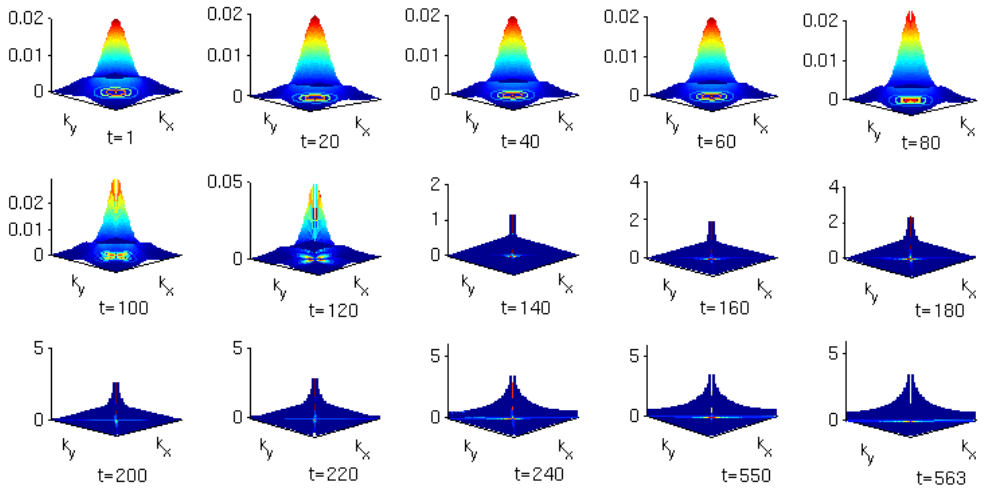

Figure 7.20: *Region ④ parametrization of PE surfaces:* The structure-factor $\rho(\vec{k})$ *relief* plot for temperature $T = 0.76$ and different times. Compare with MC simulations data of Figure 7.6.

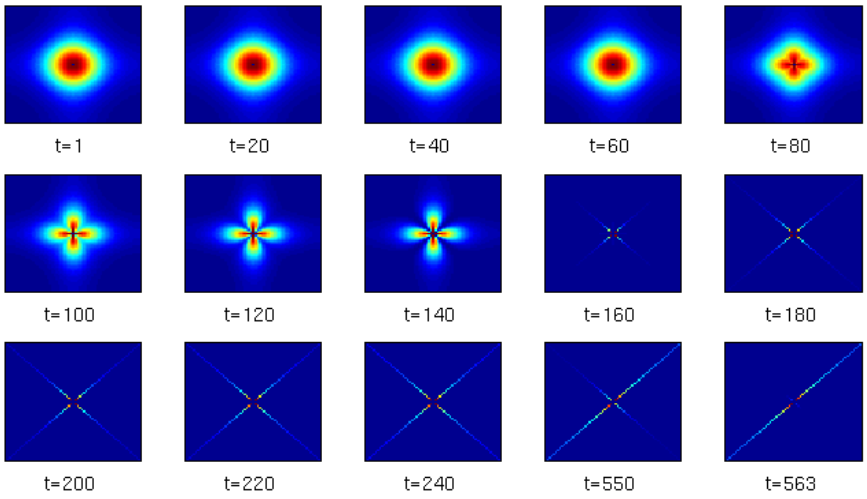

Figure 7.21: *Region ④ parametrization of PE surfaces:* The structure-factor $\rho(\vec{k})$ *colour contour* plot for temperature $T = 0.76$ and different times. Compare with MC simulation data of Figure 7.7.

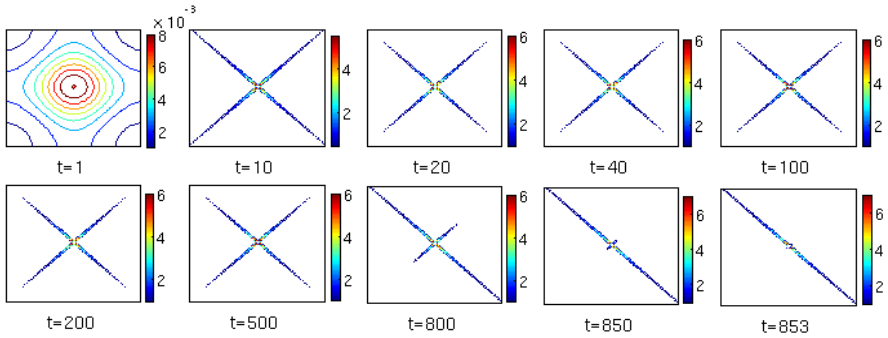

Figure 7.22: *Region ② parametrization of PE surfaces:* The structure-factor $\rho(\vec{k}, t)$ colour contour for temperature $T = 0.55$ and different times. Compare with Figure 7.10 data of MC simulation.

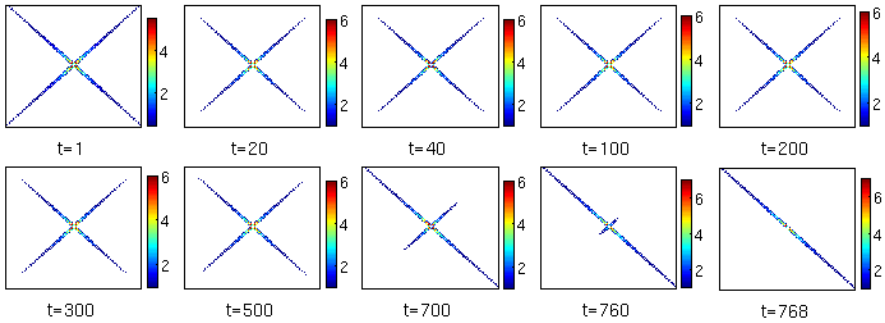

Figure 7.23: *Region ① parametrization of PE surfaces:* The structure-factor $\rho(\vec{k})$ colour contour for temperature $T = 0.4$ and different times. Compare with Figure 7.11 data of MC simulation.

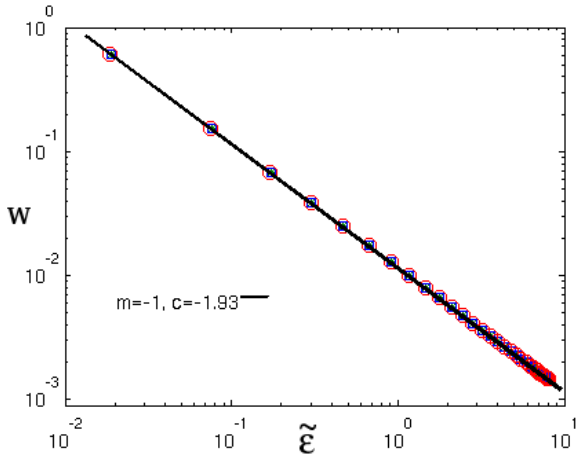

Figure 7.24: *Parametrized equilibrium energy occupancy distributions:* Plot of $log(W)$ versus $log(\tilde{\epsilon})$ where T is the temperature, after long-time equilibration to domain-wall crystal, showing $W \sim 1/\tilde{\epsilon}$.

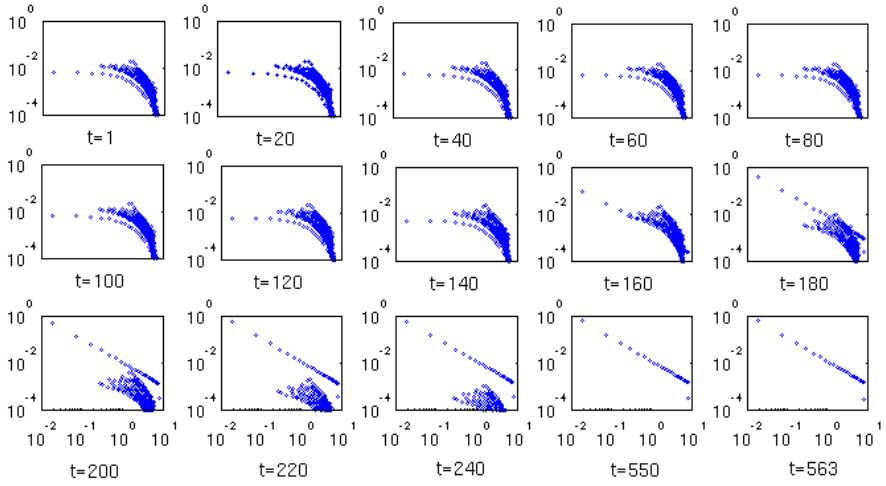

Figure 7.25: *Time evolution of energy occupancy distributions:* Plots of $log(W)$ vurses $log(\tilde{\epsilon})$ for quench into $\tau_4 > \tau > \tau_2$ for a single run, and various times.

in good agreement with simulations of Figure 7.18 (as expected, since simulations were the input). For the general case, the parametrization of $W(\tilde{\epsilon}, t)$ versus $\tilde{\epsilon}$ of for various t is shown in Figure 7.25. It is also qualitatively like the simulations, of Figure 7.17. (The jumpiness of the parametrization is from constant-$\vec{k}$ contours being different from constant-$\tilde{\epsilon}$ contours.)

Thus we have identified and parametrized the pathways on constant energy surfaces that are either constant or decreasing. This makes specific, and clarifies the general ideas of partial equilibration surfaces and entropy barriers, but here in a specific interaction model for aging in a martensitic transition [24].

7.1.8 Effective temperatures

The internal energy U_{ener} and entropy S_{entr} of the pseudospin textures can be found in a local meanfield approximation [33]. Figure 7.26 (first row) shows energy $U_{ener}(t)$ versus entropy $S_{entr}(t)$ plots, for the three quench temperatures $T = 0.76, 0.55, 0.4$ in the three Regions ④,②,① of Figure 7.1. The direction of increasing MC time t is an arrow towards the lower left corner.

To extract effective temperatures we adopt a protocol of marking t_m and t_C for that run (as by the arrows) in Figure 7.26, first row. This gives three segments of the curve. The plot of $U_{ener}(t)$ versus $S_{entr}(t)$ is then fitted to straight lines $y = mx + c$ through least square fitting for data in each of these segments (Data for $t < t_{start}$ before the critical droplet forms, are neglected in fitting.). This gives three time-dependent effective temperatures for three phases.

A microcanonical temperature would be

$$\frac{1}{T_{eff}} = \frac{\partial S_{entr}(t)}{\partial U_{ener}(t)} \tag{7.18}$$

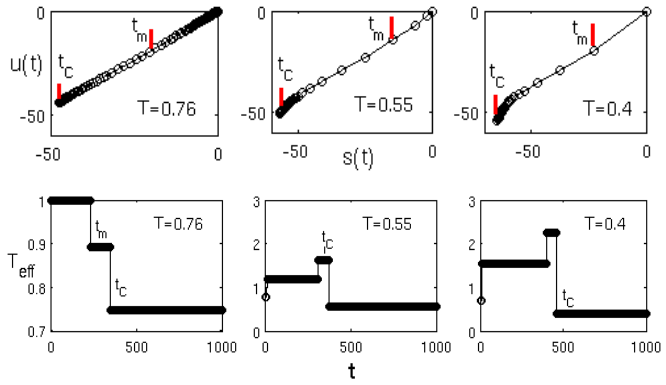

Figure 7.26: *Effective temperatures: First Row*: Plot of entropy $S_{entr}(t)$ versus internal energy $U_{ener}(t)$ for quenches into different temperature regions. *Left:* Region ④ $T_4 > T = 0.76 > T_2$. *Middle:* Region ② $T_2 > T = 0.55 > T_1$. *Right:* Region ① $T = 0.4 < T_1$. *Second Row*: Plot of $T_{eff}(t)$ from the U_{ener} versus S_{entr} slopes of (7.18), in the three quench regions, at indicated quench temperatures. Conversion and orientation imes t_m and t_C are marked.

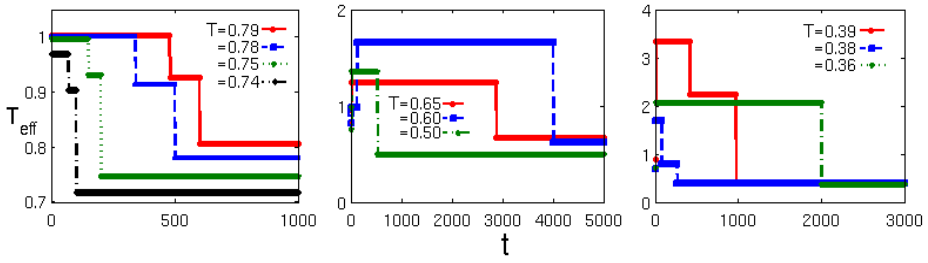

Figure 7.27: *Effective temperatures:* Plot of effective temperature T_{eff} versus time t for different quench temperatures T in Regions ④,②,①.

and we would hope that this effective temperature would tend to the bath temperature, $T_{eff} \Longrightarrow T$, finally. The slope of the curve for the final low energy and low entropy curve segment is indeed found to be the bath temperature T. In Regions ④,②,①, $t_{start} \sim 10, 5, 1$ MCS respectively.

Hotspot catalyst appearences mostly change the energy (lower the average slopes in a segment) and hence raise the effective temperature T_{eff}. Figure 7.26 second row shows T_{eff} versus time t from these simulation data fits for temperatures indicated in Regions ④,②,①. Figure 7.27 shows further effective temperature plateaus for yet other effective temperature in these Regions.

The microcanonical effective temperature has been shown by Ritort to be equal to other effective temperatures such as from the fluctuation dissipation ratios [24]. However we do not pursue this here.

7.2 Other 2D pseudospin models

In the previous Section, we have shown the re-equilibration process in 3-state pseudospin model for square-rectangle (SR) transition. The fast rapid conversions in Region ① and slow incubation delays in Region ④ of the athermal TTT phase diagram are understood through temperature dependent golf holes and funnel-like behaviour. In Chapter 4, we find conversion-delays and fast conversions in 4-state, 5-state, and 7-state pseudospin models for triangle-centered rectangle (TCR), square-rectangle (SO), and triangle-oblique (TO) transitions respectively.

7.2.1 Golf holes and funnels

We cannot here repeat the identification of search pathways for all three transition. Furthermore, for other vector-OP cases, the $H = 0$ condition is not easily treated as a vanishing $\epsilon(\vec{k})$ condition. Since $H \sim \sum_{\ell,\ell'} S_\ell S_{\ell'}$ has

the spectrum mixed with the pseudospin components. We merely plot the golf holes/funnels as seen by the pseudospin components combined. Figure 7.28, thus shows pots of $\epsilon_{22}(\vec{k})$, $\epsilon_{23}(\vec{k})$, $\epsilon_{33}(\vec{k})$. However, we present the temperature-dependent golf holes and funnels in TCR, SO, TO transitions.

The pseudospin Hamiltonian for TCR, SO, TO transitions are given in (2.32), (2.38), (2.42) with the *same* 2×2 kernel. The plots of Figure 7.28 are of,

$$\epsilon_{\ell\ell'}(\vec{k}) = g_L(\tau) + \xi^2 \vec{K}^2 + \frac{A_1}{2} U_{\ell,\ell'}(\vec{k}) \tag{7.19}$$

with $\ell = \ell' = 2, 3$.

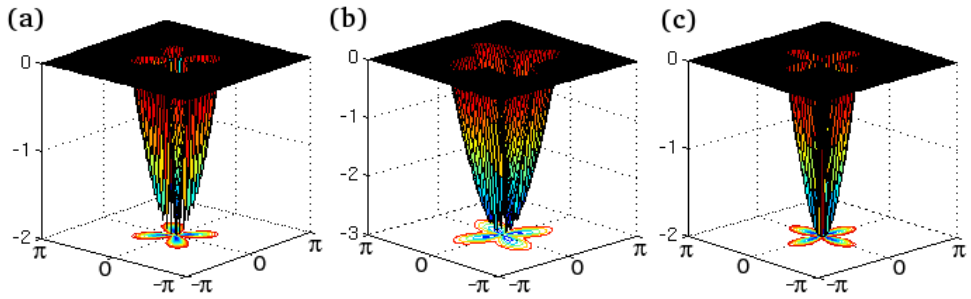

Figure 7.28: *Golf holes and funnels in Brillouin zone for TCR, SO, TO transitions:* Relief plot of $\epsilon_{\ell\ell'}(\vec{k})$ versus $\vec{k}$ for $T = 0.76$ and $A_1 = 4$, showing negative-energies golf hole/funnel below austenite energy. (a) $\epsilon_{22}(\vec{k})$; (b) $\epsilon_{23}(\vec{k})$; (c) $\epsilon_{33}(\vec{k})$. See text.

7.2.2 Re-equilibration processes in Fourier space

We present coordinate space textural evolution; Fourier space $\rho(\vec{k}, t)$ snapshots both in relief and colour contour for each of the three transitions, all in Region ④. The golf holes are shown in Figure 7.28. The Figure captions are self explanatory. There are both similarities and differences (generic behaviour) and differences, with the SR case. Figures 7.29, 7.30, 7.31 are the

TCR case. Figures 7.32,7.33, and 7.34 are the SO case and Figure 7.35, 7.36, and 7.37 are the TO cases.

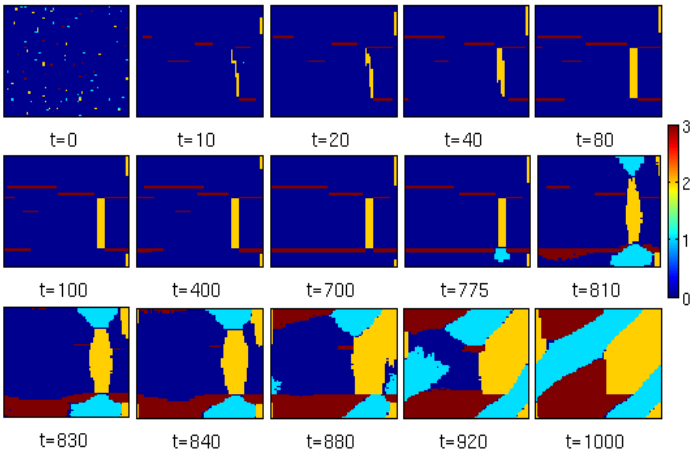

Figure 7.29: *Region ④ of TCR transition: Evolution of a droplet in coordinate space:* Snapshots for a fixed temperature $T = 0.68$ and various times. Here, the critical droplets are narrow slabs of different variants. Compare Figure 7.5 of SR case. Parameters are $T_c = 0.9$, $A_1 = 4$, $E_0 = 3$. See text.

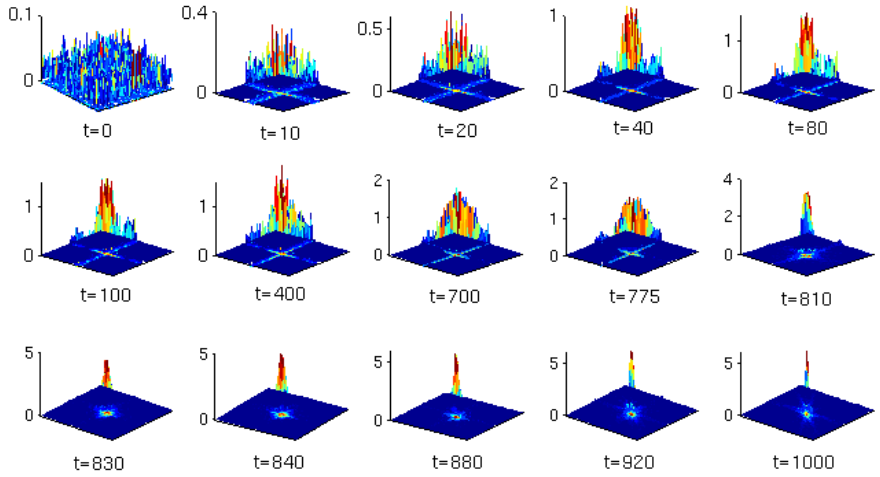

Figure 7.30: *Region ④ of TCR transition:* Fourier space as a *Relief* plot of $ln[1 + |S(\vec{k}, t)|^2]$ in the Brillouin zone for fixed temperature $T = 0.68$ and various times, corresponding to the coordinate space textures of Figure 7.29. Compare Figure 7.6 of SR case.

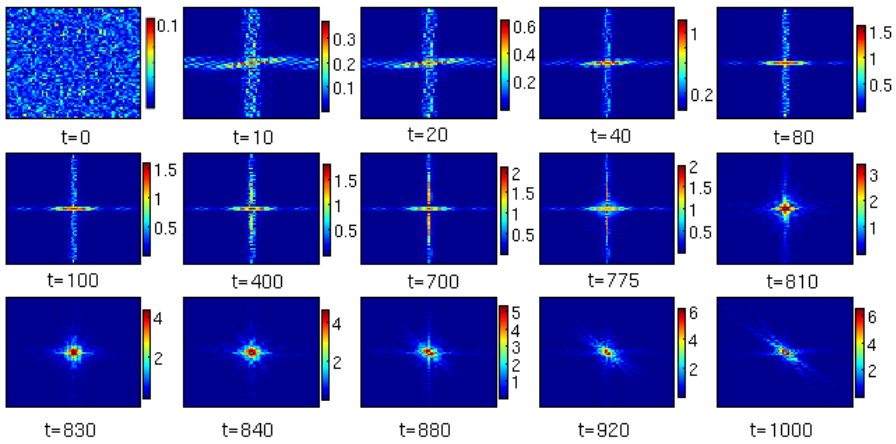

Figure 7.31: *Region ④ of TCR transition:* Fourier space as a *colour contour* plot of $ln[1 + |S(\vec{k}, t)|^2]$ of Figure 7.30. Compare Figure 7.7 of SR case.

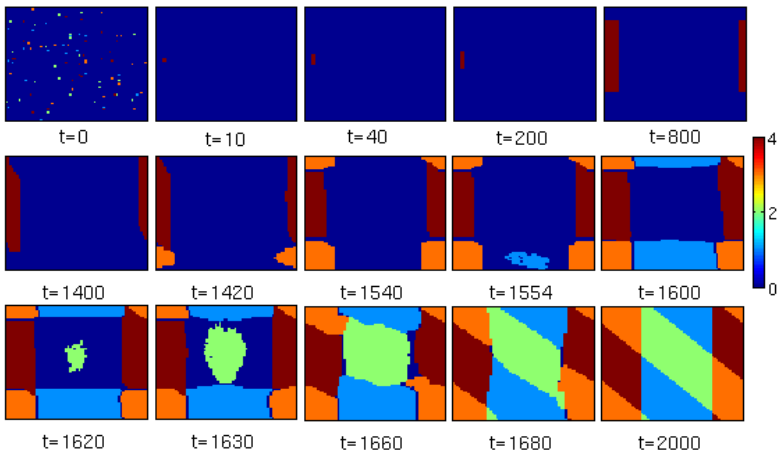

Figure 7.32: *Region ④ of SO transition: Evolution of a critical droplet in coordinate space:* Snapshots for a fixed temperature $T = 0.77$ and various times. Parameters are $T_c = 0.9$, $A_1 = 4$, $E_0 = 3$. Here, the critical droplet is a square of single-variant fluctuates to a narrow slab. Compare Figure 7.5 of SR case.

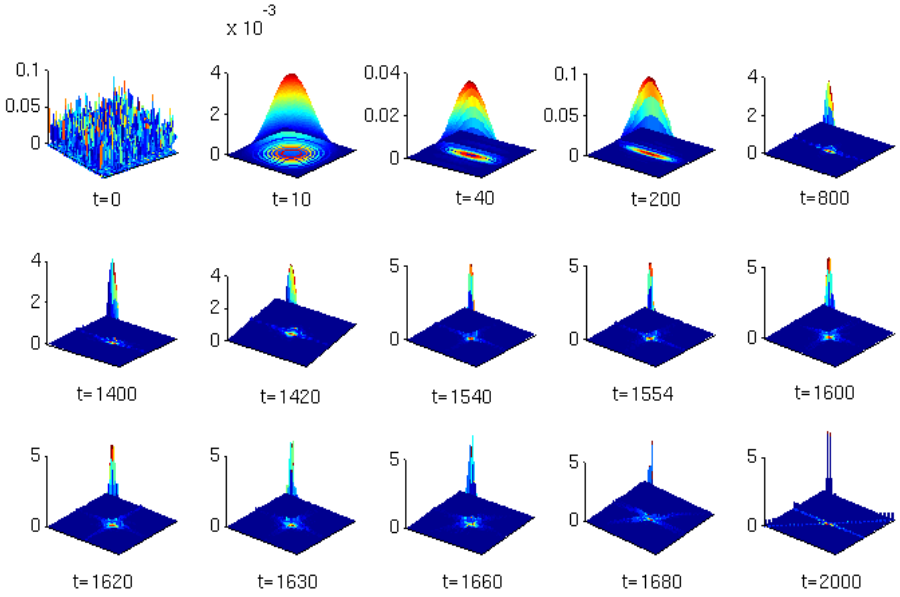

Figure 7.33: *Region ④ of SO transition:* Fourier space *relief* plot of $ln[1 + |S(\vec{k}, t)|^2]$ in the Brillouin zone for fixed temperature $T = 0.77$ and various times, corresponding to the coordinate space textures of Figure 7.32. Compare Figure 7.6 of SR case.

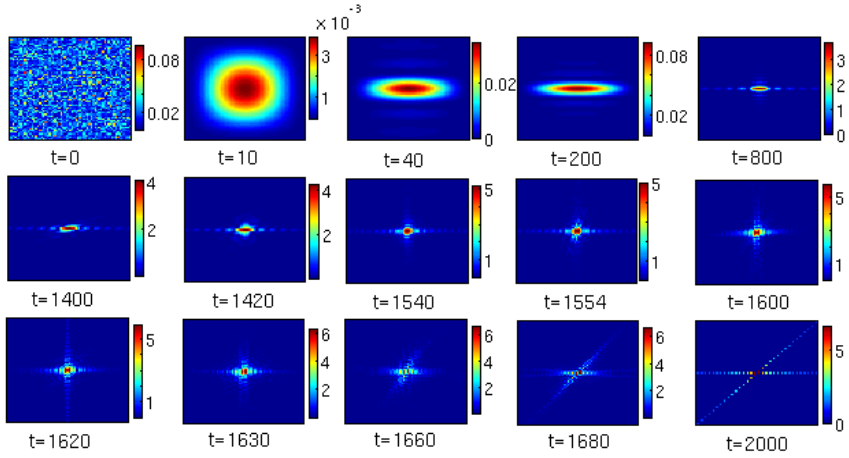

Figure 7.34: *Region ④ of SO transition:* Fourier space *colour contour* plot of $ln[1 + |S(\vec{k}, t)|^2]$ of Figure 7.33. Compare Figure 7.7 of SR case.

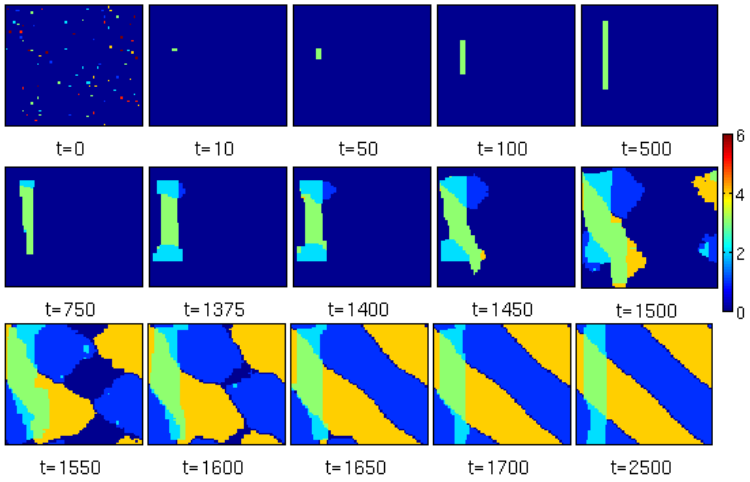

Figure 7.35: *Region ④ of TO transition: Evolution of a critical droplet in coordinate space:* Snapshots for a fixed temperature $T = 0.8$ and various times. Here the critical droplet is again a square that fluctuates to a narrow slab. Compare Figure 7.5 of SR case.

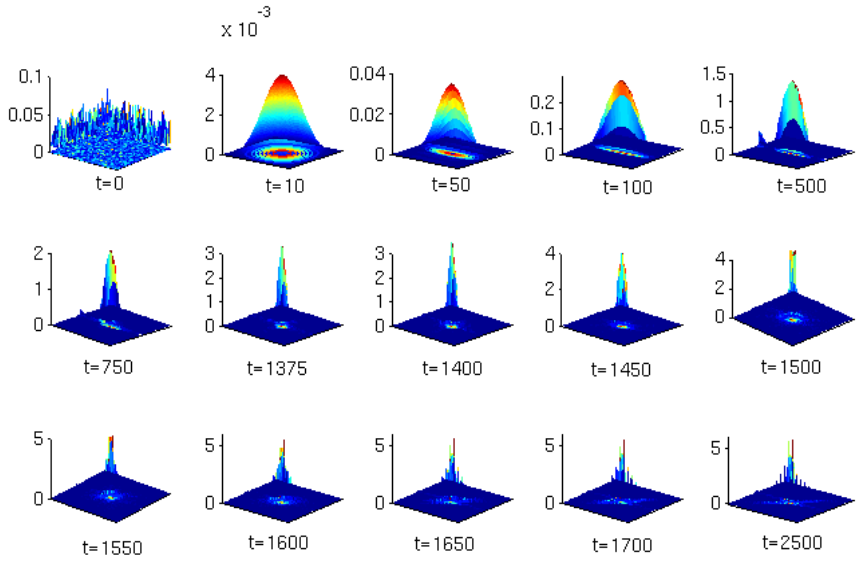

Figure 7.36: *Region ④ of TO transition:* Fourier space *relief* plot of $ln[1 + |S(\vec{k}, t)|^2]$ in the Brillouin zone for fixed temperature $T = 0.8$ and various times corresponding to Figure 7.35. Compare Figure 7.6 of SR case.

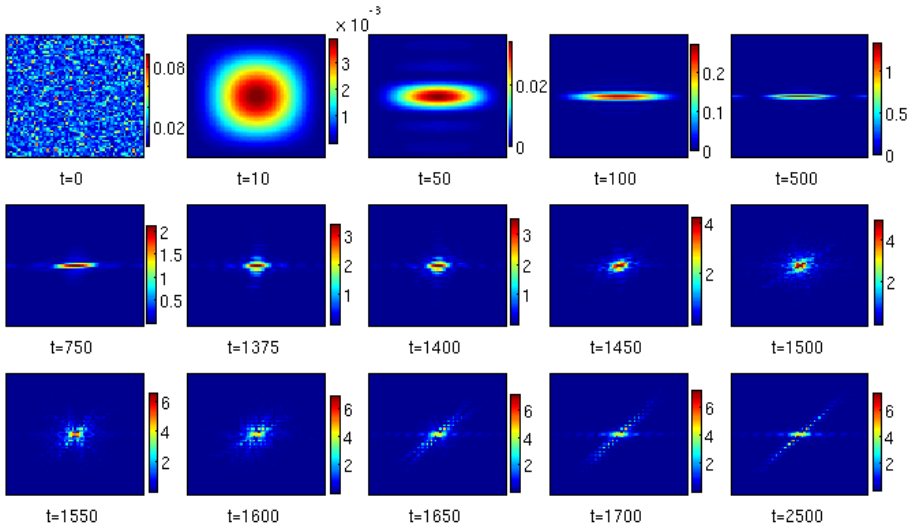

Figure 7.37: *Region ④ of TO transition:* Fourier space *colour contour* plot of Figure 7.36. Compare Figure 7.7 of SR case.

7.3 Chapter summary

In this Chapter, we understand the re-equilibration process of critical droplet of the vapour phase going to liquid, and finally crystal phases, using protein folding concepts of golf holes and funnels, here in Fourier space in detail for square-rectangle transition case of a scalar-OP.

- The Temperature-Time-Transformation diagrams that have both fast and slow dynamics are understood from the presence of anisotropic golf holes and funnels in Fourier space.
- The slow delayed conversions in the athermal martensite regime arises as the textural distributions $\rho(\vec{k},t) = |S(\vec{k},t)|^2$ has to deform and narrow to fit into the golf hole, that is smaller in the Region ④.
- The fast athermal conversions in the Region ① are as the golf hole is larger.
- The evolution of the distributions from vapour to liquid phase in Region ④ are parametrized and textural pathways are explicitly identified.
- There are linear portions in energy U_{ener} versus S_{entr} plots, that are used to obtain an effective temperature, that reach the bath-temperature in the equilibrium crystal phase.

8

Thesis summary

In this Chapter we summarize the thesis results.

Pseudospin models for martensitic transitions can differ in their number of pseudospin components N_{OP}, number of directions in the order parameter space of variants N_V, and in the anisotropy of their compatibility induced interactions. Under Monte Carlo simulations and temperature quenches from lightly seeded austenite, the microstructural evolutions can give insights into issues in materials science as well as nonequilibrium aging systems.

Generic behaviour independent of material parameters and even of symmetry can be identified and looked for in an experiment. This includes near transition temperature, Vogel-Fulcher divergence of martensitic conversion

tails from seeded austenite and their Log-normal distribution, and sparseness of successful conversions; and explosive growth at lower temperatures.

Entropy barriers or rarity of pathways from entropically critical droplet, and ergodicity breaking plays central conceptual role.

To understand the increase of conversion delays, concepts borrowed from protein folding such as golf holes and funnels, turn out to be surprisingly useful, with Fourier space description, a strong complement to conventional coordinate space approaches.

Thus relavance of martensitic transition models to protein folding and glasses could be a useful research avenue to explore to the benefit of all three fields.

A

Textural Thermodynamics

A.1 Scalar-OP: square-rectangle transition

We now present expressions for the energy and entropy of evolving textures [33], used in the Subsection 3.5.4,3.8.

The temperature dependence of the Hamiltonian implies the internal energy U_{ener} is not just the average of the Hamiltonian H. The free energy is

$$\beta F = -\ln Z, \quad Z = \sum_{\{S\}} e^{-\beta H(\tau)}, \tag{A.1}$$

where $H(\tau)$ of (3.1) and (3.2). The entropy is $S_{entr} = -dF/dT$ so

$$TS_{entr} = -F + < H > -T < dH(\tau)/dT > . \tag{A.2}$$

Requiring that $TS_{entr} = -F + U_{ener}$, yields the internal energy as

$$U_{ener} =< H > -T < dH/dT > . \tag{A.3}$$

With $H(\tau) = E_0\bar{\varepsilon}^2 \sum_{\vec{k}}[g_L + \xi^2\vec{K}^2 + (A_1/2)U(\vec{k})]|S(\vec{k})|^2$, and $T = (T_0 - T_c)(\tau - \tau_0)$ it follows that

$$U_{ener} = [1-(\tau-\tau_0)\frac{d\ln\bar{\varepsilon}^2}{d\tau}] < H > -E_0(\tau-\tau_0)\bar{\varepsilon}^2\frac{dg_L}{d\tau}\sum_{\vec{k}} < |S(\vec{k})|^2 > . \tag{A.4}$$

In meanfield approximation, $< |S(\vec{k})|^2 > \simeq | < S(\vec{k}) > |^2$ and $\beta H \simeq \sum_{\vec{k}}[Q(\vec{k})S(\vec{k}) - \frac{1}{2}Q_0| < S(\vec{k}) > |^2]$, where $Q(\vec{k}) = Q_0(\vec{k}) < S(\vec{k}) >^*$. Then, summing over $S(\vec{r}) = 0, \pm 1$ in the partion function,

$$\beta F \simeq -\sum_{\vec{r}} \ln\frac{1}{3}[1 + 2\cosh Q(\vec{r})] - \frac{1}{2}\sum_{\vec{k}} Q_0|S(\vec{k})|^2, \tag{A.5}$$

and the entropy S_{entr} is,

$$TS_{entr} = -F + U_{ener}. \tag{A.6}$$

These thermodynamic functions U_{ener}, F, S_{entr}, are *all zero in austenite*, i.e. represent the difference with austenite, that has high temperature entropy $S_{entr} = Nln3$. They depend on parameters A_1, ξ^2, E_0. We set $A_1 = \xi^2 = 0$ to obtain corresponding functions, that depend only on Landau contributions g_L denoted by a superscript (0). Subtracting and scaling in E_0, defines dimensionless *excess* functions, describing *domain-wall* thermo-

dynamics,

$$\Delta U_{ener} \equiv (U_{ener} - U^{(0)}{}_{ener})/E_0; \tag{A.7a}$$

$$\Delta F \equiv (F - F^{(0)})/E_0; \tag{A.7b}$$

$$\Delta S_{ener} \equiv (S_{entr} - S^{(0)}{}_{entr})/E_0. \tag{A.7c}$$

Replacing the meanfield local averages at a site $\vec{r}$, by the MC values, $< S(\vec{k}) > \rightarrow S(\vec{k}, t)$ yields excess functions $\Delta U_{ener}(t), \Delta F(t), \Delta S_{entr}(t)$. This is used in plotting textural thermodynamics evolutions of Figures 3.23, 3.26 and in Section 3.5.

Finally the strain evolutions lead to changing *internal* local stresses $p_2(\vec{r}) = \partial F/\partial e_2(\vec{r})$. With the full strain Hamiltonian of (3.2), a scaled stress is

$$p_2(\vec{r}) = 2[\frac{1}{2}\frac{\partial \bar{f}_L}{\partial e_2} - \xi^2 \vec{\Delta}^2 e_2 + (A_1/2)\sum_{\vec{r}'} U(\vec{r} - \vec{r}')e_2(\vec{r}')]. \tag{A.8}$$

Here $\frac{1}{2}\partial \bar{f}_L/\partial e_2 = \tau e_2 - 4e_2^3 + 3e_2^5$. Through the insertion (2.19), this can be written in terms of pseudospins, and as in (2.21), the nonlinearities collapse as $S^5(\vec{r}) = S^3(\vec{r}) = S(\vec{r})$. In Fourier space, the internal local stress evaluated from MC pseudospin states is then

$$p_2(\vec{k}, t) = 2\bar{\varepsilon}[(\tau - 4\bar{\varepsilon}^2 + 3\bar{\varepsilon}^4) + \xi^2 \vec{K}^2 + (A_1/2)U(\vec{k})]S(\vec{k}, t). \tag{A.9}$$

This is used in textural stress plots, at the bottom of Figures 3.25, 3.27, 3.28.

A.2 Vector-OP : triangle-centered rectangle, square-oblique, triangle-oblique transitions

Thermodynamic functions, internal energy and entropy were obtained through meanfield approximations for scalar-OP SR transition [33]. The

partition functions alone are obtained by Vasseur et al in [34] for vector-OP TCR, SO, TO transitions. We now use the formal thermodynamic expressions from meanfield analysis [33] and partition functions Z [34], to derive the expressions for the thermodynamic functions, internal energy, entropy and internal stresses and stress distributions for the three vector-OP transitions.

Replacing $S \Longrightarrow \vec{S}$ in A.1, the partition function Z is defined as

$$Z = \sum_{\{S\}} e^{-\beta H(\tau)} = \sum_{\{S\}} e^{-\vec{V}.\vec{S}}, \tag{A.10}$$

where $\vec{V} = (V_2, V_3), \vec{S} = (S_2, S_3) = (\cos\phi_m, \sin\phi_m)$.

$$Z = \sum_{m=1}^{N_v+1} e^{-(V_2 \cos\phi_m + V_3 \sin\phi_m)}. \tag{A.11}$$

This can also be written as [34],

$$Z = 1 + \sum_{m=1}^{N_v} e^{-(V_2 \cos\phi_m + V_3 \sin\phi_m)}, \tag{A.12}$$

where V_2, V_3 are defined as,

$$V_2 = D_0[(g_L + \xi^2 K^2)S_2 + \frac{A_1}{2}(U_{22}(k)S_2 + U_{23}(k)S_3)], \tag{A.13}$$

$$V_3 = D_0[(g_L + \xi^2 K^2)S_3 + \frac{A_1}{2}(U_{33}(k)S_3 + U_{32}(k)S_2)]. \tag{A.14}$$

The partition function Z for TCR is,

$$Z = 2e^{\frac{V_2}{2}}[e^{-V_2}\cosh(\frac{V_2}{2}) + \cosh(\frac{\sqrt{3}}{2}V_3)], \tag{A.15a}$$

where the pseudospins $V = \vec{S} = (S_2, S_3)$,

$$\vec{S} = (0,0), (1,0), (-\frac{1}{2}, \pm\frac{\sqrt{3}}{2}). \tag{A.15b}$$

The local internal stresses are, $p_2(r) = \partial\bar{F}/\partial e_2(\vec{r}), p_3(r) = \partial\bar{F}/\partial e_3(\vec{r})$ for TCR transition here are obtained as,

$$p_2(r) = \epsilon[4\epsilon^3 S_2^3 - 6\epsilon S_2^2 + 2S_2(2\epsilon^2 S_3^2 + \tau) + 6\epsilon S_3^2 + 2\xi^2\Delta^2 S_2 + A_1(U_{22}S_2 + U_{33}S_3)], \tag{A.15c}$$

$$p_3(r) = \epsilon[4\epsilon^2 S_3^3 + 2S_3(2\epsilon^2 S_2^2 + 6\epsilon S_2 + \tau) + 2\xi^2\Delta^2 S_3 + A_1(U_{23}S_2 + U_{33}S_3)]. \tag{A.15d}$$

The partition function Z for SO transition is [34],

$$Z = 1 + 2\cosh(\frac{V_2 + V_3}{\sqrt{2}}) + 2\cosh(\frac{V_2 - V_3}{\sqrt{2}})], \tag{A.16a}$$

where the pseudospins $\vec{S} = (S_2, S_3)$,

$$\vec{S} = (S_2, S_3) = (0,0), (\pm\frac{1}{2}, \pm\frac{1}{2}). \tag{A.16b}$$

The local internal stresses for SO transition here are obtained as,

$$p_2(r) = \epsilon[2S_2(3S_2^4 - 4S_2^2 + \tau) + 2\xi^2\Delta^2 S_2 + A_1(U_{22}S_2 + U_{33}S_3)], \tag{A.16c}$$

$$p_3(r) = \epsilon[2S_2(3S_3^4 - 4S_3^2 + \tau) + 2\xi^2\Delta^2 S_3 + A_1(U_{23}S_2 + U_{33}S_3)]. \tag{A.16d}$$

The partition function Z for TO transition is,

$$Z = 1 + 2\cosh(V_2) + 2\cosh(\frac{V_2 + \sqrt{3}V_3}{\sqrt{2}}) + 2\cosh(\frac{V_2 - \sqrt{3}V_3}{\sqrt{2}})], \tag{A.17a}$$

where the pseudospins $\vec{S} = (S_2, S_3)$,

$$\vec{S} = (0,0), (\pm 1, 0), (\pm\frac{1}{2}, \pm\frac{\sqrt{3}}{2}). \tag{A.17b}$$

The local internal stresses $p_2(r), p_3(r)$ are here obtained as,

$$p_2(r) = \epsilon[2S_2(3S_2^4 - 4S_2^2 + \tau) + 2\xi^2\Delta^2 S_2 + A_1(U_{22}S_2 + U_{33}S_3)], \tag{A.17c}$$

$$p_3(r) = \epsilon[2S_2(3S_3^4 - 4S_3^2 + \tau) + 2\xi^2\Delta^2 S_3 + A_1(U_{23}S_2 + U_{33}S_3)] \tag{A.17d}$$

These will be used in Figures 4.17,4.19, 4.21, and 4.22,4.23, 4.24 in the Section 4.3.

Bibliography

[1] K. Bhattacharya, *Microstructure of Martensite: Why it forms and how it gives rise to the shape memory effect*, Oxford University Press (2003); J.M. Ball and R.D. James, Phil. Trans. Roy. Soc. London A **338**, 389 (1992).

[2] M. Cohen, G.B. Olson and P.C. Clapp, Proceedings of *International Conference On Martenstic Transformations* (ICOMAT), p1-11, USA (1979); *Physical properties of martensite and bainite*: Proceedings of the joint conference organized by the British Iron and Steel Research Association and the Iron and Steel Institute, Special report **93**, London (1965); V. Raghavan, *Solid state phase tranformations*, Prentice-Hall, New Delhi (1987).

[3] V.K. Wadhawan, *Introduction to Ferroic Materials* (Gordon and Breach, New York, 2000)

[4] C. Manolikas and S. Amelinckx, Phys. Stat. Sol. A **61**,179 (1980); J. Cui, T.W. Shield and R.D. James, Acta Mater. **52**, 35 (2004); M. Ramudu, A. Satish Kumar, V. Seshubai, K. Muraleedharan, K.S. Prasad and T. Rajasekharan, Scripta Mater. **63**, 1073 (2010).

[5] L.E. Tanner, Phil. Mag **14**,111 (1966); L. E. Tanner and M. Wuttig, Mater. Sci. Eng. A **127**, 137 (1990).

[6] M. Baus and R. Lovett, Phys. Rev. Lett. **65**, 1781 (1990); S. Kartha, J. A. Krumhansl, J. P. Sethna, and L. K. Wickham, Phys. Rev. **B** 52, 803 (1995); G.R. Barsch, B. Horovitz, and J.A. Krumhansl, Phys. Rev. Lett. **59**, 1251 (1987); B. Horovitz, G.R. Barsch, and J.A. Krumhansl, Phys. Rev. B **43**, 1021 (1991); S.R. Shenoy, T. Lookman, A. Saxena, and A.R. Bishop, Phys. Rev. B **60**, R12537 (1999); D.M. Hatch, T. Lookman, A. Saxena, and S.R. Shenoy, Phys. Rev. B **68**, 104105 (2003); M. Porta, T. Castàn, P. Lloveras, T. Lookman, A. Saxena, and S.R. Shenoy, Phys. Rev. B **79**, 214117 2009); A. Saxena, T. Lookman, A. R. Bishop, and S. R. Shenoy, in *Intrinsic Multiscale Structure and Dynamics in Complex Electronic Oxides*, edited by A. R. Bishop, S. Sridhar, and, S. R. Shenoy, World Scientific, Singapore (2004); S.R. Shenoy, T. Lookman and A. Saxena, in *Magnetism and Structure in Functional Materials*, ed. A. Planes, L. Manosa and A. Saxena, Springer Verlag, Berlin (2005); D. S. Chandrasekharaiah and L. Debnath, *Continuum mechanics* (Academic, San Diego, 1994), page.218.

[7] E. Vives, J. Ortin, L. Maosa, I. Rafols, R. Perezmagrane, and A. Planes, Phys. Rev. Lett. **72**, 1694 (1994); F. J. Prez-Reche, M. Stipcich, E. Vives, L. Maosa, A. Planes, and M. Morin, Phys. Rev. B **69**, 064101 (2004); F. J. Prez-Reche, L. Truskinovsky, and G. Zanzotto, Continuum Mech. Thermodyn. **21**, 17 (2009); E.K.H. Salje, J. Koppensteiner, M. Reinecker, W. Schranz, and A. Planes, Appl. Phys. Lett. **95**, 231908 (2009); S. Sreekala, R. Ahluwalia, and G. Ananthakrishna, Phys. Rev. B **70**, 224105 (2004); S. Sreekala and G. Ananthakrishna, Phys. Rev. Lett. **90**, 135501 (2003).

[8] M. Rao and S. Sengupta, Curr. Sci. **77**, 382 (1999); Phys. Rev. Lett. **91**, 045502 (2003).

[9] T. Kakeshita, T. Fukuda and T. Saburi, Scripta Mat. **34**, 1 (1996); T. Kakeshita, T. Takaguchi, T. Fukuda and T. Saburi, Materials Transactions, JIM **37**, 229 (1996); T. Kakeshita, K. Kuroiwa, K. Shimizu, T. Ikeda, A. Yamagishi, nd M. Date, Materials Transactions, JIM, **34**, 423 (1993).

[10] U. Klemradt, M.Aspelmeyer, H. Abe, L.T. Wood, S.C. Moss and E. Dimasi, J.Peisl, Mat. Res. Soc. Symp. Proc. **580**, 293 (2000); M. Aspelmeyer, U. Klemradt, L.T. Wood, S.C. Moss, J.Peisl, Phys. Stat.Sol. (a) **174**, R9 (1999); H. Abe, M. Ishibashi, K. Ohshima, and T. Suzuki, M. Wuttig, and K. Kakurai, Phys. Rev. B **50**, 9020 (1994);

[11] A simplified outline of the argument [9] is as follows. An N-cell system contains m martensite cells, of cell-probability $p = p_0 e^{-\beta\Delta(T)}$ where $\Delta(T)$ is an energy gap; and $N - m$ austenite cells of cell-probability $1 - p$. The martensite can cluster into n-cell droplets. The transition occurs only if a droplet exceeds a threshold, $n \geq n_{thresh}$. Thus the converting droplets have $m \geq n \geq n_{thresh}$. The total probability for conversion is then $P = \sum_{m,n} C(N, m, n \geq n_{thresh}) p^m (1-p)^{N-m}$. The cell-probability is small $p << 1$, so $(1-p)^{N-m} \simeq e^{-(N-m)p}$. The sum is approximated by the most probable droplet term, and coefficients $C, \Delta(T), p_0, n_{threshold}$ are material fitting parameters. The conversion time is $t \sim 1/P$, with a minimum found by $dP/dT = 0$. This yields the time as a strong function of temperature (containing exponential of a Boltzmann factor) and of material parameters, with regimes of both isothermal minima and quasi-athermal conversion tails [9].

[12] A. Planes, F-J. Perez-Reche, E. Vives and L. Manosa, Scripta Mat. **50**, 181 (2004).

[13] These results[12] can be outlined in our notation, as follows. For a unit cell of austenite to convert to martensite, the continuous-strain energy cost is a sum of Landau barrier $\bar{f}_{barr}$ of (2.6a), and (positive) Ginzburg surface contributions. Then a *lower* bound to the cost is $\bar{f}_{barr} = \bar{f}_L(\bar{\varepsilon}_{barr})$, that can be taken as an estimate. The first passage time for high barriers is then $t_m \sim e^{E_0 \bar{f}_{barr}/T}$; while for low barriers, the time is proportional to the barrier itself [48], $t_m = E_0 \bar{f}_{barr}/T$. Hence near the bulk spinodal T_c where barriers vanish, there is a linear rise in temperature $\bar{t}_m \simeq E_0(T - T_c)/T$, that goes over to an exponential $t_m \sim e^{E_0(T-T_c)/T}$.

[14] K. Otsuka, N. Ren and T. Takeda, Scripta Mat. **45**,145 (2001); K. Otsuka, J. Phys. IV France **11**, 8 (2001).

[15] L. Müller , U. Klemradt, T.R. Finlayson, Mat. Sci. and Eng. A **438**, 122 (2006).

[16] S.R. Pati, M. Cohen, Acta Metallurgica **17**, 189 (1969); A.R. Entwisle, Metall. Trans., **2**, 2395 (1971); J.C. Guimaraes and P.R. Rios, J. Mater. Sc. **43**, 5206 (2008); K. Kakeshita, J-m. Nam and T. Fukuda, Sci. Technol. Adv. Mater. 12, 015004 (2011).

[17] G.V. Kurdjumov and O.P. Maximova, Doklad. Akad. Nauk SSSR **61**, 83 (1948); **73**, 95 (1950); V. Hardy, A. Maignan, S. Hebert, C. Yaicle, C. Martin, M. Hervieu, M. R. Lees, G. Rowlands, D. Mc K. Paul, and B. Raveau, Phys. Rev. B. **68**, 220402(R) (2003)

[18] K. Binder, W. Kob, *Glassy Materials and Disordered Solids: An In-*

troduction to Their Statistical Mechanics, World Scientific, Singapore (2005).

[19] P.G. Wolynes, J.N. Onuchi, D. Thirumalai, Science **267**, 1619 (1995); P.G. Wolynes, Proc. of the American Philos. Society **145**, 4 (2001); J. D. Bryngelson, J. N. Onuchic, N. D. Socci and P. G. Wolynes, Proteins: Structure, Function, and Genetics 21, 167 (1995).

[20] D. J. Bicout and A. Szabo, Protein Science **9**, 452 (2000).

[21] M. Cieplak and I. Sulkowska, J. Chem. Phy. **123**, 194908 (2005).

[22] N. Nakagawa, Phys. Rev. Lett. **98**, 128104 (2007).

[23] F. Ritort, Phys. Rev. Lett. **75**, 1190 (1995); S. Franz and F. Ritort, Europhys. Lett. **31**, 507 (1995).

[24] F. Ritort, J. Phys. Chem. B **108**, 6893 (2004); F. Ritort, cond-mat 0311370 v1 (2003); A. Crisanti, and F. Ritort, Europhys. Lett. **66** (2), 253 (2004); L.L. Bonilla, F.G. Padilla, F. Ritort, Physica A **250**, 315 (1998); A. Garriga and F. Ritort, Phys. Rev. E **72**, 031505 (2005); L. F. Cugliandolo, J. Kurchan, and L. Peliti, Phys. Rev. E **55**, 3898 (1997); J. Deng, X. Ding, T. Lookman, T. Suzuki, K. Otsuka, J. Sun, A. Saxena, and X. Ren, Phys. Rev. B **81**, 220101 (2010) and references therein.

[25] L. Buisson, S. Ciliberto and A. Garcimart, Europhys. Lett., **63** (4), 603 (2003).

[26] Y.H. Wen, Y.Z. Wang and L.Q. Chen, Philos. Mag. A **80**, 1967 (2000); Y. Wang and A.G. Khachaturyan, Mater. Sc. and Eng. A **438**, 55 (2006); N.A. Pertsev, J. Novak, and E.K.H. Salje, Philos. Mag. A **80**,

2201 (2000); A. M. Bratkovsky, S. C. Marais, V. Heine, and E. K. H. Salje, J. Phys. Condens. Matter **6**, 3679 (1994).

[27] S. Kartha, T. Castàn, J.A. Krumhansl, and J.P. Sethna, Phys. Rev. Lett. **67**, 3630 (1991); S. Kartha, J.A. Krumhansl, J.P. Sethna, and L. K. Wickham, Phys. Rev. B **52**, 803 (1995).

[28] A.E. Jacobs, S.H. Curnoe and R.C. Desai, Phys. Rev. B **68**, 224104 (2003); S.H. Curnoe and A.E. Jacobs,Phys. Rev. B **63**, 094110 (2001).

[29] S.R. Shenoy, T. Lookman, A. Saxena and A.R. Bishop, Phys. Rev. B**60**, R12537 (1999); T. Lookman, S.R. Shenoy, K.Ø. Rasmussen, A. Saxena and A.R. Bishop, Phys.Rev. B **67**, 024114 (2003); K.Ø. Rasmussen, T. Lookman, A. Saxena, A.R. Bishop, R.C. Albers, and S.R. Shenoy, Phys. Rev. Lett. **87**, 055704 (2001); G.S. Bales and R.J. Gooding, Phys. Rev. Lett. **67**, 3412 (1991).

[30] A. Paul, J. Bhattacharya, S. Sengupta, and M. Rao, J. Phys. Condens. Matter **20**, 365211 (2008).

[31] R. J. Baxter, *Exactly solved models in statistical mechanics*, Academic Press Inc., London (1982); M. Blume, V. J. Emery, and R. B. Griffiths, Phys. Rev. A **4**, 1071, (1971); F. Y. Wu, Rev. Mod. Phy. **235**, 60 (1982); R. Savit, Phys. Rev. B **22**, 3443 (1980).

[32] P. Lindgard and O.G. Mouritsen, Phys. Rev. Lett. **57**, 2458 (1986); E. Vives, J. Goicoechea, M.J. Ortin and A. Planes, Phys, Rev. E **52**, R5 (1995); J.F. Blackburn and E.K.H. Salje, Phy. Chem. Miner. **26**, 275 (1999); J.M. Ball and R.D. James, Phil. Trans. Roy. Soc. London A **338**, 389 (1992); D. Sherrington, J. Phys: Condens. Matt. **20**, 304213 (2008); C. Pariege, H. Zapolsky, and A.G. Khachaturyan,

Phys. Rev. B **75**, 054102 (2007); B. Cerruti and E. Vives, Phys. Rev. E **77**, 064114 (2008).

[33] S.R. Shenoy, T. Lookman and A. Saxena, Phys. Rev. B **82**, 144103 (2010); S. R. Shenoy and T. Lookman, Phys. Rev. B **78**, 144103 (2008).

[34] R. Vasseur , T. Lookman and S. R. Shenoy, Phys. Rev. B **82**, 094118 (2010).

[35] D. P. Landau and K. Binder, *A Guide to Monte Carlo Simulations in Statistical Physics*, Cambridge University Press (2009); K.P.N. Murthy, *Monte Carlo Methods in Statistical Physics*, Universities Press (2004); N. Metropolis, A. W. Rosenbluth, M. N. Rosenbluth, A. H. Teller, and E. Teller, J. Chem. Phys., **21** 1087 (1953).

[36] E.K.H. Salje, J. Koppensteiner, M. Reinecker, W. Schranz, and A. Planes, Appl. Phys. Lett. **95**, 231908 (2009).

[37] P. Bhimalapuram, S. Chakrabarty, and B. Bagchi, Phys. Rev. Lett. **98**, 206104 (2007); S. Bhattacharyya and B. Bagchi, ibid. **89**, 025504 (2002).

[38] A. Shah, S. Chakravarty and J.K. Bhattacharjee, Pramana **71**, 413 (2008); A.N. Kolmogorov, Dokl. Akad. Nauk SSSR **30**, 301 (1941).

[39] G.R. Barsch and J.A. Krumhansl, Metallurg. Trans. A **19**, 761 (1988); Phys. Rev. Lett. **53**, 1069 (1984); and in *Martensites*, ed. G.B. Olson and W.S. Owen, ASM International, Materials Park, Ohio, (1992).

[40] J.-C. Tolédano and P. Tolédano, *The Landau Theory of Phase Transitions*, World Scientific, Singapore, (1987); J.-C. Tolédano and P. Tolédano, Phys. Rev. B **21**, 1139 (1980); K. Aizu, J. Phys. Soc. Jpn.

27, 387 (1969); J. Sapriel, Phys. Rev. B **12**, 5128 (1975); H. T. Stokes and D. M. Hatch, *Isotropy Subgroups of the 230 Crystallographic Space Groups*, World Scientific, Singapore, (1988); The program ISOTROPY http://www.physics.byu.edu/~stokesh/isotropy.html by H.T. Stokes and D.M. Hatch generates all symmetry allowed invariants in strain tensor and strain gradient components.

[41] P. Chaikin and T. Lubensky, *Principles of Condensed Matter Physics*, Cambridge University Press, NY (2000); L. D. Landau and I. M. Lifshitz, *Theory of Elasticity*, Pergamon, NY (1980).

[42] S. Vedantam and R. Abeyratne, Int. J. of Nonlinear Mechanics, **40**, 177 (2003); F. Falk and J. Konopka, J. Phys:CM , **2**, 61 (1990).

[43] R.E. Newnham, *Properties of Materials*, Oxford University Press, Oxford (2005), Sections 13.6, and 23.4.

[44] S. Muto, R. Oshima and F.E. Fujita, Acta Metall. Mater., **38**, 85 (1990); S. Muto, R. Oshima and F. Fujita, Acta Metall. Mater., **4**, 685 (1990); M. Sato, B. Grier, S. Shapiro, H. Miyajima, J. of Physics F, **12**, 2117 (1982); A. Zheludev, S.M. Shapiro, F. Wochner, A. Schwarz, M. Wall and L. E. Tanner, Phys. Rev. B **51**, 11310 (1993).

[45] M. Blume, Phys. Rev. **141**, 517 (1966); H.W. Capel, Physica (Amsterdam) **32**, 966 (1966); J. Tobochnik, Phys. Rev. B **26**, 6201 (1982);

[46] A. Campa, T. Dauxois, and S. Ruffo, Phys. Reports **480** , 57 (2009); F.J. Dyson, Commun. Math. Phys. **12**, 91 (1969).

[47] J. Frenkel, *Kinetic theory of fluids*, Dover, New York (1955); A.J. Bray, Adv. Physics, **43**,357 (1994).

[48] K.P.N. Murthy and S.R. Shenoy, Phys. Rev A **36**, 5087 (1987); S.R. Shenoy and G.S. Agarwal, Phys. Rev. A **29**, 1315 (1984).

[49] D.W. Scott, Biometrika **66**, 605 (1979). .

[50] N.H. Anderson, B. Lebech, and Poulsen, Physica C 172, 31-42 (1990).

[51] (a). J. Cui, T.W. Shield, R.D. James, Acta. Materialia **52**, 35 (2004); (b). Y. Koyoma, T. Ukena and O. Nittono, J. Jap. Inst. Metals **44**, 1431 (1980); (c). T. Takaki, K. Katsuki, and K. Shimizu, Suppl. Trans. Jap. Inst. Metals. **17**, 187 (1976); (d). A. J. Morton and C. M. Wayman, Acta Metall. **14**, 1567 (1966); (e). A. B. Greninger and R. Troiano, Metals Trans. AIME **185**, 591 (1949); (f). H. Okamoto, M. Oka, and I. Tamura, Trans. Jap. Inst. Metals **19**, 674 (1978); (g). M. Watanabe and C. M. Wayman, Met. Trans. **2**, 2229 (1971); (h). L. Guttman, Tras. AIME J. Metals **188**, 1472 (1950); (i). K. Enami and S. Nenno, Metall. Trans. **2**, 1487 (1971); (j). V. Kravesec, Phys. Stat. Solidi A 30, **241** (1975).

[52] D.E. Jesson, K.M. Chen, S.J. Pennycook, T. Thundat and R.J. Warmack, Phys. Rev. B **77**, 1330 (1996).

[53] N. Gnan, C. Maggi, T.B. Scϕder, and J.C. Dyre, Phys. Rev. Lett. **104**, 125902 (2010).

[54] N. Shankaraiah, K. P. N. Murthy, T. Lookman and S. R. Shenoy, EuroPhys. Lett. (EPL) **92** 36002 (2010).

[55] N. Shankaraiah, K. P. N. Murthy, T. Lookman and S. R. Shenoy, Phys. Rev. B **84**, 064119 (2011); Solid State Phenomena, **185**, 31 (2012).

[56] N. Shankaraiah, K. P. N. Murthy, T. Lookman and S. R. Shenoy, J. Alloys Compd. (2012), doi:10.1016/j.jallcom.2012.03.034.

[57] N. Shankaraiah, K. P. N. Murthy, T. Lookman and S. R. Shenoy, (Unpublished).

List of Publications

1. Incubation times and entropy barriers in martensitic kinetics: Monte Carlo quench simulations of strain pseudospins
   N. Shankaraiah, K. P. N. Murthy, T. Lookman and S. R. Shenoy
   Europhysics Lett. 92 36002 (2010).

2. Monte Carlo simulations of strain pseudospins: Athermal martensites, incubation times, and entropy barriers
   N. Shankaraiah, K. P. N. Murthy, T. Lookman and S. R. Shenoy
   Phys. Rev. B 84, 064119 (2011).

3. Athermal Martensites, Temperature-Time-Transformation Diagrams and Thermal Hysteresis: Monte Carlo Simulations of Strain Pseudospins
   N. Shankaraiah, K. P. N. Murthy, T. Lookman and S. R. Shenoy
   Solid State Phenomena 185, 31 (2012).

4. Conversion Times and Energy/Entropy Barriers in Isothermal/Athermal Martensites
   N. Shankaraiah, K. P. N. Murthy, T. Lookman and S. R. Shenoy
   Journal of Alloys and Compounds (2012), doi:10.1016/j.jallcom.2012.03.034.

MANUSCRIPTS UNDER PREPERATION

1. Re-equilibration after deep temperature quenches in athermal martensites : Golf-holes, entropy barriers and effective temperatures
   N. Shankaraiah, K. P. N. Murthy, T. Lookman and S. R. Shenoy (*Manuscript under preparation*).

2. Microstructures, conversion-delay tails and entropy barriers in 2D martensitic models with vector strain-pseudospins
   N. Shankaraiah, K. P. N. Murthy, T. Lookman and S. R. Shenoy (*Manuscript under preparation*) .

3. Three-dimensional microstructures, conversion-delays and entropy barriers in athermal martensites
   N. Shankaraiah, K. P. N. Murthy, T. Lookman and S. R. Shenoy (*Manuscript under preparation*).

PRESENTATIONS

1. **N. Shankaraiah**, K. P. N. Murthy, T. Lookman and S. R. Shenoy Poster entitled *Microstructures at small scales in martensites: Monte Carlo study of strain pseudospins* presented at Workshop on Physics at small scales (18-19 Mar, 2011), University of Hyderabad, Hyderabad, India. **(Selected as one of the 6 best posters).**

2. **N. Shankaraiah**, K. P. N. Murthy, T. Lookman and S. R. Shenoy Poster entitled *Incubation times and entropy barriers in athermal martensites: Conceptual implications for protein dynamics ?* presented at School and conference on Mathematics and Physics of Soft and Biological Matter (2 -13 May, 2011) ICTP, Trieste, Italy.

3. **N. Shankaraiah**, K. P. N. Murthy, T. Lookman and S. R. Shenoy
   Poster entitled *Microstructures and conversion delays in martensites: Monte Carlo study of strain pseudospin models* presented at Symposium on Frontiers in Physics (28-29 Oct, 2011), University of Hyderabad, India. **(Selected as one of the 9 best posters).**

4. **N. Shankaraiah**, K. P. N. Murthy, T. Lookman and S. R. Shenoy
   Poster entitled *What happens after a deep tempearature quench in athermal martensites: Energy distributions, energy surfaces and effective tempearatures* presented at 'Unifying Concepts in Materials': J A Krumhansl School & Symposium 2012 (30 Jan- 08 Feb, 2012), JNCASR & NCBS, Bangalore.

5. **N. Shankaraiah**, K. P. N. Murthy, T. Lookman and S. R. Shenoy
   Oral entitled *Monte Carlo study of martensitic transformations: pseudospin model* presented at SERC School on Computational Statistical Physics (Dec 1-21, 2008), IIT Guwahati, India.

6. **N. Shankaraiah**, K. P. N. Murthy, T. Lookman and S. R. Shenoy
   Oral entitled *Incubation times and entropy barriers in athermal martensites: Monte Carlo simulations of strain pseudospin model* presented at ICMAT-2011 (26 June- 1 July, 2011), Suntec, Singapore.